



This is to certify that the

dissertation entitled

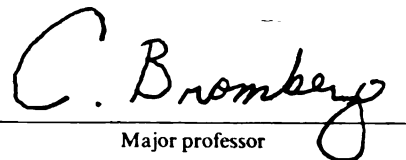
A COMPARISON OF HIGH TRANSVERSE MOMENTUM
DIRECT PHOTON AND NEUTRAL PION EVENTS
IN NEGATIVE PION AND PROTON-NUCLEUS COLLISIONS
AT 31.5 GeV CENTER OF MASS ENERGY

presented by

David Shaw Brown

has been accepted towards fulfillment
of the requirements for

Ph.D degree in Physics


Major professor

Date 12/14/92

LIBRARY
Michigan State
University

PLACE IN RETURN BOX to remove this checkout from your record.
 TO AVOID FINES return on or before date due.

DATE DUE	DATE DUE	DATE DUE
_____	_____	_____
_____	_____	_____
_____	_____	_____
_____	_____	_____
_____	_____	_____
_____	_____	_____
_____	_____	_____
_____	_____	_____

MSU Is An Affirmative Action/Equal Opportunity Institution

c:\circ\date\due pm3-p.1

AMST 12-1977

A COMPARISON OF HIGH TRANSVERSE MOMENTUM
DIRECT PHOTON AND NEUTRAL PION EVENTS
IN NEGATIVE PION AND PROTON-NUCLEUS COLLISIONS
AT 31.5 GeV CENTER OF MASS ENERGY

By

David Shaw Brown

A DISSERTATION

Submitted to
Michigan State University
in partial fulfillment of the requirements
for the degree of

DOCTOR OF PHILOSOPHY

Department of Physics

1992

ABSTRACT

A COMPARISON OF HIGH TRANSVERSE MOMENTUM DIRECT PHOTON AND NEUTRAL PION EVENTS IN NEGATIVE PION AND PROTON-NUCLEUS COLLISIONS AT 31.5 GeV CENTER OF MASS ENERGY

By

David Shaw Brown

I want to express my appreciation for the efforts of all those who made this possible, and post-docs. I know our relationship has been tough at times, but I am grateful. The quality, importance, and relevance of the work done here is a testament to the efforts of the photon group, and those who put the effort into running. Many thanks to Marek Zdzienicka, George Fanourakis, Clark Chandler, Armando Lanas, Bill Deese, Chris Lusk, and others who have helped me in many ways. Dhanmika Werasandura, Richard Benson, and others who have helped me build as well.

The purpose of this analysis is to compare the associated charged particle structure of high $p_{\perp} \pi^0$ and direct photon events to see if they are indeed different. The current theory of hadron-hadron interactions, quantum chromodynamics, makes a number of predictions indicating that they are. The charged particles recoiling from a high $p_{\perp} \gamma$ or π^0 trigger will be used to reconstruct the $\pi^0 + \text{jet}$ and $\gamma + \text{jet}$ angular and invariant mass distributions for this study. Finally, the invariant mass distributions will be employed to study the gluon structure functions of hadrons.

could not have completed my studies without his guidance and many helpful insights along the way. I thank him.

ACKNOWLEDGEMENTS

through the years. I must also thank Sudhindra Mani for enduring so many long discussions about where to go with the charged tracking analysis. We have had many arguments, but they clarified a

number of issues for me. The success of the experiment is due to the collaboration of many individuals. First, I would like to extend my gratitude to all of those involved in making E706 an operational, and successful experiment. A number of these individuals are non-physicists who didn't share in the excitement and glory of doing any physics. They worked hard within the narrow window of their specialty, often providing expert advice and getting us cocky graduate students out of numerous jams during the construction of the calorimeters.

The collaboration's senior members have been instrumental in making this experiment and used their expertise to help me. They also kept me motivated and helped me in making decisions. I want to express my appreciation for the efforts of all first run graduate students and post-docs. I know our relationship has been rough at times, but I am truly grateful. The validity, importance and relevance of my analysis rests on the monumental efforts of the photon group, and those who got the tracking code up and running. Many thanks to Marek Zielinski, Joey Huston, Phil Gutierrez, Takahiro Yasuda, George Fanourakis, Clark Chandlee, John Mansour, Dane Skow, Eric Prebys, Armando Lanaro, Bill Desoi, Chris Lirakis, Alex Sinanidis, Carlos Yosef, Ioanis Kourbanis, Dhammika Weerasundra, Richard Benson, Brajeesh Choudhary, Casey Hartman, Sajan Easo, and Guiseppe Ballochi. Oh and thanks for the grapa, Guiseppe. Maybe again sometime...

There are three individuals I want to single out as being instrumental in directing me along the path I took for my analysis. First, there is my advisor, Carl Bromberg. Carl has made many important contributions to the experiment, including a first rate MWPC system. He has endured many frustrations as well. I must admit I have been the cause more than once. His willingness to endure and overcome my hardheadedness has saved me much embarrassment. Carl's understanding of and experience in hadron-hadron collisions at high p_{\perp} provided the subject matter for my analysis. However, I

could not have completed my studies without his guidance and many helpful insights along the way. I thank him for his continual support through the years. I must also thank Sudhindra Mani for enduring so many long discussions about where to go with the charged tracking analysis. We have had many arguments, but they clarified a number of issues for me. The same goes for the noble/notorious George Ginther. He has made many extraordinary efforts, including the data summary work. Besides "canning" the data for us students, he got "canned" plenty in our sundry discussions, which more than once turned into acrimonious debate. Thank you George for your patience and help in making me an experimentalist. At least I usually look before I leap now.

The collaboration's senior members played very pivotal roles. They conceived this experiment, and used their expertise in seeing it become a reality. Thanks to the Rochester members for providing invaluable help and effort in designing the electromagnetic calorimeter. They also kept the experiment alive at Fermilab during the many years prior to data taking. The Pennsylvania State Univeristy, University of Pittsburg and Michigan State University people were instrumental in furnishing the tracking system upon whose data my analysis depends heavily.

My parents deserve special credit in providing much needed emotional support during this long arduous venture. I have not been able to see them very much these past ten years, but thanks to AT&T and the U.S. mail system the lines of communication have remained open! I also want to express appreciation for their lovingkindness during my childhood years. It was they who encouraged and initially nurtured my interest in science from an early age. Last but not least I am deeply indebted to the American taxpayers, who have shelled out the better part of a million bucks so that I could get a Ph.D. in high energy physics. I hope I am worth the investment.

TABLE OF CONTENTS	
1	Motivation
1.1	Current View of Hadron-Hadron Collisions
1.1.1	The Factorization Scheme
1.1.2	Hard-Scatter Kinematics
1.1.3	The Meaning of $d\sigma/d\hat{t}$
1.2	Direct Photons and QCD
1.3	Experimental Considerations
1.4	Thesis Goals
1.4.1	Biases in $\cos\theta^*$
1.4.2	Biases in M
1.5	Thesis Outline
2	Experimental Setup
2.1	Beamline
2.1.1	The Cerenkov Detector
2.1.2	The Hadron Shield and Veto Wall
2.2	Liquid Argon Calorimeters
2.2.1	EMLAC Design
2.2.2	EMLAC Construction
2.2.3	The Hadron Calorimeter
2.2.4	LAC Electronics

2.3	The E706 Trigger System	64
2.3.1	EMLAC p_{\perp} System	67
2.3.2	Beam and Interaction Definition	72
2.3.3	Vetoing Elements	75
2.3.4	High Level Trigger Operation	77
2.4	Charged Tracking System	78
2.4.1	SSD System	79
2.4.2	MWPC System	83
2.4.3	MWPC Gas System	104
2.4.4	Tracking System Electronics	107
2.4.5	MWPC Commissioning	110
2.5	The Forward Calorimeter	112
3	Data Reconstruction	117
3.1	EMLAC Reconstruction	117
3.1.1	EMREC Unpacking	118
3.1.2	Shower Reconstruction	119
3.1.3	TVC Reconstruction	124
3.2	Tracking Reconstruction	126
3.2.1	MWPC Space Track Reconstruction	126
3.2.2	SSD Track Reconstruction	128
3.2.3	Linking	129
3.2.4	Event Vertex Reconstruction	130
3.2.5	Relinking	133
3.2.6	Track Momentum Reconstruction	133
3.3	Track Quality Studies	135
3.3.1	Alignment and Plane's Efficiencies	135

3.3.2	Quality of Track Reconstruction	140
3.3.3	Track Quality Cuts	142
3.3.4	Comparison of Data and Monte Carlo	144
3.4	Discrete Logic Reconstruction	151
4	Event Selection	153
4.1	Whole Event Cuts	153
4.2	Muon and Hadron Backgrounds	154
4.3	π^0 Reconstruction	166
4.4	Single Photon Reconstruction	170
4.5	Systematics	170
4.6	π^0 Background Calculation	172
5	Event Features	175
5.1	Differences Between γ s and π^0 s	175
5.2	Rapidity Correlations	178
6	Jet Reconstruction	192
6.1	Jet Algorithms	192
6.1.1	Cone Algorithm	193
6.1.2	WA70 Algorithm	194
6.2	The Jet Monte Carlo	195
6.2.1	Implementation of ISAJET	195
6.2.2	Detector Simulation	196
6.3	Jet Algorithm Performance	198
6.3.1	Jet Axis Resolution	199
6.3.2	Jet Finding Efficiency	204
6.3.3	Parton Variables	205

6.4	Measurement of $\cos \theta^*$ and M	212
6.4.1	$\cos \theta^*$	213
6.4.2	Cross Sections in M	213
7	Final Results	222
7.1	π^0 Background Subtraction	224
7.2	Results for $\cos \theta^*$	229
7.3	$\pi^0 + \text{jet}$ and $\gamma + \text{jet}$ M Distributions	237
7.4	Errors	251
8	Summary and Conclusion	255
A	Corrections to the "Kick" Approximation	257
B	Fake Tracks	260
C	Track Reconstruction Efficiency	266
D	Trigger Particle Corrections	272
D.1	Corrections for Cuts	272
D.2	Corrections for Inefficiencies	273
D.3	Photon Energy Corrections	276
1.7	An illustration of the bias in $\cos \theta^*$ as a result of the detector's acceptance being $< 4\pi$	28
2.1	E706 Plan View	30
2.2	A schematic of the MWEST secondary beamline. All devices are represented in terms of their optical equivalents.	31
2.3	Examples of C pressure curves for both beam polarities. The peaks for each type of beam particle are labeled accordingly.	32

2.4	Isometric drawing of the hadron shield, showing the central vertical slab through which the beam passes. This piece was removed during LAC calibration.	34
2.5	Sketch of the beam's path through the counters. Each square represents one scintillation counter.	36
<h2 style="text-align: center;">LIST OF FIGURES</h2>		
1.1	A hadron-hadron collision according to the factorization scheme; two partons undergo a hard scatter.	7
1.2	All possible parton-parton scatters in first order QCD. The Mandelstam variables are for the constituent processes. A common factor of $\pi\alpha_s^2/s^2$ has been left out.	12
1.3	1st order direct photon subprocesses in QCD.	14
1.4	Bremstrahlung contribution to direct photon production.	16
1.5	Theoretical $\text{di-}\pi^0$ and single photon $\cos\theta^*$ distributions from Owens. The calculations for prompt photons are presented with and without the Bremsstrahlung contribution. The recoil jet is defined as the leading hadron away from the trigger in ϕ .	17
1.6	Scatter plot of $\cos\theta^*$ vs τ . The region between the two horizontal lines, and to the right of the vertical line is unbiased from the trigger over the measured interval of $\cos\theta^*$.	24
1.7	An illustration of the bias in $\cos\theta^*$ as a result of the detector's acceptance being $< 4\pi$.	25
2.1	E706 Plan View	30
2.2	A schematic of the MWEST secondary beamline. All devices are represented in terms of their optical equivalents.	31
2.3	Examples of \hat{C} pressure curves for both beam polarities. The peaks for each type of beam particle are labeled accordingly.	33

2.4	Isometric drawing of the hadron shield, showing the central vertical slab through which the beam passes. This piece was removed during LAC calibration.	33
2.5	Sketch of the Veto Wall planes. The arrows represent the beam's passage through the counters. Each square represents one scintillation counter.	34
2.6	Layout of the calorimeters on the gantry support structure. Also shown are the filler vessel, the beam tube, and the Faraday room.	36
2.7	Isometric and Cross-sectional views of an EMLAC sampling cell, showing the r - ϕ geometry of the charge collection layers.	39
2.8	Cut-view drawing of the EMLAC illustrating r -strip focusing.	41
2.9	Longitudinal segmentation as an aid to π^0 reconstruction. Showers have narrower profiles in the EMLAC's front section, allowing both decay photons to be resolved.	42
2.10	Isometric drawing of the EMLAC with an exploded view of one quadrant.	47
2.11	Drawing of the Physical Boundaries for the sensitive area of an EMLAC Quadrant.	48
2.12	Typical layout of r and ϕ strips on the readout boards for the EMLAC.	50
2.13	Signal summing scheme in the EMLAC. Signals in a quadrant are summed in the front and back sections separately. These sums are grouped into outer r , inner r , outer ϕ , and inner ϕ views.	51
2.14	Cross-sectional view of an EMLAC cell at the outer edge of the electromagnetic calorimeter.	52
2.15	Cross-sectional drawing of a quadrant support assembly for the EMLAC	53
2.16	Front and side views of the hadron calorimeter. Steel "Zorba Plates" are the absorber media. The hole, shown in the center of the front view, allows passage of beam and halo particles.	55

2.17 Exploded portion of a HADLAC charge collection cell or "cookie". . .	58
2.18 Schematic of a LAC amplifier channel showing the Sample-and-Hold, TVC, and Fast Out circuits.	61
2.19 An example of an Event Timing Sequence initiated by the BAT mod- ules. An event fires the master TVC, but fails to produce a PRE- TRIGGER signal. A short time later, an event fires the slave TVC, generating a PRETRIGGER and BEFORE pulses as well.	65
2.20 A simplified diagram for a TVC unit.	66
2.21 Octant r-channel summing scheme employed by the local p_{\perp} modules. These modules produced summed signals for groups of 8 and 32 strips. 69	69
2.22 Front-back summing scheme employed by the local discriminator mod- ules.	70
2.23 Schematic of the EMLAC charge collection circuit (one channel). . .	72
2.24 The effect of image charge on the global trigger input signal.	73
2.25 The configuration of scintillation counters used the the beam and in- teraction definitions.	74
2.26 Schematic diagram of the interaction pile-up filter, and live interaction definition circuits.	76
2.27 Schematic of the segmented target/SSD system of E706. A typical multiple event is superimposed on the planes.	81
2.28 Readout electronics schematic used to determine operating character- istics of SSD system.	82
2.29 Arrangement of sense planes in each MWPC module.	85
2.30 Electric field equipotential and field lines in a multiwire proportional chamber. The effect on the field due a small displacement of one wire is also shown.	86

2.31	Principle of construction and definition of parameters in a multiwire proportional chamber. A set of parallel anode wires is mounted symmetrically between two cathode foils.	90
2.32	Equilibrium configuration of anode wires in a large proportional chamber under the influence of the device's electric field.	94
2.33	MWPC test system used to determine latch delays.	111
2.34	A high voltage plateau curve for MWPC module 3.	113
2.35	Perspective drawing of the Forward Calorimeter with an exploded view of one of the modules.	115
3.1	The z coordinate distribution for matched vertices within the target volume. The different target elements are clearly resolved.	134
3.2	The χ^2 distributions for 16, 15, 14, and 13 hit physics tracks	138
3.3	Y distribution of tracks	145
3.4	Y-view impact parameter distribution of tracks	146
3.5	Y distributions for all tracks, and tracks passing the track quality cuts.	148
3.6	Multiplicity distributions for all tracks, and tracks passing the track quality cuts. The monte carlo result has been superimposed as a smooth curve.	149
3.7	Momentum distributions for all tracks, and tracks passing the track quality cuts. The monte carlo result has been superimposed as a smooth curve.	150
4.1	Illustration of photon directionality and related quantities. A showering muon from the beam halo will have a larger directionality than a photon emanating from the target.	157

4.2	Photon p_{\perp} vs directionality for events in which the veto wall quadrant shadowing the trigger quadrant had a hit in either wall (left), and had no hit (right).	154
4.3	TVC distributions for non- μ (left) and μ induced (right) events.	160
4.4	δ_t vs TVC time for events with a veto wall hit (top) and without a veto wall hit (bottom). The data in the region outside the vertical lines and above the horizontal line is excluded by the directionality and timing cuts.	161
4.5	Δr between showers and nearest tracks (left); Δr between high p_{\perp} photons and nearest tracks (right)	163
4.6	$E_{\text{front}}/E_{\text{total}}$ for Hadron Showers (top) and Electron Showers (bottom).	164
4.7	$E_{\text{front}}/E_{\text{total}}$ for High p_{\perp} Photon Showers (top) and μ Showers (bottom).	165
4.8	$\gamma\gamma$ Mass Spectrum	168
4.9	Asymmetry distributions for π^0 's without sidebands subtracted (top) and with sidebands subtracted (bottom).	169
5.1	ϕ density distributions for charged particles in high p_{\perp} π^0 and single photon events with $5.0 \leq p_{\perp} < 5.5 \text{ GeV}/c$.	179
5.2	ϕ density distributions for charged particles in high p_{\perp} π^0 and single photon events with $p_{\perp} \geq 5.5 \text{ GeV}/c$.	180
5.3	q_{\perp} weighted ϕ distributions for charged particles in high p_{\perp} π^0 and single photon events with $5.0 \leq p_{\perp} < 5.5 \text{ GeV}/c$.	181
5.4	q_{\perp} weighted ϕ distributions for charged particles in high p_{\perp} π^0 and single photon events with $p_{\perp} \geq 5.5 \text{ GeV}/c$.	182
5.5	p_{\perp} weighted ϕ distributions for charged particles in high p_{\perp} π^0 and single photon events with $5.0 \leq p_{\perp} < 5.5 \text{ GeV}/c$.	183
5.6	p_{\perp} weighted ϕ distributions for charged particles in high p_{\perp} π^0 and single photon events with $p_{\perp} \geq 5.5 \text{ GeV}/c$.	183

5.6	p_{\perp} weighted ϕ distributions for charged particles in high p_{\perp} π^0 and single photon events with $p_{\perp} \geq 5.5$ GeV/c.	184
5.7	Δy distributions for 1st and 2nd highest p_{\perp} recoil tracks (left), and 1st, 3rd, 4th, . . . highest p_{\perp} tracks (right).	188
5.8	Δy between highest p_{\perp} recoil track and the trigger particle.	189
5.9	Δy distribution of highest p_{\perp} recoil charged pair for ISAJET generated data (left), and phase-space monte carlo data (right). The uncorrelated	
6.10	Δy distributions appear as smooth curves.	190
5.10	Δy between the highest p_{\perp} recoil charged pair in data with the corresponding ISAJET result superimposed as a smooth curve.	191
6.1	The p_{\perp} imbalance between the two hard scatter jets in ISAJET with $\langle k_{\perp} \rangle = 0.95$ GeV/c.	197
6.2	Scatter plots of jet resolution over the acceptance for Cone (Top) and WA70 (Bottom) algorithms.	201
6.3	$\delta \cos \theta$ distributions for Cone (Left) and WA70 (Right) algorithms integrated over the acceptance.	202
6.4	Scatter plots of $\delta \cos \theta$ between WA70 and Cone algorithms over the acceptance for data (Top) and monte carlo (Bottom).	203
6.5	The jet finding efficiency for Cone and WA70 algorithms as a function of the trigger's p_{\perp} . Monte carlo is superimposed on the data.	207
6.6	Resolution plots of the reconstructed jet momentum for π^0 triggers integrated over the acceptance.	208
6.7	Resolution plots of the reconstructed jet momentum for γ triggers integrated over the acceptance.	209
6.8	$\delta x/x$ resolution plots for parton momenta in high p_{\perp} π^0 events, integrated over the acceptance.	210

6.9	$\delta x/x$ resolution plots for parton momenta in high p_{\perp} single photon events, integrated over the acceptance.	211
6.10	Effects of M and η_B cuts which unbiased the reconstructed $\cos \theta^*$ distribution.	214
6.11	η_B for high p_{\perp} π^0 's produced via proton-nucleus collisions.	215
6.12	Reconstructed and parton level $\cos \theta^*$ distributions for high p_{\perp} π^0 events. The parton level distribution is shown as a smooth curve. . .	216
6.13	Reconstructed and parton level $\cos \theta^*$ distributions for high p_{\perp} single photon events. The parton level distribution is shown as a smooth curve.	217
6.14	Reconstructed and parton level M distributions for high p_{\perp} π^0 events. The parton level distribution is shown as a smooth curve.	220
6.15	Reconstructed and parton level M distributions for high p_{\perp} direct photon events. The parton level distribution is shown as a smooth curve. .	221
7.1	Inclusive γ/π^0 ratio for π^- -nucleus collisions	227
7.2	Inclusive γ/π^0 ratio for proton-nucleus collisions	228
7.3	Scatter plots of $\cos \theta^*$ and M versus p_{\perp} for π^0 events	230
7.4	Absolute $\cos \theta^*$ plots for γ 's and π^0 's in π^- data	233
7.5	Absolute $\cos \theta^*$ plots for γ 's and π^0 's in proton data	234
7.6	γ to π^0 ratio in $\cos \theta^*$ for π^- data (top) and proton data (bottom) . .	235
7.7	Absolute $\cos \theta^*$ plots for γ 's and π^0 's in π^- data	238
7.8	Absolute $\cos \theta^*$ plots for γ 's and π^0 's in proton data	239
7.9	γ to π^0 ratios in $\cos \theta^*$ for π^- data (top) and proton data (bottom) .	240
7.10	Absolute $\cos \theta^*$ plots for γ 's and π^0 's in π^- data with no π^0 background subtraction for the γ 's	241
7.11	γ to π^0 ratio in $\cos \theta^*$ for π^- data without π^0 background subtraction	242
7.12	π^0 + jet cross section in M for π^- beam	245

7.13 γ + jet cross section in M for π^- beam	246
7.14 π^0 + jet cross section in M for proton beam	247
7.15 γ + jet cross section in M for proton beam	248
7.16 π^0 + jet and γ + jet cross sections in M for π^- beam. The γ distribution is unsubtracted.	249
7.17 Ratio of absolute π^0 + jet cross sections between π^- and proton beams. 1.1 The additive quantum numbers for the six flavors of quarks There is no $\cos \theta^*$ cut.	252
7.18 Ratio of absolute γ + jet cross sections between π^- and proton beams. 1.2 The constituent quark content of some common hadrons 2.1 There is no $\cos \theta^*$ cut.	253
beam. A.1 Top: A track's orientation in the bend plane as it passes through the 2.2 Trigger threshold settings for the magnet analyzing magnet's field. Bottom: The angles involved in magnetic 2.3 Relevant geometrical parameters for MWPC sensors field corrections.	258
2.4 Electrostatic parameters for all MWPC sensors B.1 Scatter plot of ΔX vs ΔY for tracks and nearest showers	261
B.2 EMLAC efficiency in P for high quality 16-hit tracks (top) and all high quality tracks (bottom).	262
B.3 b_y distribution for physics tracks that are linked in the x-view to an 3.1 List of MWPC Plane 3 Elements 4.1 SSD track, assigned to the primary vertex.	264
4.2 Corrections for whole event C.1 A typical relative hit multiplicity distribution for the physics tracks	269
4.3 False γ fractions in p_{\perp} for physics and π^0 events C.2 Relative hit multiplicity distributions of physics tracks for the four 7.1 separate data sets. The monte carlo prediction appears as the dotted 7.2 bars.	270
C.3 Relative hit multiplicity distributions for positive data (Left) and neg- ative data (Right). These plots are for tracks that do not project out- side the MWPC acceptance. Also shown is the binomial distribution for $\langle \epsilon \rangle = 0.92$; the binomial distribution is plotted as dotted bars.	271

Chapter I

Motivation

LIST OF TABLES

Over the past twenty years, a picture of hadronic structure and collision processes has emerged. This picture is fundamental for two reasons. First, it describes hadrons as being composed of structureless, pointlike objects called partons. Second, it views a high energy collision involving hadrons as an interaction between partons. If the collision is sufficiently violent, a simple picture of the parton level interaction emerges, which leads to predictions of the final state. There are two distinct classes of particles based on their spin quantum number. Spin-1/2 particles are called fermions and spin-0 particles are called bosons. Fermions are known as quarks and color. Color is a property of quarks and gluons, which are the carriers of the strong interaction. Fermions are composed of just two basic kinds of quarks, up and down quarks. Gluons are massless and carry no flavor or electric charge. However, they do exist in eight different superpositions of a color and anticolor state. They are thought to play a role in confining quarks within the volume of a hadron ($\sim 1 \text{ fm}^3$), hence the name	
1.1 The additive quantum numbers for the six flavors of quarks.	2
1.2 The constituent quark content of some common hadrons	2
2.1 Fractions of the various particle species in the 500 GeV/c secondary beam.	32
2.2 Trigger threshold settings by run number.	71
2.3 Relevant geometrical parameters for MWPC anodes (MKS units).	89
2.4 Electrostatic parameters for all MWPC anodes.	91
2.5 Sizes of the various cathode regions in each module.	101
2.6 Orientation and positions of the garlands in each plane.	101
3.1 List of MWPC Plane Efficiencies	139
4.1 E706 data divided by beam and target type.	154
4.2 Corrections for whole event cuts, and cuts for single photons.	172
4.3 False γ fractions in p_{\perp} for proton and π^{-} beams.	174
(d) 7.1 Monte carlo data sets by collision and trigger particle type.	225
7.2 Summary of differences between γ s and π^0 s in $\cos \theta^*$	237
B.1 List of fake track fractions.	265

Chapter 1

Motivation

Over the past twenty years or so a fundamental picture of hadronic structure and collision processes has emerged. This picture is fundamental for two reasons. First, it describes hadrons as being composed of structureless or pointlike objects called partons. Second, it views a high energy collision involving hadrons as an interaction between partons. If the collision is sufficiently violent, a simple picture of the parton level interaction emerges, which leads to predictions for absolute cross sections.

There are two distinct classes of partons based on the spin quantum number. Spin-1/2 or fermionic partons are called quarks. Quarks carry electric charge such that $e_q = \pm \frac{1}{3}|e|$ or $e_q = \pm \frac{2}{3}|e|$ where e_q is the quark charge and $|e|$ is the absolute value of the electron's charge. Quarks possess two other discrete quantum numbers known as flavor and color. Six different flavor states and three different color states are possible. Flavor is important in the weak interactions involving quarks, whereas color plays a role in the strong interaction. While it is true that some quarks are known to be massive, a quark's mass appears to be completely correlated with its flavor quantum number. Table 1.1 gives the additive quantum numbers for the six different flavors of quarks. Note that the top quark has not yet been discovered. Nucleons and pions are composed of just two kinds of quarks, up (u) and down (d). The quark content of the more common hadrons is shown in Table 1.2.

The other major group of partons consists of spin-1 objects called gluons. Gluons are massless and carry no flavor or electric charge. However, they do exist in eight different superpositions of a color and anticolor state. They are thought to play a role in confining quarks within the volume of a hadron ($\sim 1 \text{ fm}^3$), hence the name.

Sometimes a violent collision involving a small amount of energy can produce a large component of its momentum transverse to the collision axis.

Table 1.1: The additive quantum numbers for the six flavors of quarks.

Quark Flavors						
Quantum Number	d	u	s	c	b	t
Q-electric charge	$-\frac{1}{3}$	$+\frac{2}{3}$	$-\frac{1}{3}$	$+\frac{2}{3}$	$-\frac{1}{3}$	$+\frac{2}{3}$
I_3 -isospin	$-\frac{1}{2}$	$+\frac{1}{2}$	0	0	0	0
S-strangeness	0	0	-1	0	0	0
C-charm	0	0	0	+1	0	0
B-bottomness	0	0	0	0	-1	0
T-topness	0	0	0	0	0	+1

Table 1.2: The constituent quark content of some common hadrons

Hadron	Quark Contents
p	uud
n	udd
π^+	$u\bar{d}$
π^0	$u\bar{u}, d\bar{d}$
π^-	$\bar{u}d$
K^+	$u\bar{s}$
K^-	$\bar{u}s$
K^0	$d\bar{s}$
\bar{K}^0	$\bar{d}s$

Sometimes a violent collision involving a quark produces a photon with a large component of its momentum transverse to the collision axis. Such photons are called direct or prompt photons. The processes responsible for their production are analogous to electron bremsstrahlung in the nuclear coulomb field, electron-positron annihilation into gamma rays, and the Compton scattering of electrons by high energy X-rays. The study of direct photons is interesting for several reasons:

- Prompt photons emanate from the hard scatter with no further scattering among constituents. They are thus a direct probe of the parton-parton interaction, and allow the kinematics to be more clearly understood.
- Only a few subprocesses produce them so the overall interaction is easier to interpret.
- A direct measurement of the gluon content of hadrons is possible.
- It is possible to ascertain at least qualitatively the differences between quarks and gluons. Such differences, if they exist, can be compared to those expected from theory. In particular, it can be determined whether or not quark and gluon final states produce different hadronic spectra.

Unfortunately, direct photon events are quite rare, representing less than .1% of the total proton cross section. One reason is that the fraction of events containing particles whose transverse momenta are a significant portion of the c.m. energy is very small. Even if the experiment selects only high p_{\perp} events online the prompt photon sample will be sparse for two reasons. First, direct photon production relative to high p_{\perp} parton production goes as $\lesssim \alpha_{em}/\alpha_s$. α_{em} and α_s are the coupling constants for the electromagnetic and strong interactions respectively. Naively, $\alpha_s \lesssim 1$ so the cross section is already down two orders of magnitude. Second, there are considerably more types of processes available for producing generic hard scatters as opposed to the

limited number capable of generating direct photons. It is a great technical challenge indeed to collect a statistically significant and normalizable sample of these events.

1.1 CURRENT VIEW OF HADRON-HADRON COLLISIONS

Before delving into the 1988 data analysis an elaboration of the high momentum transfer, Q^2 , scattering process is in order. This discussion will clarify the terminology used in the analysis procedure, and provide a description of the kinematics governing such reactions. As far as labelling is concerned, all hadron names and dynamical variables will be denoted by uppercase letters. Parton names and variables will appear in lowercase.

1.1.1 The Factorization Scheme

Figure 1.1 provides a schematic illustration of a typical high p_{\perp} collision between two hadrons, A and B. The hadrons are viewed as clouds of partons passing through one another such that a parton from A and a parton from B experience a violent scattering. Partons c and d then emerge from this collision with large components of their momenta transverse to the collision axis. Q^2 refers to the momentum exchanged between a and b. While Q^2 cannot, generally speaking, be expressed in terms of experimental quantities, it is certainly true that $Q^2 \propto p_{\perp}^2$. This is because p_{\perp} is invariant under Lorentz boosts along the collision axis.

The interaction of hadrons A and B is believed to occur in three stages:

- At some instant as the hadrons A and B pass through one another partons a and b have momenta $p_a = x_a P_A$, $0 < x_a < 1$ and $p_b = x_b P_B$, $0 < x_b < 1$ respectively. The probability density for parton a's momentum distribution is denoted by $G_A(x_a, Q^2)$ and similarly for b inside B.

- Partons a and b interact on a time scale much shorter than the lifetime of the

initial parton states. $d\sigma/d\hat{t}$ denotes the constituent interaction's cross section.

- The final state partons, c and d, radiate additional partons, creating a cascade that results in two clusters of outgoing hadrons known colloquially as jets. This process is called fragmentation; it is assumed that c and d don't begin radiating until they are far from the hard scatter region. The probability that hadron C is produced by parton c with a fraction, z_c , of c's momentum is given by $D_C(z_c, Q^2)$. One can also construct fragmentation functions as the number of hadrons per unit z from parton i, and then sum over flavors.

This 3-step process is known as the factorization scheme. The implication is that quantum mechanical interference effects between different sets of initial and final states can be ignored since they are distinguishable. Only interference effects among the processes contributing to $d\sigma/d\hat{t}$ need be taken into account. The reaction has the following shorthand notation

$$A + B \rightarrow \text{jet1} + \text{jet2} + X \quad (1.1)$$

where X represents all the hadrons associated with the non-interacting partons. These non-interacting partons are referred to as spectators. The hadron fragments of these constituents emerge in very narrow forward and backward cones parallel to the collision axis. These forward and backward clusters of fragments are called the beam and target jets respectively.

The reader may wonder why it is assumed that partons radiate in such a way that only hadrons appear in the final state. Simply stated, no free quarks have been observed. It seems that, whatever force acts between partons, it must be strongly attractive over macroscopic distances. The current view is that hadrons represent singlet states of the field responsible for the parton-parton interaction.

Mathematically factorization leads to a general expression for the hadron-hadron cross section at high Q^2 ; it is written as a product of structure functions, and $d\sigma/d\hat{t}$

as follows:

$$\begin{aligned} & \frac{d\sigma}{d\eta_1 d\eta_2 dp_\perp^2} (A + B \rightarrow \text{jet1} + \text{jet2} + X) = \\ & \sum_a \int_0^1 \int_0^1 dx_a dx_b G_{a/A}(x_a, Q^2) G_{b/B}(x_b, Q^2) \frac{\hat{s}}{2} \frac{d\sigma}{dt} (ab \rightarrow 12) \times \\ & \delta((x_a + x_b) \frac{\sqrt{s}}{2} - (\cosh \eta_1 + \cosh \eta_2) p_\perp) \times \\ & \delta((x_a - x_b) \frac{\sqrt{s}}{2} - (\sinh \eta_1 + \sinh \eta_2) p_\perp) \end{aligned} \quad (1.2)$$

This form for the cross section trivially generalizes to other processes such as deep inelastic lepton-nucleon scattering, and Drell-Yan production of high mass dilepton pairs.

1.1.2 Hard-Scatter Kinematics

Equipped with this view of the collision process, the reader is now given a description of the kinematics relevant to the analysis. At the parton level the collision is a simple 2-2 scatter with well defined initial and final states. A complete kinematical description of such a process is provided by the Mandelstam invariants s , t , and u [1]. The Mandelstam variables corresponding to the interacting partons are denoted by \hat{s} , \hat{t} , and \hat{u} . They are defined in terms of the incoming and outgoing parton 4-momenta as follows:

$$\hat{s} = (p_a + p_b)^2 \quad \hat{t} = (p_a - p_c)^2 \quad \hat{u} = (p_a - p_d)^2 \quad (1.3)$$

These special scalars obey the following sum rule;

$$\hat{s} + \hat{t} + \hat{u} = \sum_i m_i^2 \quad (1.4)$$

where m_i is the mass of the i th particle either entering or exiting the interaction. For massless quarks and gluons the rule becomes

$$\hat{s} + \hat{t} + \hat{u} = 0 \quad (1.5)$$

The reader should be aware that while s applies to the collision at the hadron level t and u do not because the overall collision is not a simple 2-body scatter.

It is important to relate experimental quantities to the underlying parton hard scatter. The hard scatter can be specified by \hat{s} and $\cos \theta^*$; θ^* is the angle between an outgoing parton's 3-momentum and the beam direction in the colliding partons' c.m. frame. If one assumes an observed jet's direction is also the direction of the parton which produced it, then $\cos \theta^*$ is the orientation of the dijet system in a frame where the jets are back-to-back. Furthermore, \hat{s} is just the dijet system's invariant mass squared, M^2 .

The initial state can be specified by the variables x_1 and x_2 . The variables represent the fractional momenta of the beam and target partons respectively, in the hadrons' c.m. frame. x_1 , x_2 , \hat{s} and $\cos \theta^*$ are all related to the variables by the following set of equations,

$$\hat{s} = x_1 x_2 s, \quad \cos \theta^* = \frac{2\sqrt{\hat{s}}}{\sqrt{s}} \frac{p_{1\perp} + p_{2\perp}}{\sqrt{s}} \quad (1.6)$$

$p_{1\perp}$ and $p_{2\perp}$ are the 4-vectors of the scattered jets. In principle, at least, they are measurable. If it is further assumed that the dijet system possesses no net p_{\perp} and the jets are massless, the variable M can be expressed as follows:

$$M = \frac{2p_{\perp}}{\sin \theta^*} \quad (1.7)$$

where p_{\perp} is the measured transverse momentum of one of the jets. In the context of E706 this would be the transverse momentum of a high p_{\perp} dijet photon. The p_{\perp} balancing assumption is incorrect on general grounds. A simple application of the Heisenberg uncertainty principle shows that the transverse momenta of the jets on the order of ~ 1 fm result in momenta on the order of 300 MeV/c.

The variable $\cos \theta^*$ can be calculated from the corresponding pseudorapidity, η^* . η^* in turn can be obtained by solving the following set of equations, where it has been

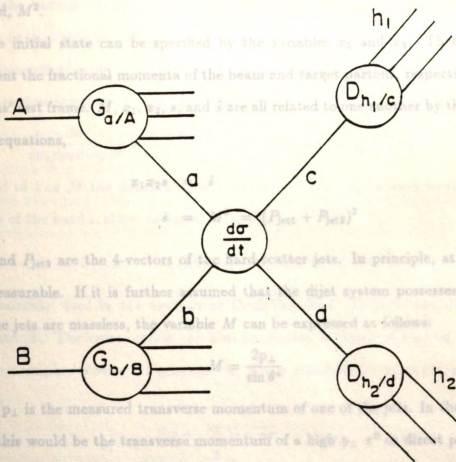


Figure 1.1: A hadron-hadron collision according to the factorization scheme; two partons undergo a hard scatter.

The reader should be aware that while s applies to the collision at the hadron level t and u do not because the overall collision is not a simple 2-body scatter.

It is important to relate experimental quantities to the underlying parton hard scatter. The hard scatter can be specified by \hat{s} and $\cos \theta^*$; θ^* is the angle between an outgoing parton's 3-momentum and the beam direction in the colliding partons' c.m. frame. If one assumes an observed jet's direction is also the direction of the parton which produced it, then $\cos \theta^*$ is the orientation of the dijet system in a frame where the jets are back-to-back. Furthermore, \hat{s} is just the dijet system's invariant mass squared, M^2 .

The initial state can be specified by the variables x_1 and x_2 . These variables represent the fractional momenta of the beam and target partons, respectively, in the hadrons' rest frame. M , x_1 , x_2 , s , and \hat{s} are all related to one another by the following set of equations,

$$\frac{ds}{dx_1 dx_2 d\cos \theta^*} = \frac{x_1 x_2 s}{2} \sum_{ab} G_{a/1}(x_1, Q^2) G_{b/2}(x_2, Q^2) \frac{d\sigma}{dt}(ab \rightarrow 12) \quad (1.5)$$

Instead of \hat{s} or M the dimensionless variable $\tau = \hat{s}/s$ can be used to represent energy of the hard scatter. In $\hat{s} = M^2 = (P_{\text{jet}1} + P_{\text{jet}2})^2$ (1.6)

$P_{\text{jet}1}$ and $P_{\text{jet}2}$ are the 4-vectors of the hard-scatter jets. In principle, at least, they are measurable. If it is further assumed that the dijet system possesses no net p_\perp and the jets are massless, the variable M can be expressed as follows:

$$M = \frac{2p_\perp}{\sin \theta^*} \quad (1.7)$$

where p_\perp is the measured transverse momentum of one of the jets. In the context of E706 this would be the transverse momentum of a high p_\perp π^0 or direct photon. The p_\perp balancing assumption is inexact on general grounds. A simple application of the Heisenberg Uncertainty Relation between position and momentum for distances on the order of ~ 1 fm results in momenta on the order of 300 MeV/c.

The variable $\cos \theta^*$ can be calculated from the corresponding pseudorapidity, η^* . η^* in turn can be obtained by solving the following set of equations, where it has been

assumed that the jet and corresponding parton pseudorapidities are the same.

$$\begin{aligned}\eta_{p1}^* &= \eta_{jet1}^* = \eta_{jet1} + \eta_B \\ \eta_{p2}^* &= \eta_{jet2}^* = -\eta_{jet1}^* = \eta_{jet2} + \eta_B \\ \eta_{p1}^* &= -\eta_{p2}^* = \frac{\eta_{jet1} - \eta_{jet2}}{2}\end{aligned}\quad (1.8)$$

Clearly, the Lorentz boost to the parton-parton rest frame, η_B , is nonzero whenever $x_1 - x_2 = \Delta x \neq 0$. This method for determining $\cos \theta^*$ assumes that the c.m. of the colliding hadrons is related to the rest frame of the interacting partons by a boost along the hadrons' collision axis. In other words, intrinsic transverse momentum effects i.e. k_\perp , are ignored.

The invariant cross section, expressed by equation 1.3, can also be written in terms of the parton variables.

$$\frac{d\sigma}{dx_a dx_b d\cos \theta^*} = \frac{x_a x_b s}{2} \sum_{ab} G_{a/A}(x_a, Q^2) G_{b/B}(x_b, Q^2) \frac{d\sigma}{dt}(ab \rightarrow 12) \quad (1.9)$$

Instead of \hat{s} or M the dimensionless variable $\tau = \hat{s}/s$ can be used to represent the energy of the hard scatter. In terms of x_1 and x_2

$$\tau = \hat{s}/s = x_1 x_2 \quad 0 < \tau < 1 \quad (1.10)$$

τ is generally used in the analysis of Drell-Yan data. In fact, $s d\sigma/d\hat{t}$ is Lorentz invariant [2]. The cross section can also be written in terms of τ or M , $\cos \theta^*$, and Δx by a simple Jacobian transformation. These variables are related to x_1 and x_2 as follows:

$$\begin{aligned}x_1 &= \frac{\Delta x + \sqrt{\Delta^2 x + 4\tau}}{2} \\ x_2 &= \frac{-\Delta x + \sqrt{\Delta^2 x + 4\tau}}{2} \\ \frac{s d\sigma}{d\Delta x d\tau d\cos \theta^*} &= \frac{d\sigma}{d\Delta x 2M dM d\cos \theta^*} = \frac{s}{(x_1 + x_2)} \frac{d\sigma}{dx_a dx_b d\cos \theta^*}\end{aligned}\quad (1.11)$$

Because of the manner in which the data will be binned, M is the variable of choice together with $\cos \theta^*$.

One piece of nomenclature still needs to be clarified. All high p_{\perp} events will be divided into two hemispheres of azimuth. The events that will be analyzed contain either a high p_{\perp} single photon or π^0 , responsible for triggering the detector in the first place. The set of all points closer than $\phi = \pi/2$ to this trigger particle will be defined as the trigger hemisphere. The complimentary set of points comprises the recoil hemisphere. All variables expressing quantities in the trigger hemisphere will be subscripted by **trig**, and all corresponding variables in the recoil hemisphere by **recoil**.

1.1.3 The Meaning of $d\sigma/d\hat{t}$

The calculation of $d\sigma/d\hat{t}$ for purely hadronic collisions requires a field theory for the strong interaction. Quantum Chromodynamics or QCD for short is the best candidate for such a theory. This theory assigns a dynamical role to the color quantum number which is analogous to the role of electric charge in QED.

However, there is one very important conceptual difference between Quantum Electrodynamics and Quantum Chromodynamics. Gluons carry color so they can interact with one another. When radiative corrections are applied to the Born terms in a perturbation series, an effective strong coupling constant emerges with the following Q^2 dependence [3]:

$$\alpha_s = \frac{12\pi}{(11n - 2f)\ln(Q^2/\Lambda)} = \frac{12\pi}{25\ln(Q^2/\Lambda)} \quad (1.12)$$

where n is the number of color degrees of freedom $n = 3$ and f is the number of flavor states within the accessible phase space. $f = 5$ for this experiment. Λ is a free parameter to be determined by experiment. It is an artifact from summing only a finite portion of the perturbation expansion; an exact result would not contain this parameter. Obviously as $Q^2 \rightarrow \infty$, $\alpha_s \rightarrow 0$. Thus, in the high Q^2 limit the partons behave like free particles within the volume of a hadron. This property is called

asymptotic freedom. Since high p_{\perp} implies high Q^2 , high p_{\perp} hadron interactions may serve as an application for perturbative QCD.

Gluon-gluon collisions take place also at the Born level. As a result, a large number of subprocesses can contribute to the hard-scatter cross section at lowest order. Figure 1.2 lists the various mechanisms contributing to generic parton scatters. Referring back to Figure 1.1, both the G and D functions have a dependence on Q^2 . In the high Q^2 regime the partons behave like free particles so the structure and fragmentation functions should cease to depend on the momentum transfer *i.e.* they should scale. All of the p_{\perp} dependence in the cross section would then reside in $d\sigma/d\hat{t}$, and QCD predicts that all subprocesses fall as $1/p_{\perp}^4$. Unfortunately, the data is observed to fall as $1/p_{\perp}^6$ or faster in E706's kinematic regime [4]. Clearly G and D have a dependence on Q^2 there. This ambiguity is not as bad as might be supposed. While G and D cannot be calculated at the present time, their Q^2 variation is completely predicted by the Altarelli-Parisi Equations [5]. Measuring G and/or D at some Q^2 and using these equations allows one to know the behavior of these functions at any other momentum transfer where perturbation theory is applicable.

1.2 DIRECT PHOTONS AND QCD

Although QCD may provide a theoretical framework that leads to predictions for absolute cross sections, the picture is nonetheless very complicated. There is little if any sensitivity in discriminating between quark and gluon effects. Worst of all is the fact that jets are fuzzy objects from an experimental standpoint. It is not straightforward to determine which jet each particle belongs to. In addition, the distinction between hard-scatter and minimum bias events isn't always clear, especially at E706 energies.

The technical difficulties peculiar to studying generic jet production can be overcome by studying only those events containing a high p_{\perp} hadron *i.e.*, a π^0 . However,

such events are still very complicated at the hard scatter level. The large number of contributing subprocesses involve a mixture of quarks and gluons in the initial and final states, and separating the effects of gluons and quarks is compromised.

Direct photon events stand in sharp contrast to this rather murky situation. In lowest order only two subprocesses contribute to their production. These are illustrated in Figure 1.2. The process involving the collision of a quark and gluon is referred to as the Compton process by analogy with the scattering of electrons by high-energy photons. The QCD formulas for the two production mechanisms are also shown, being expressed in terms of the Mandelstam variables.

Compton production is expected to dominate direct photon production in proton-nucleon collisions because at first order there are no anti-quarks in the nucleon. Being able to measure this process in terms of the photon and outgoing quark 4-vectors yields a direct measurement of the gluon structure function for nucleons. Only a quark approximation in the final state is used.

For the production of direct photons in proton-nucleus collisions, direct photon production in proton-nucleon collisions should be dominant. However, the overall dependence of $d\sigma/dt$ on the atomic number A is somewhat uncertain. If "u-quark dominance" is simply taken to mean that direct photon events are more likely to be produced by u-quark interactions, then for the production of direct photons in proton-nucleus collisions, there will be an enhancement of u-quark jets in the final state. For the production of direct photons in proton-nucleus collisions, an extra factor of two arising from there being twice as many u-quarks as d-quarks in the nucleon is somewhat uncertain. In this experiment because the strong interaction is charge independent and π^+ 's contain equal numbers of u and d-quarks, the enhancement is expected for high p_T jets. The strong interaction is charge independent and π^+ 's contain equal numbers of u and d-quarks.

Figure 1.2: All possible parton-parton scatters in first order QCD. The Mandelstam variables are for the constituent processes. A common factor of $\pi\alpha_s^2/s^2$ has been left out.

Figure 1.2: All possible parton-parton scatters in first order QCD. The Mandelstam variables are for the constituent processes. A common factor of $\pi\alpha_s^2/s^2$ has been left out.

such events are still very complicated at the hard scatter level. The large number of contributing subprocesses involve a mixture of quarks and gluons in the initial and final states. So, the ability to separate the effects of gluons and quarks is compromised.

Direct photon events stand in sharp contrast to this rather murky situation. In lowest order only two subprocesses contribute to their production. These are illustrated in Figure 1.3. The process involving the collision of a quark and gluon is referred to as the Compton process by analogy with the scattering of electrons by high energy photons. The other Feynman graphs describe the annihilation of a quark and anti-quark into a photon and gluon. This process is similar to e^+e^- annihilation into photons. The QCD formulas for the two production mechanisms are also shown, being expressed in terms of the Mandelstam variables.

The Compton process is expected to dominate direct photon production in proton-nucleus collisions because to first order there are no anti-quarks in the nucleon. Being able to measure this cross section in terms of the photon and outgoing quark 4-vectors yields a direct measurement of the gluon structure function for nucleons. Only a quark appears in the final state along with the photon. Thus, direct photon production in proton-nucleus collisions should yield information on quark fragmentation. The overall dependence of $d\sigma/d\hat{t}$ on the quark charges results in an effect known as "u-quark dominance". It simply means that direct photon events are more likely to be produced by u-quark interactions. For the Compton subprocess, there will be an enhancement of u-quark jets in the data. In fact, one expects an 8-fold enhancement of u-quark jets over d-quark jets for pp interactions, an extra factor of two arising from there being twice as many u as d-quarks in the proton. The effect is diluted somewhat in this experiment because nuclear targets have been used. No such enhancement is expected for high p_\perp π^0 production since the strong interaction is charge independent and π^0 's contain equal numbers of u and d-quarks.

The annihilation process is expected to be responsible for most of the cross section at high p_T in π^- -nucleus collisions. This follows from the form for $d\sigma/d\hat{t}$ and the gluon structure function is believed to fall faster than the valence quark distributions at high x . In this regime the recoil jet is being produced by a gluon. Thus, it would be interesting to compare the hadronic spectra between proton induced direct photon events, which contain a quark generated recoil jet, and π^- induced events.

Generally speaking, the QCD production mechanisms for direct photons result in the photon being isolated. In other words the photon always comprises a one particle jet so there should be no enhancement of the cross section near it in phase space. This is in contrast to high p_T π^0 events. There the high p_T particle is only one of several products of a final state parton's fragmentation. The overall charged structure of high p_T π^0 and single photon events should be sensitive to such a difference between Compton Diagrams .

$$\frac{d\hat{\sigma}}{d\hat{t}} = \frac{-e_q^2 \pi \alpha \alpha_s}{3\hat{s}^2} \left(\frac{\hat{u}}{\hat{t}} + \frac{\hat{t}}{\hat{u}} \right)$$

Going back to the expressions for the production mechanisms in Figure 1.3, if one substitutes the ingoing and outgoing 4-momenta in place of the variables \hat{s} , \hat{t} , and \hat{u} they will obtain formulas with $1/(1 \pm \cos \theta^*)$ terms in them. This is a general result for elementary processes containing only fermionic propagators. Among the more general subprocesses responsible for high p_T π^0 production are some that contain gluon propagators, i.e. spin-1 bosons. It follows from general considerations that $d\sigma/d\hat{t}$ will have $1/(1 \pm \cos \theta^*)^2$ terms. As a result, the $\cos \theta^*$ distributions for π^0 +jet events should be more sharply peaked than for γ +jet events. As θ^* approaches 1.

Unfortunately, the picture is not quite as simple as this. Single γ s can be produced via a bremsstrahlung Annihilation Diagrams .

$$\frac{d\hat{\sigma}}{d\hat{t}} = \frac{9e_q^2 \pi \alpha \alpha_s}{9\hat{s}^2} \left(\frac{\hat{u}}{\hat{t}} + \frac{\hat{t}}{\hat{u}} \right)$$

Figure 1.3: 1st order direct photon subprocesses in QCD. It should be important at E706 energies for $p_T \lesssim 4.0 \text{ GeV}/c$, so there may be some ambiguity in the interpretation of the data. However, calculations by Owens [6] predict that the direct

The annihilation process is expected to be responsible for most of the cross section at high p_{\perp} in π^- -nucleus collisions. This follows from the form for $d\sigma/d\hat{t}$ and the gluon structure function is believed to fall faster than the valence quark distributions at high x . In this regime the recoil jet is being produced by a gluon. Thus, it would be interesting to compare the hadronic spectra between proton induced direct photon events, which contain a quark generated recoil jet, and π^- induced events.

Generally speaking, the QCD production mechanisms for direct photons result in the photon being isolated. In other words the photon always comprises a one particle jet so there should be no enhancement of charged particles near it in phase space. This is in contrast to high p_{\perp} π^0 events. There the high p_{\perp} particle is only one of several products of a final state parton's fragmentation. A study of the overall charged structure of high p_{\perp} π^0 and single photon events should be sensitive to such a difference between the two event types.

Going back to the expressions for the production mechanisms in Figure 1.3, if one substitutes the ingoing and outgoing 4-momenta in place of the variables \hat{s} , \hat{t} , and \hat{u} they will obtain formulas with $1/(1 \pm \cos \theta^*)$ terms in them. This is a general result for elementary processes containing only fermionic propagators. Among the more general subprocesses responsible for high p_{\perp} π^0 production are some that contain gluon propagators. Since gluons are bosons, it follows from general considerations that $d\sigma/d\hat{t}$ will have $1/(1 \pm \cos \theta^*)^2$ terms. As a result, the $\cos \theta^*$ distributions for π^0 +jet events should rise more sharply than for γ +jet events as $|\cos \theta^*|$ approaches 1.

Unfortunately, the picture is not quite as simple as this. Single γ s can be produced via a bremsstrahlung type mechanism illustrated in Figure 1.4. Although higher order in α_s , $\alpha_s \approx .1$ yields $\approx 10\%$ contribution. This subprocess is thought to be important at E706 energies for $p_{\perp} \lesssim 4.0 \text{ GeV}/c$, so there may be some ambiguity in the interpretation of the data. However, calculations by Owens [6] predict that the direct

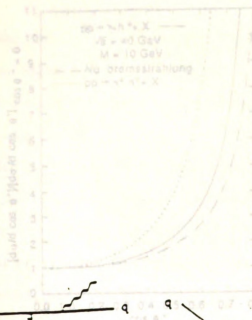


Figure 1.5: Theoretical π^0 and single photon distributions from Owens. The calculations are presented with and without the Bremsstrahlung contribution. The recoil jet is defined as the leading hadron away from the trigger in

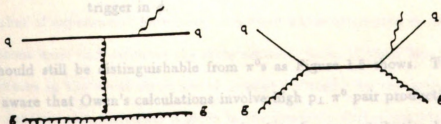


Figure 1.4: Bremsstrahlung contribution to direct photon production.

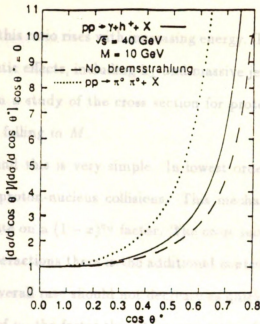


Figure 1.5: Theoretical π^0 and single photon $\cos\theta^*$ distributions from Owens. The calculations for prompt photons are presented with and without the Brehmsstrahlung contribution. The recoil jet is defined as the leading hadron away from the trigger in ϕ .

A number of experiments have been performed which attempted to determine if direct photons exist and estimate the cross section. Some of these experiments should still be distinguishable from π^0 s as Figure 1.5 shows. The reader should be aware that Owen's calculations involve high p_{\perp} π^0 pair production rather than generic π^0 + jet production, and there may be a larger contribution by subprocesses with gluon propagators in the former than the latter.

The cross sections in M for high p_{\perp} direct photon and π^0 events should be different. The photon cross section should fall more slowly with M since there is no attenuation due to a fragmentation function in lowest order. It would be interesting to see if the two rates cross over within the accessible kinematic range. At higher energies direct photon production would increasingly dominate! The "hardness" of the gluon distribution can be studied by examining the ratio of γ + jet cross sections in π^- -nucleus collisions to proton-nucleus collisions as a function of M . In particular, it can

be seen how quickly this ratio rises with increasing energy. Taking the ratio cancels out a number of systematic effects, including k_{\perp} and massive jets. These effects introduce large uncertainties in a study of the cross section for proton-nucleus collisions alone because it is steeply falling in M .

The physics behind this is very simple. In lowest order only the Compton subprocess is active in proton-nucleus collisions. This mechanism results in an overall dependence of the rate on a $(1-x)^{\eta\sigma}$ factor. The cross section thus dies out at large x . In π^- -nucleus interactions there is the additional contribution of quark-antiquark annihilation so the overall rate should not decrease as quickly in this case. Therefore, the larger the value of η_G the faster the π^- /proton ratio of γ + jet cross sections rises with M .

1.3 EXPERIMENTAL CONSIDERATIONS

A number of experiments have been performed which attempted to determine if direct photons exist and estimate the cross section. Some of them also looked for unique features in the event structure of prompt photons. An excellent review of these first generation experiments is given in the article by Ferbel and Molzon [7].

Experiment E706 is one of several second generation experiments, designed to obtain a quantitative measure of the direct photon cross section. In addition, E706 hopes to measure the gluon structure functions for protons and pions with unprecedented precision. The rather large acceptance of the spectrometer ($\approx 65\%$ of the solid angle) gives it a greater sensitivity to differences in the overall event structure between single γ s and high p_{\perp} single hadrons as well as between various types of direct photon events. The experiment is capable of obtaining single γ events in the p_{\perp} range of 4.0 GeV/c to 10.0 GeV/c.

The rarity of prompt photon events requires a detector much more efficient at selecting them than in selecting the more common hard-scatter events. There are two major steps in solving this problem. High energy photons interact with dense forms of matter, producing showers of minimum ionizing electrons. A detector is needed that is capable of measuring the electron shower energy while being insensitive to the passage of high energy hadrons. Such devices are known as electromagnetic calorimeters. The second step involves implementing a special electronic circuit to sense the presence of a high p_{\perp} electromagnetic shower in the detector, and to send a signal to the data acquisition system that the event information should be latched. This circuit is known as the trigger. The trigger must be capable of generating latch signals on the same time scale as the interaction rate in the target, which is 1 MHz for E706.

Even for data taken using these techniques, there is still a large background to the direct photon signal. The background is produced from π^0 and η decays, and it is at least as large as the prompt photon signal over most of the kinematic region. π^0 s decay into two photons with a 99.9% branching fraction; η s decay similarly 40% of the time. However, the η production rate is only 40% of π^0 production rate. By reconstructing the 4-vectors of these particles from their decay products, a quantitative measurement of the photon cross section is possible. However, the electromagnetic calorimeter must have a fine enough spatial granularity so that both decay photons can be reconstructed. Unfortunately, electromagnetic showers have a natural width associated with them, making it very difficult to separate showers closer than ~ 1 cm at energies typically found in the data. This difficulty can be circumvented by moving the detector farther downstream of the target, but a price is paid in acceptance. A 65% solid angle coverage was chosen so that the two decay photons from a 100 GeV/c π^0 could be separated. Such a coverage lies between ± 1.0 unit of rapidity and 2π in

the direct photon signal from a substantial background due to neutral meson decays. azimuth.

Because the acceptance is less than 4π , and the detector itself has an energy threshold (~ 5 GeV), not all neutral mesons will be reconstructed. By measuring the π^0 and η cross sections, the contribution of π^0 and η decays to the observed single photon spectrum can be calculated. This false direct photon spectrum can then be subtracted from the reconstructed single photon spectrum, resulting in the true p_T spectrum for prompt photons.

An experiment sensitive to the event structure associated with direct photons must have some ability to determine the 4-vectors of the recoiling hadrons. For this reason a magnetic spectrometer was used to measure the 4-vectors of charged hadrons. Although the experiment's ability to reconstruct the neutral component of jets has been compromised, the information gained from the charged tracking system suffices for this analysis. The magnetic spectrometer provides excellent solid angle coverage, allowing containment of the recoil jet within the apparatus. This has been accomplished by using a set of silicon microstrip detectors to reconstruct the event vertex, which allows the production target to be placed right up next to the analyzing magnet's aperture.

1.4 THESIS GOALS

The major goal of this thesis is to compare direct photon and π^0 events. The associated charged particle structure of these events will be used in making comparisons. The events will be studied to see how isolated the single photons are. The angular and invariant mass spectra will also be compared between the two event types. In addition, they will be checked to see how well they conform to QCD expectations.

Being able to observe all the expected differences between direct photons and π^0 s has a twoedged advantage. First, it means the experiment is capable of resolving

the direct photon signal from a substantial background due to neutral meson decays. Second, it further validates the QCD interpretation of hadron-hadron collisions. Attempts will be made to see if differences between γ s and π^0 s can be found without a background subtraction. Such a finding would greatly bolster the direct photon results with a background subtraction. The conformity to QCD will be checked by comparing data distributions with those generated by a physics monte carlo. All cuts applied to the data will be applied to the monte carlo along with the p_{\perp} balancing and massless jet assumptions. In so doing, the systematics affecting both types of data can be equalized.

In addition to looking for differences between γ s and π^0 s, the ratio of absolute M cross sections between proton and π^- beam data will be studied to see how hard the gluon distribution is. By "hardness" or "softness" is meant whether the value of η_G is small or large respectively. The data ratio is to be compared with monte carlo predictions, using two different sets of structure functions; the sets are distinguished by their value for η_G . As a check on this method's validity, the corresponding M ratio for high p_{\perp} π^0 s will be examined and compared with monte carlo predictions.

The calculation of M and $\cos \theta^*$ is straightforward as shown in section 1.1. However, the M and especially the angular distributions for the E706 data sample possess large systematic biases. These biases are due primarily to the p_{\perp} cuts imposed on the trigger particle. The p_{\perp} cut is necessitated by the trigger apparatus' p_{\perp} threshold. In addition, the calorimeter's limited acceptance in rapidity causes variable losses in $\cos \theta^*$ over the measured range. While these biases could be compensated for by applying corrections based on a physics monte carlo, such a procedure introduces a model dependence. Instead, cuts will be applied so that the true shapes of these distributions can be observed, albeit over a restricted range. A cut in M and η_B are required to remove the bias in the angular distributions, but cuts in M and $\cos \theta^*$ are needed for the cross sections.

by the trigger bias because no points in this region lie on the boundary curve. It follows that for the data in this region each bin of $\cos \theta^*$ has the same \hat{s} spectrum.

1.4.1 Biases in $\cos \theta^*$

Therefore, the true dependence of the cross section on $\cos \theta^*$ may be observed there. The uncut $\cos \theta^*$ distributions contain two sources of bias. One, triggering on events according to p_{\perp} introduces a large artificial enhancement of events around $\cos \theta^* = 0$. Second, the detector's geometric acceptance is considerably less than 4π . These acceptance edges result in an enhancement of events around $\cos \theta^* = 0$ relative to those near $\cos \theta^* = \pm 1$.

The p_{\perp} trigger bias can be removed by applying a cut in either \hat{s} or τ . Figure 1.6 shows how this cut works. In this plot $\cos \theta^*$ is plotted against τ . The absolute kinematic boundaries are defined by $\cos \theta^* = \pm 1$ and $\tau = 0, \tau = 1$. However, the plotted points do not cover the whole region of phase space, but are constrained to lie within a region determined by the trigger threshold. The equation for this region's boundary curve is given by

$$\sin \theta^* = \frac{2p_{\perp}}{\sqrt{\hat{s}}} \cdot \frac{1}{\tau}, \quad \tau \geq \frac{2p_{\perp}}{\sqrt{\hat{s}}} \quad (1.13)$$

Note that for $p_{\perp \text{th}} = 0$ this boundary merges with the absolute one. Clearly the density of points is not uniform, but increases rapidly as τ decreases towards the minimum dictated by the trigger threshold. This behavior stems from the fact that the cross section is a steeply falling function of \hat{s} . At $\cos \theta^* = 0$, $\sqrt{\hat{s}} \cong 2p_{\perp}$ but away from $\cos \theta^* = 0$, $\sqrt{\hat{s}} > 2p_{\perp}$. Events with the same p_{\perp} may have different values of \hat{s} depending on their orientation in $\cos \theta^*$. So, selecting events according to p_{\perp} will enhance those with lower values of \hat{s} over those with larger values. Because the cross section is so steeply falling, this artificial enhancement will completely wash out the shape of the true distribution, rendering any comparisons meaningless.

Consider dividing the data in Figure 1.6 by the line $\tau = \tau_{\text{cut}}$. This line intersects two points on the curve defined by Equation 1.13. The line $\cos \theta^* = \pm \cos \theta^*_{\text{cut}}$ passing through these intersection points defines a region to the right of $\tau = \tau_{\text{cut}}$ unaffected

by the trigger bias because no points in this region lie on the boundary curve. It follows that for the data in this region each bin of $\cos \theta^*$ has the same \hat{s} spectrum. Therefore, the true dependence of the cross section on $\cos \theta^*$ may be observed there.

The cut in τ only allows for an unbiased measurement of $\cos \theta^*$ within the region $\cos \theta^* = \pm \cos \theta_{\text{cut}}^*$. Increasing the τ cut allows greater coverage of $\cos \theta^*$, but with a substantial loss in statistics. This analysis of the 1988 E706 data will employ τ cuts yielding an unbiased $\cos \theta^*$ distribution out to $\cos \theta^* = \pm 0.5$.

The acceptance bias is purely geometrical and easily understood in terms of η_{trig} , η^* , η_B and η_{LAC} where η_{LAC} represents the edge of the electromagnetic calorimeter's acceptance in pseudorapidity

$$\eta^* - \eta_B = \eta_{\text{trig}} \quad (1.14)$$

It is easy to show that $\eta_B = \frac{1}{2} \ln(x_2/x_1)$. Since x_1 , x_2 , and $\cos \theta^*$ are physically independent, the η_B distribution is the same for all η^* . The detector's acceptance, however, causes the boost distribution to be different for η^* near η_{LAC} from $\eta^* \approx 0$. This is shown in Figure 1.7. There are pieces of each η_B distribution that are unaffected by acceptance, namely $|\eta_B| < |\eta_{\text{LAC}} - \eta_{\text{max}}|$. If a cut in η_B is imposed such that the inequality is satisfied, then there is uniform acceptance in $\cos \theta^*$. The true shape of the angular distribution will then be observed.

1.4.2 Biases in M

Referring again to Figure 1.6, the τ distribution inside the rectangle is unbiased with respect to the trigger. Including regions outside the rectangle would bias the absolute cross section in such a way that if the cross section were flat with respect to τ , the trigger would produce a cross section increasing in τ . This bias is not a problem when comparing two distributions having identical trigger thresholds and acceptances. In the case of the 1988 run of E706 though, the data can be divided into

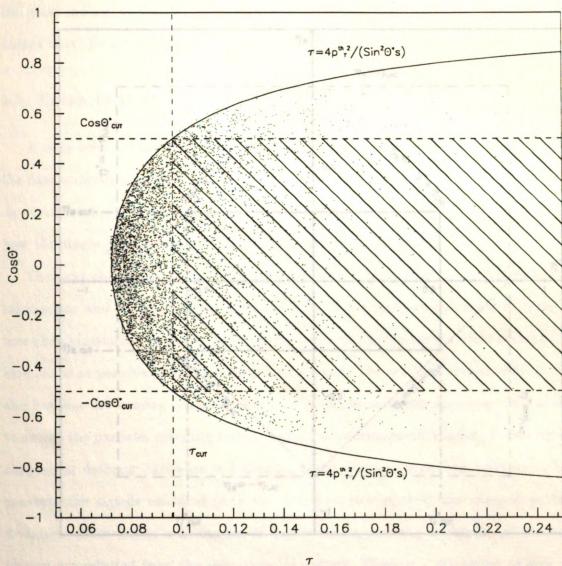


Figure 1.6: Scatter plot of $\cos \theta^*$ vs τ . The region between the two horizontal lines, and to the right of the vertical line is unbiased from the trigger over the measured interval of $\cos \theta^*$.

three distinct sets according to trigger threshold. Comparing a pair of cross sections in M from different threshold sets could be misleading. In addition, there are problems combining data from different threshold sets into the same distribution. For this reason, only data within the unbiased region will be used. In order to gain statistics the mass cut will be smaller than the one employed for the $\cos \theta^*$ plots. However, this means that the $\cos \theta^*$ limits in the M distributions are also correspondingly tighter.

1.5. THESIS OUTLINE

A very brief outline of this thesis is now presented for the reader interested only in the data analysis as advised by the rest of the chapters. Apart from the chapter on event reconstruction, the next two chapters are devoted to understanding how the single photon and π^0 background is eliminated from the data.

The next chapter describes the π^0 background subtraction in terms of calorimeter and its associated uncertainties. The background is discussed in terms of how they maximize this by fitting the π^0 peak in the data while making it as insensitive as possible to the very large background. The trigger system is dealt with also because the ensuing analyses heavily rely on the muon spectrometer's ability to detect the particles recoiling from a high p_T electromagnetic trigger. Following the chapter on detector hardware is a chapter about the reconstruction software, which converts the signals recorded from the detectors into photon and charged particle 4-vectors. Next comes a chapter about the selection of high p_T photons and charged

photon are selected from the reconstructor output. There is a discussion of how the muon and π^0 backgrounds are eliminated from the single photon data set. Finally, there is a presentation of the cross section results. The next two chapters are devoted to understanding how the single photon and π^0 background is eliminated from the data. The next chapter describes the π^0 background subtraction in terms of calorimeter and its associated uncertainties. The background is discussed in terms of how they maximize this by fitting the π^0 peak in the data while making it as insensitive as possible to the very large background. The trigger system is dealt with also because the ensuing analyses heavily rely on the muon spectrometer's ability to detect the particles recoiling from a high p_T electromagnetic trigger. Following the chapter on detector hardware is a chapter about the reconstruction software, which converts the signals recorded from the detectors into photon and charged particle 4-vectors. Next comes a chapter about the selection of high p_T photons and charged

Figure 1.7: An illustration of the bias in $\cos \theta^*$ as a result of the detector's acceptance being $< 4\pi$.

three distinct sets according to trigger threshold. Comparing a pair of cross sections in M from different threshold sets could be misleading. In addition, there are problems combining data from different threshold sets into the same distribution. For this reason, only data within the unbiased region will be used. In order to gain statistics the mass cut will be smaller than the one employed for the $\cos \theta^*$ plots. However, this means that the $\cos \theta^*$ limits in the M distributions are also correspondingly tighter.

1.5 THESIS OUTLINE

A very brief outline of this thesis is now presented. The reader interested only in the data analysis is advised to skip the next three chapters and start with the chapter on event features. It may be wise to skim the fourth chapter in order to understand how the single photon and π^0 data samples were initially determined.

The next chapter describes at considerable length the major design features of the calorimeter and its associated electronics. These features are discussed in terms of how they maximize this device's sensitivity to direct photon events while making it as insensitive as possible to the very large background. The tracking system is dealt with also because the ensuing analysis relies heavily on the magnetic spectrometer's ability to detect the particles recoiling from a high p_\perp electromagnetic trigger. Following the chapter on detector hardware is a chapter about the reconstruction software, which converts the signals recorded from the detectors into photon and charged particle 4-vectors. Next comes a discussion of how events containing a high p_\perp π^0 or single photon are selected from the reconstructor output. There is a discussion of how the muon and π^0 backgrounds are eliminated from the single photon data set. Finally, there is a presentation of the various corrections applied to the trigger particles in order to obtain absolute cross sections. Some of these corrections are also required in obtaining the proper $\cos \theta^*$ and M distributions.

This data analysis really begins in the chapter on event features. The charged particle structure associated with the γ and π^0 samples is examined. This study has two major goals. First, it will be shown that a difference exists between single photon and π^0 events at high p_\perp without a background subtraction. Second, it must be shown that the tracking system is capable of “seeing” the recoil jet structure. Correlations in rapidity will be used to demonstrate this is so. The recoil jet reconstruction is studied in chapter 6. Much of this work depends on the output of a physics monte carlo. The aim here is to determine how correctly and efficiently the recoil jet direction is calculated over the acceptance. It will be shown that the reconstruction of $\cos\theta^*$ and M is meaningful within the conceptual framework of QCD.

The reconstructed $\cos\theta^*$ and M distributions are presented in the last chapter. The cuts and corrections used will be elaborated upon further. A generalized method of computing the π^0 component of an unsubtracted single photon distribution is given, and the effects of π^0 background in the direct photon sample will be studied. Again, the emphasis is on comparing direct photons and π^0 s in data and monte carlo.

Chapter 2

Experimental Setup

The design, operation and performance of the various detector systems is now discussed. The main hardware components are the beamline, the liquid argon calorimeters, the online trigger system, the charged tracking spectrometer, and the forward calorimeter. The online trigger system consists of a set of scintillation counters, and a special high speed electronics system that analyzes signals coming from the liquid argon calorimeters in real time. The scintillation counter data can also be employed offline in whole event selection. The analysis to be presented in the following chapters centers around the electromagnetic liquid argon calorimeter (EMLAC), and the charged tracking system. Consequently, only these detector components will be dealt with in great detail. Figure 2.1 shows a plan view of the apparatus.

2.1 BEAMLINE

The MWEST beamline is designed to produce and transport a 500 GeV/c hadron beam. This hadron beam can be either positive or negatively charged, but different charges have to be transported at different times. The secondary beam originated in a $3/4$ interaction length piece of aluminum, whenever 800 GeV/c protons from the Tevatron impinged upon it. One accelerator cycle occurs every 57 s. For 23 out of those 57 seconds, primary beam is available for producing the 500 GeV/c secondary beam. The period for which the primary beam is available each cycle is termed a spill.

The primary beam was rotated 1.9 mrad relative to the secondary beam during positive running. This was done to prevent primary beam from entering the experimental hall. The two beams had no relative angle during the negative beam run-

ning. The intensities for positive and negative beam were about $6.5 \times 10^7/\text{spill}$ and $2 \times 10^7/\text{spill}$ respectively. The primary intensity delivered to the MWEST beamline was $2 \times 10^{12}/\text{spill}$.

A string of dipole and quadrupole magnets directed and focused the secondary beam unto a nuclear target in the experimental hall. The string of magnets also contained special toroids, called spoilers, which swept the halo particles out of the E706 detector's acceptance. A set of collimators selected the beam's momentum and regulated its intensity. The momentum spread was $\Delta P/P = 6\%$. The collimators responsible for regulating the beam's intensity were left wide open during negative running, but had to be closed down for positive beam so that the interaction rate would be $\lesssim 1 \text{ MHz}$.

Figure 2.2 shows a schematic of the beamline. All bending and focusing elements are represented by their optical equivalents. A D or Q in the device name indicates a dipole or quadrupole respectively. An S stands for a spoiler while C designates a collimator. H or V indicates whether the device affects the beam horizontally or vertically. The primary target is designated as MW6TGT.

2.1.1 The Cerenkov Detector

The positive beam contained a mixture of proton, π^+ , and K^+ particles while the negative beam was composed of π^- , K^- , and \bar{p} particles. To identify which type of particle produced a particular event, a differential \hat{C} counter was installed in the beamline. The beam was tuned so that dispersion was minimized as it traversed this piece of apparatus. The \hat{C} detector is 42m long and filled with helium gas, which functions as the radiator.

The helium pressure varied from 4 – 6 PSI over the course of the 1987-88 run. The counter's Cerenkov angle is 5 mrad. So, by varying the pressure different beam particle species could be detected and pressure curves constructed (see Figure 2.3).

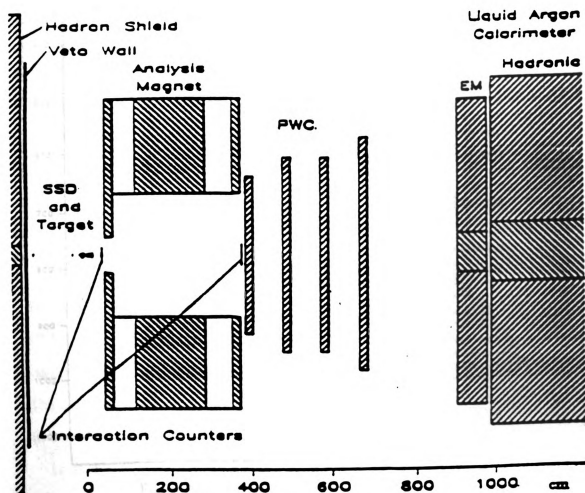


Figure 2.1: E706 Plan View

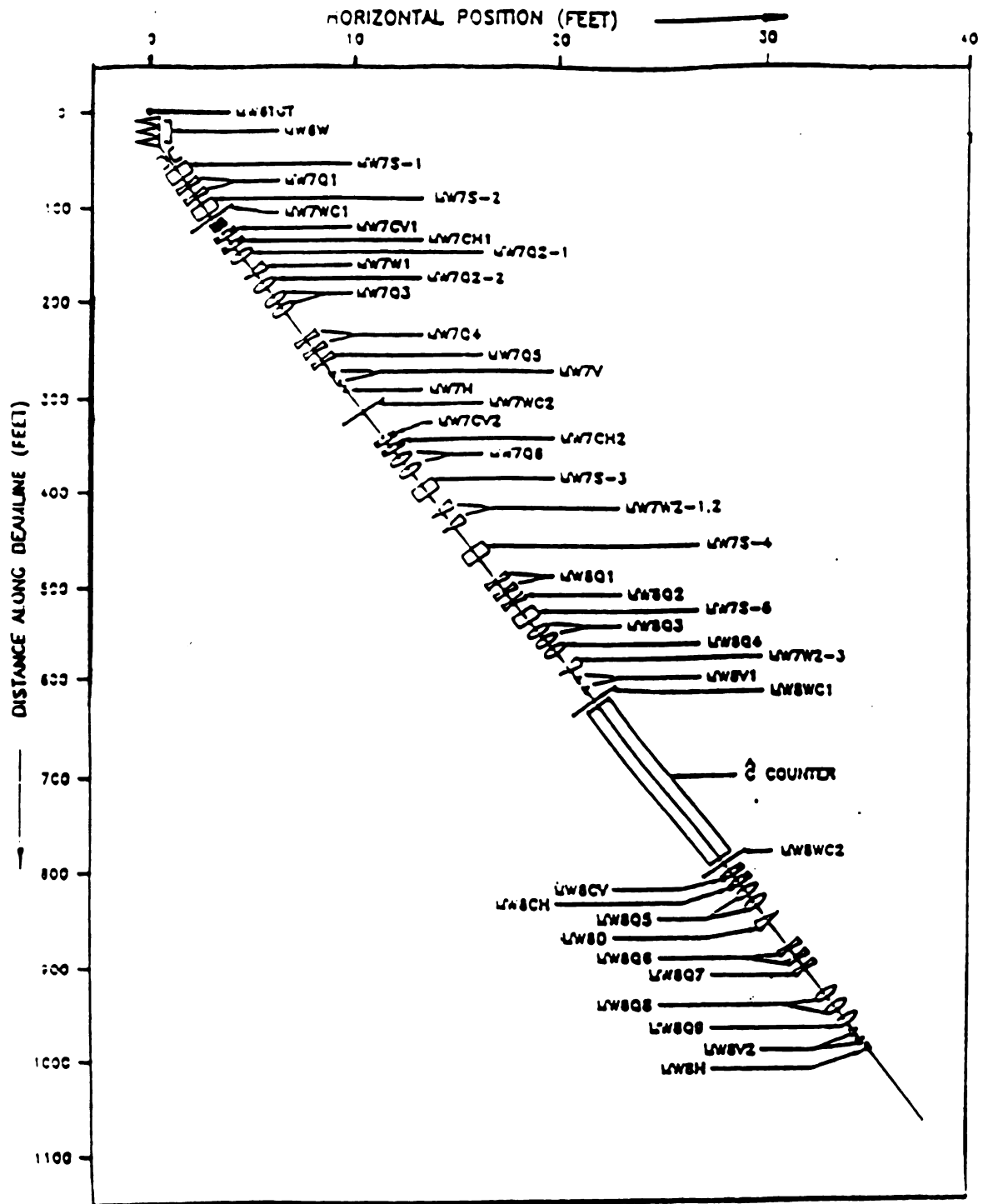


Figure 2.2: A schematic of the MWEST secondary beamline. All devices are represented in terms of their optical equivalents.

The relative fractions of particle species were determined by comparing the peak amplitudes in these graphs. In addition, the efficiency was measured by sitting at a particular peak pressure and comparing the \hat{C} counter rate to the corresponding prescaled beam rate. The \hat{C} pressure was set to tag π^+ during positive running and K^- during negative running. Table 2.1 lists the fraction of each particle type in the secondary beam. The \hat{C} tagging efficiency in negative beam was 42% and 87% for positive beam [8].

Table 2.1: Fractions of the various particle species in the 500 GeV/c secondary beam.

Negative beam		Positive beam	
π^-	97.0%	p	91.3%
K^-	2.9%	π^+	7.2%
\bar{p}	0.2%	K^+	1.5%

2.1.2 The Hadron Shield and Veto Wall

A 5 m long stack of steel slabs blocks the entrance of the beam enclosure into the MWEST hall. This stack is known as the hadron shield. Its purpose is to stop all halo hadrons from entering the detector. Such high energy particles can produce tracks, showers and possibly triggers which would obscure the true event structure. The beam pipe passes through the center of a special vertical slab that divides the hadron shield in half. Figure 2.4 contains a drawing of it.

Immediately downstream of the hadron shield lies an array of scintillation counters called the veto wall. While the hadron shield stops the hadronic halo, it is transparent to high energy muons. Muons are copiously produced in the primary target and the spoiler magnets cannot sweep the entire flux out of the electromagnetic calorimeter's acceptance. A large number of muons will penetrate the EMLAC during data taking;

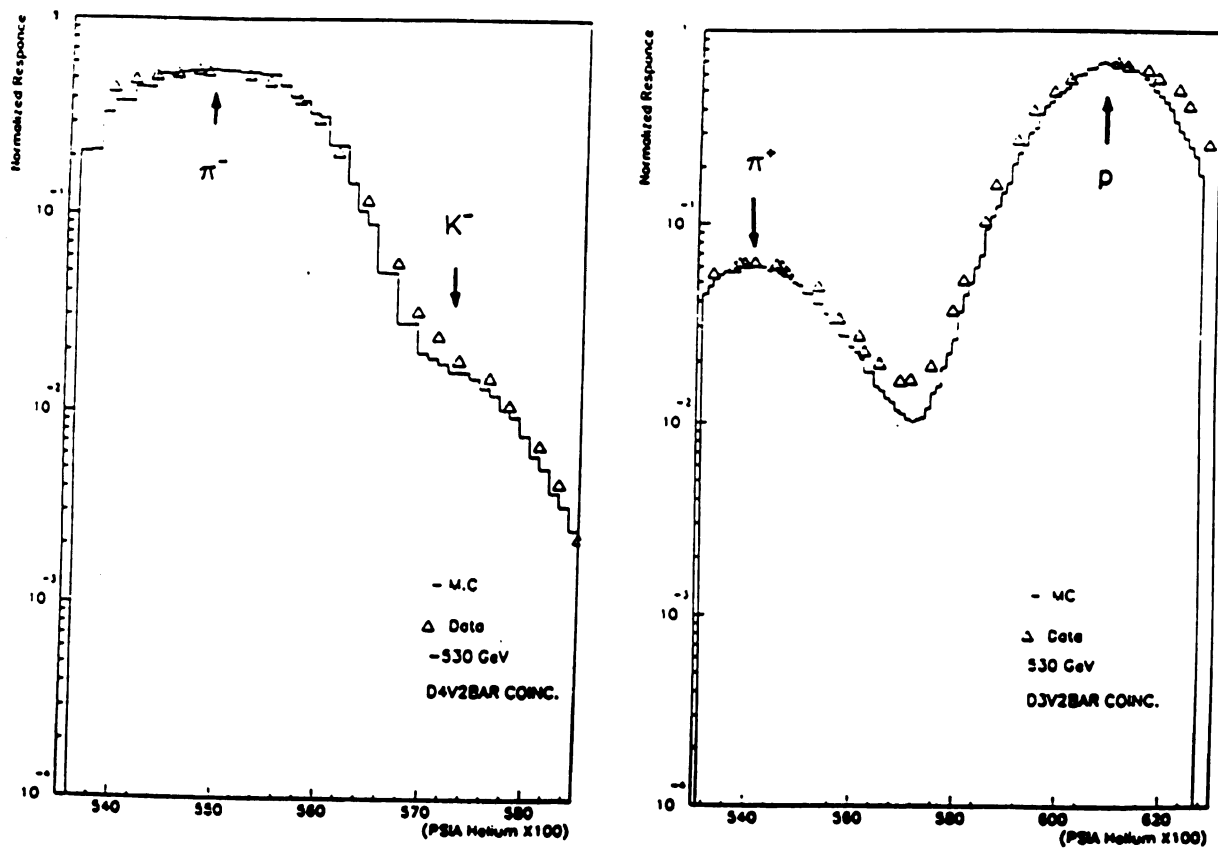


Figure 2.3: Examples of \hat{C} pressure curves for both beam polarities. The peaks for each type of beam particle are labeled accordingly.

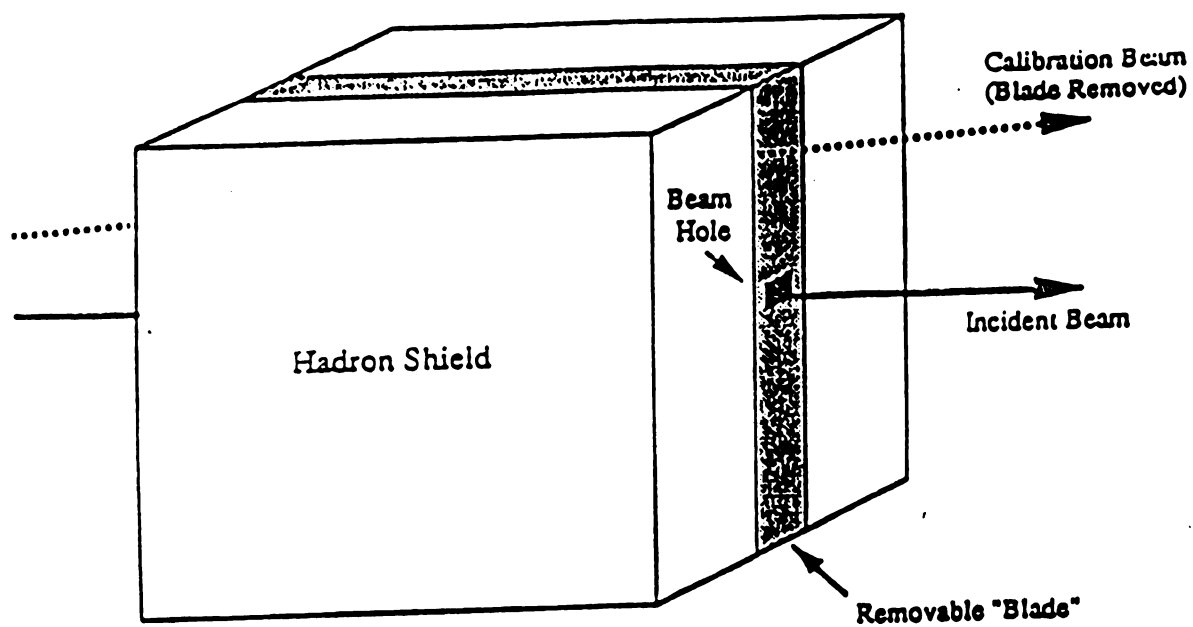


Figure 2.4: Isometric drawing of the hadron shield, showing the central vertical slab through which the beam passes. This piece was removed during LAC calibration.

some fraction of them will produce electromagnetic showers with apparent high p_{\perp} . Depending on the true single photon rate, these showering muons could completely overwhelm the direct photon signal. To help prevent this possibility, the veto wall detects the passage of charged halo particles exiting the downstream face of the hadron shield, and disables the trigger system if a certain configuration of counters fires. See the section on the E706 trigger system for more details.

As Figure 2.5 illustrates, the veto wall is actually two separate walls, containing 32 counters apiece. Each wall is subdivided into 4 quadrants. The individual counters are each $50 \times 50 \text{ cm}^2$ in area. The quadrants within a particular wall overlap each other by 10 cm vertically and horizontally on shared sides. This creates a $10 \times 10 \text{ cm}^2$ hole in the middle to allow passage of beam particles without introducing gaps between active regions. An event was vetoed online if both walls registered a hit. Offline, events were cut from the data sample if the quadrant shadowing the EMLAC octant with the highest p_{\perp} had a hit in either wall. A discussion of the offline cut is given in chapter 4.

2.2 LIQUID ARGON CALORIMETERS

There are two liquid argon calorimeters in the experiment. They reside in the same cryostat and sit one behind the other along the beam direction. The electromagnetic calorimeter (EMLAC) is positioned in front of the hadron calorimeter (HADLAC). The cryostat was made from 5/8 in stainless steel, covered with thermal insulating material. Between the EMLAC and the front wall of the dewar is a filler vessel. This vessel is made from stainless steel sheet metal and is filled with Rohacell, a low density compound. The filler vessel's purpose is to reduce as much as possible the number of radiation lengths of material in front of the calorimeters. Passing through the central region of the calorimeters along the beam axis is a hollow stainless steel tube with a diameter of 40 cm. This vessel is pressurized with helium; its purpose is

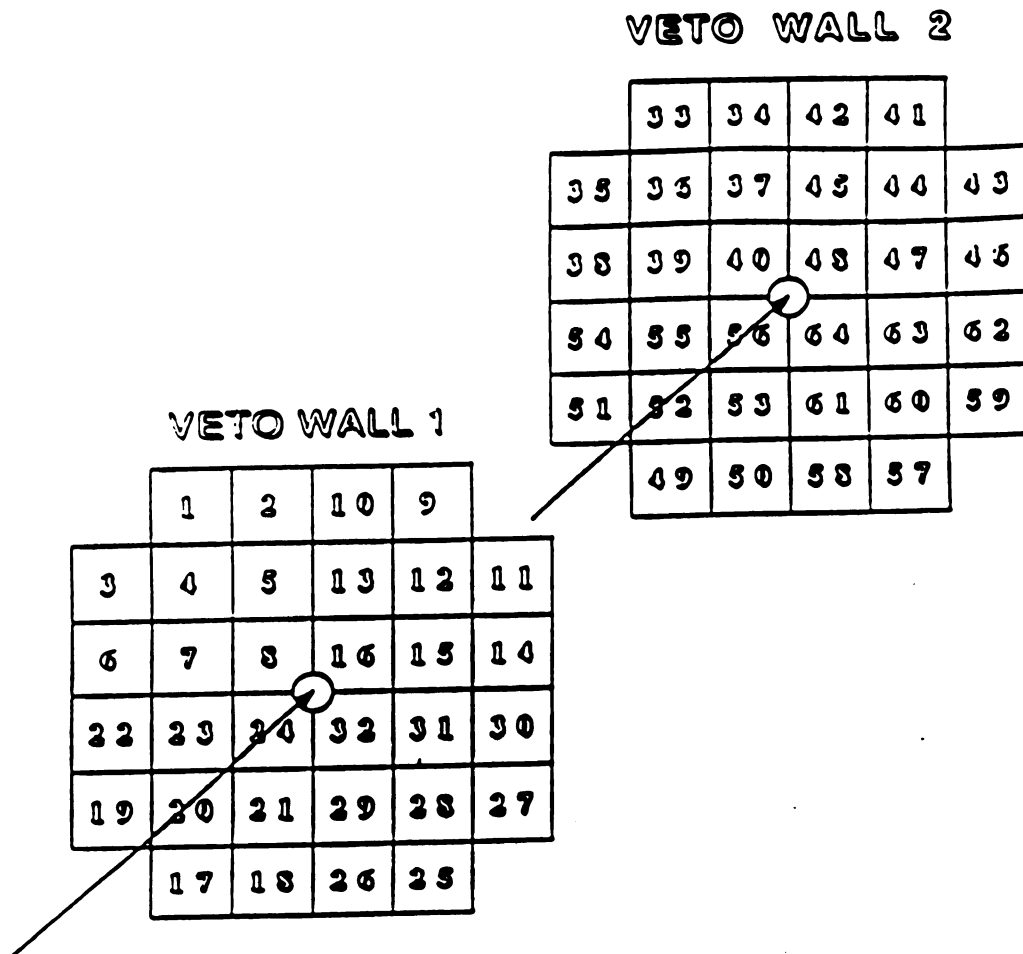


Figure 2.5: Sketch of the Veto Wall planes. The arrows represent the beam's passage through the counters. Each square represents one scintillation counter.

to minimize the number of interaction and radiation lengths between the target and the forward calorimeter. Finally, the cryostat was sealed at the top by a soft steel structure known as the top-hat. The argon was kept below its boiling point by circulating liquid nitrogen through copper cooling coils situated immediately beneath the top-hat. A layer of insulating plastic between the top-hat and these coils kept the top hat at room temperature.

The calorimeters are suspended from threaded rods which are attached to a steel gantry structure. The cryostat can be moved vertically by another set of threaded rods that are also fixed to the gantry structure. The gantry itself rest on Hillman rollers which allow movement transverse to the beam direction. Such movement is used for calibration purposes and to move the calorimeters over to the service area should the need ever arise. A Faraday cage completely surrounds the top-hat structure. This cage is actually a room lined with sheet metal. The calorimeter electronics and high-level trigger system reside in a Faraday room since they are very sensitive to radio-frequency noise. In addition the room is air-conditioned in order to maintain a temperature at which the solid state circuitry can operate properly. Figure 2.6 shows the arrangement of all these modules on the gantry structure.

The EMLAC measured the energies and positions of incident photons and electrons; this device also provided the high level online trigger signal for selecting events with high p_{\perp} photons. As the name implies, a liquid argon calorimeter measures the energy of incident particles by measuring the amount of ionization they generate in liquid argon. The EMLAC is a sampling calorimeter, containing 66 ionization cells. Each cell contains, in addition to liquid argon, a 0.3 radiation length lead absorber plate and a copper-clad printed circuit board to collect the ionization electrons. The EMLAC is more than 27 radiation lengths thick longitudinally thereby insuring complete containment of all electromagnetic showers. This device employs a strip readout

scheme for recording the energy deposited by individual showers, and measuring their positions. Such a scheme is very cost-effective, and greatly simplifies the formation of a high level trigger.

2.2.1 EMLAC Design

The electromagnetic calorimeter is the heart of the experiment. The data gathered from this device is used to reconstruct the high p_{\perp} γ , π^0 , or η that triggered the events, and ultimately to measure the direct photon signal. To achieve this goal this detector had to be able to operate in a high rate environment, allow for efficient π^0 reconstruction, and contribute small systematic uncertainties to the π^0 cross section. These qualities necessitated the following design criteria:

- The detector must operate reliably with a 1-2 MHz interaction rate.
- The device should have the ability to distinguish electromagnetic showers from those produced by hadrons.
- The detector should have as large an acceptance as possible.
- The energy resolution and response linearity, *i.e.* pulse height to energy relation, must be good enough for π^0 s and η s to be reliably reconstructed.
- The lateral segmentation of the calorimeter should be fine enough so that photons emanating from π^0 or η decays can be resolved.
- The lateral segmentation should be designed so that a trigger based on electromagnetic p_{\perp} can be easily formed.
- The large number of channels needed to achieve the desired lateral segmentation requires the channel electronics to be stable over time, since frequent calibration would introduce unacceptable down time.

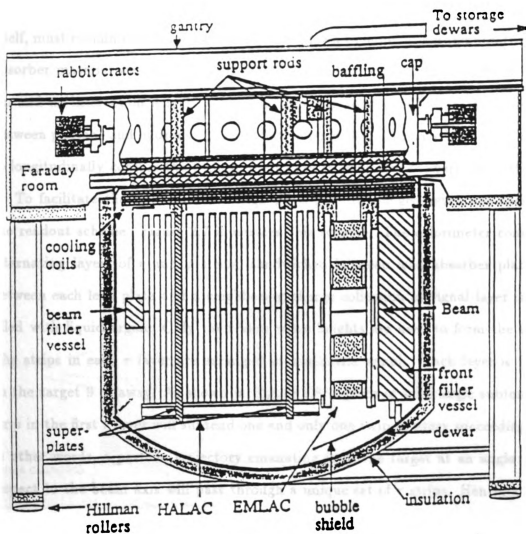


Figure 2.6: Layout of the calorimeters on the gantry support structure. Also shown are the filler vessel, the beam tube, and the Faraday room.

In order to have good π^0 reconstruction efficiency, reliable triggering capability and keep costs down, a sampling calorimeter design with a strip readout scheme was chosen. Liquid argon was selected for the sampling medium because of its homogeneity, high density, and stability in a high radiation environment. The major drawback in using liquid argon is that a large cryogenics support system must be furnished, and the other materials used in constructing the device, as well as the mechanical design itself, must remain sound during and after cooldown to liquid argon temperature. The absorber material was lead. Lead is a high Z material with a radiation length of .56 cm and an interaction length of 17.1 cm, allowing good longitudinal discrimination between photons and hadrons. 27.76 radiation lengths of lead have been used in order to longitudinally contain the highest energy electromagnetic showers (≈ 250 GeV).

To facilitate the formation of a high p_{\perp} trigger an r - ϕ geometry was chosen for the readout scheme. Figure 2.7 illustrates this scheme. The calorimeter consists of alternating layers of r and ϕ strips, sandwiched between lead absorber plates. In between each lead plate and a neighboring charge collection or signal layer is a gap filled with liquid argon. Only the r -view pulse heights are used to form the trigger. The strips in each r layer are arranged in concentric annuli. Each layer is focused on the target 9 m away. As shown in Figure 2.8, a piece of solid angle subtending a strip in the first r layer will subtend one and only one strip in every succeeding layer. In other words, a particle trajectory emanating from the target at an angle α with respect to the beam axis will pass through a unique set of r strips. Hence, a simple $\sin \theta$ weighted energy summing scheme over groups of r strips can be used to trigger on electromagnetic p_{\perp} .

The ϕ layers comprise sectors of a circle. There are two sets of ϕ strips in each ϕ layer. The inner- ϕ set divides the sector into $\pi/192$ subsectors while the outer ϕ set divides the sector into $\pi/384$ pieces. The inner-outer ϕ boundary occurs at $r = 40$ cm

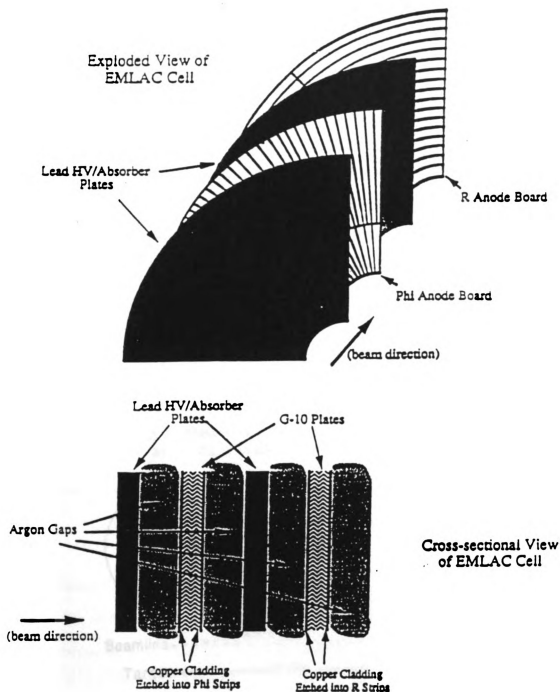


Figure 2.7: Isometric and Cross-sectional views of an EMLAC sampling cell, showing the $r-\phi$ geometry of the charge collection layers.

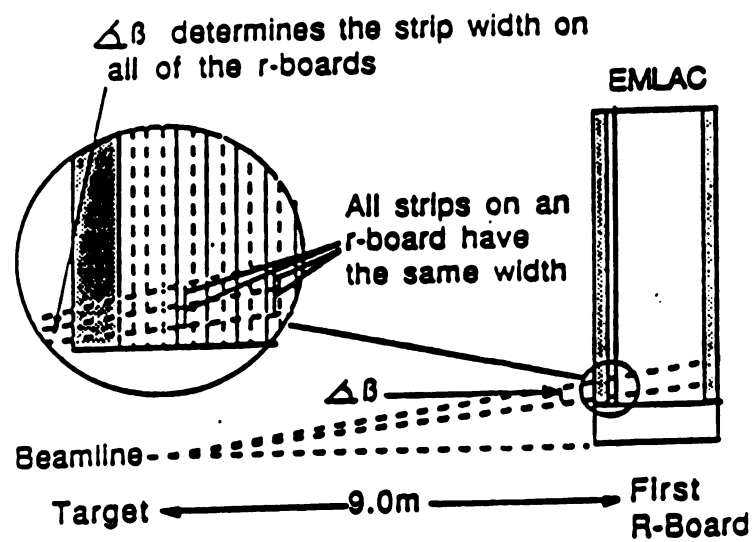


Figure 2.8: Cut-view drawing of the EMLAC illustrating r-strip focusing.

in the first layer, and is focused in succeeding layers. Such a division corresponds to $\approx 90^\circ$ in the nucleon-nucleon cm frame. The EMLAC has a central hole of radius 20 cm. This hole allows the passage of beam particles and accompanying halo. The detector cannot reliably operate in this region of the acceptance where particle rates exceed 10 MHz.

The ability to function in a high rate environment, *i.e.* 1 MHz is primarily a function of the argon gap width [9], since this determines the rise-time of the device. A rise time of $\approx 1 \mu\text{s}$ is required for operation at a 1 MHz rate. To see how this comes about consider the following formula:

$$Q(t) = N_e \frac{tv_d}{d} \left(1 - \frac{1}{2} \frac{tv_d}{d} \right), \quad t < \frac{d}{v_d} \quad (2.1)$$

where $Q(t)$ is the charge collected in a time t off of the signal strips, v_d is the electron drift velocity, d is the gap width, and N_e is the total charge deposited in the gap which can be collected by a particular group of strips. According to this formula, the maximum amount of charge that can be collected is $N_e/2$. If the rise-time is defined as time required to collect 90% of the charge, then

$$t_{\text{rise}} = 0.63 \frac{d}{v_d} \quad (2.2)$$

Argon cannot sustain electric fields much above 10 kV/cm so this places an upper limit on the drift velocity such that $v_d = 4.5 \times 10^5 \text{ cm/s}$. Therefore, a gap no larger than 7 mm can be used if the detector is to function properly with a 1 MHz interaction rate.

However, a small gap width decreases the signal-to-noise ratio because the channel capacitance increases as more sampling cells are added. This assumes the total number of radiation lengths in the detector remains fixed. Choosing a particular gap width involves a compromise between energy resolution and rate limitations.

The lower limit on the gap width is determined by the intrinsic energy resolution. The energy resolution of a sampling calorimeter is limited by the fluctuations in the number of charged tracks, N , traversing the sampling gap. If the track crossings are independent, and the particles are minimum ionizing then

$$(\sigma(E)/E)_{\text{Sampling}} = 1/\sqrt{N} \quad (2.3)$$

There are variations in the measured energy due to path length fluctuations of showering particles, and fluctuations in the energy deposition processes themselves. The energy deposition processes for electromagnetic showers are pair production, bremsstrahlung, and multiple coulomb scattering in the absorber medium. The corresponding fluctuations are known as Landau fluctuations and are parametrized as follows

$$(\sigma(E)/E)_{\text{Landau}} \approx 1/\sqrt{N}(Z/\ln(10^4 x)) \quad (2.4)$$

where x is in g/cm^2 . Therefore, the total energy resolution can be expressed in the following form:

$$\left(\frac{\sigma(E)}{E}\right) = \left(\frac{\sigma(E)}{E}\right)_{\text{Sampling}} \left(1 + \left[\frac{Z}{\ln(10^4 x)}\right]^2\right)^{\frac{1}{2}} \quad (2.5)$$

To minimize ionization losses in the absorber medium the thickness per absorber layer should be minimized. The availability of lead sheets from industry starts at $\approx 2.0 \text{ mm}$ in thickness so this is what was used. Thus, the argon gap determines the energy resolution. The energy resolution was found not to vary significantly from $2.0 - 7.0 \text{ mm}$ gap thickness. Gaps below 2.0 mm encounter HV breakdown problems because the necessary mechanical tolerances for flatness and smoothness cannot be maintained. Therefore, an argon gap of 2.5 mm was chosen.

The lateral segmentation, *i.e.* the r and ϕ strip widths, of the calorimeter is important for reconstructing π^0 s and η s. The segmentation must be fine enough so that the individual decay photons can be accurately and efficiently reconstructed offline. This

reduces the direct photon background, making the corresponding cross section less dependent on monte carlo technique. However, very high energy π^0 s, decaying with low asymmetry will be not be reconstructed as such because the natural or Molière width of the showers causes them to coalesce. Consequently, there is a practical limit to the strip width, which is dictated by the natural shower width. The π^0 s lost due to coalescence are a very small fraction of the total. A monte carlo study was done, using a simulation of the EMLAC that included the intrinsic energy resolution and the noise due to channel capacitance. The strip width was a free parameter. The response to high energy π^0 decays was simulated and the showers reconstructed. It was found that the probability of π^0 and single γ having the same width was minimized for a strip width of 6 mm. Hence, the r strips were designed to be 5 mm wide in the first layer, increasing in successive layers to accommodate the focusing. The lateral segmentation of the ϕ layers was done so that the average ϕ width was 6 mm.

The electromagnetic calorimeter was longitudinally divided into front and back sections. This was done to enhance π^0 reconstruction efficiency since showers spread laterally with depth in the detector. Showers that may coalesce in the back section may appear as two photons in the front section as illustrated in Figure 2.9. Also, dividing the EMLAC in this fashion provides for photon-hadron discrimination. Hadrons have a longitudinal profile considerably different from photons because the shower maxima are typically in different places due to the interaction and radiation lengths of lead being different. A monte carlo study determined that the EMLAC could resolve photons from π^0 decays with optimum efficiency with a front to back ratio of 15/51 layers [10]. Due to considerations of channel capacitance noise in the back section, a ratio of 11/22 layers was selected separately for the r and ϕ views [11].

2.2.2 EMLAC Construction

The electromagnetic calorimeter was built in 4 mechanically independent units, called quadrants, because each cell represents $1/4$ of the detector's azimuthal acceptance. Each quadrant contains 66 sampling cells with 33 r signal layers interleaved with 33 ϕ layers. Between each r and ϕ pair there is a lead plate. An aluminum plate was placed in front of the first layer to reduce the systematic energy loss. The lead plates are quadrant sized, but the r and ϕ layers octant sized. Special G-10 spacers placed around perimeter of each cell maintain the cell thickness. Figure 2.10 shows the entire detector in its assembled configuration. Also shown is an exploded view of one of the quadrants. The details regarding the various components shown in this figure are discussed in the following text.

The r and ϕ layers are composed of copper clad G-10 boards 1.59 mm thick. The boards are clad on both sides, and the appropriate strip patterns were routed out, using a specially designed computer controlled tool [12]. Each layer is composed of two boards fitted together at the quadrant bisection by special two-headed G-10 buttons having a yo-yo shape. There are 31 single-headed buttons placed in the active region of each board. Half of these buttons have heads on one side of the board, and half of them on the opposite side. These buttons are uniformly distributed on each board, and are randomly displaced between layers. Their purpose is to maintain the proper argon gap width. A strip ≈ 1 cm on the readout edge of each board was tinned to provide a good low contact potential junction with the readout connector. The charge collection boards have holes drilled out on the sides corresponding to a quadrant perimeter. Special stainless steel rods with graphite epoxy coating for insulation are inserted through these holes. Figure 2.11 shows the dimensions and

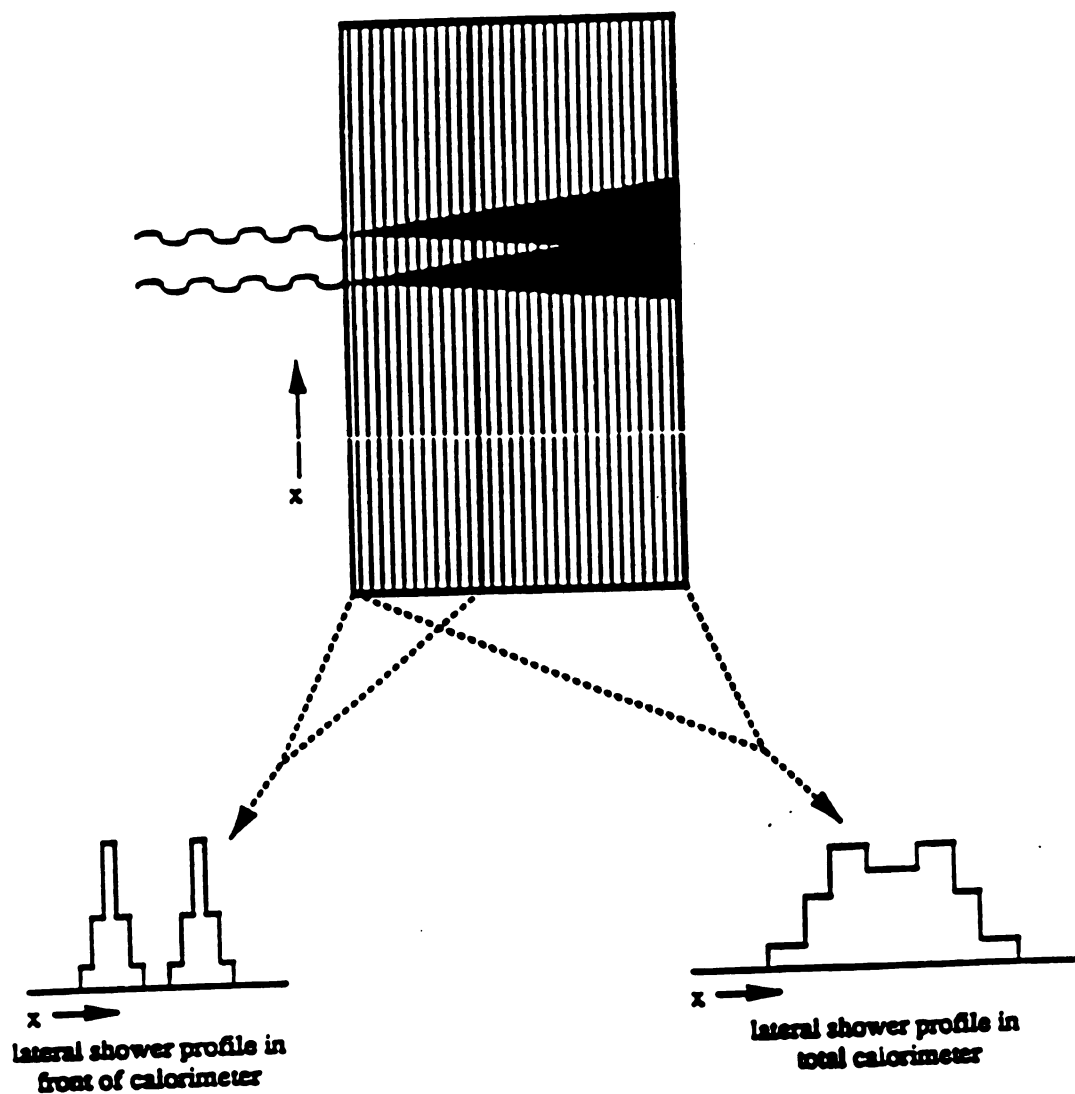


Figure 2.9: Longitudinal segmentation as an aid to π^0 reconstruction. Showers have narrower profiles in the EMLAC's front section, allowing both decay photons to be resolved.

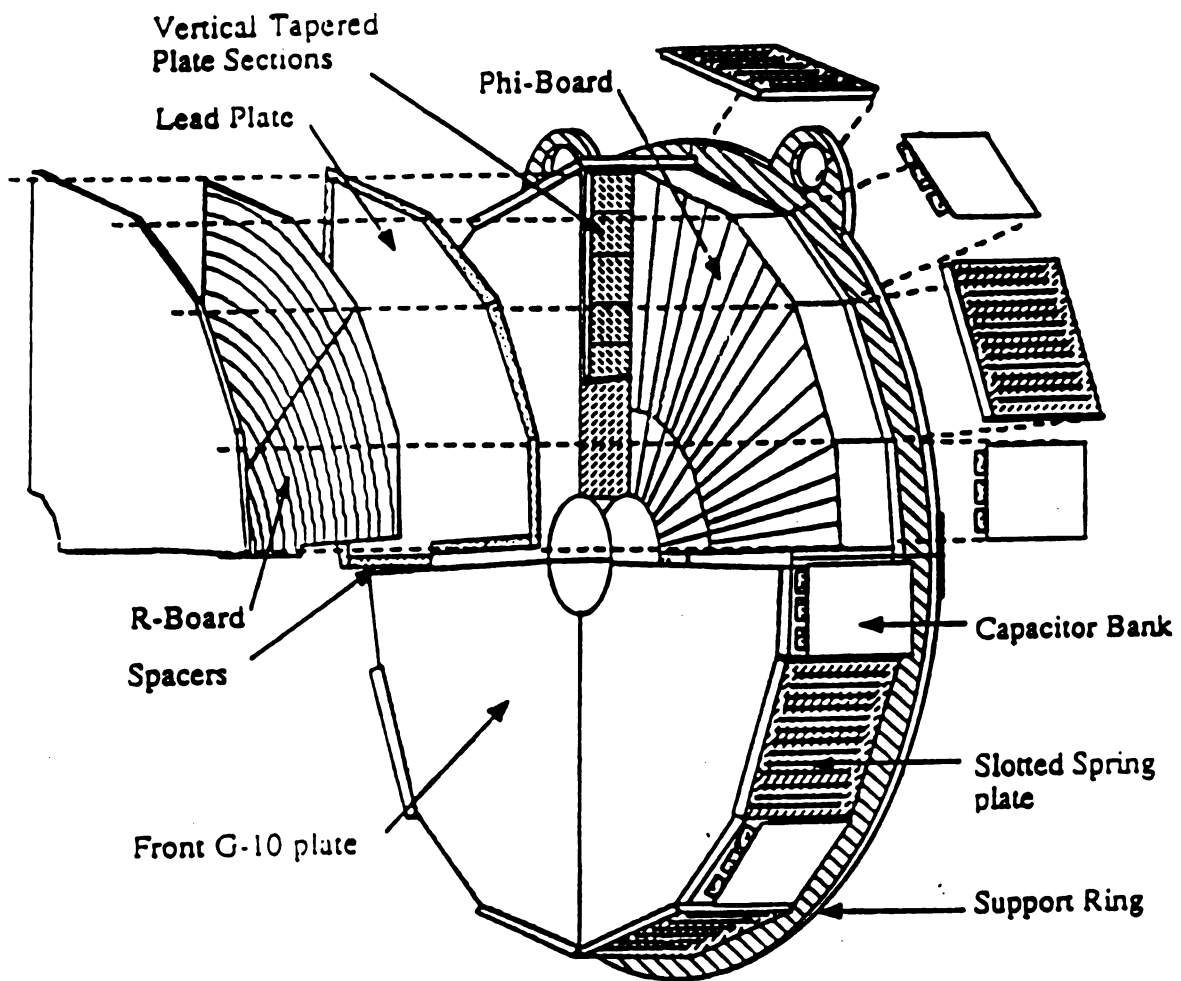
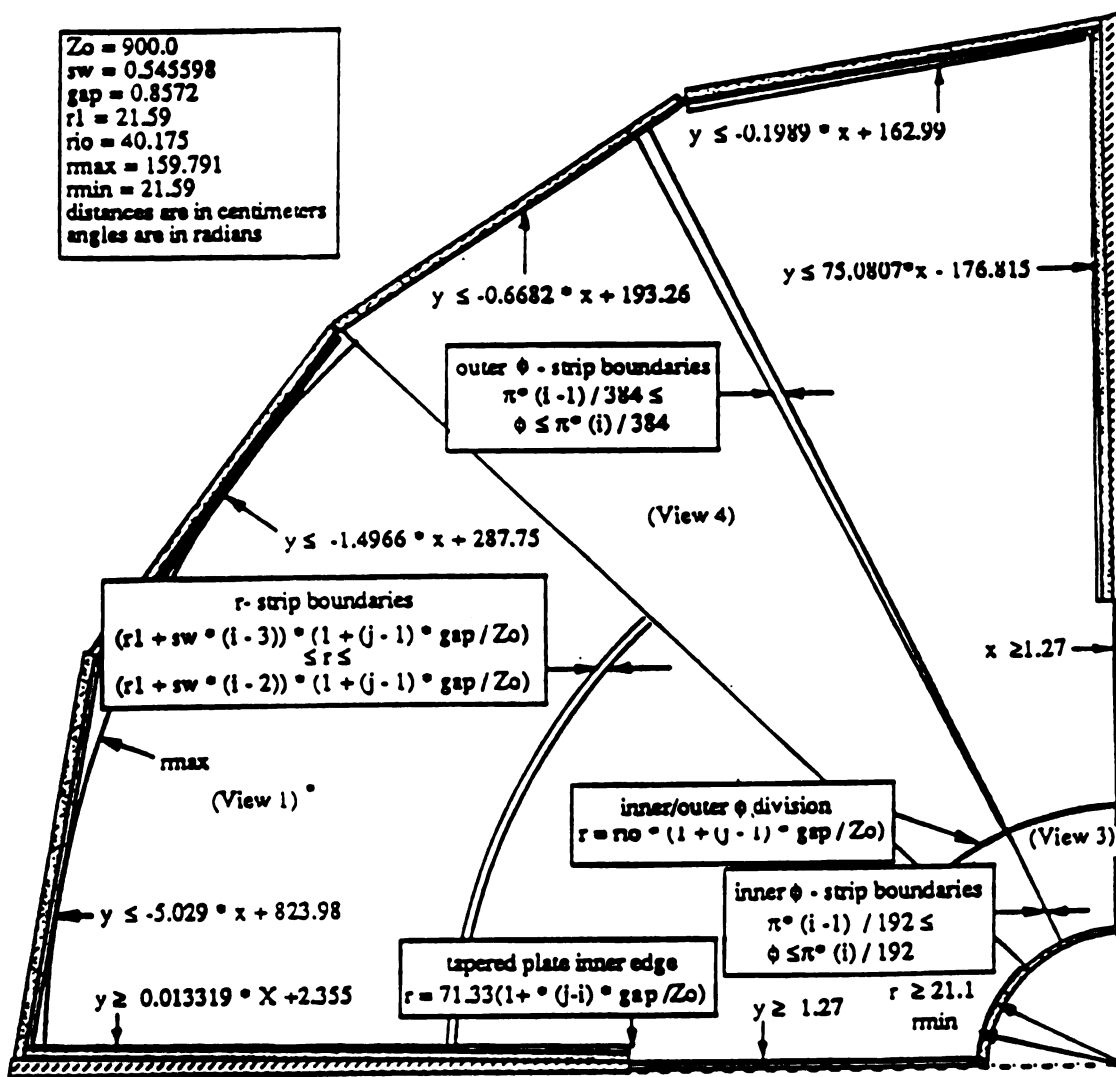


Figure 2.10: Isometric drawing of the EMLAC with an exploded view of one quadrant.

divisions of an EMLAC quadrant's active area.

At the front and back of a quadrant stack are two 3.6 cm thick G-10 plates. The threaded rods hold the stack together laterally during assembly. The rods are then bolted to the thick G-10 support plates at the end of assembly, and the entire quadrant stack is held together under compression. Between the active stack and each G-10 support plate lie three layers of readout boards. The front set of readout boards read out the front section of the EMLAC, and the other set read out the back. Unlike the signal boards, the readout boards were scored only on one side; the other side's cladding served as a ground flash, which was removed around the edges. Thick G-10 buttons separated the various readout layers from each other. One layer in each set contains the summed inner-outer ϕ channels. Another fans in the summed inner r channels, while the third contains the longitudinal sum of outer r channels. Figure 2.12 illustrates the layout of channel strips on r and ϕ readout boards. The summed signals are fanned into a series of connectors on the azimuthal perimeter of each board. Cables are attached to these connectors that lead up to the feed-thru connectors for the calorimeter electronics crates attached to the dewar top hat.

The longitudinal summing of signals is done using specially designed connector cables. Each cable is composed of a 1/32 in copper braided wire to which special clamps have been attached. The clamps are stamped from bronze spring metal. There are eight classes of these connector strings, corresponding to the four views in each longitudinal section of the EMLAC. The spacing of the clamps on a connector string corresponds to the r or ϕ cell spacing. In addition, the clamp that attaches to the readout board has to be positioned according to the placement of the particular readout board in the quadrant stack. The connector strings lay in channels along the various sides of a quadrant, and the clamps fit through special slots in the G-10 spacers of each cell, grabbing the appropriate signal or readout strip. All connector cables were tinned to provide good electrical connections and minimize contact poten-



* View 2 same as view 1 but covers area where view 3 and 4 are

** i - strip number; j - layer number

Figure 2.11: Drawing of the Physical Boundaries for the sensitive area of an EMLAC Quadrant.

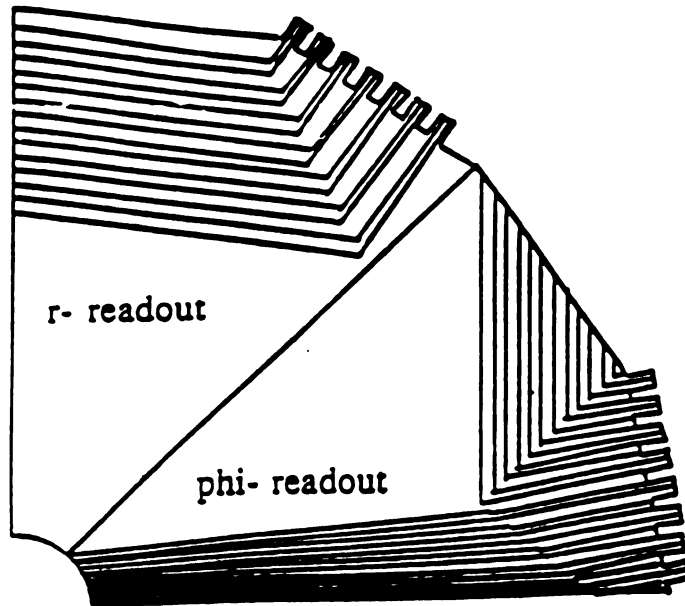


Figure 2.12: Typical layout of r and ϕ strips on the readout boards for the EMLAC.

tials. A schematic illustration of the summing of the various signal strips is given in Figure 2.13.

Figure 2.14 shows a typical EMLAC pair of r and ϕ cells with spacer and connector. A special plunger appears in the figure too. In fact, there is a set of plungers along the outer edges of each lead plate in the bottom quadrants. The other two edges are used for the high voltage hookup to the ballast capacitors for each absorber plate. The plungers are spring loaded, and their purpose is to provide a force on the lead plates during and after cooldown to liquid argon temperature. Such a compression force is needed because the lead contracts laterally more than the rest of the quadrant stack. Since the absorber plates are not mechanically fastened to the stack, they could pull free from the inner part of the detector, compromising the acceptance.

Going back to Figure 2.10 the reader can see how the four quadrants are assembled together to form one functioning unit. The vertical quadrant boundaries are fastened together via tapered steel plates that run along them. Thin stainless steel plates are

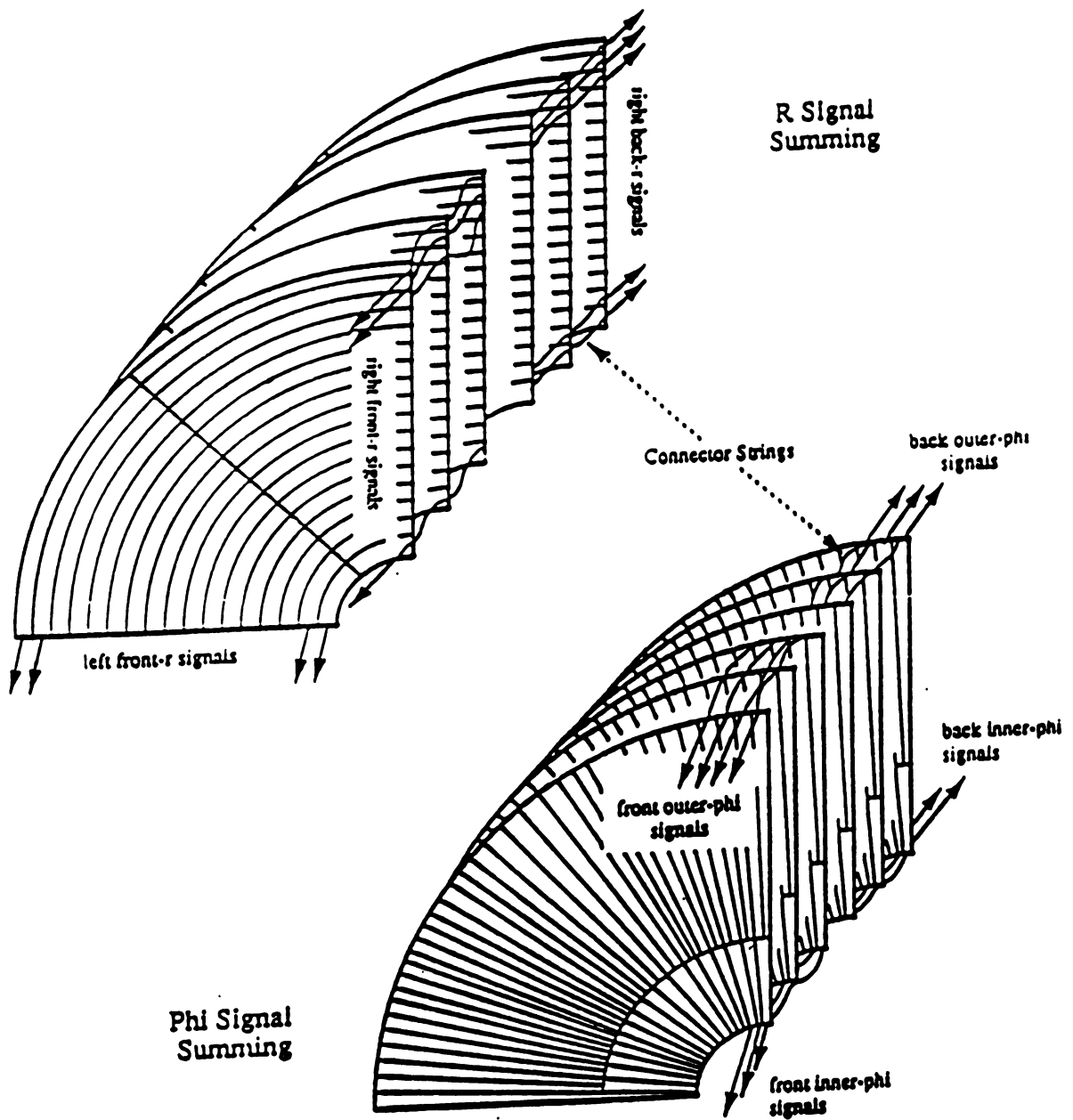


Figure 2.13: Signal summing scheme in the EMLAC. Signals in a quadrant are summed in the front and back sections separately. These sums are grouped into outer r, inner r, outer ϕ , and inner ϕ views.

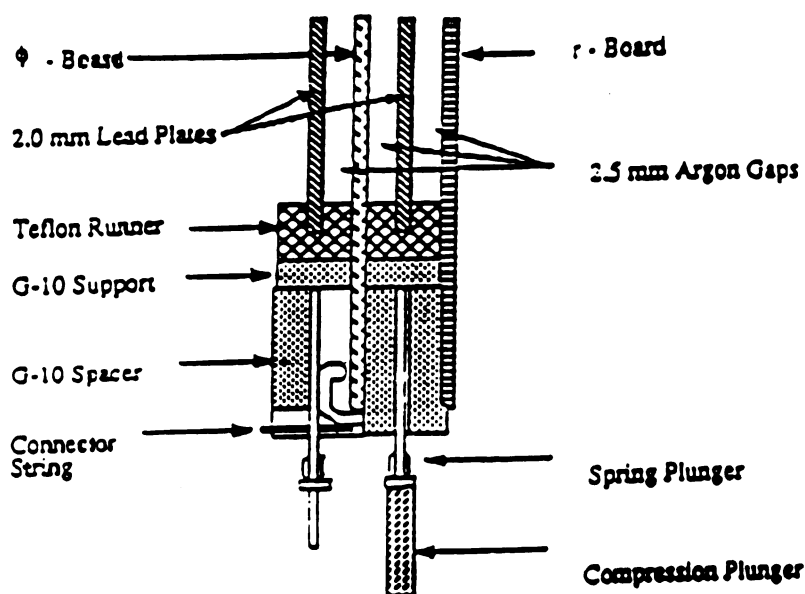


Figure 2.14: Cross-sectional view of an EMLAC cell at the outer edge of the electromagnetic calorimeter.

are fastened to all individual horizontal boundaries. There is no mechanical connection along the horizontal boundary between quadrants. Slotted stainless steel plates are positioned around those sides of the quadrants that contain the spring loaded plungers. They are bolted to the thick G-10 support plates. These plates help maintain the lateral stack alignment, but more importantly they connect the EMLAC quadrants to the main support rings via the support bars. The threaded rods are bolted to the G-10 plates using Bellville compression washers as are the slotted plates to the support bars. The washers insure that compression is adequately and evenly distributed during the differential contraction associated with cooldown. Finally, the support bars are bolted to the support rings, and the rings are joined together via patch plates. Figure 2.15 shows the cross-sectional view of the quadrant support assembly. The assembled detector was then suspended from the gantry by four four clevises attached to the loops on the top support rings. A full discussion of the construction procedure for this detector as well as the properties of the materials used to

fabricate it is found in Bill DeSai's thesis [13].

2.2.3 The Hadron Calorimeter

The hadron calorimeter or HADLAC was positioned directly behind the electromagnetic calorimeter, and it shared the same cryostat and gantry structure. This calorimeter operated in the same fashion as the EMLAC, but it was designed to measure the energy of hadronic rather than electromagnetic showers. For this reason a sampling design with steel absorber media and a pad type charge collection scheme was selected. Figure 2.16 shows the assembled device as it resides inside the cryostat.

The hadron calorimeter consists of 53 steel plates each 2.5 cm thick, interleaved with sampling cells called "cookies". An exploded view of one of these "cookies" appears in Figure 2.17. As the reader can see, the charge collection layer consisted of two large circuit boards facing back-to-back between a pair of high voltage planes. Both the signal and high voltage boards were made from copper clad G-10. The signal boards were tessellated with horizontal rows of equilateral triangular pads. Signals from these pads were brought to the edge of the boards via signal traces, running between rows of pads. Each pair of signal boards was relatively aligned such that a row of pads on one plane corresponded to a row of signal traces on the other plane.

The signal planes are separated from the high voltage planes within a cell by a 3 mm gap filled with liquid argon. Hence, the rise times of both liquid argon calorimeters are similar. The HADLAC also has a central hole focused on the target. The gap width is maintained by G-10 spacers that run horizontally between the high voltage and signal planes. The spacers are positioned so that they cover the readout lines on the signal boards. This prevents charge from being collected on the signal lines, reducing the channel-to-channel variation in response to a shower of a given energy.

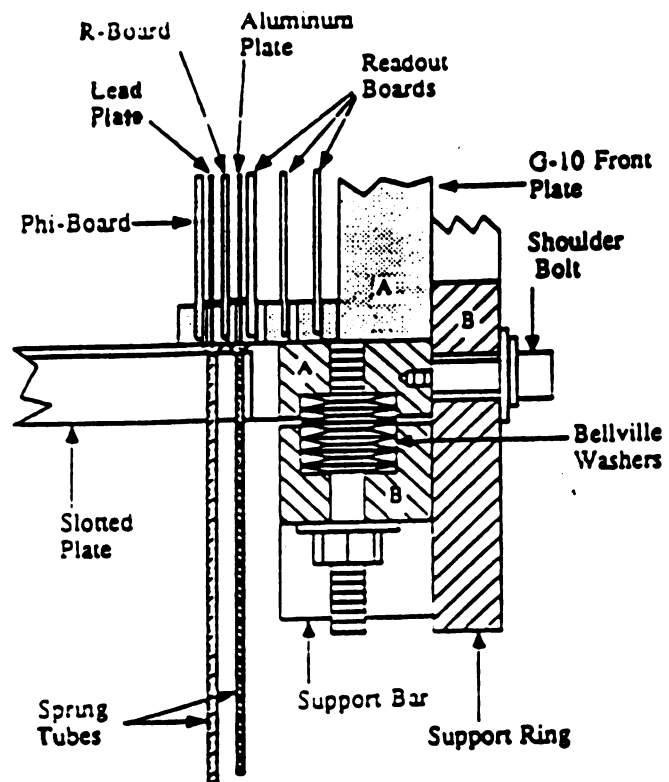


Figure 2.15: Cross-sectional drawing of a quadrant support assembly for the EMLAC

The HADLAC's signal pads were designed such that corresponding pads in successive cookies subtend the same solid angle as the pad in the front cookie. The pad height in the front was 10 cm and it increased to 14 cm in the last cookie. The calorimeter was longitudinally divided into a front section with 14 sampling cells and a back section with 39 sampling cells. The cookies in each section had all longitudinal sets of focused pads electrically connected together into a tower. The summed signal from every tower was hooked up to an amplifier channel in the Faraday Room.

The high voltage planes are clad on both sides with copper. The side facing the signal plane is held at negative high voltage while the other side is grounded. There is enough capacitance between high voltage and ground that ballast capacitors are not required for this detector.

The energy resolution of this device was determined by using π^- beams of 50 and 200 GeV in energy. The resolution was parametrized in the following form

$$\frac{\sigma(E)}{E} = 0.04 + \frac{1.83}{\sqrt{E}} \quad (2.6)$$

One cause for the rather poor performance of this device was that the sampling was not fine enough. Also a substantial fraction of the ionization occurred in a region outside the drift field so it could not be collected. Another factor that degraded the HADLAC's energy resolution was the rather large channel capacitance due the pad sizes being too large. This capacitance decreased the signal-to-noise ratio. Finally, the neutron energy fraction was never seen. Neutrons are copiously produced in hadronic showers, but they leave no ionization in liquid argon because they are electrically neutral. Plastic scintillator, on the other hand, does respond to neutrons. Plastic materials generally contain a large number of hydrogen nuclei. Neutrons traversing the material will knock these nuclei out of the molecular structure a significant fraction of the time. The hydrogen nuclei will recombine generating UV light which can be detected by a phototube.

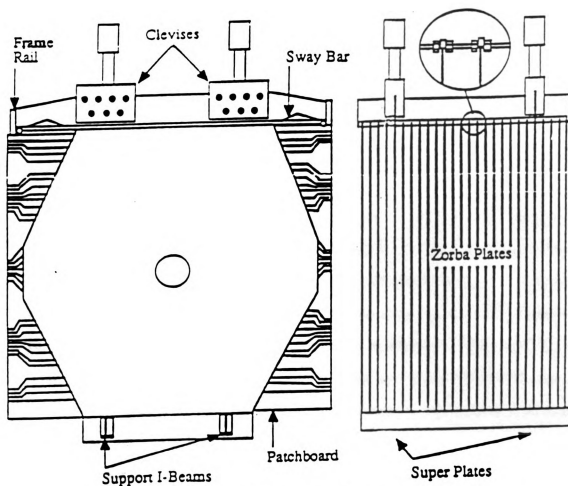


Figure 2.16: Front and side views of the hadron calorimeter. Steel "Zorba Plates" are the absorber media. The hole, shown in the center of the front view, allows passage of beam and halo particles.

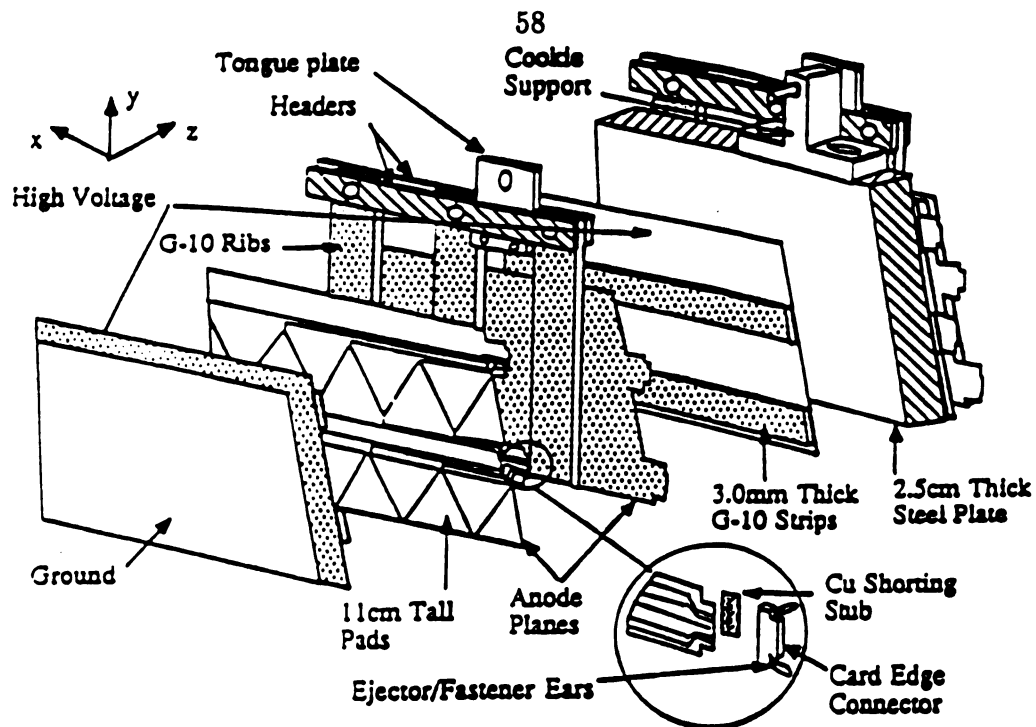


Figure 2.17: Exploded portion of a HADLAC charge collection cell or "cookie".

2.2.4 LAC Electronics

The RABBIT system was used to readout the liquid argon calorimeters. This electronics system was developed at Fermilab; RABBIT is the acronym for Redundant Analog Bus Based Information Transfer. The Rabbit system is based on a special bus capable of transmitting analog signals. Digital information in the form of address and control signals can also be transmitted over a set of differential ECL and TTL signal lines. The RABBIT bus is contained in the backplane of every RABBIT crate. The backplane is actually divided into two separate busses: a top bus and a bottom bus. This feature allows the RABBIT system to function in a low access environment such as a high energy collider. In principle a detector channel can have two completely independent and redundant data transfer paths to the data acquisition computer. This allows full hardware function to be maintained in the event of an electronics failure along one of these paths.

Each slot within a RABBIT crate is assigned an address, and so every module is referenced according to the slot in which it resides. Individual channels within a module are referenced by a subaddress. There are 64 analog and 64 digital subaddresses per slot. A crate contains two controller modules called EWE's. One EWE controls the top bus while the other controls the flow of information in the bottom bus. Each EWE is capable of controlling either bus in accordance with the redundancy feature. Because the Faraday room was accessible under running conditions, the redundancy feature was not exploited so that the number of crates could be kept to a minimum. This helped reduce costs along the entire data transfer path.

Three other modules were employed in the experiment. The BAT module (before and after timer) was used to terminate the end of the backplane opposite the EWE modules. The module monitored the various voltage levels in a crate, the amount of current being consumed, and the crate temperature. However, its most important function was, as its name implies, to provide timing pulses for the sample-and-hold and TVC circuits of the LACAMP modules. The LACAMP modules each contained 16 channels for amplification and readout of the signals coming from the calorimeters. The amplifier modules were also capable of providing a fast output signal. The fast output signals generated from the electromagnetic calorimeter pulses were used to form the high level electromagnetic trigger. In order to have a reliable and efficient triggering capability special summing modules known as p_{\perp} -ADDER cards were used to sum the individual fast output pulses for each octant separately. The details of their operation is described in the section discussing the trigger apparatus.

The EWE module is designed to receive the analog data coming from the LACAMP modules, digitize it, and buffer it for transfer to the next element of the data acquisition system. Each controller possess a 16-bit analog-to-digital converter that is used to digitize the analog signals coming from the amplifier modules. Having only

one ADC per bus simplifies the design and calibration procedures, and it keeps costs down as well. The main drawback to this approach is that it takes more time to read out the amplifier channels, each digitization cycle taking about $17\mu\text{s}$ to complete. Two steps were taken to overcome this problem. First, the simultaneous readout of two channels is possible if the redundancy option is not utilized. Second, a zero suppression window was set whereby a channel was not digitized if its analog level failed to exceed a predetermined value. The zero suppression procedure takes about $1/6$ as much time as digitization. The EWEs are readout by processor-buffer units known as MXs. The crate controllers also receive sets of instructions for executing different procedures from the MX units. Each MX can control up to 4 RABBIT crates with separate cabling for top and bottom busses.

The 16 channels in each LACAMP module are clustered into four groups of nearest neighbors. All channels in a group of four are tied to the same reference voltages. Such a clustering is natural because the summed output from every group of four is fed into a time-to-voltage converter circuit (TVC). Figure 2.18 shows the four basic components of an amplifier channel together with the summing scheme used for the TVC inputs. The four major circuits in a LACAMP channel are:

- A charge integrating amplifier
- A sample-and-hold circuit to measure energy deposition
- A TVC circuit to measure the time at which energy was deposited relative to a particular interaction
- A fast output circuit to provide trigger signals

The charge integrating amplifier had a capacitor in the feedback loop for an operational amplifier. The charge collected from a longitudinal sum of calorimeter sampling cells was proportional to the charge, and hence the voltage, on the feedback capacitor.

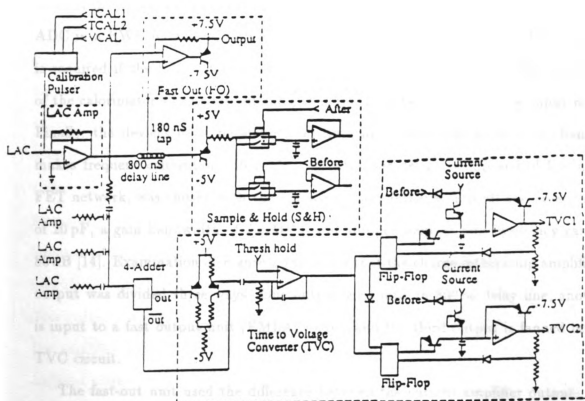


Figure 2.18: Schematic of a LAC amplifier channel showing the Sample-and-Hold, TVC, and Fast Out circuits.

Therefore, a linear relationship exists between the energy deposited in a channel and the voltage or pulse height appearing on the capacitor. A resistor was hooked up in parallel with the capacitor so that the circuit would return to its ambient state over a time interval much longer than the rise-time of a LAC pulse. The decay-time of the resistor capacitor loop was $\approx 150 \mu\text{s}$ as opposed to a rise-time of $\approx 350 \text{ ns}$ for the calorimeters. The design of this circuit was governed by four criteria. First, the amplifier had to have a low input impedance to match the rather low impedance of the input cable, which was around 10 to 20Ω . Otherwise, there would be several large reflections during the signal rise-time that would distort the actual signal from the calorimeter. Second, the amplifier must have a high gain. The charge collected per channel in the calorimeter is on the order of pico Coulombs while the range of the ADC in a EWE module is 2.5 volts. Considerable amplification of the LAC signals is required if the full 16 bit precision of the ADC is to be utilized. The smallness of the calorimeter signals also dictates that the amplifier must have low input noise. Finally, the devices must be stable over time since that large number of channels makes frequent calibration infeasible. An amplifier design, composed of low noise FET network, was chosen with the following characteristics: a feedback capacitance of 20 pF, a gain bandwidth of 700 MHz, and an open-loop or zero frequency gain of 80 dB [14]. Examination of Figure 2.18 reveals that the charge integrating amplifier's output was divided three ways. One output goes into an 800 ns delay line, another is input to a fast output unit (EMLAC only), and the third output is fanned into a TVC circuit.

The fast-out unit used the difference between the current amplifier output, and the value it had 180 ns earlier to make a short negative pulse. This was accomplished by tapping the delay line at an intermediate point. A pulse was produced only if the difference was above a specified threshold. The generated pulse height was proportional to the integrated signal, so it provided useful information to the trigger

logic, described in a following section. The fact that the shape of the integrated signal is the same for all pulse heights insures the validity of this method, because the signal value at 180 ns is always the same fraction of the full pulse height. The trigger logic used the fast-out signals to determine whether or not enough p_{\perp} had been deposited in the EMLAC to make an event a high p_{\perp} γ , π^0 , or η candidate. If $\gtrsim 1.7$ GeV/c of p_{\perp} was deposited in an EMLAC octant, a PRETRIGGER signal was generated by the trigger electronics. The PRETRIGGER signal resulted in an EVENT signal being sent to the BAT modules. Upon receiving this signal, the BAT's initiated an event timing sequence, illustrated in Figure 2.19. Two logic signals known as BEFORE and AFTER were sent to all LACAMP channels in each crate.

The sample-and-hold circuits consisted of two precision capacitors which looked at the delayed output of the amplifiers. Between each capacitor and the delayed output was an electronic switch. Under ambient conditions the switches were closed, and the outputs were sampled. Upon receiving a BEFORE or AFTER pulse the switches were opened and the corresponding voltages were held on the capacitors, hence the name sample-and-hold. The BEFORE signal was issued so that one capacitor measured the level just before the amplifier pulse arrived. The AFTER pulse, generated ≈ 640 ns later, caused the peak level of the output to be retained. Upon command by the EWE module these levels were read for each channel and subtracted before digitization. This reduced the effects of low frequency line noise as well as pile-up, which involves the amplifier signals from a second event arriving before the circuit returned to its ambient state.

Events that deposited energy within a few hundred nanoseconds of one another could not be distinguished by the sample-and-hold circuitry. TVC circuits were employed to solve this pile-up problem. Each TVC unit is composed of two circuits in a master slave arrangement. Figure 2.20 shows a simplified schematic diagram of the cir-

cuit. The differentiated output of a group of four amplifiers is fanned into a given TVC input. Each sum is compared to a crate-wide threshold set by the BAT. All sums that exceed the threshold fire their respective discriminators which in turn clock the flip-flops of the corresponding master TVCs. Ordinarily, all current from the source drains through the flip-flop, but when the flip-flop unit is clocked the resulting change in the voltage level prevents this. As a result, the capacitor is charged at a constant rate. The slave TVC flip-flop is enabled whenever the master TVC is clocked. If a second input signal arrives before a global reset or a BEFORE signal, then the slave TVC is clocked, causing its capacitor to charge up. The BEFORE signal breaks the path between the current source and the capacitor, thereby holding the capacitor's voltage level.

If no BEFORE signal arrives within 150 ns of a TVC's firing, then the unit is automatically reset. The BEFORE signal was timed to always arrive ≈ 800 ns after the triggering event, and the TVC circuit was designed to read half of full scale under this condition. The event timing sequence of Figure 2.19 shows the usefulness of the slave circuit. Here, an event fires the master TVC, but doesn't produce a PRETRIGGER signal so no BEFORE pulse is generated. Later, a second event arrives that does generate a PRETRIGGER pulse, and its time relative to the interaction responsible for it is recorded by the slave TVC.

2.3 THE E706 TRIGGER SYSTEM

If one examines an unbiased sample of hadronic interactions, the occurrence of a high $p_{\perp} \pi^0$ or single photon event will be very rare. To enrich the E706 data with these types of events a special electronics system was devised to select only those events, containing a significant amount of electromagnetic p_{\perp} (~ 3.0 GeV/c), for writing out to tape. This selection mechanism, known as the trigger, is composed of very fast

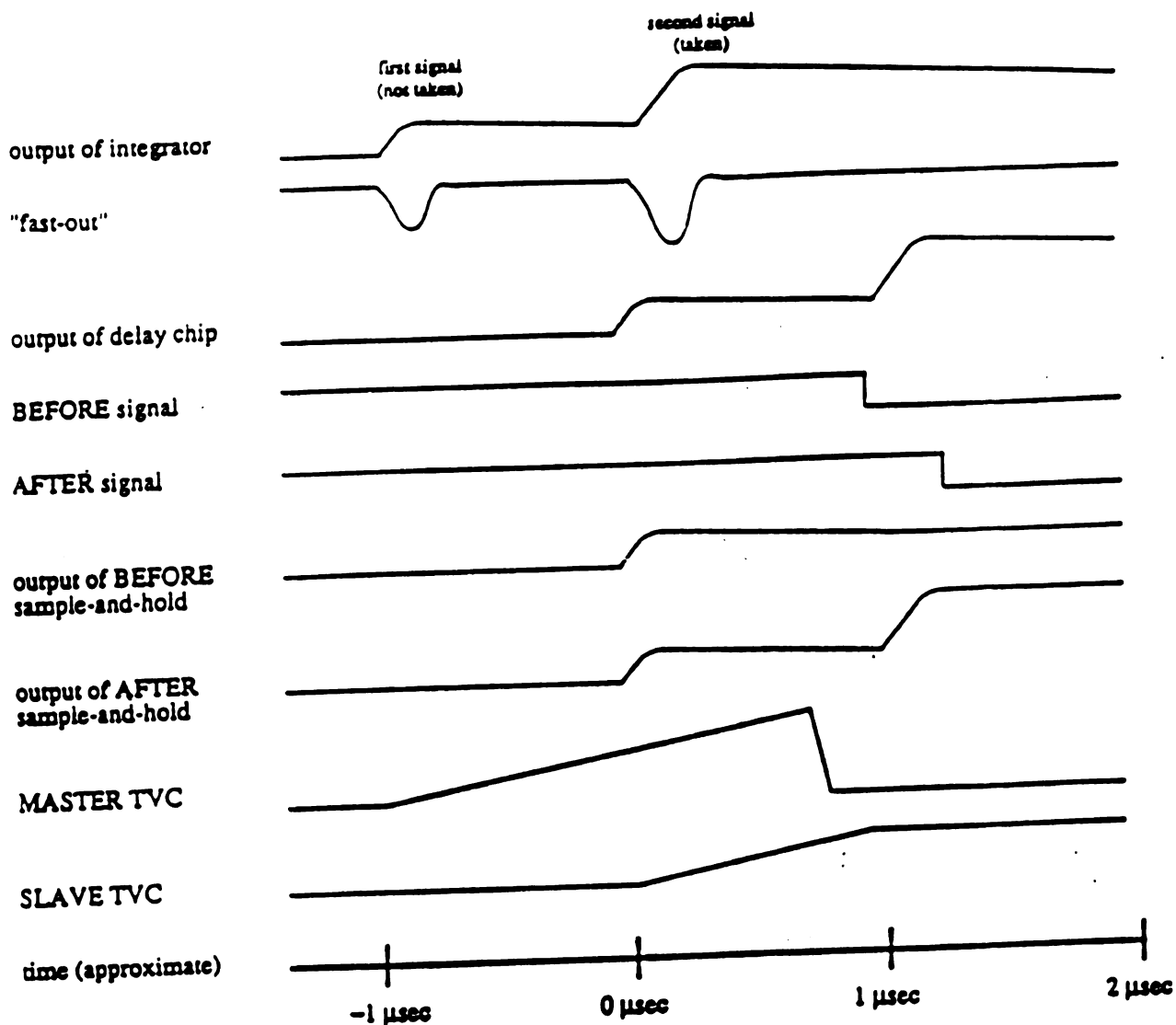


Figure 2.19: An example of an Event Timing Sequence initiated by the BAT modules. An event fires the master TVC, but fails to produce a PRETRIGGER signal. A short time later, an event fires the slave TVC, generating a PRETRIGGER and BEFORE pulses as well.

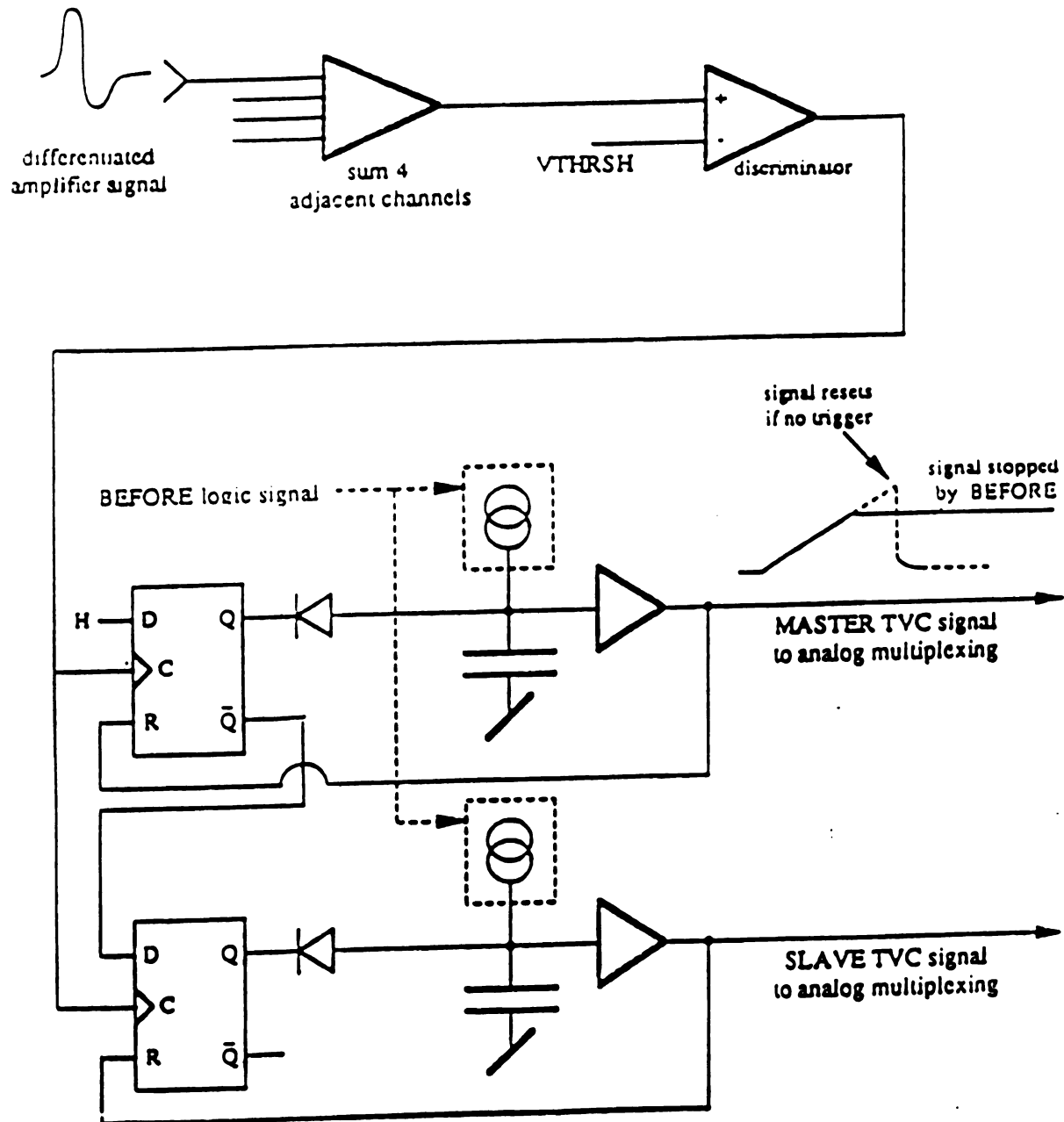


Figure 2.20: A simplified diagram for a TVC unit.

circuits. There are three major portions of the trigger system. First, there are the electronics associated with the EMLAC which estimate the amount of p_{\perp} deposited in the detector. Another part of the circuit provides the beam and interaction definition. Finally, there are several counters and modules that generate vetoing signals. These vetoes halt the trigger's operation for up to $30 \mu s$.

2.3.1 EMLAC p_{\perp} System

The EMLAC was used to detect local depositions of large amounts of p_{\perp} . The p_{\perp} deposited is obtained from the deposited energy by the following

$$p_{\perp} = E \sin \theta \quad (2.7)$$

The detector's focused $r - \phi$ geometry made the formation of the trigger straightforward. The r-strips were used to form a p_{\perp} sum in the following manner:

$$p_{\perp} = \sum_i e_i \sin \theta_i \quad (2.8)$$

p_{\perp} is the amount of transverse momentum in a particular r-region of an octant. The sum is over the strips in the front and back sections within the region. e_i is the energy deposited in the i th readout strip in a summed region, and θ_i is the production angle corresponding to the i th readout strip.

Figure 2.21 shows how the r-strips of each EMLAC octant are grouped together to form the various p_{\perp} sums. The analog summing begins by taking the sum of adjacent fast-outputs from the LACAMPs, and putting the signals into 8-bit linear attenuators. The attenuators provide the $\sin \theta$ weighting of the pulse heights. The attenuator outputs are then summed in groups of 8; front and back sections are summed separately at this stage. Adjacent groups of 8 are subsequently summed into non-overlapping groups of 32 channels. The groups of 8 provided the input to the local discriminator modules, while the sums of 32 were used to form the global trigger signals.

The local discriminator modules are shown schematically in Figure 2.22. At this stage the sums of corresponding front and back groups of 8 are summed together on input. Furthermore, adjacent groups of 8 are summed together into groups of 16 channels, overlapping one another by 8 channels. If any sum of 16 exceeds a specified threshold, then a single-signal (SLOC) trigger signal is generated. There were two local discriminator modules per octant for the 1987-1988 data taking period. They produced logic signals referred to as LOCAL_PT_HI and LOCAL_PT_LO, indicating the relative magnitudes of the thresholds.

The sums of 32 are discriminated in a similar fashion by a set of devices called the global p_{\perp} modules. However, the groups of 32 are summed in a different manner. There is a sum of the 3 innermost groups of 32 channels, a sum of the next 4 groups of 32, and a sum over all groups of 32 in each octant. Thus, each octant had three different global p_{\perp} sums assigned to it, and there were two global p_{\perp} thresholds per octant. The three global sums are expressed mathematically as follows:

$$\begin{aligned}
 \text{glpt13} &= \sum_{i=0}^{95} p_{\perp i} \\
 \text{glpt47} &= \sum_{i=96}^{233} p_{\perp i} \\
 \text{glpt17} &= \sum_{i=0}^{233} p_{\perp i} \\
 p_{\perp i} &\propto E_i \sin \theta_i
 \end{aligned} \tag{2.9}$$

Besides forming a global p_{\perp} logic signal, the global p_{\perp} sums glpt13 and glpt47 were used to generate octant PRETRIGGER signals. The generation and purpose of the PRETRIGGER signal as well as the high level interrupt signal are given in a following subsection. Table 2.2 lists the nominal thresholds for both the local and global p_{\perp} trigger modules. Notice that several of them were changed from time to time during the data taking period.

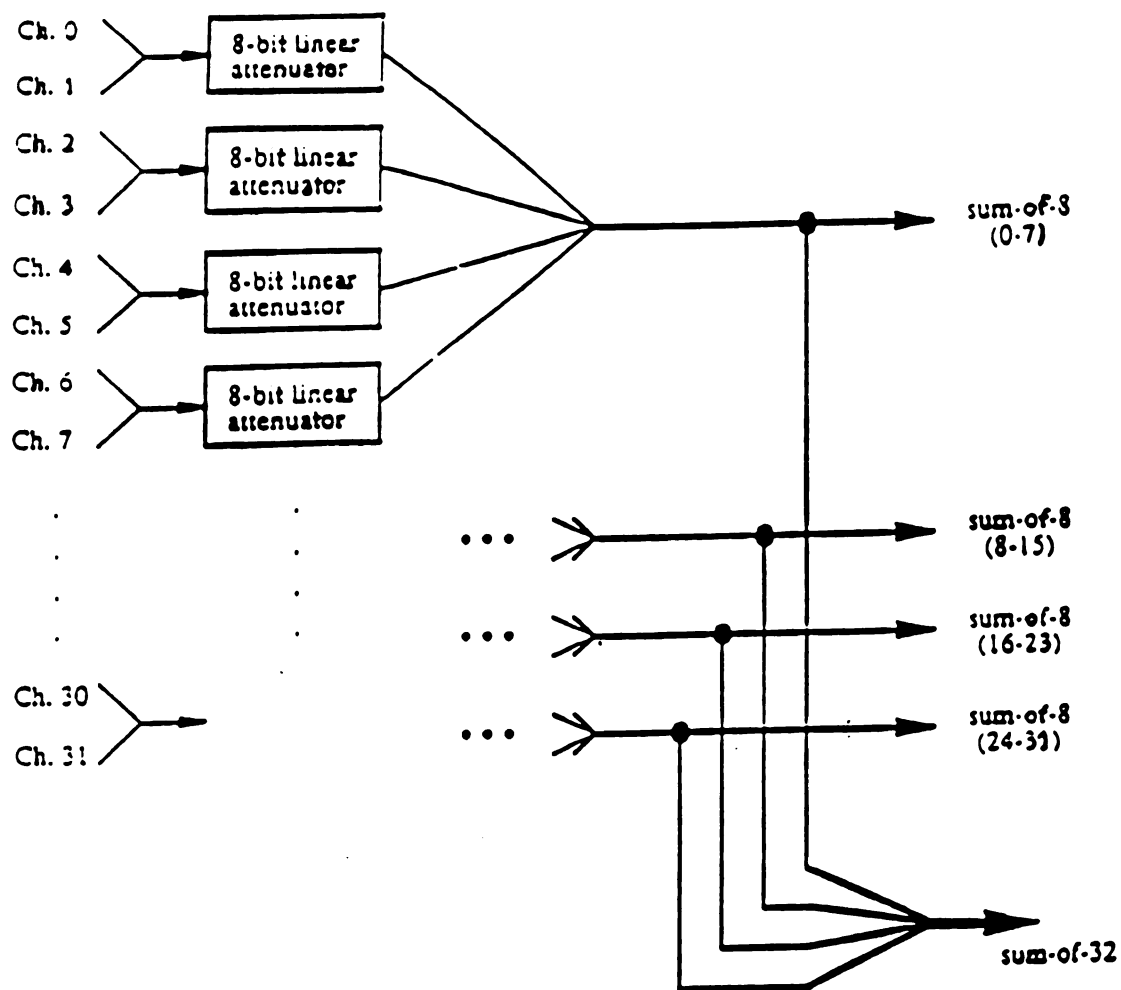


Figure 2.21: Octant r-channel summing scheme employed by the local p_{\perp} modules. These modules produced summed signals for groups of 8 and 32 strips.

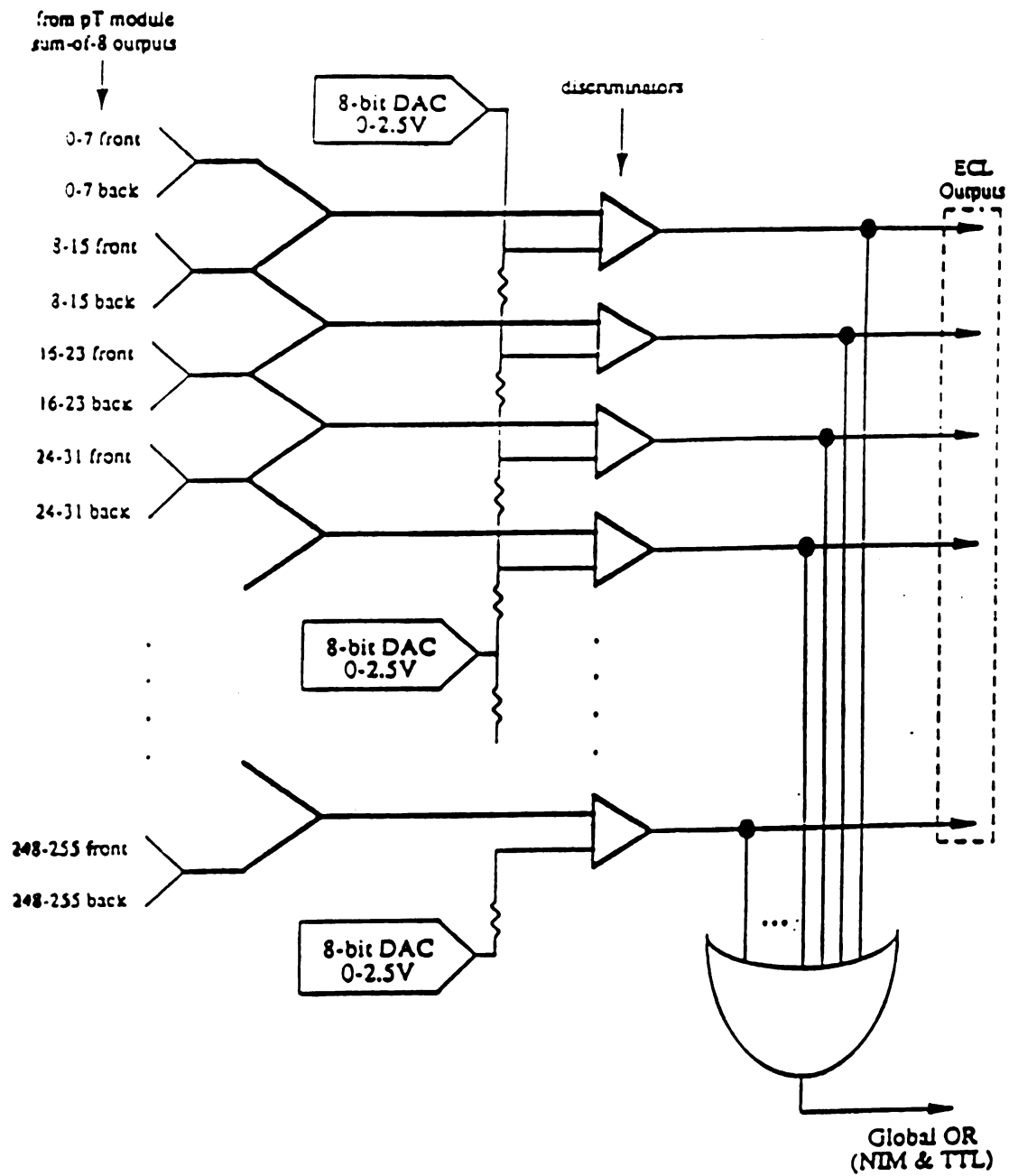


Figure 2.22: Front-back summing scheme employed by the local discriminator modules.

Table 2.2: Trigger threshold settings by run number.

Logic Signal	Threshold (GeV/c)			
	runs 1811-2292	runs 2293-2310	runs 2311-2904	runs 2905-3036
LOCAL_PT_LO	1.2			
LOCAL_PT_HI	4.2	3.6		3.0
GLOBAL_PT_LO	2.5			
GLOBAL_PT_HI	4.0		3.6	

At this point a brief discussion of the image charge effect is in order. The effect of image charge can be understood by examining Figure 2.23. As the ionization electrons drift towards the anode under the influence of the electric field between the lead plate and the grounded readout board, a current is induced. This current was originally intended to flow out through the amplifier signal cables and return to the lead plates via the high voltage ballast capacitors. However, when the EMLAC was put into operation, it was found that due to impedances in the ground path between the ballast capacitors and the amplifiers the return current flowed through the amplifiers adjacent to the ones sensing the actual ionization during the first 200 ns or so of pulse formation. The result was a signal of opposite sign and nearly equal magnitude on the channels surrounding a high energy electromagnetic shower during the time of trigger pulse formation.

When summing a group of 16 channels for the local trigger, the image charge contribution is small since the typical shower width is about 16 strips. However, the global sums result in a serious loss of signal, greatly compromising the global trigger's efficiency as Figure 2.24 illustrates. What's even worse is that the image charge contribution grows with radius due to the r-strips' increasing capacitance, and

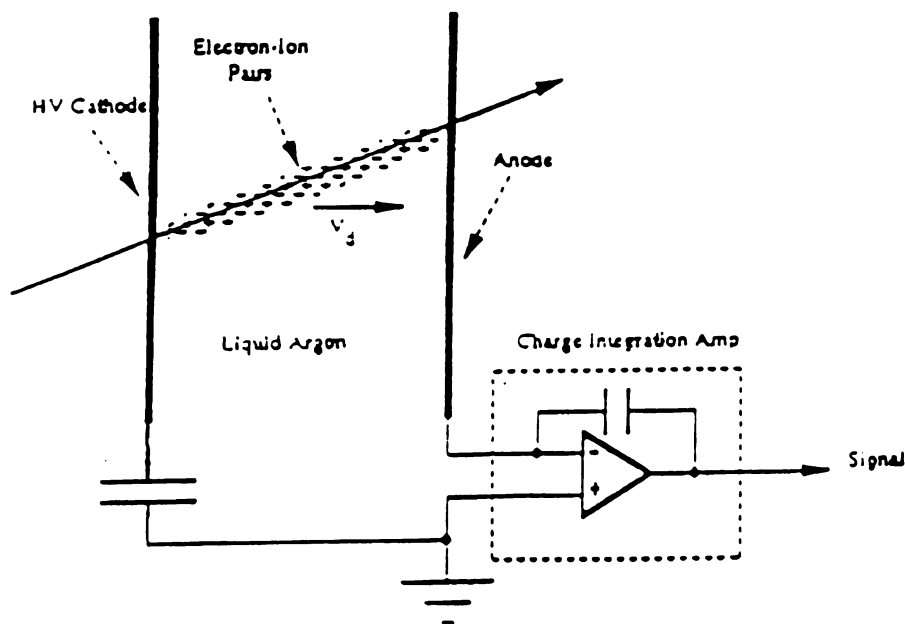


Figure 2.23: Schematic of the EMLAC charge collection circuit (one channel).

the increase in the $\sin \theta$ weighting. To alleviate the image charge problem cut off diodes were installed on the inputs to the modules performing the sums of 32. These diodes shunt the “wrong sign” image charge current to ground. In addition, The outermost 32 channels were not utilized in forming a trigger. Because diodes have a characteristic turn on voltage, not all of the image current was shunted to ground, and so the global trigger’s performance was indeed compromised.

2.3.2 Beam and Interaction Definition

A trigger logic signal from the EMLAC should be “in time” with a particular interaction in the target if it corresponds to an event of interest. The interaction itself should be in coincidence with the passage of a beam particle through the apparatus. To avoid pile-up effects in the calorimeter and constrain the event kinematics the interaction responsible for a high level trigger should not be accompanied by another interaction within a time window of 150 ns. Finally, it is useful to know whether

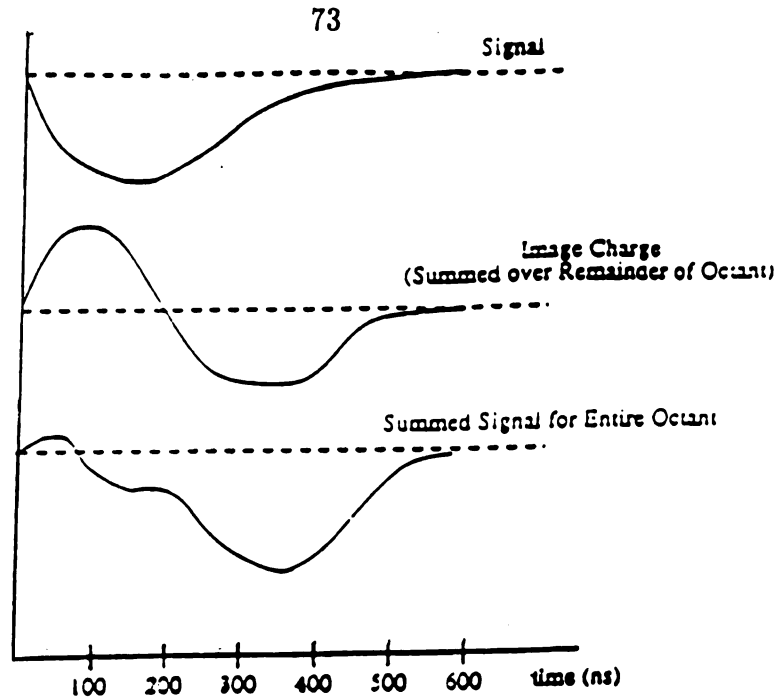


Figure 2.24: The effect of image charge on the global trigger input signal.

or not the beam particle associated with a given interaction was part of the beam halo since it was possible for halo particles to generate interaction signals and/or electromagnetic showers.

The layout of the scintillation counters used in the beam and interaction definitions is shown in Figure 2.25. The presence of a beam particle was signalled by counters BA, BB, and BH. BH was a counter with a 1.0 cm hole to allow true beam particles to pass through it. A signal from BH indicated a halo particle's passage. In addition, the signals from the beam counters were put in coincidence with the RF clock and beam gate provided by the accelerator control room. The RF clock provides pulses with a period of 19.4 ns, which matches the beam's bucket structure. The beam gate is activated when the extraction magnets are energized. The beam signal for the 1987-1988 data taking period is given by the following logical expression,

$$BM = BA \cdot BB \cdot \overline{BH} \cdot BMGATE \cdot RF_CLOCK \quad (2.10)$$

Beam signals were generated once every 19.4 ns.

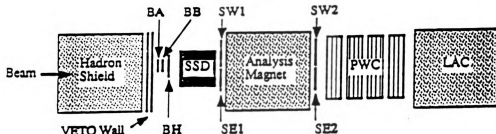


Figure 2.25: The configuration of scintillation counters used the the beam and interaction definitions.

The interaction signal was formed from the coincidence of any one of the interaction counters, SW1, SW2, SE1, or SE2 with the BM signal. Each interaction counter had a semicircular hole in it, allowing passage of the beam. Otherwise there would be an "interaction" every 20 ns and the pile-up filter would veto every event selected by the EMLAC trigger electronics. The interaction pile-up filter circuit is shown schematically in Figure 2.26. The signal from each interaction is delayed 16 times in successive 20 ns intervals. The ninth delay port was defined to be $t = 0$, and put in coincidence with the logic signals coming from the calorimeter and vetoing elements. A clean interaction signal was produced if a signal exiting port nine was not in coincidence with any signals from the three adjacent ports on either side. Thus, a triggerable interaction was isolated in time from other interactions by ± 60 ns. A live interaction was defined as the coincidence of a clean interaction, the BM signal and a computer-ready gate. The computer-ready was required since the DA system had to be capable of reading out the detectors should a trigger occur; this was the quiescent

state of the DA system. It was the live interaction signal that was actually put in coincidence with the high level trigger from the EMLAC.

2.3.3 Vetoing Elements

There are three online veto requirements. All of them have to be satisfied at the PRETRIGGER level. The first requirement is that no PRETRIGGER has occurred within the previous 300 ns of the current PRETRIGGER. The PRETRIGGER signals are delayed in a manner similar to the interaction signals so that a coincidence backward in time can be made. This veto is known as the early p_{\perp} kill. Its purpose is to prevent two low p_{\perp} events, separated in time by less than the LAC risetime, from satisfying the high- p_{\perp} trigger.

Another veto is provided by the veto wall described earlier. The hadron shield is very effective at stopping the diffuse beam halo. However, the muon flux is so high during data taking that many halo muons penetrate the shield, and shower in the EMLAC. Enough high p_{\perp} showers could be generated this way to seriously contaminate the single photon sample. Therefore if both veto walls register at least one hit in time with an EMLAC trigger, then a signal is produced that disables the trigger for ~ 150 ns.

Finally, there was an SCR kill which disabled the trigger for $30 \mu\text{s}$. The SCR spikes are detected by a set of HADLAC channels, discriminated and then sent as a veto to ports on the trigger electronics modules responsible for the PRETRIGGER signal. SCR noise spikes are generated by the 400 Hz RABBIT power supplies inside the Faraday room. Such noise spikes induced LACAMP oscillations capable of producing false triggers. These oscillations are damped out within $30 \mu\text{s}$.

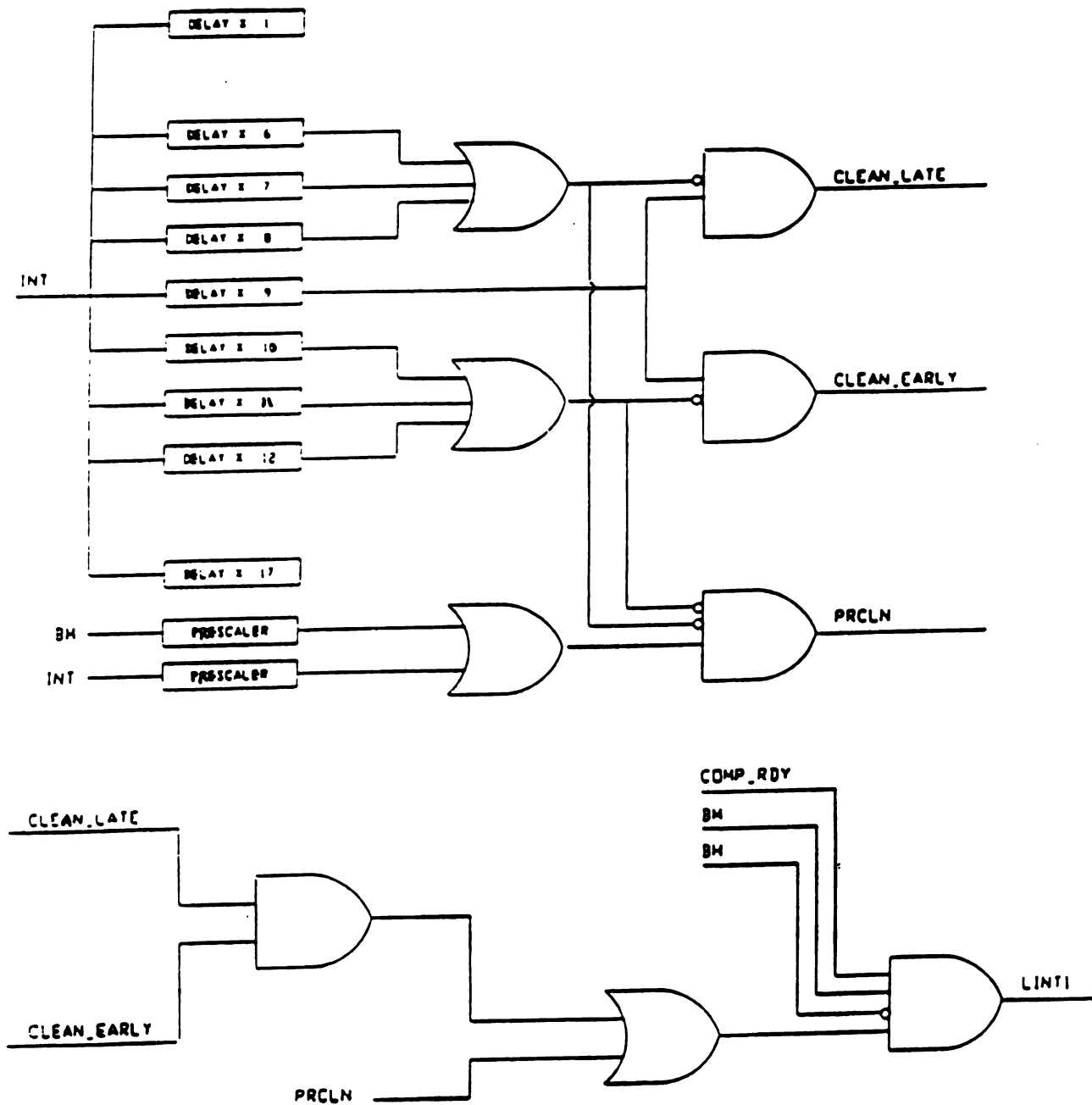


Figure 2.26: Schematic diagram of the interaction pile-up filter, and live interaction definition circuits.

2.3.4 High Level Trigger Operation

The operation of all the high level triggers is essentially the same. If the sum $glpt17$ for any octant has more than $1.7 \text{ GeV}/c$ of p_{\perp} then an octant pretrigger signal is generated. Provided that a live interaction signal is in coincidence with the octant pretrigger and there are is no trigger veto then a LAC pretrigger is generated. The use of zero-crossing discriminators allows a given pretrigger to be put in coincidence with the proper interaction. At this point a “load” and “event” signal are sent to the tracking system’s latches and the BAT modules respectively. In addition, the pretrigger circuit is disabled from generating another pretrigger pulse. This guarantees that there is only one “load” signal given per high level trigger, which must be the case if the tracking system’s electronic readout system is to function correctly.

If the high level trigger logic generates a signal, then the DA sends out a busy signal, suspending all further data taking. All latched information is then read by the DA and transferred to the proper PDP-11 memory. When all PDP-11s have finished reading out the detectors, the computer-ready gate is enabled, and data taking may resume. A master clear signal is also generated which resets all the electronics. The master clear prevents trigger operation for $5 \mu s$ so that the trigger electronics may settle into a quiescent state. If no high level trigger is formed within 300 ns of a given pretrigger, then a clear signal is sent to the tracking system electronics and the pretrigger circuit is enabled once more.

Four distinct types of high level triggers were implemented during the first data taking period of E706. They were constructed from the logic signals listed in Table 2.2.

- *Local-Global-Hi*, the trigger generated by a logical AND of the GLOBAL_PT_HI and LOCAL_PT_LO logic signals. This trigger indicated that a large amount of p_{\perp} had been deposited within an octant with a significant fraction localized

in a small region. Its purpose was to provide efficient detection of high p_{\perp} η particles.

- *Single-Local*, defined only by the LOCAL_PT_HI signal, signified a large local deposition of p_{\perp} within some octant ($\gtrsim 3.0$ GeV/c). This trigger was very efficient at selecting single photon and high p_{\perp} π^0 events.
- *Local-Global-Lo*, was similar to the *Local-Global-Hi* trigger except that the GLOBAL_PT_LO signal was used instead of the high threshold global signal. Its purpose was to study the *Local-Global-Hi*'s performance. This trigger was prescaled by a factor of 10 so it wouldn't dominate the trigger rate.
- *Two-Gamma*, defined by the logical AND of the LOCAL_PT_LO signal from one octant with the same signal from any of the three opposing octants. This trigger selected events containing massive π^0 and single photon pairs at high p_{\perp} .

Triggers based on only the beam and interaction definitions were also implemented for diagnostic purposes and various detector studies. They were prescaled by tremendous factors so as not to dominate the trigger rate. The E672 experiment also supplied a high level dimuon-muon trigger which was or'd with the E706 trigger. However, these triggers are not pertinent to this analysis.

2.4 CHARGED TRACKING SYSTEM

The charged tracking system consisted of 14 planes of silicon microstrip detectors (SSDs), a dipole analyzing magnet, and 16 planes of multiwire proportional chambers (MWPCs). The SSDs are positioned upstream of the analyzing magnet. They have been used to reconstruct the primary event vertex and the beam track responsible for the interaction. The MWPCs are placed downstream of the magnet. Only the

MWPCs possess stereo capabilities and can therefore reconstruct tracks in space. As its name implies, the magnet was used for momentum analysis of tracks and to determine the sign of their respective electric charges.

2.4.1 SSD System

The 14 planes of SSD are grouped into modules by pairs. Each pair of planes consists of an X-Plane (strips vertical) and a Y-Plane (strips horizontal). Four of these X-Y modules are positioned downstream of the target and have been used to reconstruct the primary vertex. Three of the X-Y modules are positioned upstream of the target. Their purpose was to reconstruct the tracks of the beam particles appearing within the primary interaction's vertex. The SSD modules are composed of an aluminum plate which has the PC boards containing the SSD wafers attached to it. The plates lay in precision milled slots on a one-piece cradle. The cradle sits on an optical table which is mounted at three points to the SSD cart. The cart is a steel structure that sits on rails rigidly attached to the floor of the experimental hall. The cart has the ability to move horizontally transverse to the beamline.

Figure 2.27 gives a schematic layout of the SSD system in the X and Y-Views. The three X-Y modules upstream of the target and the first X-Y module downstream of the target contain $3 \times 3 \text{ cm}^2$ wafers. The other three modules have $5 \times 5 \text{ cm}^2$ wafers installed in them. Each wafer is $250 - 300 \mu\text{m}$ thick. After the wafers are mounted onto their respective PC boards two holes are drilled in the board. The holes are on either side of the wafer 6 inches apart, centered on and parallel to the central strip. These holes mate with precision located pins in the aluminum module plates. The module plates are seated in precision milled slots on the SSD cradle. Thus, each SSD strip's location can be known in a surveyor's coordinate system thereby permitting an alignment of the full SSD system. A complete description of how the wafers are mounted into the modules and connected electrically strip by strip with the outside

world is given in a NIM article [15].

There are a total of 7120 active strips in the SSD system. Each strip is $50\text{ }\mu\text{m}$ wide and is essentially a p-i-n diode. A minimum ionizing particle that traverses one of these strips deposits $(2.0 - 2.4) \times 10^4$ electron-hole pairs. The charge is collected in $\sim 20\text{ ns}$. This charge is picked up by a Rel-Lab IO-323-C charge sensitive preamplifier. The preamplifier output is input for the NANOMETRIC digitization system which is described in a subsequent section.

The apparatus shown in Figure 2.28 was used to measure the operating characteristics of the SSDs. A ^{106}Ru β -source with an endpoint of 3.4 MeV was used as the source of minimum ionizing radiation. S_1 and S_2 were scintillation counters put in coincidence to form a trigger for generating load signals. The load signals were sent to the latches for the SSD plane being tested. For pulse height measurements, a post-amplifier designed to imitate the N-277C was used to drive a LeCroy 2249A ADC. The pulse height measurements yielded a minimum ionizing peak at 71 KeV above an ADC pedestal peak. The pedestal peak had a HWHM of 3.4 KeV, which yielded a ratio of 21. A threshold study using the N-277C amplifier yielded a plateau region between 1.5 and 2.5 volts. When normalized to the number of source electrons traversing the detector, the plateau region corresponds to an efficiency of $\sim 100\%$.

The small amount of charge produced per strip and the corresponding high gain of the amplifier stages makes the SSD system vulnerable to stray electromagnetic radiations coupling into the amplifier stages and dominating the signal. The SSD modules and the preamplifier stages were enclosed in an aluminum housing which formed a Faraday cage. The cables leading from the preamplifiers to the NANOMETRIC amplifiers passed through shielded conduits; the same is true for the cables going from the discriminated outputs of the N-277Cs to the latch modules. The power supplying the preamplifiers was passed through XENTEC isolation transformers. All amplifiers were grounded in parallel to the SSD table which was connected to the MWEST hall

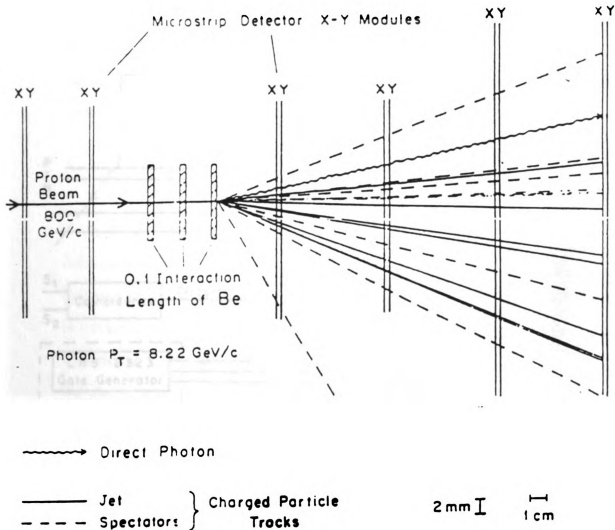


Figure 2.27: Schematic of the segmented target/SSD system of E706. A typical multiple event is superimposed on the planes.

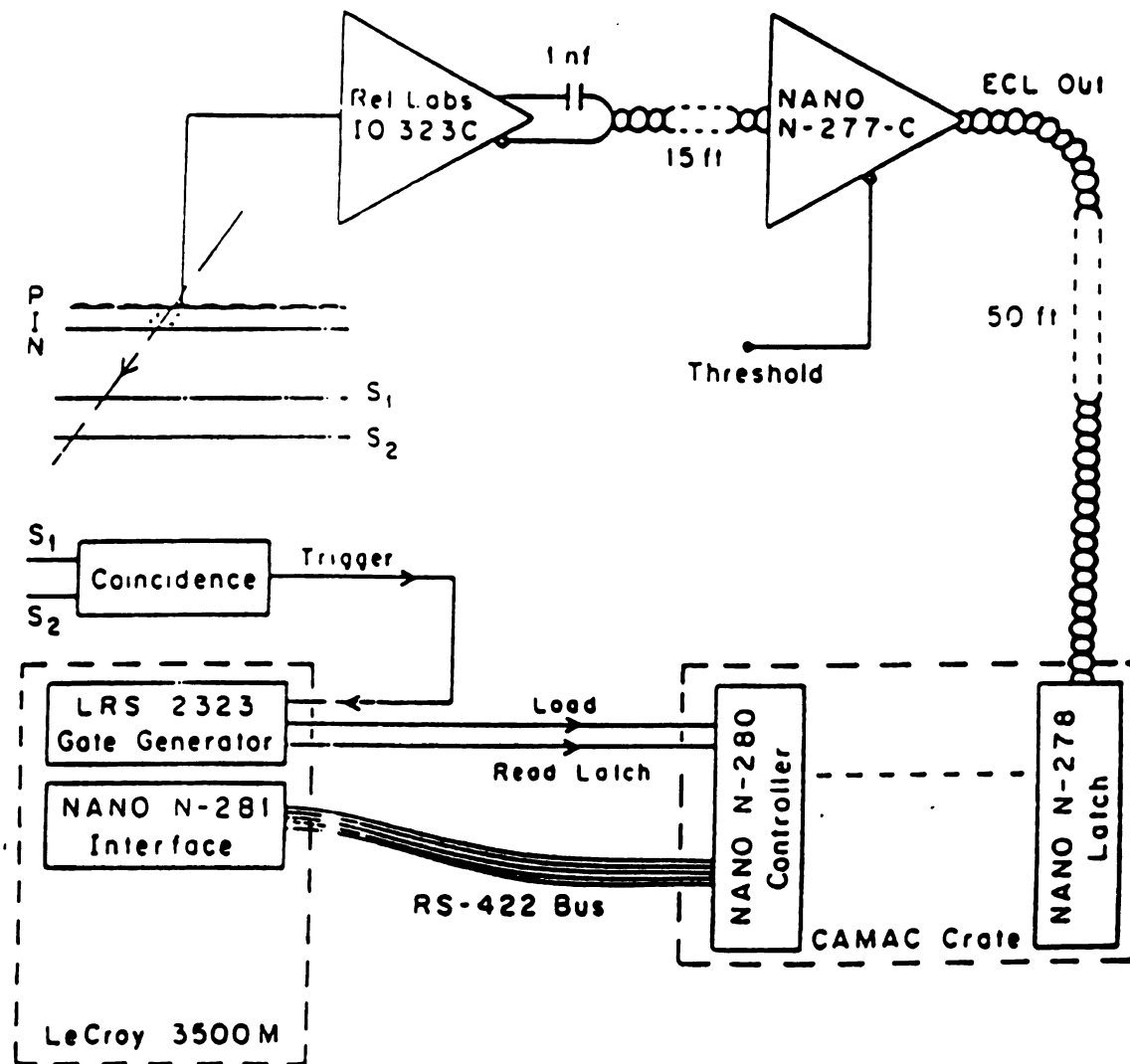


Figure 2.28: Readout electronics schematic used to determine operating characteristics of SSD system.

ground via a thick braided cable.

2.4.2 MWPC System

The 16 planes of MWPC are grouped into 4 views (X, Y, U, and V). Each view contains 4 planes. The views are grouped into pairs with the members of each pair being mutually orthogonal. The pairs are X-Y and U-V; the U-V system is rotated about the Z-axis with respect to the X-Y system such that the intersections of X, Y, and U lines form 3-4-5 triangles, i.e. the two systems are related by the following transformation:

$$\begin{aligned} U &= \frac{4}{5}X + \frac{3}{5}Y \\ V &= -\frac{3}{5}X + \frac{4}{5}Y \end{aligned} \tag{2.11}$$

In terms of hardware the MWPCs are grouped into 4 modules. Each module contains 4 anode planes, one for each view. The sense planes have independent facing cathodes for a total of twelve layers. In addition, there is a spacer layer at either end of the stack to provide clearance for the high voltage leads of the end cathodes. The sandwich is held together in compression by two massive frames. The alignment of the planes is accomplished by 12 precision steel pins which fit through bushings on each plane and precision located brass bushings in the frames. Figure 2.29 shows the manner in which the sense planes are stacked in each MWPC module.

The operation of these chambers is fairly simple. Charged particles traversing the chambers ionize argon atoms in the gap between the anode and cathode layers. The cathodes are held at around -2900 V while the anodes are grounded. As a result, the ionization electrons drift towards the anodes. An illustration of the electric field lines in a multiwire proportional chamber is given in Figure 2.30 [16]. The electrons drift along the field lines towards one of the anode wires. The anode planes typically consist of 800 $20\text{ }\mu\text{m}$ gold plated tungsten wires positioned precisely parallel

to and coplanar with one another. The spacing between neighboring wires in the E706 MWPC chambers is maintained at 2.5 mm. As drifting electrons get within close proximity of a wire, they acquire enough kinetic energy per mean free path to ionize other argon atoms due to the $\sim 1/r$ behaviour of the electric field near a long filamentary conductor. These liberated electrons are in turn able to ionize additional atoms, and so an exponentially increasing amount of ionization occurs as the ions drift towards a given wire. This phenomenon is called an avalanche.

An avalanche generally yields a gain of 10^6 in the amount of ionization collected on a given anode wire over the amount originally deposited in the gap. If the wire is terminated with a resistor, then a current on the order of several μA will flow through it during the first 100 ns of signal formation. The resulting voltage is detectable by a high bandwidth amplifier. The amplifier outputs were discriminated in this experiment so the only information available was whether or not a given wire had registered the nearby passage of a charged particle. By determining which wires had experienced an avalanche in an event, and knowing their positions it was possible to reconstruct the trajectories of the charged particles which passed through the system during the event. The spatial resolution of these chambers is only a function of the wire spacing. In fact, it is given simply by $\sigma = s/\sqrt{12}$ where s is the wire spacing.

The avalanche process is the basis of operation for all proportional type counters. It is fairly simple to quantify it. If α^{-1} and n are the mean free path and number of electrons at position x , then after travelling a distance Δx the increase in electrons, Δn is given by

$$\Delta n = n\alpha(x)\Delta x \quad (2.12)$$

This proportionality between the incremental increase in ionization and the total amount of ionization is what gives proportional counters their name. A simple inte-

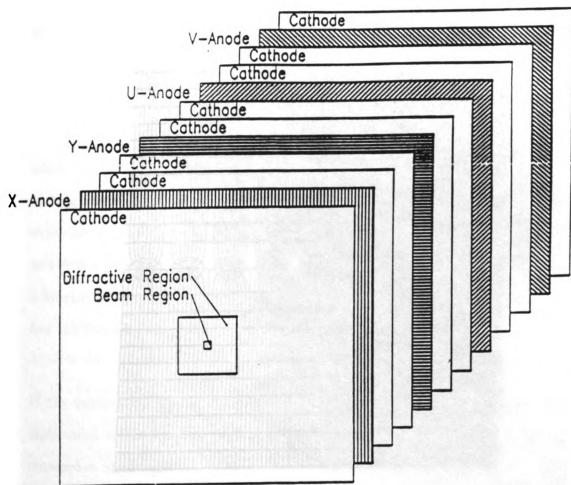


Figure 2.29: Arrangement of sense planes in each MWPC module.

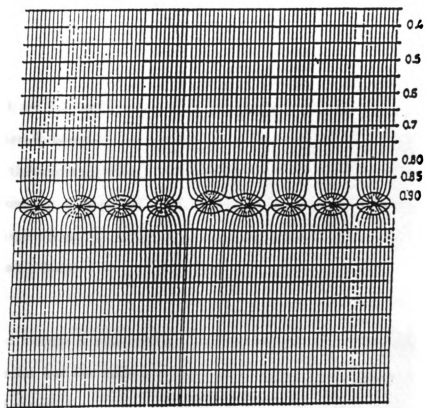


Figure 2.30: Electric field equipotential and field lines in a multiwire proportional chamber. The effect on the field due a small displacement of one wire is also shown.

gration leads to an expression for the multiplication factor M .

$$M = \frac{n}{n_0} = \exp \left[\int_{x_1}^{x_2} \alpha(x) dx \right] \quad (2.13)$$

It is possible to determine the form of $\alpha(x)$ exactly for a proportional tube counter. Such a detector is composed of a hollow conductive cylinder with a fine wire running along its axis, which is held at positive high voltage. The voltage at a distance r from the anode inside the tube and the capacitance per unit length are given by the following equations,

$$\begin{aligned} V(r) &= \frac{CV_0}{2\pi\epsilon_0} \ln \frac{r}{a} \\ C &= \frac{2\pi\epsilon_0}{\ln(b/a)} \end{aligned} \quad (2.14)$$

where a and b are the counter's inner and outer radii respectively and V_0 is the applied voltage. Generally speaking α has the form $\alpha = k\rho\epsilon$ where ρ is the number density of molecules in the ionizing medium, ϵ is the ionization electrons' average kinetic energy and k is a constant of proportionality. Given that an electron acquires on average a kinetic energy ϵ from the applied electric field between collisions, it follows that α has the following form:

$$\alpha(r) = \sqrt{\frac{k\rho CV_0}{2\pi\epsilon_0}} \frac{1}{r} \quad (2.15)$$

If the applied voltage is much greater than the ionization potential, then the multiplication factor has the following simple form where K is another constant with dimension of charge⁻¹.

$$M = \exp(K(CV_0)) \quad (2.16)$$

The electric field configuration in multiwire proportional chambers is much more complex than in cylindrically symmetric proportional tube counters. However, the same simple description of the avalanche process does apply as will now be demonstrated. For a description of the parameters and coordinates used to describe the

field in an MWPC the reader is referred to Figure 2.31. The field, potential and capacitance per unit length have been found to be of the following form [17],

$$\begin{aligned} E(x, z) &= \frac{CV_0}{2\epsilon_0 s} \left(1 + \tan^2 \frac{\pi x}{s} \tanh^2 \frac{\pi z}{s}\right)^{1/2} \left(\tan^2 \frac{\pi x}{s} + \tanh^2 \frac{\pi z}{s}\right)^{-1/2} \\ V(x, z) &= \frac{CV_0}{4\pi\epsilon_0} \left[\frac{2\pi l}{s} - \ln \left(4 \left(\sin^2 \frac{\pi x}{s} + \sinh^2 \frac{\pi z}{s}\right)\right) \right] \\ C &= \frac{2\pi\epsilon_0}{\pi l/s - \ln(2\pi a/s)} \end{aligned} \quad (2.17)$$

These expressions are valid for the boundary conditions $V(a) = V_0$, $V(l) = 0$. Note that a is the nominal radius of the anode wires, s is the wire spacing, and l is the distance between anode and cathode planes. Now, for the region very close to a given wire i.e. $x \ll s$ and $z \ll s$ the electric field expression reduces to the following

$$E(x, z) \simeq \frac{CV_0}{2\pi\epsilon_0} \frac{1}{r}, \quad r \simeq \sqrt{x^2 + z^2} \ll s \quad (2.18)$$

This is identical to the field for a simple proportional tube counter and so the description of the avalanche phenomenon is identical in both cases! Table 2.3 lists the relevant geometric parameters for each anode plane in the MWPC system; Table 2.4 summarizes the electrostatic parameters of the anode planes. Note that the operating voltage is actually applied to the cathodes and the anode wires are held at ground.

There are two fundamental design considerations in building proportional chambers of the size used in E706. First, there is the variation in gain due to variations in the geometrical parameters a , s , and l . Second, the high electric fields required to operate such devices create considerable forces which tend to pull the anode wires out of plane and attract neighboring cathode and anode planes together. Such mechanical deformations will, at the least produce variations in gain and at the worst the electrical breakdown of the chamber due to broken wires and/or the cathode and anode planes coming into actual contact with one another.

The gain variations can be estimated by taking the differential of 2.16,

$$\frac{\Delta M}{M} = \ln M \frac{\Delta Q}{Q}, \quad Q = CV_0 \quad (2.19)$$

Table 2.3: Relevant geometrical parameters for MWPC anodes (MKS units).

Plane	Module	View	Aperture (in m ²)	Z (in m)	Channels
1	1	X	1.6256×1.2192	3.4790	640
2	1	Y	1.6256×1.2192	3.4965	480
3	1	U	1.6256×1.2192	3.5140	704
4	1	V	1.6256×1.2192	3.5315	672
5	2	X	2.0320×2.0320	4.5458	800
6	2	Y	2.0320×2.0320	4.5633	800
7	2	U	2.0320×2.0320	4.5808	896
8	2	V	2.0320×2.0320	4.5983	896
9	3	X	2.0320×2.0320	5.6126	800
10	3	Y	2.0320×2.0320	5.6301	800
11	3	U	2.0320×2.0320	5.6476	896
12	3	V	2.0320×2.0320	5.6651	896
13	4	X	2.4384×2.4384	6.6794	960
14	4	Y	2.4384×2.4384	6.6969	960
15	4	U	2.4384×2.4384	6.7144	1120
16	4	V	2.4384×2.4384	6.7319	1120

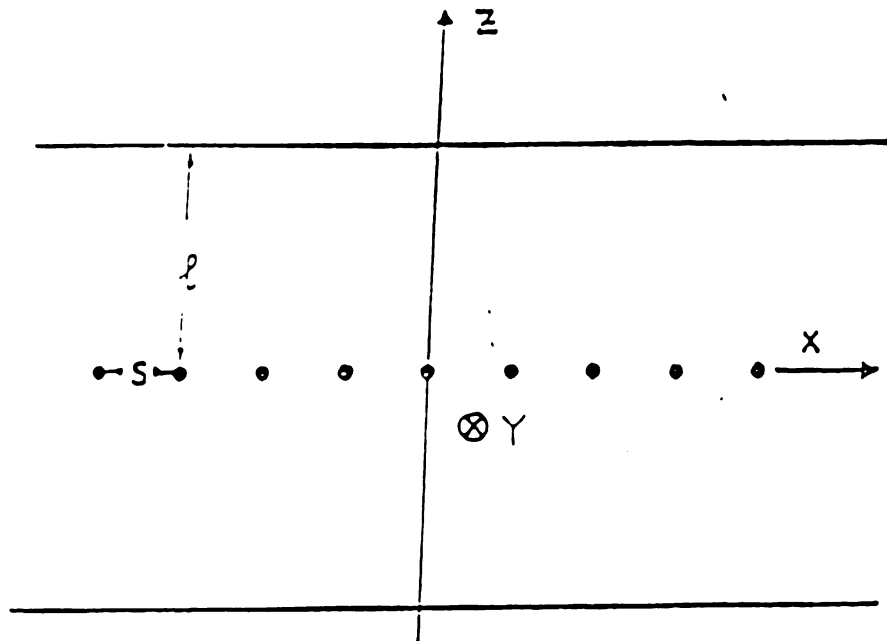


Figure 2.31: Principle of construction and definition of parameters in a multiwire proportional chamber. A set of parallel anode wires is mounted symmetrically between two cathode foils.

Table 2.4: Electrostatic parameters for all MWPC anodes.

MWPC Electrostatic Parameters (MKS units)	
Parameter	Value
C	$5.15 \times 10^{-12} \text{ Fm}^{-1}$
V_0	2900 V
l	0.0574 m
s	0.0254 m
a	$2.0 \times 10^{-6} \text{ m}$

Using the formula for the capacitance per unit length, one can derive the following relationships between $\Delta M/M$, a , s , and l :

$$\begin{aligned}
\frac{\Delta M}{M} &= \ln M \frac{C}{2\pi\epsilon_0} \frac{\Delta a}{a} \\
\frac{\Delta M}{M} &= \ln M \frac{Cl}{2\epsilon_0 s} \frac{\Delta l}{l} \\
\frac{\Delta M}{M} &= \ln M \frac{Cl}{2\epsilon_0 s} \left(\frac{1}{s} + \frac{1}{\pi l} \right) \Delta s
\end{aligned} \tag{2.20}$$

For gains of $\sim 10^6$, and using the parameters for the largest module one obtains,

$$\begin{aligned}
\frac{\Delta M}{M} &= 4.3 \times \frac{\Delta a}{a} \\
\frac{\Delta M}{M} &= 9.7 \times \frac{\Delta l}{l} \\
\frac{\Delta M}{M} &= 9.7 \times \left(\frac{1}{s} + \frac{1}{l} \right) \Delta s
\end{aligned} \tag{2.21}$$

The gain variations are not critical for the experiment since only the discriminated outputs of the amplifiers are used in data processing. However, to keep the gain variations $\lesssim 50\%$ requires $\Delta l \lesssim 0.1 \text{ mm}$, and $\Delta s \lesssim 50 \mu\text{m}$. $\Delta a/a$ is known to vary by about 1% and the gain variation is weakest in this parameter anyway. The wirespacing was the most difficult tolerance to maintain. The wire laying procedure

relied on using printed circuit boards with a precision spacing between the pads on which the wires were laid. As will be described later, these printed circuit boards were mounted on the anode frames to 1 mil precision.

Once laid, the wires are tensioned in order to compensate for the electrostatic forces that pull them out of plane with one another. This technique works so long as the tension component normal to the plane of wires becomes large enough before an undesirable amount of distortion occurs. Care must be taken that the applied tension does not exceed the elastic limit of the wire.

It is possible to be more quantitative about this issue. Trippe [18] has shown that for chambers of the aperture used in this experiment a stable equilibrium arises when the tensioned wires are alternately displaced up and down as shown in Figure 2.32. If the following expression, valid in the approximation of tangents to arcs, is used for the force between two anode wires,

$$F = \frac{(CV_0)^2}{2\pi\epsilon_0} \frac{1}{r} \quad (2.22)$$

then the force per unit length on a given wire in the direction normal to the wire plane is given by,

$$\sum F_{\perp} \simeq 2 \frac{(CV_0)^2}{2\pi\epsilon_0} \left(\frac{1}{s} \frac{2\delta}{s} + \frac{1}{3s} \frac{2\delta}{3s} + \dots \right) = \frac{(CV_0)^2 \pi}{4\epsilon_0} \frac{\delta}{s^2} \quad (2.23)$$

where $\delta(x)$ is the wire's displacement along its length. This formula describes the force at a point on a given wire as a sum of forces between pairs of linear charges. These linear charges are in the direction of the tangents to the wires at a distance x along the given wire. This formula is valid in the limit of small displacements. Now, if T is the applied tension on the wire, then the restoring force perpendicular to the anode plane per unit length is expressed as

$$R = T \frac{d^2\delta}{dx^2} \quad (2.24)$$

One thus obtains a second order differential equation of the form,

$$\frac{d^2\delta}{dx^2} + \frac{(CV_0)^2}{T4\pi\epsilon_0 s^2} \delta = 0 \quad (2.25)$$

with $\delta(0) = \delta(L) = 0$ as the boundary conditions. L is wire's length. The solution of this differential equation consistent with the boundary conditions is

$$\delta(x) = \delta_0 \sin\left(\frac{CV_0}{2s} \sqrt{\frac{\pi}{\epsilon_0 T}} x\right) \quad (2.26)$$

The boundary condition $\delta(L) = 0$ implies that if T exceeds the critical tension, T_C , given by

$$T \geq T_C = \frac{1}{4\pi\epsilon_0} \left(\frac{CV_0 L}{s}\right)^2 \quad (2.27)$$

then the anode wires will remain coplanar. Substituting the parameters of Table 2.4 into this equation yields a critical tension of 175 g, which exceeds the elastic limit of a 20 μ m tungsten filament. The applied tension should be kept below the elastic limit by about a factor of two in order to allow variations in wire diameter and applied tension during wire laying. For this reason a nominal tension of 40 g was selected. The critical length, L_C , beyond which the wires will move out of plane to the equilibrium configuration of Figure 2.32 is 1.2 m. Therefore, some form of mechanical spacer between anodes and cathodes is required in order to maintain the desired planar arrangement of anode wires.

The mechanical spacers between neighboring anode and cathode surfaces are also needed just to keep the planes from coming into contact with one another due to unstable electrostatic attraction. The cathode planes are composed of 1 mil MYLAR sheet held under tension to which a conducting graphite film has been applied. The amount of tension necessary to maintain the proper anode-cathode spacing, l , can be found from the following equation

$$\Delta l = \frac{p}{T} \frac{H^2}{8} \quad (2.28)$$

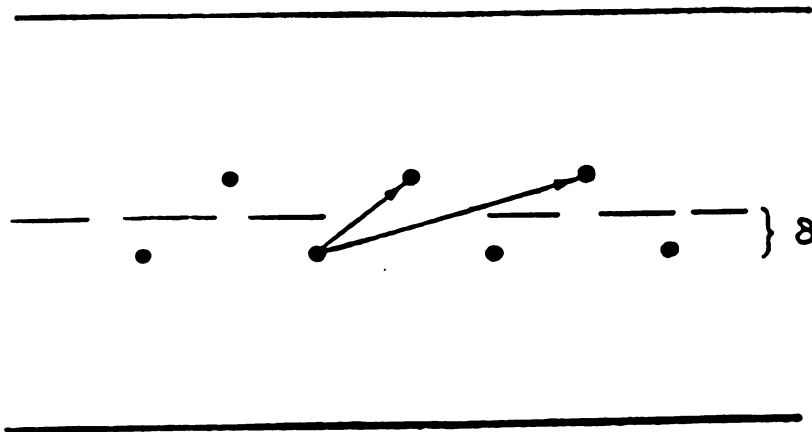


Figure 2.32: Equilibrium configuration of anode wires in a large proportional chamber under the influence of the device's electric field.

where H is the surface's area, T is the applied linear tension, and p is the electrostatic pressure defined by

$$p = \frac{1}{2}\epsilon_0 E^2 = \frac{(CV_0)^2}{8\epsilon_0 s^2} \quad (2.29)$$

Requiring $\Delta l \sim 0.1$ mm results in an applied tension that exceeds the cathode material's elastic limit.

The overall design and construction of the MWPC modules are very similar to the large MWPCs used in the NA3 experiment at CERN [19, 20, 21]. The modifications to the NA3 design arose from the constraints of fabricating such devices at a modest university laboratory, and a dependence on industrial vendors for all major components. The main differences between the E706 and NA3 chambers is in the mechanism for insertion and removal of the stainless steel pins that hold the module sandwich together, and in the gas manifolds around the perimeter of each module.

With the exception of the first module the frames which hold the stack of planes within a module together are made of steel. The frames for module one are fashioned

out of aluminum to prevent any coupling with the spectrometer magnet's field. The twelve stainless steel pins, responsible for the planes' alignment, are arranged around the frames three per side. The pins are spherically convex at one end to facilitate passage through the stack during insertion and removal when a chamber is opened and closed respectively. The other end of each pin is spherically concave to allow mating with an identical pin which is used to push the pin already in place through the stack. These pins are hollow along their axes in order that threaded rods may be inserted through them. Stack compression is achieved by placing flat washers over the bushings in the frames, and nuts with lockwashers onto the threaded rods. The nuts are then tightened with a torque wrench to 7 kg m.

The chamber frames are constructed of 6 in \times 1 in pieces of steel or aluminum plate that are welded together at the corners or fastened there by blocks and bolts. C-channel has been welded along the outer faces to provide additional strength and rigidity. The frames were designed to be square within 5 mil. The inner faces have been machined flat in order to apply even pressure on the chamber stack and keep it properly aligned. Holes were tapped around the outside edges of each frame so the gas manifolds could be attached after stack assembly.

The bronze bushings for the steel pins were precisely located in the frames. Each bushing has an interior O-ring groove with an O-ring seated inside which provides a gas seal between the pins and the bushing.

Aluminized MYLAR sheets 3 mil in thickness were glued to the inner face of each frame with EPON epoxy. These sheets formed windows which sealed the chambers, allowed them to be pressurized, and prevented water vapor from diffusing in. An additional very important function of these windows is to provide a radio-frequency radiation shield for the anode planes. When the gas manifolds are attached, the MWPC planes are enclosed in an excellent Faraday cage.

Modules one and two were put together at Pennsylvania State University while chambers three and four were assembled at Michigan State University. Each institution employed different construction techniques. The work done by the MSU team will be presented below. A good discussion of the PSU group's effort can be found in another thesis [22].

Both anode and cathode planes are constructed from square frames of G-10 fiberglass pieces that have been glued together at the corners. An anode plane then has a special printed circuit boards glued onto two opposing sides of a frame. The anode wires are then laid onto tiny pads located on the printed circuit boards and attached mechanically by glue and electrically with solder. A cathode plane is made by gluing a MYLAR sheet, which is held under tension, to the inside edge of a frame. The assembly of these G-10 frames as well as the construction and finishing of the anode and cathode elements, required two special tools.

First, a set of so called transfer frames had to be made for each module. The transfer frames kept individual planes flat and rigid during fabrication and stack assembly. Two frames were made for each module. Those for module three are constructed out of aluminum C-channel, which has been welded together. The frames for the fourth module are made out of a composite honeycomb-celled material, covered with aluminum sheet metal. These transfer frames have concave spherical bushings that mate with the steel pins, and keep the attached plane in proper orientation for transfer to the chamber stack.

The other important tool was an assembly jig for putting the frames together. This jig was just a simple wooden box-frame structure with inner and outer sides. A steel frame could be seated inside of it with the inside face up. The steel pins would then be inserted into the bushings. It was then a simple matter to put the anode and

cathode frames together such that they would eventually fit onto the actual chamber stack without any difficulty. The assembly jig possessed a set of clamps around the top inner and outer edges. Once a frame had been glued together in the jig, steel plates were laid over it, the clamps were brought to bear on them, and they were locked in place. This provided an even pressure that held the frame pieces flat and in place until the glue set.

The frames had one pair of opposing sides thinner than the other pair. The thin pair of sides possessed a series of wide channels, which had been milled out of them. For the cathode planes, an additional thin piece of G-10 was laid down on top of the thin frame pieces. The anode frames had the printed circuit boards laid on top instead. The milled channels thus became slots that allowed the chamber gas to seep into all parts of a module, displacing the air. The G-10 material used to make the frames had been sanded flat to within 1 mil. The frame pieces were glued together with 3M 2216 epoxy. There are four basic pieces in a frame each forming a side. These pieces have holes cut out for the steel pins to go through. However, they are considerably larger in diameter than the pins, but when a frame was being assembled, special brass bushings were slipped over the steel pins. The frame pieces were then laid down with the holes fitting around these bushings. 2216 epoxy was used to bind the frame pieces to the bushings.

Greater care was required in fabricating an anode frame since the alignment of the readout pads for the individual wires is critical. Five printed circuit boards laid end to end made up one readout side of an anode plane. The central board had a precision milled hole located with respect to the readout pads. The other boards possessed precision milled semicircular notches. These notches formed a circular hole when the boards were joined at the outer pins on a side. The steel pins had one turn of scotch tape around them during assembly so there would be no slop in the readout

boards about the steel pins. The inner corners of the thick G-10 pieces had been milled square so the printed circuit boards could be aligned straight, having no rotations about the steel pins. In order to have the inner edges of the thick G-10 pieces at the proper positions along the axis containing the center of the pins, the anode frames required brass bushings with tolerances better than 1 mil. To keep costs down only those bushings needed to make the eight anode planes for both modules had such fine tolerances. The U and V anodes had the readout boards laid along a portion of the thick G-10 sides as well. Of course, those portions had been milled thin.

Once a cathode frame had been assembled, it was attached to a transfer frame using cable ties. The cable ties were placed through the gas slots. The transfer frame was then placed beneath a special box-channel frame supported by four screw jacks. This jacked up frame was used to stretch the 1.0 mil MYLAR sheet that formed the cathode surface. After the MYLAR sheet was attached to the frame and held under tension, a bead of EPON was applied around the cathode frame's inside edge. The stretcher frame was lowered until the MYLAR sheet pressed against the epoxy. Wooden blocks were then placed over the glued MYLAR to eliminate any gaps.

When the glue had cured, the excess plastic was cut away. The three active regions of the cathode were masked out with 1/8 in wide scotch tape. The outer boundary of the main cathode region, including the transfer frame, was masked off with tape and brown paper. A 1/8 in hole was cut out at one corner of each active cathode region, using a special hand held punch. A short strip of aluminized MYLAR was then glued with conductive epoxy over each hole on the cathode's back side.

The front or anode facing side of the cathode was then sprayed with a colloidal suspension of graphite in isopropyl alcohol and epoxy binder. After the paint dried a number of small bumps and ridges remained behind. These were successfully removed by buffing the graphite coated surface with a lens tissue. The finished surfaces have

a resistance of $10 - 20 \text{ k}\Omega/\text{sq}$. Such resistances will not affect operation in an environment where the particle flux from the target is $\sim 10^8 \text{ s}^{-1}$. The aluminized MYLAR terminals were attached to TEFLON insulated high voltage leads, running along the back sides of the cathodes. The leads are held under mechanical tension by DELRIN buttons attached to the thin G-10 pieces covering the gas slots. These leads connect in turn to high voltage bus lines running along the outer frame edge against the thin G-10 piece to a DELRIN connector. This connector mates to a connector attached to a feed-thru cable on a gas manifold.

The mechanical spacers needed to keep the anode wires in plane, and maintain the nominal anode-cathode spacing were fastened to the finished cathode planes. These spacers are called garlands. They are made from KAPTON strips; these strips were first folded in a zig-zag pattern similar to that of corrugated sheet metal. A hole was punched through each folded stack of plastic. An elastic thread was then run through this hole and the plastic strip allowed to unfold. Metal clips were attached at either end of the thread and they were in turn fastened to DELRIN buttons like the ones used to attach the high voltage leads. The ends of the KAPTON strips were fastened to the buttons also.

Because of KAPTON's dielectric properties, the garlands will reduce the electric field in their vicinity around the anode wires. The chamber efficiency will thus be reduced near the garlands. To compensate for this effect a PVC insulated wire is strung across the edge of each garland that faces the anode. The wires are attached to the garlands at several points with NYLON fishing line, and they are fastened at both ends to the buttons holding the garlands under tension. These wires were held at 1000 V potential during the 1987-1988 data taking period.

The number of garlands strung on each cathode depends on which cathode they are for. The orientation depends on which type of anode they correspond to. The X

and U views have their garlands strung horizontally while those for the Y and V views are strung vertically. Table 2.5 lists the the active areas' dimensions for each cathode; Table 2.6 lists the orientations and positions of the garlands relative to the center of each plane *i.e.* the nominal intersection with the beam axis.

The finished cathode planes were stored on a wall mounted structure at MSU. A protective dust cover was furnished for the mounting so the cathodes could be kept as clean as possible during storage. Once all the cathode frames were finished, it was time to make the anode planes. The sense wires were laid down on the readout pads using a winding machine at FNAL. Two frames were wound on each trip to the laboratory since only two free transfer frames were available at any given time. The finished anode planes were shipped back to MSU where they and their respective cathodes were assembled into a portion of the chamber stack.

As mentioned previously, the individual anode wires consisted of $20\text{ }\mu\text{m}$ gold plated tungsten filaments. The tungsten provided tensile strength while the gold served as a conductor of avalanche electrons to the amplifier inputs. Besides being a good conductor, there are two additional reasons for choosing gold as the plating metal. First, it makes it easy to solder the wires to the pads on the readout boards. Second, gold is chemically inert so it won't react with the chamber gas. In addition, the gold protects the tungsten from corrosion and subsequent mechanical failure.

The anode frames were mounted onto transfer frames, again by running cable ties through the gas slots, while still in the assembly jig. They were then carted off to Fermilab. The transfer frames were mounted on the winder platen such that the inner edges of the readout boards were parallel to the threaded rod that drove the wire laying carriage. Aluminum bars were laid along the edges of the platen, and strips of double-stick tape were applied along the bars. As the platen revolved, the tensioned wires would be held in place by the tape. Of course, the first wire had to be

Table 2.5: Sizes of the various cathode regions in each module.

	Aperature ($X \times Y \text{ cm}^2$)		
Module	Beam	Diffraction	Main
1	2.54×2.54	15.24×15.24	162.56×191.52
2, 3	3.81×3.81	20.32×20.32	203.20×203.20
4	5.08×5.08	30.48×30.48	243.84×243.84

Table 2.6: Orientation and positions of the garlands in each plane.

Module	View	Garlands	
		Orientation	Position
1	X, U	Horizontal	$\pm 2.54, \pm 38.1, \pm 43.2 \text{ cm}$
1	Y, V	Vertical	$\pm 17.8, \pm 22.9, \pm 58.4, \pm 63.5 \text{ cm}$
2, 3	X, U	Horizontal	$\pm 12.7, \pm 17.8, \pm 43.2, \pm 48.3, \pm 73.7, \pm 78.7 \text{ cm}$
2, 3	Y, V	Vertical	$\pm 12.7, \pm 17.8, \pm 43.2, \pm 48.3, \pm 73.7, \pm 78.7 \text{ cm}$
4	X, U	Horizontal	$\pm 15.2, \pm 20.3, \pm 50.8, \pm 55.9, \pm 86.4, \pm 91.4 \text{ cm}$
4	Y, V	Vertical	$\pm 15.2, \pm 20.3, \pm 50.8, \pm 55.9, \pm 86.4, \pm 91.4 \text{ cm}$

laid manually. The wires were laid with 40 g of tension via a tensioning arm on the winder carriage. Barring any breaks in the wire filament, it took around 12 hr to wind a single anode plane.

Once a wind had been completed, a rounded bead of EPON was placed between the readout pads and the inner edge of the readout boards. This was done to provide strain relief for the solder joints. After the glue cured the wires were taped down along the outer edge of the readout boards. All excess wire was then cut away. The transfer frame was then removed from the platen, and placed on a flat table. All the anode wires were then soldered at either end to the readout pads. The reader should be aware that the anode wires are read out at only on end. Adjacent groups of sixteen channels in the X and Y views are read out on opposite sides of the chambers. For the U and V views the channels are grouped into sets of 32. The portion of each wire between the solder joint and the tape was cut at the solder joint. The tape along with the excess wire was then easily removed. A check was made for sharp edges on the solder beads. If any were found, they were filed smooth.

No wire was laid on the last three channels at each end of an X or Y-view anode plane. Instead 1.0, 1.2, and 5.0 mil diameter wires were laid by hand at each end, and tensioned to 40 g. The increasing diameter of these so called guard wires reduced the large fringe fields at the planes' edges. Otherwise, these fields might have caused electrical breakdown in the chambers.

Because 40 g of tension is near the tungsten filaments' elastic limit, it is important that variations about this nominal value be kept to a minimum. Reducing the variations in tension also guarantees that the wires will remain coplanar during chamber operation. The winding machine should in principle maintain a sufficiently constant tension on the MWPC wire as it is being laid down. However, after the first wind it was decided that variations in the wire tension should be checked. An elegant method

was used to perform this task. The natural or first harmonic frequency, ω_0 , of a taut wire is related to the tension by the following formula:

$$\omega_0 = 2\sqrt{\frac{2T}{ML}} \quad (2.30)$$

where T is the tension, L is the wire's length, and M is its mass. This formula is valid whenever the changes in tension over one period of oscillation are small compared to the static tension, *i.e.* in the limit of small oscillations. A bar magnet was placed under the midpoint of each wire in succession. At the same time a small sinusoidal electric current was put through the wires, and the frequency varied until a resonance was observed. The current was kept low enough that the resonance was sufficiently damped. From this study it was determined that the winding technique had sufficient tolerances. In fact, none of the wires were found to be stretched beyond the elastic limit.

Nevertheless, wire breakage was a serious problem at the beginning. The origin of it appears to have been due to the presence of tiny kinks in the wire on the spools. The wire was examined and it was found that there were enough good spools to finish the chambers. The bad spools were subsequently discarded. The breakage rate dropped dramatically, but there was still some breakage over time periods of several weeks when the chambers were first put into operation. These breaks have been attributed to mechanical flaws in the manufacturing process. The wires could be fixed while a particular anode was on the chamber stack, so repairs were not a major problem. As the flaws were eliminated the breakage rate decreased even more until it is currently on the order of one data taking period *i.e.* 1000 hr.

The gas manifolds are box structures made from aluminum sheet metal. Each manifold extends along the entire outside edge of a module; there are four manifolds per module. The manifolds have gaskets running along both underside edges. These gaskets form a gas tight seal when the gas boxes are bolted in place on the chambers.

The chambers are sealed at the corners with 3.0 mil sheets of aluminized MYLAR; all gaps are filled with RTV compound. Each manifold has a series of baffles in it which insure the chamber gas is dispersed evenly to all parts of the device, displacing all of the initial air or nitrogen.

A series of 16-pin connectors runs along the top side of each gas manifold. These connectors are designed to hold the 16-channel amplifier/discriminator cards, described in a following section. Ribbon cables run from the feed-thru connectors to another set of connectors that mate with tabs on the printed circuit boards. These connectors are either 20-pin (16 signal and 4 ground lines), or 36-pin (32 signal and 4 ground lines). The 36-pin connectors are used only on the U and V planes. The 16-pin connectors were bolted in place with feed-thru cables attached. A layer of RTV compound was then poured onto the inside face of each manifold's top plate, thereby providing a gas seal. The gas boxes also contain power buses for the amplifiers. In addition, there are trays for the signal cables. Finally, there are lines for the discriminator threshold voltages and for test pulses to be broadcast to the amplifiers.

2.4.3 MWPC Gas System

A standard gas mixture was chosen for use in the proportional chambers. By mass this mixture consists of 80.4% argon, 18% isobutane, 0.1% FREON, and 1.5% isopropyl alcohol vapor. The functions of these various components is discussed qualitatively below. A comprehensive survey and description of gas mixtures for wire chambers, including the one utilized by this experiment, is found in the article by Sauli [23].

The role of argon is to provide an ionizing medium for charged particles traversing the chamber system. Atoms of argon are ionized about the charged particle trajectories in the gaps between anode and cathode planes. These electrons drift toward the anode wires, produce avalanches, and so generate signals. Noble gases are desirable

for use as ionizing media because they are chemically inert and their ions will only recombine with electrons to produce other noble atoms. Generally, the higher an atom's nuclear charge the lower is its first ionization potential. Since the operating voltage of a proportional counter varies directly with the ionization potential, it is best to use as heavy a noble gas as possible. Argon represents a compromise between cost and running at the lowest possible operating voltage.

The isobutane and FREON act as quenching agents, spurious avalanches. Argon atoms emit ultraviolet radiation during recombination that can ionize other atoms in distant parts of the chamber. In addition, the avalanche process also produces photons with energies greater than the ionization potential of carbon (11.6 eV); ionization electrons can thus be produced off the cathodes, inducing false signals. Isobutane absorbs UV light in a range overlapping the emission spectrum of argon. The molecule has a highly non-spherical shape, giving it many rotational and vibrational modes. These excited states are reached from the ground state by absorption of UV photons with no subsequent emission of ionizing radiation. FREON is an electronegative molecule with a high affinity for photo-ionization electrons, emanating from the cathodes. While large amounts of any electronegative gas are undesirable, trace quantities at the 0.1% level improve the signal-to-noise ratio. Negative FREON ions do not produce avalanches at the anode wires because they are so massive.

The avalanche process generates enough heat to polymerize the isobutane molecules and bind them to the anode wires. Over time a non-conductive layer can accumulate and literally cause the chamber to turn off. To prevent the binding of these polymers isopropyl alcohol is added to the gas mixture at the 1.0% level. Alcohols have considerable dipole moments, *i.e.* they are polar and miscible in water. So, the isopropyl molecules tend to concentrate only near the anode and cathode surfaces. This is why such small amounts are required. The chamber gas is flowed through these detectors to keep the concentrations of these polymers to a minimum.

The gas delivery system consists of two basic modules: a mixing station and a distribution rack. The distribution rack fanned out the mixed gases to each MWPC module. The gas flow to each module was controlled separately. The typical flow requirement was 1.5l/min or 2.5 SCFH for each module. The flow was under automatic control such that the pressure in each chamber was somewhere between .02 – .08 in H₂O. Each module was furnished with a flow meter and a pressure gauge. Limit switches on the pressure gauge allowed solenoidal valves at the input and output gas ports to be shut in the event of a high pressure or low pressure condition, respectively. The expended gas was piped out to a blower which vented to the atmosphere. It is possible to switch the flow to each module from the standard gas mixture to a nitrogen purge line. The chambers are purged at the beginning and end of each data taking period. After purging at the end of data taking they are sealed.

A mixing station is necessary because the required gas mixture is unavailable commercially. The scheme is to mix argon gas venting off a storage dewar with a 4% argon-FREON mixture. A resulting mixture of 99.88% argon and .12% FREON is then bubbled through isopropyl alcohol at 283 K. The alcohol has a vapor pressure of .026 atm at this temperature. So, by keeping the bubbler vessel pressure around 6.0 PSIG the alcohol fraction is 1.8%. The isobutane is mixed in after the bubbler because it liquifies above 283 K around STP conditions. The desired mix is achieved after the addition of isobutane. The chamber gas was then transported to the distribution rack after passing through a blender to insure homogeneity.

While the alcohol fraction is adjusted by varying the bubbler vessel's pressure at constant temperature, a more sophisticated device is needed to control the mixture of the other gases. Three DATAMETRICS model 825 mass flow controllers are used in conjunction with a model 1511 control unit. The mixing apparatus was configured to operate in a flow-on-demand mode which means that whatever flow is required at

the distribution station proper gas mixture will be maintained. To achieve this the control unit monitors the flow of argon, the majority gas, and adjusts the rate through the other slave controllers accordingly. The majority gas controller is left wide open; a check valve at the bubbler vessel's input port shuts off the gas flow whenever the pressure inside the vessel exceeds 6.5 PSIG. A second check valve before the blender closes whenever the bubbler pressure goes below 5.5 PSIG.

A digital display on the DATAMETRICS controller unit monitors the relative flow rates of the premixed argon-FREON and isobutane. The individual flow rates for all the bottled gases are monitored by precision mechanical flow meters as well. A mechanical flow meter also measures the flow of mixed gases as they enter the bubbler vessel.

2.4.4 Tracking System Electronics

After the preamplifier stage of the SSD system the MWPC and SSD electronic readout systems were identical and operated in a parallel fashion up to the input of the PDP-11 data acquisition (DA) computer. This common readout system was furnished by a commercial vendor, Nanometrics Systems, Inc. It consisted of four distinct types of modules. Only a brief sketch of this system's operation is given here. The reader interested in a more detailed description, including the CAMAC protocol, should consult the Nanometric Systems document [24].

At the front end are 16-channel N – 277 amplifier-discriminator cards, which are mounted in the connectors potted into the MWPC gas manifolds. Each channel has a 330Ω input impedance, making it sensitive to currents as small as $1/2\mu\text{A}$. The discriminator produces an ECL pulse in a time-over-threshold configuration. However, very long inputs are limited to 45 ns output pulses by a simple differentiator circuit between the amplifier and discriminator units. The discriminator thresholds

are set by an external voltage applied to a special pin on the service tab of each card. The conversion factor is $1\text{ V} = 1\text{ }\mu\text{A}$ over a range of $0 - 20\text{ }\mu\text{A}$. The typical threshold voltage for the MWPC's was $\sim 1.2\text{ V}$. Each N-277 card requires $+5.0\text{ V}$ at 0.4 A and -5.2 V at 0.68 A . Module 4 with its 4160 channels has the largest current requirement with 104 A and 177 A at 5.0 V and -5.2 V respectively. The service tab on each card also has a special pin for TTL test pulses, allowing for diagnostic testing of the entire readout system.

The ECL outputs from the amplifier cards pass through twisted pair cables approximately 50 ft in length on their way to the N-278 data latch modules. The latch units can receive up to 32 input signals, which are first delayed by a cascade of one-shot units, and then loaded into a 32-bit buffer register. The data in the buffer is latched whenever the leading edges of the input pulses are in coincidence with a 100 ns "load" pulse, generated by the pretrigger under standard running conditions. The delay time for each individual latch channel is programmable in a range from 300 - 650 ns for fully reliable operation. While the delays could be set up to $\sim 700\text{ ns}$, the reliability was less than optimum in this region. Nevertheless, the time required to form a pretrigger signal and transport it to the N-278 units forces the delays to be on the order of 700 ns, causing some detector inefficiencies.

These latch modules reside in CAMAC crates whose buses are controlled by Nanometric N-280 crate controller units. When a LAC pretrigger is followed by an associated high level trigger, the PDP-11 computers generate interrupt signals. One of these signals provides a "read" pulse to the N-280 crate controller units, which then process the data residing in the latch units' buffers. Otherwise, the buffers are reset by a clear signal, provided by the trigger logic. This is necessary because the latched data is cumulative over successive loads. The processing of the N-278 data involves reading only the non-zero words in the buffers and assigning to each non-zero bit within a word a wire address. The wire address is a 15-bit word, allowing the system

to handle up to 32,768 channels. The wire addresses are assigned by a wire map stored in a RAM memory under computer control. The addresses corresponding to actual hits are stored sequentially in the controller unit.

The N – 280 modules for the MWPC and SSD systems are serially connected to separate N – 281 CAMAC Interface units. The DA program running in the PDP-11 reads the data currently in each unit, and then transfers the data in each controller unit into a new stack within the Interface unit. It is therefore possible to have three events worth of tracking system data in the readout system simultaneously: while one event resides in the two CAMAC Interface modules, the next event in time resides in the N – 280 memories, while the most recently triggered event gets latched into the buffers of the N – 278 modules. Each PDP-11 interrupt only pushes each event into the next level of buffers, greatly reducing the DA system's dead time.

The determination and loading of delays as well as the loading of the wire map is all under computer control. A program called NANEX [25] performs these tasks. It is run on the PDP-11 which reads the CAMAC Interface units. In addition, it is used to diagnose problems in any channel along the dataway. Faulty modules can thus be identified and replaced. NANEX cannot run concurrently with the DA, but can be exercised between runs. In order for this program to perform its tasks the amplifier-discriminator cards must be pulsed. A special load signal must also be generated and delayed by the appropriate amount from the pulse going to the amplifiers. This delay should be equal to the time interval between the generation of amplifier signals and the arrival of the pretrigger signal at the latches, centered around 100 ns. All this is accomplished by using a programmable pulse delay generator accessed over a serial CAMAC highway by NANEX. Figure 2.33 gives a schematic of the MWPC test system run by NANEX.

2.4.5 MWPC Commissioning

Once the chambers were mounted on their support frames in the experimental hall, several operations were required to ready them for data taking. First, the gas manifolds had to be attached and the chambers sealed. Second, the amplifiers had to be mounted and the signal cables neatly installed. The signal cables had to be bundled and routed to the latch units, which reside in CAMAC crates inside a special air-conditioned room. In addition, the amplifiers had to be hooked up to the power distribution system, the threshold lines and the test pulse lines. Each module is equipped with its with a pair of FASTBUS switching supplies, providing the necessary power at the right voltage to operate all the amplifiers. Third, the electronics read-out system had to be prepared for data taking. This procedure has been described in the preceeding paragraphs. Finally, the modules had to be filled with chamber gas and "plateaued".

The "plateauing" procedure involved finding at what voltage each module operated in the middle of the proportional region. There were two ways in which this voltage was determined. One method is to use a ^{106}Ru source and two scintillator paddles. One paddle is positioned near the upstream face of the chamber while the other resides immediately downstream. The two counters are put in coincidence and the ratio of MWPC hits in the overlapping region to scintillator firings is taken. This ratio is plotted as a function of voltage for each plane. An example of this so called plateau curve appears in Figure 2.34. An operating voltage of 2900 V was found adequate for each chamber. A second approach is to use low intensity beam and take the ratio of MWPC hits to the beam count. This procedure also yielded an operating voltage of 2900 V.

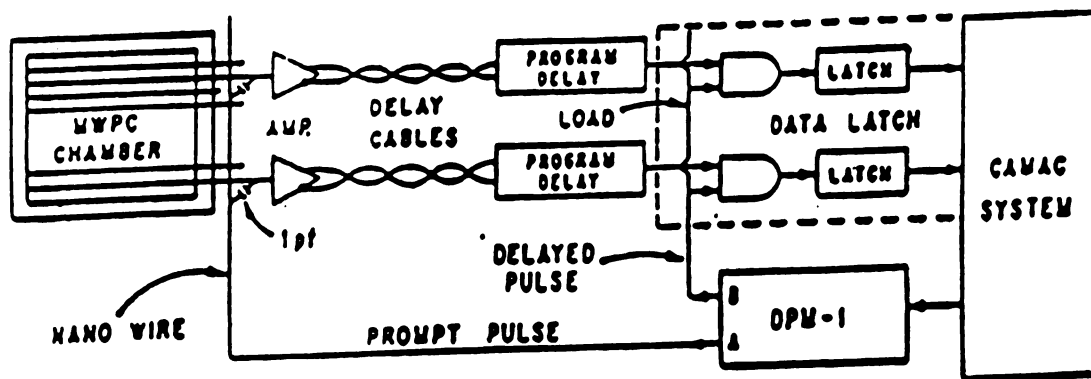


Figure 2.33: MWPC test system used to determine latch delays.

The high voltage distribution system is such that each chamber has its own independent supply. All cathode regions within a module are kept at the same voltage. A separate supply for each module held the garlands at 1000 V. However, each beam region had a $10\text{ M}\Omega$ resistor between it and the supply. By using a large resistor a voltage drop of several hundred volts occurs during the beam's passage. Such a voltage drop insures that the beam region falls below the voltage required for proportional operation. The anode wires passing through the beam region are thus sensitive to avalanches outside of it; the information outside the beam cathode region is more interesting and important from a physics point of view. In addition, the chambers cannot operate properly in regions where the rate exceeds $\sim 10^7$. The reason is that the total drift time across the gap is $\sim 100\text{ ns}$. So, at rates higher than 10^7 s^{-1} ionization from earlier events will create avalanches within the time window of the load signal. This is true even when shorter gate widths are used. Furthermore, radiation damage can occur in the beam region, and the organic components in the chamber gas can breakdown, causing polymerization in distant regions.

In order to maximize the planes' efficiencies the discriminator thresholds should be kept as low as possible. However, they cannot be so low that the discriminators continually fire on ambient noise. By studying the ambient rate and the efficiency as a function of threshold at the 2900 V operating point, a threshold of 1.2 V was deemed optimal.

2.5 THE FORWARD CALORIMETER

It is expected that a high p_{\perp} interaction will produce a significant amount of energy within the hollowed out region of the LAC. This energy is in the form of particles which are either fragments from the spectator partons or the ensuing nuclear breakup. In order to measure the amount of that energy and its direction of flow a special

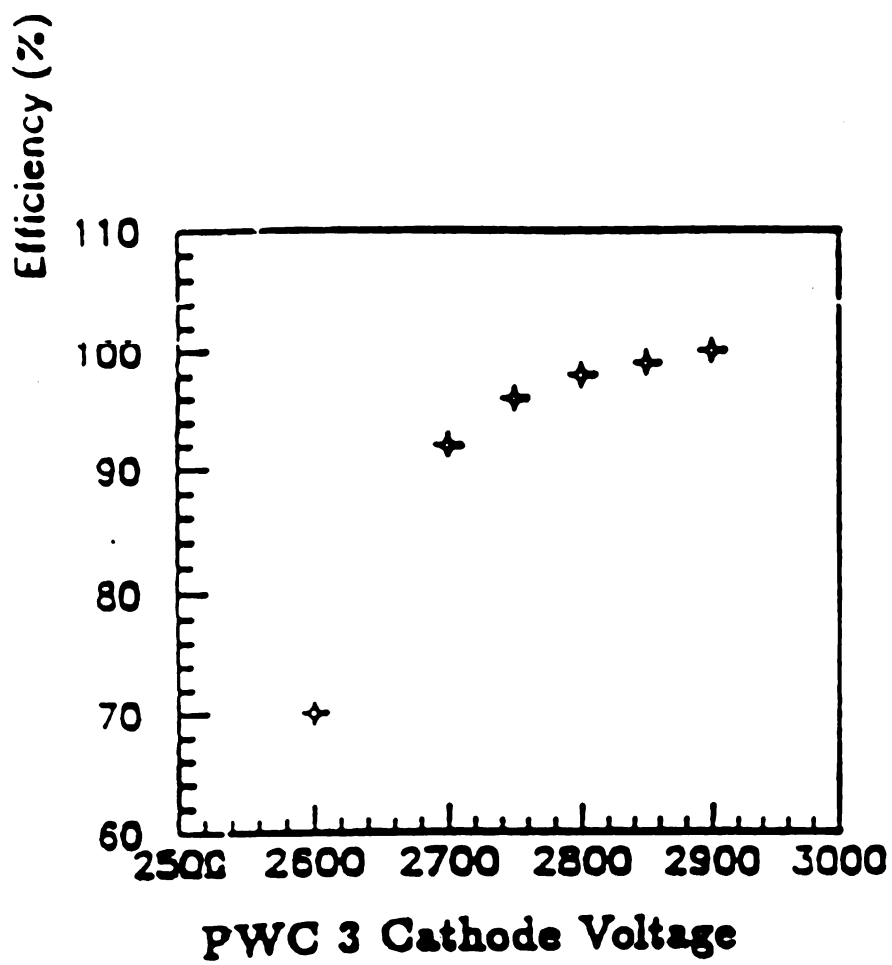


Figure 2.34: A high voltage plateau curve for MWPC module 3.

calorimeter was constructed. It is known appropriately as the forward calorimeter or FCAL.

Figure 2.35 shows an expanded view of this device in perspective. It consists of three separate modules. Each module is 3.17 interaction lengths thick for a total of 9.5 interaction lengths. Within each module are 28 circular steel absorber plates 114 cm in diameter and spaced 6.9 mm apart. 29 plexipop scintillator sheets are sandwiched between the plates and positioned at either end of a module. The scintillator sheets are 4.6 mm thick. A set of 76 holes, drilled on an 11.5 cm grid, exists in each scintillator sheet and absorber plate. 76 wave-shifter rods 1.0 cm in diameter are inserted longitudinally through the aligned holes. The wave-shifter material is an acrylic doped with BBQ which shifts the ultra violet light, produced by the scintillator, into the green wavelengths so that it can be detected by phototubes. In addition, the doping absorbs UV light produced by particles traversing the length of the rods that would otherwise produce an anomalous signal.

A phototube is attached at one end of each wave-shifter rod. The extinction length of the rods was short enough to make the detector's response was very sensitive to the longitudinal shower profile, which has large fluctuations for hadronic showers anyway. To minimize the sensitivity half the rods had phototubes attached to the upstream end, and half had their phototubes attached to the downstream ends. The energy resolution could then be maximized by making corrections to the total energy based on the front-to-back ratio. The details concerning the construction and performance of this device can be found elsewhere [26]

The signal from each phototube was digitized by a flash ADC clocked into a 256×4 bit memory at 100 MHz. The reference voltage to the ADC obeys the relation

$$V_{\text{ref}} = V_0 + A \times V_{\text{input}} \quad (2.31)$$

This allows the ADC's to have a dynamic range of 8 bits for $A = 3/4$, but the

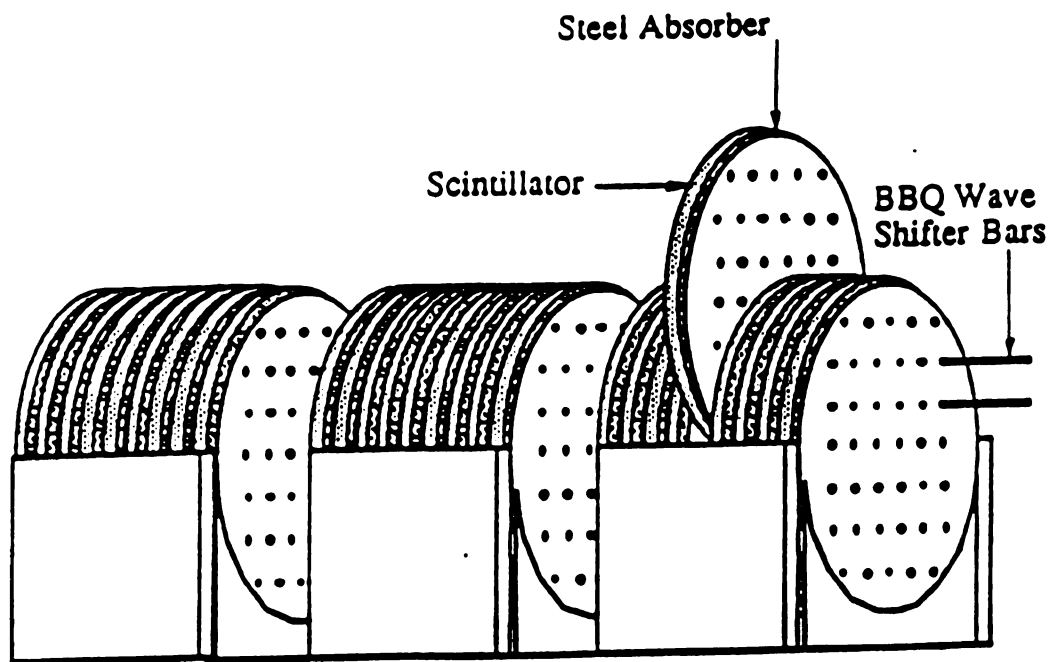


Figure 2.35: Perspective drawing of the Forward Calorimeter with an exploded view of one of the modules.

resolution of pulses near the top of the range is compromised. A $2.56\mu\text{s}$ history of each phototube about the trigger time can be readout.

The energy resolution of the FCAL was parametrized using a monte carlo. The energy scale was determined from data taken with a 530 GeV pion beam. Unfortunately, the energy resolution was dominated by systematic losses in the wave-shifter rods; the resolution has a quoted value of $161\%\sqrt{E}$. The position resolution of single showers was estimated by monte carlo to be 0.75 mm. For the actual data only the centroid of the energy flow could be determined. The reason is that several showers typically deposited energy within the device in a single event, and their energy was shared globally among the various phototubes.

Chapter 3

Data Reconstruction

The data for each event is collected from the detectors and written onto magnetic tape. This stored data must be subsequently processed to obtain the following quantities for every event: 1) the number, trajectories and momenta of charged particles traversing the tracking system, 2) the number, transverse positions, and energies of showers in the EMLAC, and 3) the status of the various scintillation counters, the trigger logic, and the scaler counts. The information in the HADLAC and FCAL was also processed, but the details are not pertinent here. A good discussion of how the data from these devices is analyzed can be found elsewhere [27, 28].

Each major piece of the apparatus has its own reconstruction program. The reconstructors for the tracking system, the electromagnetic calorimeter, and the discrete logic are known as PLREC, EMREC, and DLREC respectively. All of the reconstructors are embedded in a larger program called MAGIC. MAGIC controls the program flow, handles I/O operations, and provides memory management via the ZEBRA package [29]. The entire data reconstruction package was written in ANSI standard FORTRAN77.

3.1 EMLAC RECONSTRUCTION

During data taking the pulse heights from individual amplifier and TVC channels were written out to tape. These pulse heights have to be converted into energies and time values which are then input to a reconstruction program. This translation procedure is known generally as unpacking. The reconstructor uses the channel energies to compute the energies and centroids of the electromagnetic showers. It also determines the time of arrival for the reconstructed showers relative to the interaction

responsible for the trigger. A complete description of EMREC is found in the thesis of J.P. Mansour [30]. Only the basic steps in the algorithm are given in the following discussion.

3.1.1 EMREC Unpacking

The amplifier channel pulse heights are given in ADC counts. These ADC values are converted to channel energies by the formula

$$e_i = A_{em} G_i (N_i - N_i^0) \quad (3.1)$$

where e_i is the energy deposited in channel i , and N_i is the raw number of ADC counts. A_{em} is the conversion of ADC counts to energy and represents a global energy scale factor. This factor was determined from the electron beam calibration studies; it was found to have the value of 3.1 MeV/count. The global energy scale for each octant was later modified slightly in order to reproduce the nominal π^0 mass using 2-photon combinations. G_i and N_i^0 represent the individual channel gains and pedestals respectively. The pedestals were obtained by reading out the calorimeter with pulser triggers. The gains were computed by pulsing each amplifier channel with a precision charge injection capacitor and analyzing the pulse height distribution.

A correction for dead channels was made during the unpacking procedure. Some channels were known to contain strips which either had shorts or bad connections, making them unusable. Also, the amplifiers themselves occasionally developed problems as revealed by the calibration tasks. Under such circumstances a channel was labelled “dead” and assigned an energy value that was the mean of the two adjacent channels.

The unpacking program also performed a sum of energies for corresponding channels in the front and back sections of the EMLAC. The set of summed channels was known as the summed section. The pattern recognition routines in EMREC used the

summed and front sections' channels of unpacked energies to reconstruct the showers.

The TVC data was unpacked in a manner similar to the amplifier channels. Recall that four amplifier channels were used to generate one channel of raw TVC data. The conversion of raw pulse height to time-of-arrival is given by the following expression:

$$t_i(\text{in ns}) = A_{\text{ADC}}(T_i - T_i^0 - C(E_i)) \quad (3.2)$$

t_i is the arrival time with respect to the triggering interaction, and T_i is the raw pulse height. T_i^0 is the channel pedestal, which represents the average time-of-arrival for in time pulses. It was determined by a special calibration task described in the thesis of E.J. Prebys [31]. Nominally, T_i^0 was half of the full scale value for a single TVC channel. The $C(E_i)$ term represents a correction stemming from the fact that smaller pulses *i.e.* lower energy showers, tended to trigger the TVC's later than larger ones.

3.1.2 Shower Reconstruction

The purpose of the shower reconstruction algorithm is to ascertain the energies, positions and arrival times of all photons and electrons incident on the EMLAC. EMREC reconstructs showers on a quadrant by quadrant basis. Each quadrant is divided into four views. The r channels are subdivided into r_{left} and r_{right} views; the ϕ channels are divided into ϕ_{inner} and ϕ_{outer} views at the inner-outer ϕ boundary of the readout boards. The same pattern recognition procedures are performed on the views in the summed and front sections. This is done in order to estimate $E_{\text{front}}/E_{\text{total}}$ for a shower in a particular view, and to aid in splitting showers which may have merged into a single shower in the back section, and appearing as such in the summed section.

The basic program flow of EMREC goes as follows. First, individual channels are gathered into groups in each view and section. The number of peaks in each group is then computed. Each peak represents a shower whose energy, position and time-of-arrival is to be reconstructed. Second, showers are reconstructed in each view about

the peaks found earlier. These view showers are called “gammas”. The reconstructed “gammas” in ϕ and r are then correlated by energy to obtain reconstructed photons. The arrival times are then assigned to these photons. The energy resolution function used for all weighting and decision making criteria is given by

$$\sigma_i = \sqrt{(0.1)^2 + (0.14)^2 e_i} \quad (3.3)$$

where σ_i is the resolution of a particular amplifier channel. The 0.1 term is the incoherent noise contribution to an individual channel. The other term is the intrinsic energy resolution due to sampling fluctuations; e_i is the measured channel energy.

Four requirements must be met before a set of strips can be classified as a group.

- For r_{left} , r_{right} , and ϕ_{in} there must be at least three consecutive strips above threshold. Only two channels are required for ϕ_{out} because the readout strip widths are larger.
- The summed channel energies must be greater than 700 MeV.
- The average energy per strip must be greater than 150 MeV.
- The highest energy channel must contain more than 300 MeV of energy.

The peak finding procedure is straightforward. Starting at one edge of a group, the energy of each channel is examined. When a channel is found to have less energy than the preceeding one, the preceeding channel is termed a “peak”. When a channel’s energy is greater than the preceeding channel’s or the edge of a group has been reached then the previous channel is termed a “valley”. If the energy of a peak is more than $2.5\sigma(E_{\text{peak}})$ from either valley, then the peak is flagged for reconstruction as a gamma.

The gamma reconstruction algorithm is split into two parts. One set of routines is used on groups containing a single peak channel. Another set of routines is initially used on groups possessing multiple peaks. To begin with the single peak case will be

described. First, the position of the shower in the view is determined. The median position of the peak channel is taken and shifted by an amount depending on the relative amounts of energy in the adjacent channels. Calling this position X , two other trial positions at $X \pm 0.2$ cm are successively chosen as the shower centroid and input to a shower shape-fitting routine. This routine compares a parametrized shower shape to the actual shape of the group energy distribution and calculates a χ^2 [32]. The trial centroid position corresponding to the lowest χ^2 is taken as the true shower centroid. Furthermore, the relative fraction of energy per channel, z_i , is computed from the fit to the shower shape.

The estimated channel energy fractions relative to the full shower energy are then used to statistically determine the shower's energy by minimization of the following likelihood function:

$$\chi^2 = \sum_{i=1}^{N_s} \frac{1}{\sigma_i^2} (e_i - E z_i)^2 \quad (3.4)$$

If this $\chi^2 \leq 5.0$, then the shower energy is computed to be

$$E_{\text{shower}} = E_{\text{tail}} + E, \quad E_{\text{tail}} = E \left(1 - \sum_{i=1}^{N_s} z_i\right) \quad (3.5)$$

Otherwise,

$$E_{\text{shower}} = \sum_{i=1}^{N_s} e_i \quad (3.6)$$

Two caveats are in order. E_{tail} is an estimate of the energy in the shower tails. The tail energy cannot actually be measured because of zero suppression (nominally 150 MeV), and because N_s may be less than the number of channels in the group. N_s is the number of channels about the peak for which the energy measurements are not dominated by fluctuations *i.e.* the energy estimate is better than 50%. N_s was determined from monte carlo studies, using the beforementioned shower parametrization function and measured energy resolution of the detector.

For multiple peak groups, each shower's contribution to the energy in a particular channel has to be estimated. To do this the fraction of each shower's energy in a

particular channel of the group was calculated by applying the shower shape-fitting routine used in the single peak group algorithm to each peak. The shower centroids corresponding to each peak were also measured. The number of channels N_S used for each peak was less than or equal to the number of channels between the two valleys surrounding the peak. The energy of each shower was obtained by minimizing the following likelihood function:

$$\chi^2 = \sum_{i=1}^N \frac{1}{\sigma_i^2} (e_i - \sum E_k f_k^i)^2 \quad (3.7)$$

Here, N is the total number of channels in the group, E_k is the total energy of the k th shower, and f_k^i is the fraction of the k th shower's energy in the i th channel. e_i and σ_i are the i th channel's energy and resolution respectively.

From E_k and f_k^i the channel energies corresponding to each shower were separately computed. Each calculated distribution was then input to the algorithm implemented for the single-peak groups. The final energy and shower centroid estimates for each gamma were then obtained.

If a group in the front section contained two reconstructed gammas while the corresponding summed section had only one gamma, the summed section gamma was split into two. The positions of the split gammas were taken to be the positions of the front section gammas. The split gamma energies were determined from the following condition:

$$\begin{aligned} E_{1 \text{ split}} + E_{2 \text{ split}} &= E_{\text{sum}} \\ \frac{E_{1 \text{ split}}}{E_{2 \text{ split}}} &= \frac{E_{1 \text{ front}}}{E_{2 \text{ front}}} \end{aligned} \quad (3.8)$$

Finally, all gammas reconstructed in the r view had their centroids for the back section as well as the front section calculated and assigned to them on output from the gamma reconstructor. This was done so that front and back coordinates could be assigned to the fully reconstructed photons.

The reconstructed gammas in the two r views are then correlated with those reconstructed in the ϕ views. The gammas are correlated on the basis of their energies and front-to-total energy ratios. The interleaving of r and ϕ readout layers in the electromagnetic calorimeter results, on average, in equal amounts of energy being deposited in both views. At the simplest level a gamma from the r view can be correlated with a ϕ view gamma by finding the one which has an energy and $E_{\text{front}}/E_{\text{total}}$ closest to its own. If these quantities match within the expected resolution, then a fully reconstructed photon can be formed. This simplest of correlations is called a 1-1 correlation.

However, there are a number of complications which introduce ambiguities and inefficiencies into the pattern recognition for gamma correlation. One complication is the splitting of a shower in a particular view, resulting in two reconstructed gammas. Another is the loss of a gamma in a particular view, and the subsequent mismatching of the corresponding gamma in the orthogonal view. Still another problem is the presence of two showers with nearly equal energies in a single quadrant. The correlation routine's performance can be optimized using monte carlo events, but there is a physics bias due to the reconstruction efficiency's dependence on quadrant and octant multiplicities.

The basic philosophy of the correlation procedure is to divide all gammas into three groups. One group involves ϕ view gammas at the inner-outer ϕ boundary and the octant boundary. The second group consists of r view gammas at the octant boundary. The third group is composed of all gammas which are away from the boundaries and are not likely to suffer problems with shower splitting.

The correlation algorithm first tries to match r_{left} and r_{right} gammas at the octant boundary with those from the ϕ views near the boundary. The routine first checks if an r_{left} , r_{right} pair can be matched with a ϕ pair based on energy sums of each pair. A

single photon is reconstructed if a match is found; the r and ϕ positions are determined from energy weighted sums. Such a correlation is termed a 2-2 correlation. After these 2-2 correlations have been found the algorithm then matches the remaining r_{left} , r_{right} gamma pairs with single gammas from the ϕ views. Whenever a match is found, a single photon is formed. This type of correlation is termed 2-1. The routine then attempts to match ϕ_{in} , ϕ_{out} gamma pairs near the inner-outer ϕ boundary with single r view gammas. Again, if a match is found for a pair, a single photon is reconstructed.

Finally, r and ϕ gammas away from boundaries are correlated. The algorithm first looks for 2-1 type correlations. Whenever such a match is found, the single gamma is split into a pair whose energies have the following relationship,

$$\begin{aligned} E_{1 \text{ split}} + E_{2 \text{ split}} &= E_{\text{gamma}} \\ \frac{E_{1 \text{ split}}}{E_{2 \text{ split}}} &= \frac{E_1}{E_2} \end{aligned} \tag{3.9}$$

The positions of the reconstructed photons in the split view are both equal to the position of the unsplit gamma. This change in philosophy is due to the fact that away from boundaries such 2-1 correlations are more likely to arise from π^0 and η decays. All 1-1 correlations are found at the end, and the energies, positions, and $E_{\text{front}}/E_{\text{total}}$ of all photons are written to output.

After each correlation is found the ϕ position of the reconstructed photon is recalculated based on its r position. This is because the width of the ϕ strips increases with increasing r . So, a better estimate of the ϕ coordinate can be achieved using the improved ϕ strip width.

3.1.3 TVC Reconstruction

The reconstruction of the TVC data takes place at the group level. No TVC criterion is used at any stage of the shower reconstruction. Within each group of amplifier channels used to reconstruct gammas, corresponding TVC channels are

clustered together. The clustering involves taking each TVC channel in a group and forming a set of TVC values containing the given TVC and all other TVCs within ± 45 ns of the given TVC's time value. Hence, there is a one-to-one correspondence between all TVC channels belonging to an EMREC group, and the TVC time clusters associated with that group.

A time value is computed for each cluster based on the energy weighted sum,

$$T = \frac{\sum_i t_i E_i}{\sum_i E_i} \quad (3.10)$$

where E_i is the energy in the i th channel and t_i is the TVC time value for the channel. The clusters are then ranked in a hierarchal order according to three criteria. They are listed on the following page.

- The number of TVCs in a cluster.
- Clusters not ordered by the above are ordered according to the cluster energy.
- Clusters still not ordered are ranked according to how close their times were to the time of the interaction which triggered the event.

The two highest ranked times from the above set are assigned to all gammas reconstructed from the EMREC group.

TVC times for reconstructed photons are obtained by ordering all clusters, assigned to the gammas from which the photon is formed, by the same ordering criteria presented above. The photon has the two highest ranked TVC values assigned to it. If less than two TVC values get assigned to a photon, then the photon is assumed to be in time with the triggering interaction. Besides being assigned time values, a photon is also given a TVC quality value. This quality value is defined as follows,

$$\text{TVC}_{\text{quality}} = 10^3 \times (\# \text{ of TVCs used}) + (\text{summed energy of TVC channels}) \quad (3.11)$$

Clearly, a photon's TVC values have meaning only if the quality value is greater than 2000.

3.2 TRACKING RECONSTRUCTION

The reconstruction of tracks from raw hits is now described. The MWPC and SSD planes provide two coordinates for every track. The data is stored as a wire address, which is transformed into a real coordinate value by an unpacker program. The program responsible for reconstructing the tracking system data is called PLREC.

The basic program flow is as follows. The four views in the MWPC system enable the reconstruction of tracks in space. Tracks in the SSD system are only reconstructed in the X-Z and Y-Z projections. The SSD tracks are used to reconstruct the vertex of the interaction responsible for the high p_{\perp} trigger. Space tracks are assigned X and Y view SSD tracks, taking into account changes in trajectory due to the analyzing magnet's field. Each space track is assigned a value of momentum, and the sign of the charge which corresponds to that of the particle responsible for the space track. All charges are assumed to be either ± 1 . The details of the PLREC functions are given in the following subsections.

3.2.1 MWPC Space Track Reconstruction

The reconstruction begins with the formation of tracks in the X, Y, U, and V projections. Reconstruction in the various projections proceeds in the following manner for each view. First, a pair of hits is chosen from modules 1 and 4. Second, a line is constructed from the pair. Third, the points on this line that intersect planes in modules 2 and 3 are computed; the closest hits in these searched modules within 1.5 wire spacings are used to reconstruct a view track. Fourth, the program calculates the view track's parameters via a least-squares fitting routine. The fitting procedure yields a χ^2 ; if this χ^2 is less than a cut value, reflecting 95% confidence, then the track parameters are retained for further processing. Otherwise, if the track contains four hits, then the hit with the largest residual is dropped and a 3-hit track

is reconstructed. Any 3-hit track that fails the χ^2 cut is dropped. PLREC performs this procedure for every pair of hits in modules 1 and 4. All 4-hit combinations for which a track was reconstructed are flagged. After all combinations in modules 1 and 4 have been checked the view track algorithm takes hit pairs in modules 2 and 3 as seeds for view track reconstruction. The purpose of this is to pick up 3-hit tracks missed during the first iteration. In fact, no 4-hit combinations from the first pass, which resulted in a reconstructed track, were reused in the second pass.

Once the view tracks have been reconstructed, a cleanup procedure removes duplicate tracks. All 4-hit tracks are grouped into sets such that each track in a set shares 3 or more hits with some other track in the set. These sets are known as global clusters. If a global cluster contains only two tracks, then the one with lowest χ^2 is retained. Otherwise, the two tracks with lowest χ^2 s are saved for further processing. The same procedure culls all the 3-hit tracks as well, except that the hit sharing requirement is reduced to 2 or more hits. Finally, 3-hit view tracks that share 2 or more hits with a 4-hit view track are dropped from the ZEBRA structure.

The tracking reconstructor takes the cleaned view tracks and forms tracks in space. The algorithm starts by taking all pairs of X and Y view tracks and computing the corresponding U and V projections. The intersections of these U and V projections are determined for each U and V plane. The closest U and V hits within 1.5 wire-spacings are then used to construct a space track, provided that each view contains 2 or more hits and there are 13 or more hits in all. A space track is defined in terms of its X and Y projections, which are obtained from the following likelihood function:

$$\chi^2 = \frac{1}{N-4} \sum_i^{16} \left(\frac{x_i - \xi_{\text{fit}}}{\sigma_i} \right)^2 \quad (3.12)$$

$$\xi_{\text{fit}} = (b_x z_i + a_x) \cos \alpha_i + (b_y z_i + a_y) \sin \alpha_i$$

where b_x , a_x , b_y , and a_y are the space track's parameters in the X and Y projections respectively. N denotes the total number of hits. $\cos \alpha_k$ and $\sin \alpha_k$ project the space

track's parameters into the proper view for each plane. If the i th MWPC plane has no hit for a particular track candidate then the corresponding term in the sum is skipped in the calculation. After the X and Y view track combinations have been exhausted the program goes through all U and V combinations, searching for matching hits in the X and Y views. This step recovers all those tracks which contain only two hits in either the X or the Y view, and would therefore have been missed in the first iteration.

Clearly, a space track is typically reconstructed twice by this procedure. So, another routine removes all the duplicate space tracks by the following method:

- Any space track possessing 9 or more unique hits is always retained for output.
- If a pair of tracks share 6 or more hits between them, the procedure eliminates the track with fewer hits. In the event that both tracks contain the same number of hits, the selection is made according to smallest χ^2 .
- If a pair of space tracks had 7 or more shared or adjacent hits, the algorithm executes the above procedure for shared hits.

3.2.2 SSD Track Reconstruction

The SSD system consists of two distinct parts with separate functions. The beam SSD system is located upstream of the target and contains three modules. The information provided by this group of planes is used to reconstruct the track of the beam particle that produced a particular event. The vertex SSD system resides immediately downstream of the target. As its name implies, this set of planes enabled a triggered event's vertex to be reconstructed.

Before any SSD track reconstruction is performed all adjacent hits in each plane are clustered. A cluster's position is simply the mean position of the strips comprising it; this position is the "hit" coordinate input to the reconstruction software. The hits have to be clustered for two reasons. One, the ratio of strip width to plane

thickness is typically 1:5 for the SSD's. Thus, a 30 mrad track has $\approx 25\%$ chance of firing the discriminators of two adjacent strips. Second, the cross talk between adjacent preamplifier channels enhances the double hit count for wide angle tracks, and degrades the pair resolution for low angle tracks.

The reconstruction scheme for the vertex SSD's is identical to the MWPC view reconstruction. For the beam SSD's, the view track reconstruction procedure is used first to find all 3-hit tracks in the beam SSD system. Afterwards 2-hit tracks are made from the unused 2-hit combinations. The XY combination of view tracks with the smallest impact parameter about the vertex becomes the beam track for the event.

3.2.3 Linking

Once the SSD and MWPC track reconstruction has been performed, an attempt is made to match each MWPC space track with an X-view and Y-view upstream track from the vertex SSD system. This requires that the effects of the analyzing magnet's field be accounted for. Ideally, the analyzing magnet produces a uniform field parallel to the y-axis in the experiment's coordinate system. This field is produced between $z_c \pm L/2$ where z_c is the magnet's geometric center, and L is the length of the pole pieces. In addition, the momentum kick $\sim 450 \text{ MeV}/c$ is very small compared to typical track momenta $\sim 10 \text{ GeV}/c$. Under these circumstances charged particles with $p_y \ll p_z$ travel through the magnet unaffected in the YZ plane and undergo uniform circular motion in the XZ plane. Because $\Delta p/p \ll 1$ for most tracks, the X-view SSD tracks intersect the X-projections of the corresponding space tracks at the magnet's center.

However, in reality the analyzing magnet's field is asymmetric in z due to the upstream and downstream apertures being considerably different in size. A measurable B_z component exists also, which is non-negligible at the entrance and exit planes of the magnet. The B_z component introduces $p_x B_z$ and $p_y B_z$ couplings that produce a

helical motion about the beam direction. This twisting effect prevents upstream and downstream tracks from intersecting at the center of the magnet. Also, many tracks possess a non-negligible p_y component so they make a non-zero angle with respect to the bend plane. In this case there is a change in the y-view slope of a track due to the change in p_s , which occurs in the bend plane. Finally, for low momentum tracks the kick approximation breaks down *i.e.* $\Delta p/p \sim 1$, so the x-view tracks are not expected to meet at the middle of the magnet.

The field asymmetry, produced by the difference in upstream and downstream apertures, is easily accounted for. The geometric center and length are replaced by an effective center and length. These quantities were obtained from the field map. The corrections for the other effects involve a rather detailed analysis of the field. They have been worked out, and are summarized in an appendix [33].

The x-view SSD tracks that projected to within ± 0.7 cm of a particular downstream track are arranged in ascending order of the projection difference. The five upstream tracks with the smallest difference are retained for further processing. The y-view linking procedure imposes a cut in the slope difference between upstream and downstream tracks of ± 2.5 mrad. All y-view SSD tracks that match to a downstream track within this window are assigned a χ^2 . This χ^2 is a weighted sum of the slope and projection differences. The linked upstream tracks are put in ascending order of the χ^2 parameter, and the five tracks with the lowest χ^2 are kept in the ZEBRA structure.

3.2.4 Event Vertex Reconstruction

The event or primary vertex is formed from the vertex SSD tracks. The efficiency of the vertex algorithm is critical since the high $p_{\perp \text{event}}$ selection involves a vertex cut. To study the nuclear A dependence of the π^0 and direct photon cross sections one must know which part of the target a given interaction occurred in. This implies

that the vertex finder's z resolution has to be better than 1 mm.

The algorithm first reconstructs a vertex in the X and Y views. If view vertices are found, then the program attempts to match the vertices based on the difference in their z positions. When a match is found, a matched vertex is computed whose z coordinate is the weighted average of the view vertices' z coordinates.

The view vertex reconstruction algorithm first culls the SSD view tracks and takes a subset of them to construct the vertex. This procedure has three possible outcomes,

- The subset of vertex SSD tracks consists of all linked 4-hit tracks.
- If there are less than three linked 4-hit tracks in a view, then the set of all 4-hit tracks formed.
- If there are less than three 4-hit tracks, the procedure uses the set of all 3-hit linked tracks as input to the next stage of vertex reconstruction.
- In the event that all of the above sets contained less than three tracks, no view vertex was reconstructed.

A special likelihood function is used to calculate the position of each view vertex, (X_0, Z_0) . This function expresses a track's χ^2 as a Taylor series of the χ^2 with the vertex constraint, $a'_k = X_0 - b'_k Z_0$. This function therefore possesses the following form,

$$\begin{aligned}
 \chi_k^2(a_k, b_k) &= \chi_k^2(a'_k, b'_k) + (a_k - a'_k) \frac{\partial \chi_k^2}{\partial a_k} \Big|_{a'_k} + (b_k - b'_k) \frac{\partial \chi_k^2}{\partial b_k} \Big|_{b'_k} \\
 &+ (a_k - a'_k)^2 \frac{\partial^2 \chi_k^2}{\partial a_k^2} \Big|_{a'_k} + (b_k - b'_k)^2 \frac{\partial^2 \chi_k^2}{\partial b_k^2} \Big|_{b'_k} \\
 &+ (a_k - a'_k)(b_k - b'_k) \frac{\partial^2 \chi_k^2}{\partial a_k \partial b_k} \Big|_{a'_k, b'_k} + \dots
 \end{aligned} \tag{3.13}$$

The χ^2 minimization condition forces the first order terms to vanish. By imposing the vertex constraint, and the additional condition that $b_k \approx b'_k$ within the detector's

resolution, one obtains the following 2nd order expression:

$$\Delta\chi_k^2 = (a_k - (X_0 - b_k Z_0))^2 \bar{\sigma}_{a_k}, \quad \hat{\sigma}_{a_k} = \left. \frac{\partial^2 \chi^2}{\partial a_k^2} \right|_{a'_k} \quad (3.14)$$

Summing over all tracks in the input set gives,

$$\Delta\chi^2 = \sum_k (a_k - (X_0 - b_k Z_0))^2 \bar{\sigma}_{a_k} \quad (3.15)$$

Minimizing this likelihood function yields X_0 and Z_0 .

Once the vertex coordinates are calculated for a particular view, the algorithm checks whether or not the average impact parameter of the input tracks is greater than $20\text{ }\mu\text{m}$, or the highest impact parameter is larger than $50\text{ }\mu\text{m}$. Should this situation arise, the track with the highest impact parameter is dropped from the input set, and the resulting set of tracks is used to refit the vertex. The program repeats the refitting procedure until the impact parameter cuts are satisfied, or only two tracks remain in the input set.

If vertices are reconstructed in both views, then a routine is called to find a matched vertex. To start with the routine takes the difference in the z coordinates of the view vertices. If this difference is less than 3.0 mm , then construction of the matched vertex takes place immediately. Otherwise, all X-view tracks, used to reconstruct the view vertex, within $\pm 1.0\text{ cm}$ of the Y-view vertex's z position are used to recalculate the X-view vertex's coordinates. This assumes, of course, that two or more X-view tracks exist which satisfy the foregoing criterion. The Y-view vertex is recalculated in the same fashion. When the program fails to find a matched vertex, it assigns a nominal vertex position to the event. This nominal position is just the target's geometric center.

The vertex reconstructor was determined to be 95% efficient. It possesses a z resolution of $600\text{ }\mu\text{m}$; this is sufficient to resolve the target elements as Figure 3.1 demonstrates. The quoted resolution comes from the Δz distribution of X and Y-view vertices. The z resolution calculated from the likelihood function is $300\text{ }\mu\text{m}$.

This discrepancy arises from the clustering of hits in individual planes, decay vertex tracks being assigned to the primary vertex, and secondary interactions. The vertex resolution in X and Y, estimated from the track residual distributions, is $20\ \mu\text{m}$.

3.2.5 Relinking

Any time PLREC finds a primary vertex, it reorders each space track's X and Y links. The program places all links belonging to the primary vertex at the top of each list. Furthermore, each list of links associated with the event vertex is put in ascending order of a χ^2 parameter. The parameter is the weighted sum of a link's impact parameter and the projection difference at the center of the magnet. The calculation of the track momenta employs those links with the lowest value of this χ^2 . In the event that a space track has no links in a particular view, the upstream trajectory is estimated by constructing a line between the vertex and the projection point at z_c . The nominal vertex position is used if an event contains no matched vertex.

3.2.6 Track Momentum Reconstruction

The space track momenta are determined using the square field and p_{\perp} kick approximations with an effective length, L_0 , for the magnet. The momentum calculation proceeds by solving the following three equations,

$$\begin{aligned} \sqrt{p_x^2 + p_z^2} &= \frac{p_{\perp \text{ kick}}}{|\sin \alpha - \sin \beta|}, & p_{\perp \text{ kick}} &= eB_0L_0 \\ \frac{p_x}{p_z} &= \frac{\tan \eta}{\sin \alpha} \\ \frac{p_y}{p_z} &= \frac{\tan \eta}{\cos \alpha} \end{aligned} \tag{3.16}$$

$\tan \alpha$ and $\tan \beta$ are the upstream and downstream slopes, respectively in the x-view.

In addition, the sign of the particle's charge is given by,

$$q = \text{sign}(\alpha - \beta)\text{sign}(B_0) \tag{3.17}$$

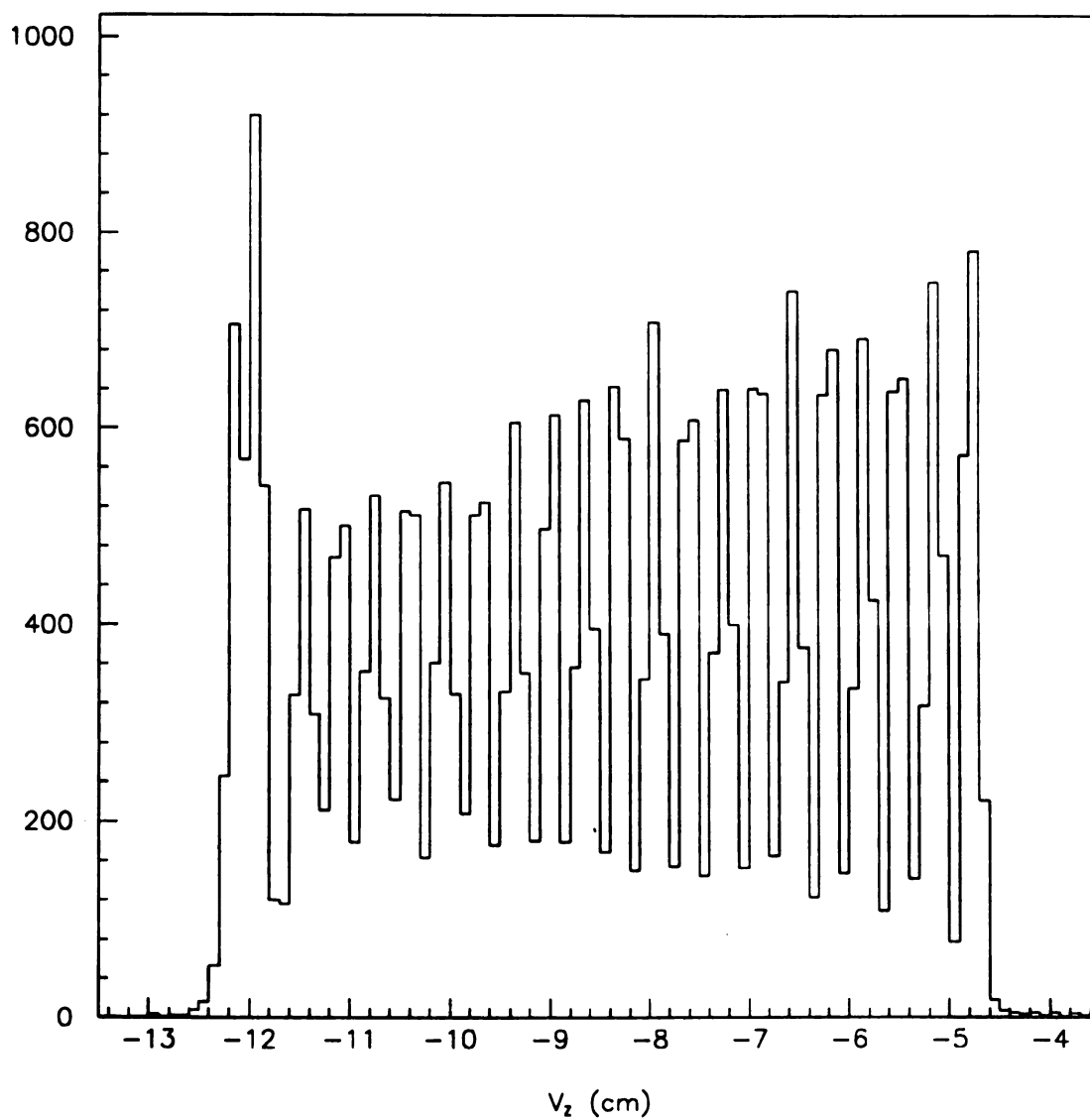


Figure 3.1: The z coordinate distribution for matched vertices within the target volume. The different target elements are clearly resolved.

It should be noted that $\tan \eta / \sin \alpha$ and $\tan \eta / \cos \alpha$ are just the x and y view slopes of the upstream links respectively. The magnet's momentum kick was originally estimated to be 450 MeV/c. A subsequent analysis of the J/ψ and K_S masses indicate that the kick is 449 MeV/c instead; this data analysis will employ this $p_{\perp \text{ kick}}$ value.

3.3 TRACK QUALITY STUDIES

Because the ensuing analysis relies heavily on the tracking system's data, it is important to understand its quality. The analysis uses the physics tracks, obtained from the MWPC data, to study the charged particle structure of high p_{\perp} π^0 and γ events. Therefore, the following discussion will focus almost entirely on the quality of the physics tracks. The SSD data is relevant only in so far as linking is concerned, and with the associated systematic effects on the track momentum calculation. Several issues must be dealt with in obtaining a quantitative understanding of track quality. First, it must be determined what fraction of the physics tracks is false. By false it is meant that the reconstructed track does not correspond to an actual charged particle's trajectory in an event. Second, the reconstruction efficiency for true physics tracks needs to be ascertained. Third, how reliable is the momentum calculation? Fourth, can those charged hadrons emanating from the primary vertex be so identified? Finally, how well do the multiplicity, rapidity, and momentum spectra of the physics tracks compare with the monte carlo simulation used in comparing data with theory?

3.3.1 Alignment and Plane's Efficiencies

To guarantee the highest quality tracks possible the various modules in the tracking system had to be aligned relative to one another, and to a universal coordinate system. Aligning things to a precision better than the spatial resolution of the tracking system insures that the reconstruction program is limited in principle only by the

device's inherent resolution. The alignment procedure consists of two steps. To begin with a survey is performed. The survey establishes a universal coordinate system for the entire experiment, including the beamline, with respect to a U.S. Geological Survey marker. The survey had a precision of < 1 mm.

The universal coordinates of a point on the SSD cart was established by the survey. A transit, whose position was known relative to this point, was then used to locate the transverse positions of all SSD modules. The modules' positions along the beam direction are known from the SSD cart's dimensions. The MWPC modules were leveled square with the beam direction *i.e.* the z -axis, and plumbed vertical. The transverse y -position was determined by measuring the bottom center pins' height above the floor, which was assumed to be flat. The transverse orientation in x was found by centering a plumb bob about a survey line on the floor parallel to the z -axis. The plumb line hung from a rod which passed through the top center pin on each chamber. Another vertical plumb line was dropped which passed across the face of the top and bottom center bushings. A tape measure was then placed between the survey plug ($z = 0$), and the plumb bob, yielding each chamber's z -position. From the known positions of each anode plane within a module stack, the position of every anode wire was determined in the universal coordinate system.

A computer program was used to reduce the uncertainties in the transverse alignments to a negligible level. It systematically centered all residuals between track projections and hits about 0. In addition, a relative alignment between SSD and MWPC systems was performed so that the linking procedure could be optimized. The SSD system was moved relative to the MWPC system, and then each sense plane in the tracking system was transformed back to the universal coordinates as established by the point on the SSD cart. Both non-interacting beam and minimum bias events were processed by the alignment program. The data was taken at low intensity with the analyzing magnet's field off. The algorithm found no rotations about

the z-axis, but small shifts in z were detected. However, these shifts were so small that their effect on the reconstruction was negligible. Besides residual distributions, the χ^2 distributions provide some information on alignment quality. Figure 3.2 shows χ^2 distributions for 16, 15, 14, and 13-hit tracks. The 16-hit distribution provides the best indication since it involves all planes. The 13-hit distribution looks rather poor, but this is because PLREC did not utilize the narrowest window cuts possible. This was so that the reconstruction efficiency would be maximized.

The measurement of individual MWPC sense plane efficiencies is important in understanding the reconstruction efficiency. Even if the reconstruction program generated no losses, the reconstruction efficiency is ultimately limited by the efficiencies of the various planes. The method used to determine the planes' efficiencies was as follows. The hit information for a given plane was not used to reconstruct tracks, and only 15-hit tracks were reconstructed. The fraction of times there was a hit within a one wirespacing window of a projected track's intersection with the given plane was computed; this fraction is the given plane's detection efficiency. This method takes into account all equipment effects, including the readout electronics. Efficiencies have been determined for the three separate cathode regions, using low intensity minimum bias data. The reader should be aware that under standard running conditions the beam region is essentially off. Table 3.1 provides a complete list of all MWPC plane efficiencies [34].

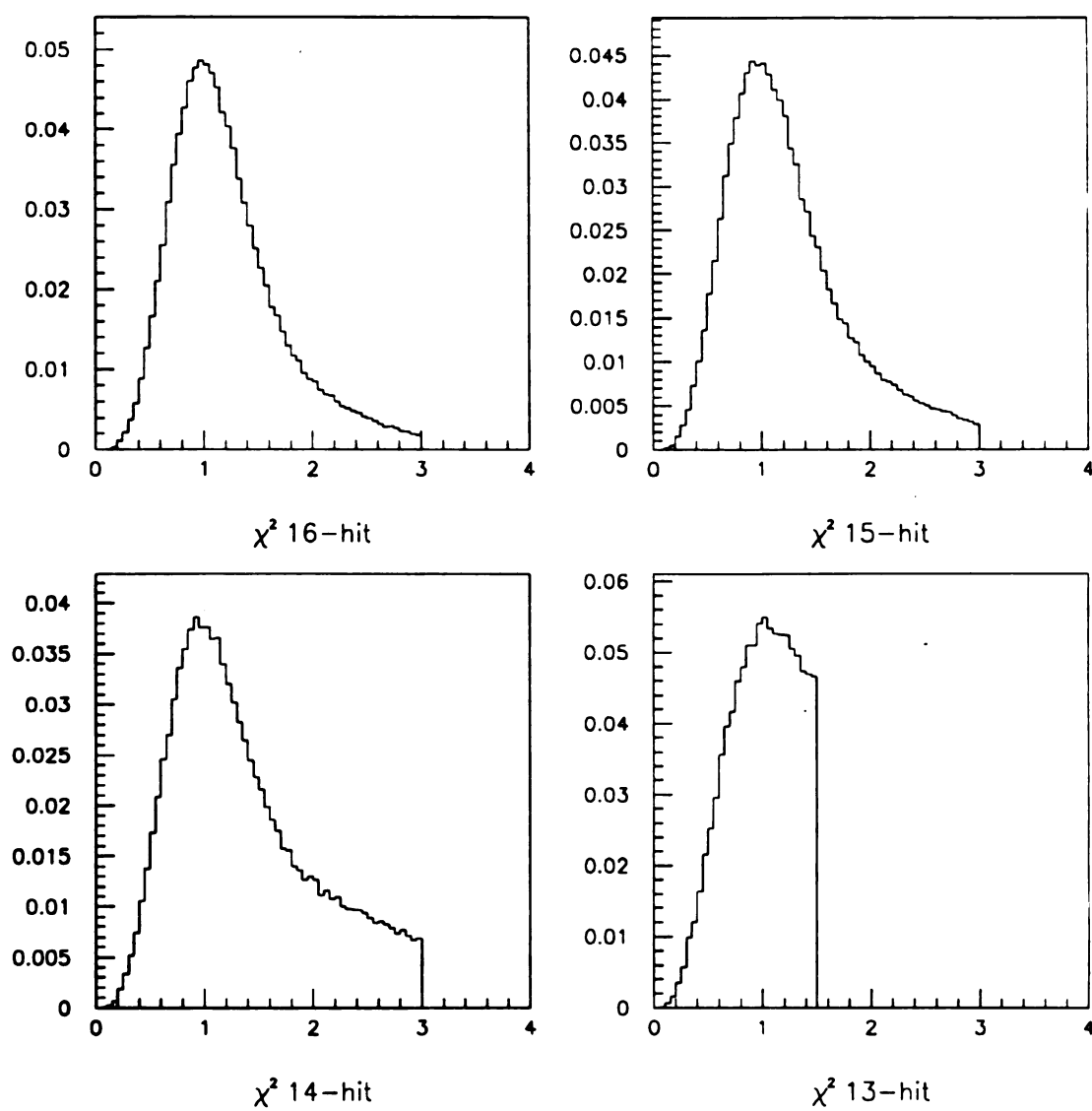


Figure 3.2: The χ^2 distributions for 16, 15, 14, and 13 hit physics tracks

Table 3.1: List of MWPC Plane Efficiencies

Plane	Efficiency	
	Diffraction	Main
1	0.8862	0.9365
2	0.9463	0.9565
3	0.8751	0.9450
4	0.9233	0.9488
5	0.9488	0.9455
6	0.9168	0.9338
7	0.9395	0.9488
8	0.9134	0.9263
9	0.9483	0.9603
10	0.9822	0.9594
11	0.9726	0.9463
12	0.9799	0.9470
13	0.8405	0.9008
14	0.9535	0.9327
15	0.9127	0.8998
16	0.9340	0.9167

3.3.2 Quality of Track Reconstruction

The fraction of fake tracks in the data summary output has been estimated using the data itself. Various distributions have been studied which are sensitive to misreconstructions. From these studies two techniques have been developed for measuring the fraction of fake tracks. These two techniques involve different cuts and track selection criteria, although there is a significant amount of overlap between the two sets. A common assumption for both techniques is that all high quality 16-hit tracks are real. The definition of high quality implies that a given track has a $\chi^2 \leq 1$, a y-view impact parameter, $|b_y|$, of ≤ 1 cm, and is linked in the x-view to an SSD track, belonging to the primary vertex.

The first technique is known as the LAC method because it considers the matching of tracks (or the lack thereof) to showers in the electromagnetic calorimeter. The high quality 16-hit tracks are used to estimate the device's efficiency for detecting charged particles impinging upon it as a function of their momenta. The number of generic tracks, which failed to match with a shower, can then be corrected for those real tracks that failed to match because of inefficiency. The second method utilized the y-view impact parameter distributions for physics tracks that linked in the x-view to a matched vertex. It is known as the b_y technique. The basic idea here is that such physics tracks with high impact parameters are suspect because the linking information indicates they are associated with the primary vertex; a high y-view impact parameter indicates otherwise. Of course, there may be some real tracks in the tails of the b_y distribution due to improper linking. The fraction of such tracks has been estimated by studying the corresponding distribution for the high quality 16-hit tracks, and the tails of the generic b_y distribution have been corrected accordingly. The LAC method used only those tracks with $|y| \leq 0.7$ while the b_y

technique used tracks between ± 1.5 units of rapidity. The reader interested in the exact details of the two methods, and all the selection criteria for the tracks should consult the appendices.

Both techniques have been found to yield consistent results. The LAC method gives a higher estimate for fake tracks than the b_y one, but the variation is also considerably larger and overlaps with the results of the impact parameter study. It appears that the fraction of fake tracks is $\lesssim 1\%$ for $|b_y| \leq 1$ cm and $\lesssim 2\%$ for all impact parameters.

The reconstruction efficiency can be estimated from a study of the relative 16, 15, 14, and 13-hit multiplicity distribution. If the reconstruction program results in miniscule losses, then the shape of such a distribution is governed by the individual planes' efficiencies and the geometric acceptance. A monte carlo study has been done using the output from ISAJET. The charged particles generated by the ISAJET monte carlo are projected through a simulation of the analyzing magnet's field. The altered trajectories are subsequently projected through the MWPC acceptance to determine the number of intersections with active regions of the sense planes. In addition, an intersection with a particular active region is considered to be a "hit" only a certain fraction of the time; this fraction or probability is just the measured efficiency for that active region. The monte carlo result yields a relative multiplicity distribution corresponding to a higher reconstruction efficiency than the data. However, data and monte carlo are close. An effective planes' efficiency has been determined for each data distribution. This efficiency corresponds to a reconstruction efficiency of 96% or better for the data; the monte carlo distribution yields an efficiency of 98%. Again, the reader interested in the details of this analysis, and the exact means by which these two numbers were arrived at should consult the appendices.

3.3.3 Track Quality Cuts

These results indicate that the quality of the track reconstruction is very high. The physics tracks almost always represent an actual charged particle's trajectory in the MWPC system, and only a few trajectories are missed. It can be inferred that the reconstruction program, PLREC, introduces a very small inefficiency and that the pattern recognition is almost always reliable. However, the momentum calculation does rely on the linking of upstream and downstream tracks. In the event that a space track is improperly linked a spurious momentum may be assigned to it. This systematic effect can be overcome by recalculating the track momentum, using only the vertex position and the space track parameters. What one does is project the space track to the magnet's center in the x-view. One then calculates the slope of the segment between the vertex point and the projected point. The difference in slope between this segment and the space track is used to calculate the momentum in the manner dictated by equation 3.17. The expected statistical variation between recalculated and PLREC momenta, δP , is given by the following expression,

$$\delta^2 P = (.002 P_{\text{Recal}}^2)^2 + (.001 P_{\text{PLREC}}^2)^2 \quad (3.18)$$

If the two momenta differ by more than $3\delta P$, the recalculated value is used. Note that the above expression ignores a constant multiple scattering term. Such a contribution is negligible above 5 GeV/c.

This technique has two underlying assumptions. First, the event contains a reconstructed primary vertex, and second, the space track corresponds to a particle produced at the main vertex. All of the data used in this analysis is required to have a primary vertex. The second assumption can be satisfied by applying a selection criterion. Such a cut is indeed necessary for this analysis since only charged hadrons emanating from the primary vertex are of interest.

A set of track quality cuts has been developed for preferentially selecting those MWPC tracks produced by hadrons coming from the vertex, and rejecting those which do not. An additional cut in p_{\perp} of 300 MeV/c selects out the jet candidate tracks, used by the jet reconstruction algorithm. The first cut requires $|y| \leq 1.5$. This cut can be better understood by examining the rapidity distributions of tracks shown in Figure 3.3. This distribution is asymmetric due to the effect of the magnet and the MWPC acceptance. Such an asymmetry will produce a systematic uncertainty in the pseudorapidity, η , distribution of reconstructed jets. A cut of $|y| \leq 1.5$ prevents this. Furthermore, the quality of reconstruction beyond rapidities of 1.5 is compromised by the beam region's inefficiency, and there is a degradation in momentum resolution due to a constant wire spacing.

Because no change in trajectory occurs in the YZ-plane as a particle passes through the analyzing magnet's field, a cut in the y-view impact parameter of the physics tracks will select only those coming from the primary vertex. The b_y distribution of all tracks is shown in Figure 3.4. There is a dominant peak between ± 1.0 cm on top of a fairly flat tail. Therefore, a quality cut of $|b_y| \leq 1.0$ cm is imposed on all charged tracks. The flat tails of the b_y plot contain tracks from strange decays (K^0 s and Λ s), muon halo and fake tracks. All such tracks would not have a correct momentum assigned to them by either method employed by this analysis. The impact parameter cut guarantees that the momentum recalculation is valid within its resolution, and so all tracks satisfying the track quality cuts will have the recalculated momentum assigned to them, if it differs significantly from the value assigned by the reconstruction program.

Finally, the foregoing cuts do not discriminate between electrons and hadrons. Electrons can arise from photon conversions in the target, and by certain heavy quark decays. The decay electrons are effectively removed by the impact parameter cut, but the vast majority arise from photon conversions. A detailed study concerning electron

identification has been carried out [35]. This study resulted in an electron identifying algorithm, which was implemented during the reconstruction pass through the data. Those tracks so identified as being electrons will be removed from the sample satisfying the track quality criteria.

3.3.4 Comparison of Data and Monte Carlo

The data and monte carlo will be compared by studying the rapidity, multiplicity, and momentum distributions of tracks. Separate data distributions have been constructed for all tracks, and those satisfying the track quality cuts. The monte carlo results are superimposed on the data as smooth curves. Since it is the shapes of these distributions that are of interest, all plots have been area-normalized.

The studies of fake tracks and reconstruction inefficiencies, presented earlier, indicate that the track reconstruction code for the MWPC's does not introduce any major systematic effects. Such a result allows for a great simplification to the detector portion of the monte carlo with a great saving in computer time. The monte carlo used for this study takes the ISAJET output for high p_{\perp} π^0 and single photon events and projects the charged particles through a simulation of the analyzing magnet and MWPC system only.

The magnet is assumed to be a simple dipole, and the p_{\perp} "kick" approximation is used. The slight change of slope in the y-view is accounted for also as well as the acceptance at the entry and exit apertures. Tracks that project into the iron yoke are dropped from further consideration. A track is considered to have produced a "hit" in a given MWPC sense plane in the same manner as it was in the study of track reconstruction efficiency. Only the main and diffractive cathode regions are considered active. Those tracks that produce 13 or more "hits" are used to generate the various monte carlo distributions. The reader should be aware that in addition to

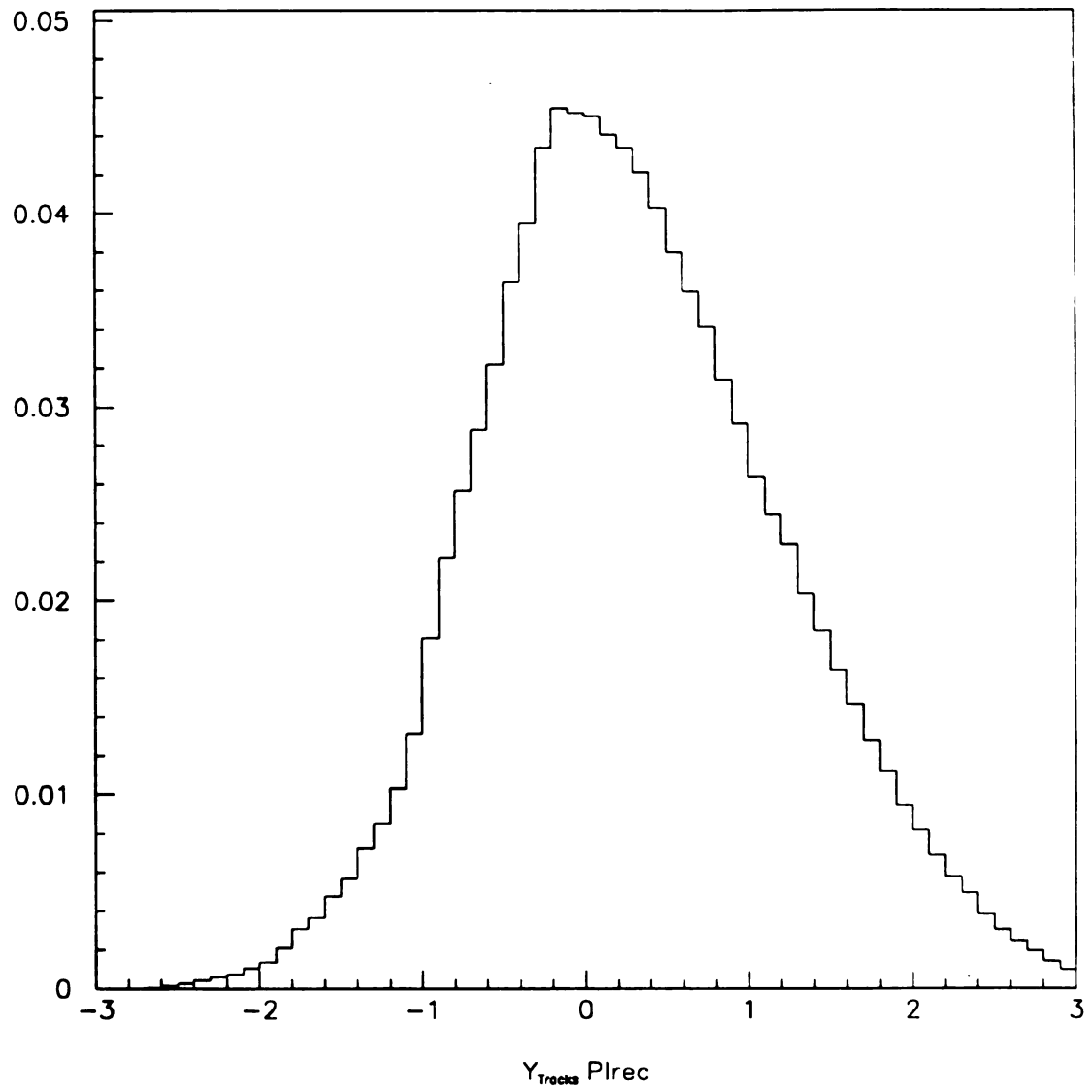


Figure 3.3: Y distribution of tracks

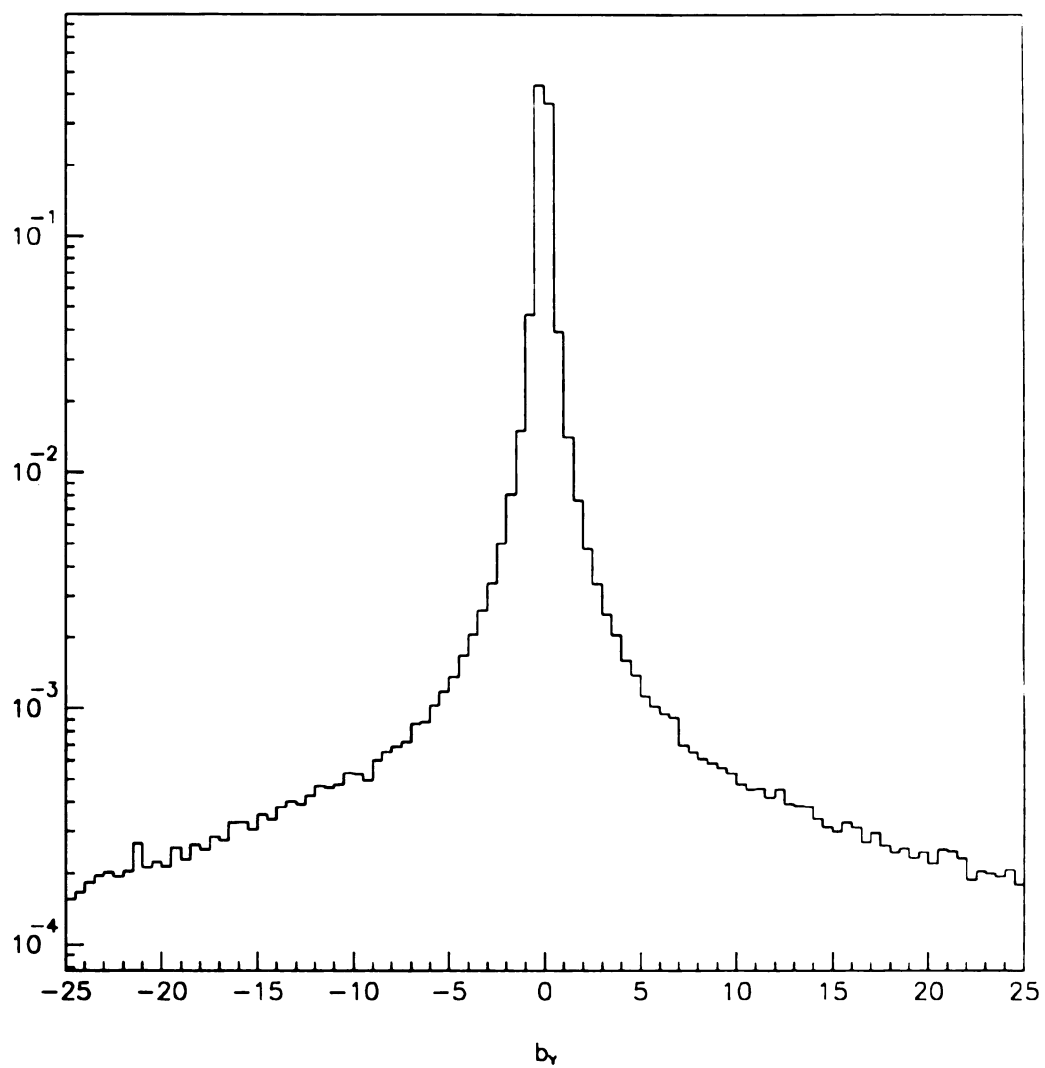


Figure 3.4: Y-view impact parameter distribution of tracks

ignoring PLREC effects this monte carlo does not account for secondary interactions and nuclear rescattering effects.

The rapidity, multiplicity, and momentum distributions are displayed in Figures 3.5 through 3.7 respectively. The rapidity distributions agree very well although the backward acceptance seems to have been underestimated in the monte carlo. Overall, the data possesses higher multiplicity than the monte carlo, and an excess of low momentum tracks. These discrepancies are reduced in the sample of tracks that meet the track quality criteria. Such behavior is expected, indicating the cuts are doing their job. The discrepancy in the rapidity distributions may in fact be due to an excess of low momentum tracks in the data.

A similar study has been carried out for the jet candidate tracks ($p_{\perp} \geq 0.3 \text{ GeV}/c$) with the same trends and discrepancies present. The discrepancies are reduced only slightly over those in the set for which the track quality cuts have been applied. While the observed differences in multiplicity and momentum may be due secondary interactions, nuclear rescattering, and/or prompt strange decays, the fact that they appear in the jet candidate sample with its substantial p_{\perp} cut indicates that the monte carlo fragmentation may be too stiff. Additional evidence is provided by the jet reconstruction efficiency as a function of p_{\perp} , which is presented in Chapter 6. The efficiency is about 10% higher in the monte carlo than real data.

While there are systematic discrepancies between data and monte carlo, they are only at the 10% level. They are not due to PLREC effects. Therefore, the simple monte carlo should suffice for the more sophisticated comparisons and distributions studied in Chapters 5, and 7. In particular, the $\gamma\text{-}\pi^0$ comparison should not be compromised. The $\pi^0 + \text{jet}$ and $\gamma + \text{jet}$ cross sections can be affected, but their ratios should be insensitive to the observed discrepancies. These systematic effects are negligible compared to the statistical uncertainties as shall be seen.

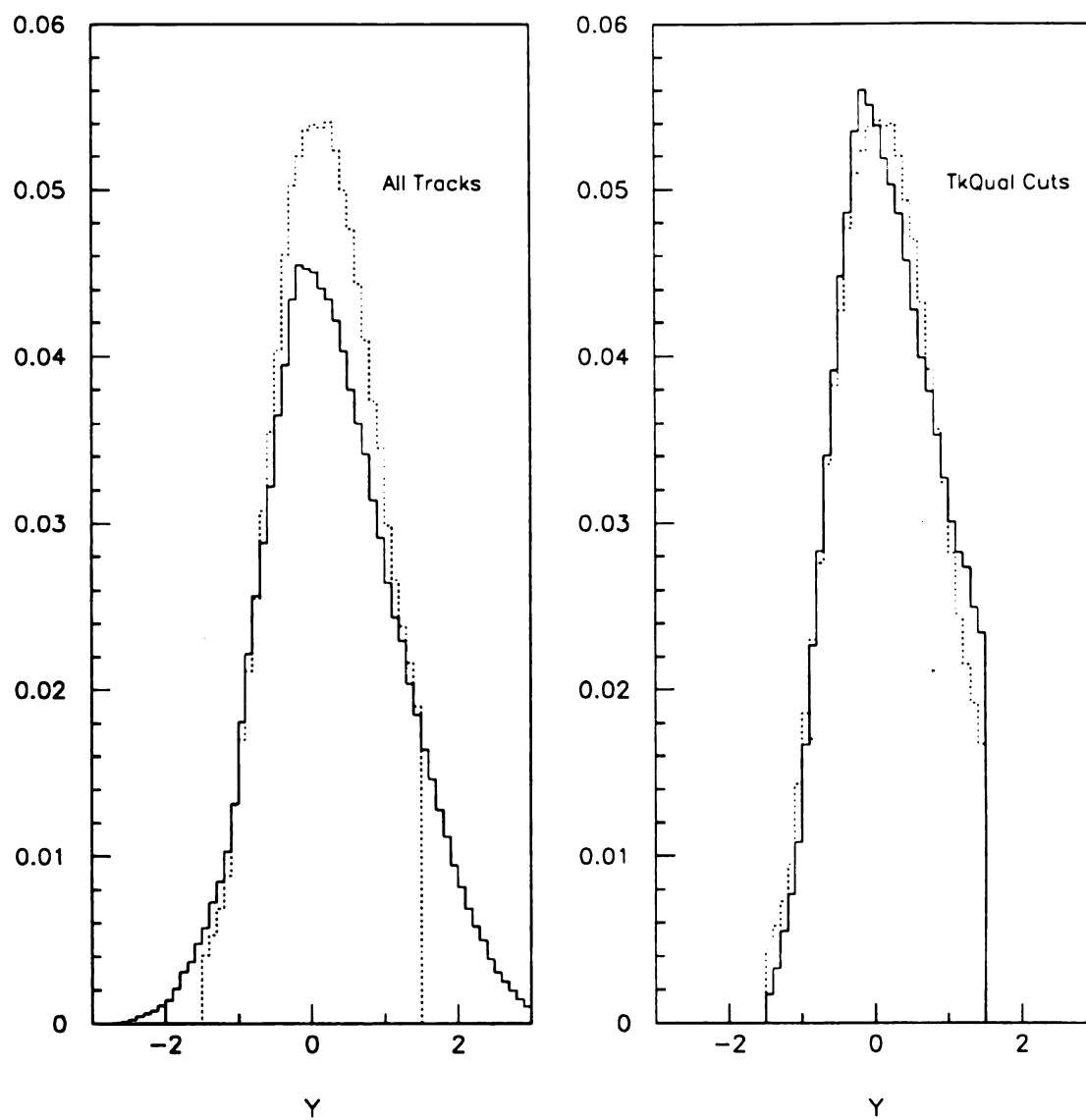


Figure 3.5: Y distributions for all tracks, and tracks passing the track quality cuts. The monte carlo result has been superimposed as a smooth curve.

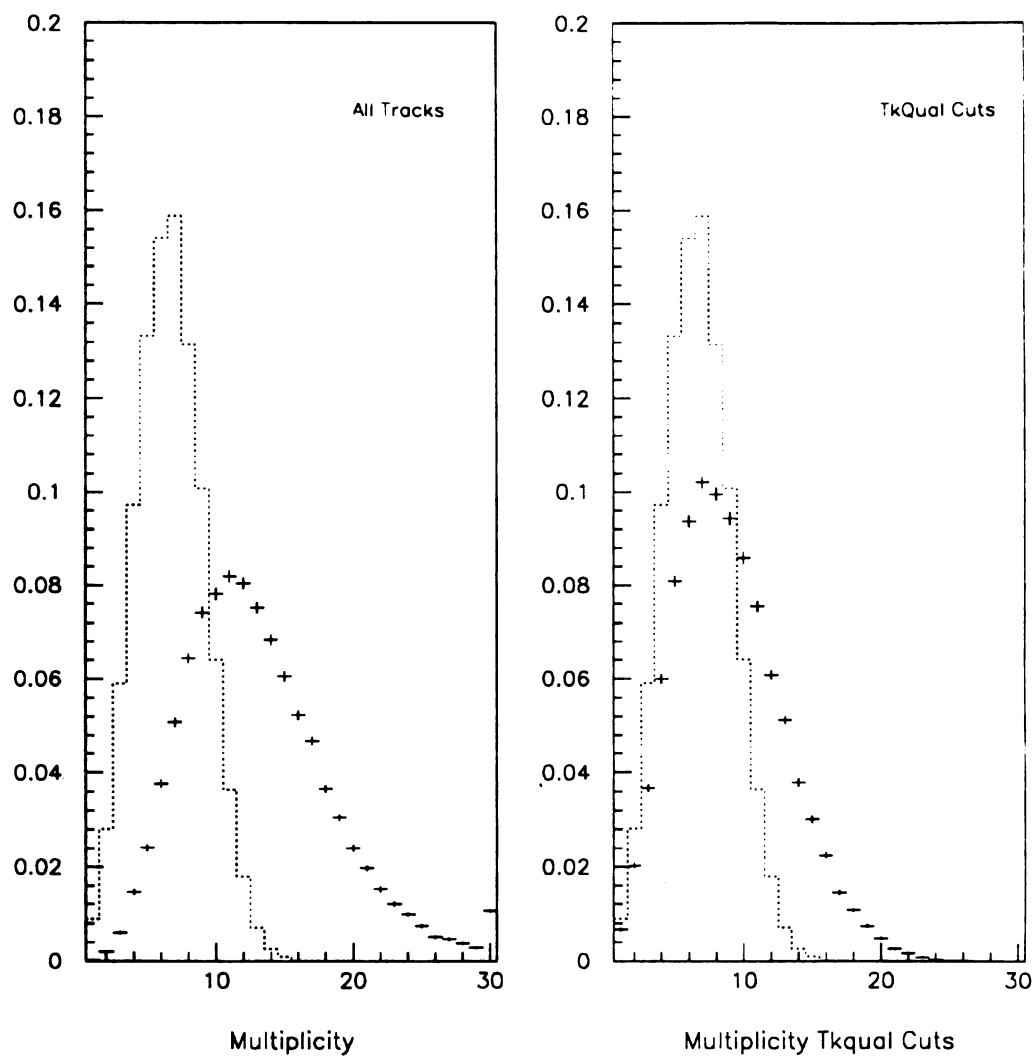


Figure 3.6: Multiplicity distributions for all tracks, and tracks passing the track quality cuts. The monte carlo result has been superimposed as a smooth curve.

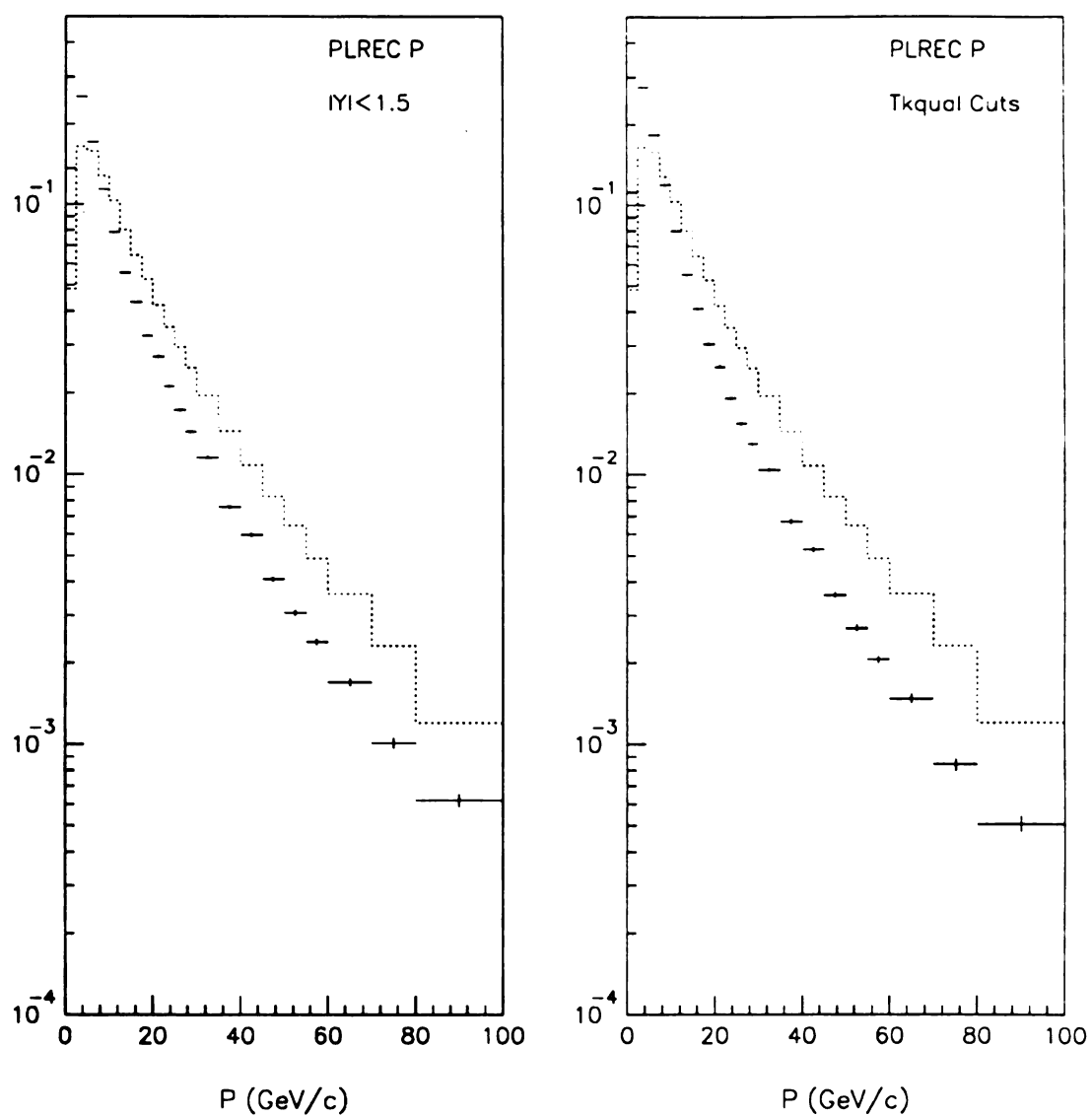


Figure 3.7: Momentum distributions for all tracks, and tracks passing the track quality cuts. The monte carlo result has been superimposed as a smooth curve.

3.4 DISCRETE LOGIC RECONSTRUCTION

The latching of various logic levels took place during the 1987-1988 data taking period. These latched outputs are represented as specific bit patterns in a portion of each event word known as the event header. The offline analysis of these bit patterns has two major purposes. One is to accumulate and interpret the information from those detectors which provided only discrete logic output. The other purpose is to ascertain the types of high level triggers associated with a given event, and to determine whether or not any inconsistencies in the outputs of modules, used to construct the high level trigger, occurred. The following detectors yielded only discrete logic data:

- The veto wall
- The beamline Cerenkov (\hat{C}) counter
- The beam and interaction counters. The accumulated information from these counters provides absolute normalization of cross sections, and live-time estimates.

The interaction counter data included a bit which was set if the clean interaction definition had been satisfied.

All of these counters had their information stored in the Minnesota latch modules. These modules latched data at a clocked rate. Each latched word gets stacked into a buffer, capable of storing up to 255 consecutive words. If a buffer overflowed, only the most recent words with respect to a given pretrigger remained. The clock stopped whenever a trigger signal arrived from the Faraday room, and the buffers were read out. Only the information latched on the 15 clock pulses centered about the interaction time are available to the offline analysis.

The \hat{C} counter's data allows one to know what type of beam particle interacted in the target by determining which differential and anticoincidence counters had fired. The counter configuration is represented by dNM where N and M are the minimum and maximum number of anticoincidence and differential counters, respectively, that fired. For data taken with positive beam the combination d23 indicates a π^+ produced a particular event. Otherwise, one should assume a proton has interacted in the target.

The veto wall data is checked to see if either wall contains a hit. If a hit exists, then the veto wall quadrant possessing the hit is determined. A bit is set whenever a veto wall quadrant, containing a hit, shadows an EMLAC quadrant that produced a trigger. For reasons discussed in the next chapter, all events having this bit set, are cut from the DST level analysis.

An examination of the beam and interaction counter data shows one if the beam and clean interaction definitions used in the online trigger have actually been satisfied. A set of scalers accumulated the beam and interaction signals during each spill. The total beam count, corrected for the fraction of time the detector was incapable of taking data, is used to normalize all cross sections. Scalers also counted how many times the \hat{C} detector satisfied the online d23 requirement.

The EMLAC's trigger logic formed a tree structure with a LeCroy 4508 programmable logic unit (PLU) at each branch point. The 4508 units can latch the input signal configuration upon being strobed. All 4508 units at the pretrigger and higher levels had this feature enabled. Every time an interrupt occurred, these units were read out. The trigger logic can then be analyzed offline to see whether or not the 4508s' logic states were consistent with the logic state corresponding to the high level trigger signal. Besides this diagnostic role, the 4508 data also tells one which octants triggered and what type of trigger they contained.

Chapter 4

Event Selection

The reconstruction of high p_{\perp} γ , π^0 , or η events from the compressed data summary tapes is the subject of this chapter. The selection of events containing high p_{\perp} triggers, and the filtering out of muon induced triggers will be described. A discussion of the cuts pertaining to the direct photon sample, and their systematic effects is presented. The π^0 background to the direct photon signal is also dealt with. However, the analysis of the recoil features and the problem of jet reconstruction are discussed in the next two chapters. The major subsamples of the data used are given in Table 4.1.

4.1 WHOLE EVENT CUTS

Each reconstructed event was subjected to a series of general cuts in order to obtain a sample of enhanced high p_{\perp} events containing a non-muon induced electromagnetic trigger. These cuts are listed below:

- There was no hit in either veto wall corresponding to a trigger quadrant.
- There was a single-local trigger.
- The event contained a matched vertex
- The event contained physics tracks, and reconstructed photons.

The veto wall cut provided an excellent filter for removing muon induced events from the sample. The performance of this device is the subject of the next section. The vertex cut insures that an interaction in the target is associated with the event. This helps cover for inefficiency in the veto wall, and the possibility of upstream

Table 4.1: E706 data divided by beam and target type.

Set	Beam Polarity	Target	Run Interval	Triggers
A	Negative	Cu+Be	2852-3036	786K
B	Positive	Cu+Be	2588-2670	440K
C	Positive	Cu+Be	2387-2586	1225K
D	Negative	Be	2062-2382	1247K
E	Positive	Be	1728-2007	1508K
F	Positive	C	2588-2670	161K

and downstream interactions contributing to the sample. The latter possibility could result in a compromise of the raw data reconstruction.

The single local trigger requirement was necessary for two reasons. First, the events of interest are those containing a high p_{\perp} γ , π^0 , or η so a high threshold trigger from the LAC is necessary. Second, the single-local trigger is the only high-level trigger for which reliable corrections exist. The global triggers experienced problems in their turn on characteristics due to image charging effects, and these effects are still not completely understood. Hence, no corrections exist.

4.2 MUON AND HADRON BACKGROUNDS

The veto wall is sensitive to beam halo particles which penetrate the hadron shield. Clearly, the only particles capable of traversing the shield and forming high p_{\perp} showers in the electromagnetic calorimeter are muons. In this section the efficiency of the veto wall in rejecting muon background is explored. There are actually two veto wall requirements. The online veto wall requirement was part of the trigger. If the same quadrant in both walls had a hit in coincidence with a LAC pretrigger, the event was vetoed. The offline requirement is just the veto wall cut described

above. The offline requirement is necessary because of inefficiency, gaps in the two-wall coincidence, and the fact that the online veto signal window was not centered in time about the pretrigger signal as shall be seen.

Besides the veto wall there are two other ways of identifying muon events. The first one involves studying the directionality of a high p_{\perp} shower in the LAC. The directionality of a shower is defined as follows

$$\delta_r = R_f - \frac{Z_{\text{front}}}{Z_{\text{back}}} R_b \quad (4.1)$$

R_f and R_b are the r coordinates of the shower at the beginning of the front and back sections of the LAC respectively. The quantities

$$Z_{\text{front}} = 900 \text{ cm} \quad (4.2)$$

$$Z_{\text{back}} = 918.5 \text{ cm}$$

are the positions of front and back sections of the LAC along the beam direction relative to the target center. Particles which travel parallel the beamline, i.e. muons, will tend to have larger values of δ_r than those which emanate from the target. In fact, particles coming from the target are expected to have directionalities distributed about zero. This effect is illustrated in Figure 4.1.

In the left half of Figure 4.2 the p_{\perp} distribution of the highest p_{\perp} photon is plotted against its directionality for all events containing a hit in either veto wall quadrant that shadows the trigger quadrant. Two bands of directionality are easily distinguished. The high directionality band dominates the high p_{\perp} spectrum indicating a large muon background. The band of low directionality is centered about $\delta_r = 0$ as is expected for photons originating from interactions in the target. A similar plot appears in the right half of Figure 4.2, but with the requirement that neither veto wall contains a hit in the quadrant corresponding to the LAC trigger quadrant. Very little is left of the high directionality band, while the band corresponding to photons

originating in the target is intact. In fact, the remaining distribution is quite symmetric about $\delta_r = 0$ except at very high p_\perp . Thus, the online veto wall requirement in the trigger should predominately reject muon induced triggers. Imposing an offline veto wall or requirement is necessary in direct photon candidate events because of the high muon background. The loss of true direct photons due to the offline cut can be investigated with high p_\perp π^0 events.

The other quantity of interest is the time at which a shower's energy was deposited in the LAC relative to the time the interaction for a particular event occurred. Muons are expected to have a time distribution that is considerably broader than for showers truly associated with a particular interaction. This is because there is no *a priori* correlation between the muon shower and the interaction which was detected in coincidence with it by the trigger logic. In reality the muon showers are peaked before the interaction due to the online veto wall requirement being shifted such that an event having a LAC pretrigger was vetoed if there was a hit in both walls from $\sim -20\text{ns}$ to 120ns about the interaction time.

The timing information was provided by the TVC circuits described in chapter 2. There were two factors which, unfortunately, hindered the performance of these devices. One, the TVC's were susceptible to firing by high frequency noise, which blocked real signals from being timed. Evidence for this effect occurs in the TVC efficiency curve as a function of energy; the efficiency flattens out at about 90%. The other problem is that the TVC efficiency was lower in earlier runs due to malfunctioning units and threshold problems. A complete description of TVC calibration, and reconstruction of TVC data is given in a thesis [36]. The time distributions for the highest p_\perp photon in each event with and without the offline veto wall hit requirement are shown in Figure 4.3. When there is no hit in the veto wall, a distribution sharply peaked at zero emerges with only a slight forward skew. On the other hand, the time

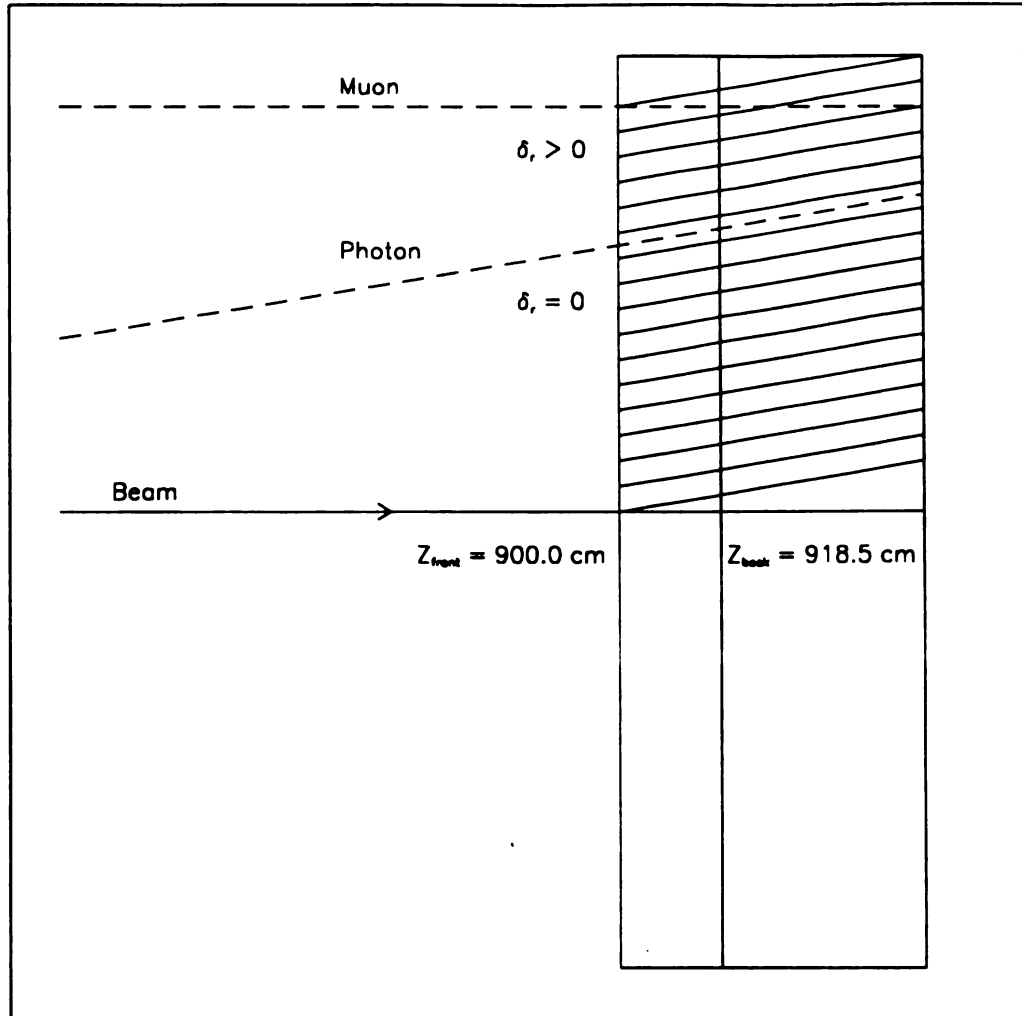


Figure 4.1: Illustration of photon directionality and related quantities. A showering muon from the beam halo will have a larger directionality than a photon emanating from the target.

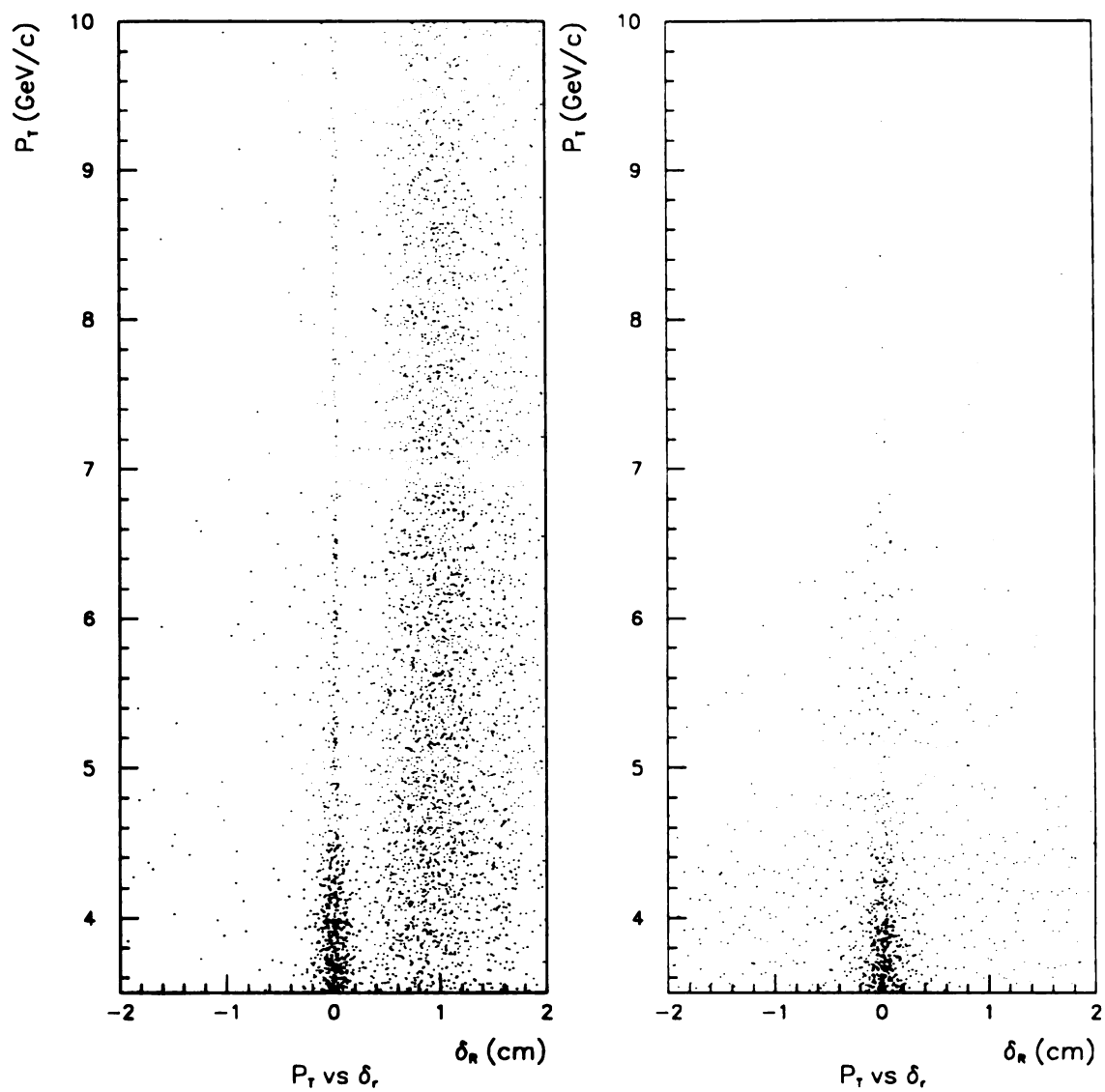


Figure 4.2: Photon p_{\perp} vs directionality for events in which the veto wall quadrant shadowing the trigger quadrant had a hit in either wall (left), and had no hit (right).

distribution without the offline veto requirement is broadly peaked at ~ -40 ns. There is also a large flat tail extending forward in time, which reflects the inefficiency in the online veto requirement. One expects the offline veto to be more efficient and the evidence for this is the much smaller tail in the non- μ induced distribution.

At the top of Figure 4.4 the photon directionality is plotted against the TVC time for events containing a veto wall hit. Two distinct regions of clustering exist. In-time photons strongly populate the low directionality region, while those that are early cluster in the high directionality region. The flat tail of the time distribution, having only the online veto requirement, also has high directionality, indicating the presence of muons missed by the online requirement. The lower plot in Figure 4.4 results when there is no hit in the veto wall. The highly clustered region of in-time photons with good directionality remains with small uncorrelated tails extending vertically and horizontally. The in-time tail extending towards negative directionality is assumed to be entirely due to single photons. The other tails are a mixture of single photons and muons, resulting from TVC inefficiency and ambiguity in directionality on the inner part of the EMLAC. A discussion of the systematic effect of TVC and directionality cuts on the single photon distribution is given in a following section.

The muon cuts are very effective. However, charged and neutral hadrons as well as electrons can also contribute to the direct photon signal. It is imperative to at least ascertain the magnitude of their effect. Two quantities enable discrimination against hadrons. One is the front to total energy ratio of EMLAC showers. The other quantity is the distance of a charged track to a shower as seen by the MWPC system.

A proximity distribution for showers and nearest tracks appears in Figure 4.5 for the hemisphere opposite a high p_{\perp} trigger. There is a very sharp peak for $\Delta r < 2.0$ cm, demonstrating a clear signal for showers produced by charged particles. Figure 4.5 also contains the corresponding distribution for high p_{\perp} photons where directionality and

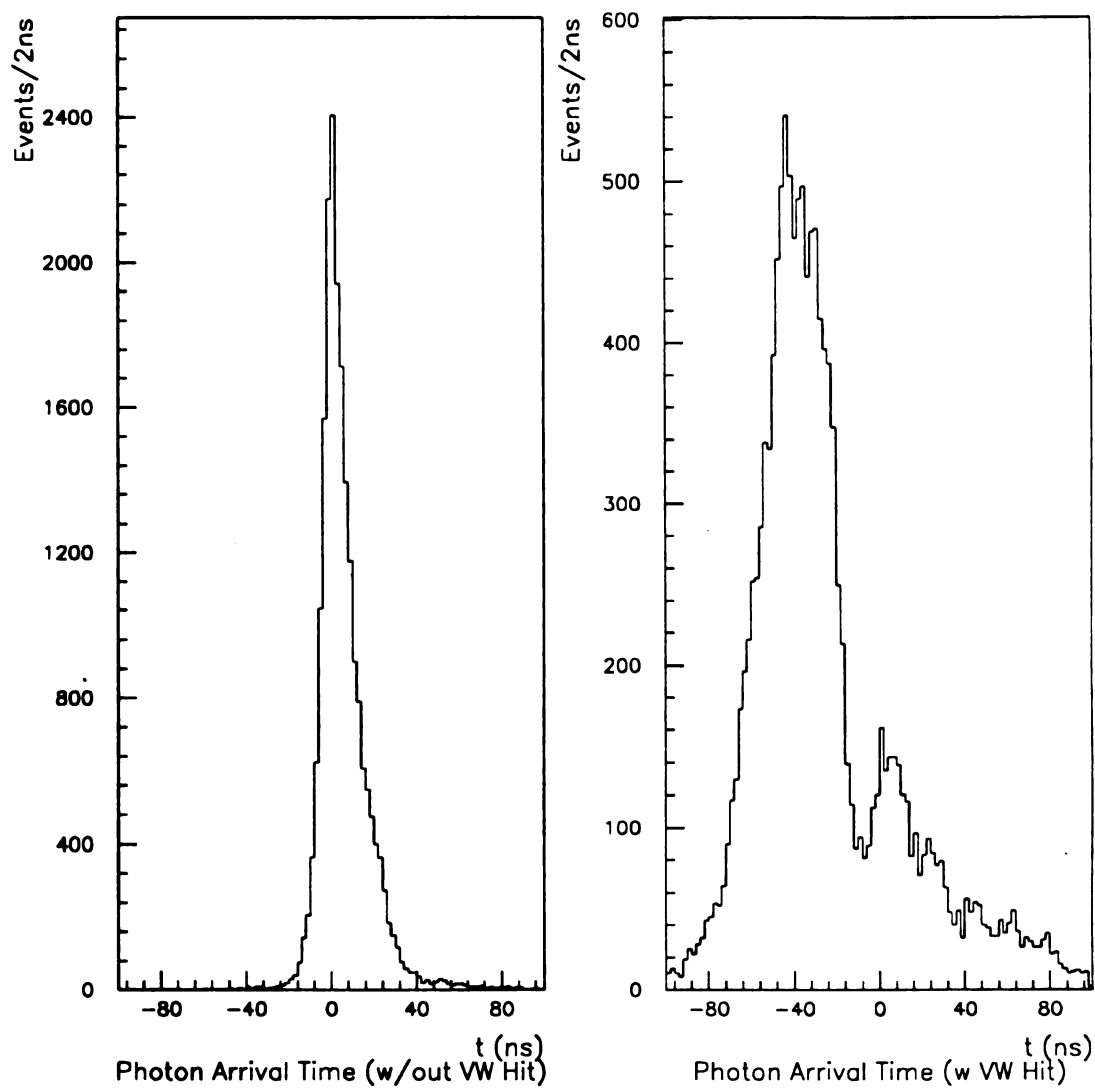


Figure 4.3: TVC distributions for non- μ (left) and μ induced (right) events.

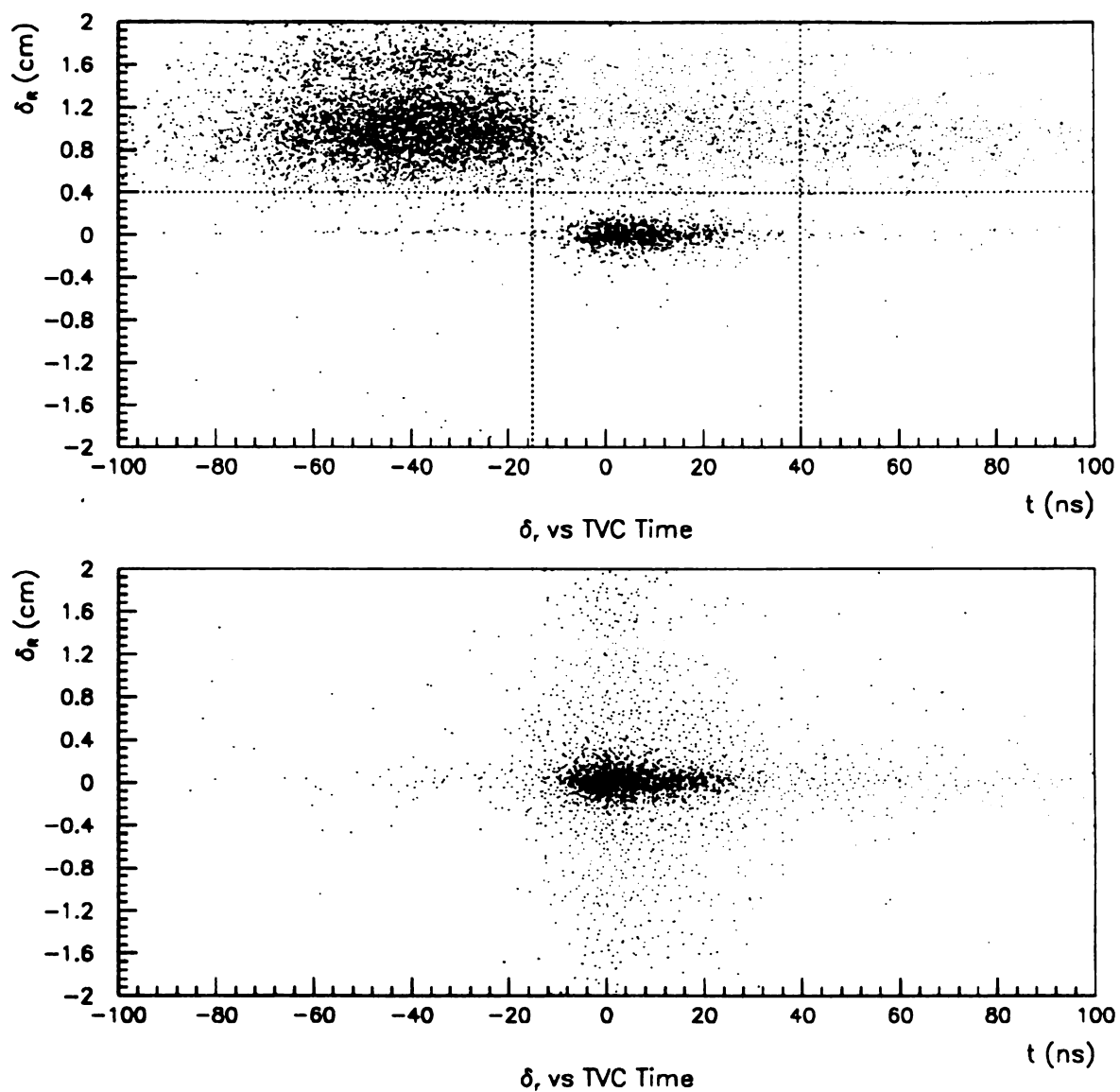


Figure 4.4: δ_r vs TVC time for events with a veto wall hit (top) and without a veto wall hit (bottom). The data in the region outside the vertical lines and above the horizontal line is excluded by the directionality and timing cuts.

timing cuts have been imposed as outlined in Figure 4.4. Again there is a sharp peak at small Δr , but it is narrower than for showers that don't possess a high trigger bias. In addition, we expect direct photons to be more isolated because they can be produced without accompanying hadron fragments. To eliminate the charged hadron background an isolation cut will be imposed on all direct photon candidates.

Generally speaking, showers in the EMLAC can be hadronic or electromagnetic in origin. The electromagnetic showers associated with charged tracks are due to electrons (positrons), generated from π^0 decay photons that have converted in the target. Detailed studies of conversion pairs have been performed, and a method exists for identifying them, using only the charged tracking system. This method relies on the fact that the mass spectrum of conversion pairs peaks sharply at zero since the photon has no rest mass. For this reason a pair of conversion electrons is referred to as a zero-mass-pair or ZMP for short. The reader who is interested in the details of this procedure should consult the thesis by Hartman [37]. The EMLAC's response to electromagnetic energy can be studied quite well with these reconstructed ZMPs.

The front-to-total ratios for showering electrons from conversion pairs are plotted in Figure 4.6. The $E_{\text{front}}/E_{\text{total}}$ distribution for hadron showers is also shown. For the conversion pairs a large peak at high $E_{\text{front}}/E_{\text{total}}$ dominates, and only a small tail extends to 0. The non-conversion plot contains a dominant $E_{\text{front}}/E_{\text{total}}$ peak below about 0.2 with a tail extending to 1.0. Clearly electromagnetic and hadronic showers have very different longitudinal characteristics in the EMLAC. The $E_{\text{front}}/E_{\text{total}}$ plot for photons that are in time and have low directionality appears in Figure 4.7. This distribution is similar to the one for the electrons, possessing only a slight hump at $E_{\text{front}}/E_{\text{total}} \approx 0$. The plot for the muon showers, selected by requiring a veto wall hit, and an out-of-time shower with large directionality, is completely different. The

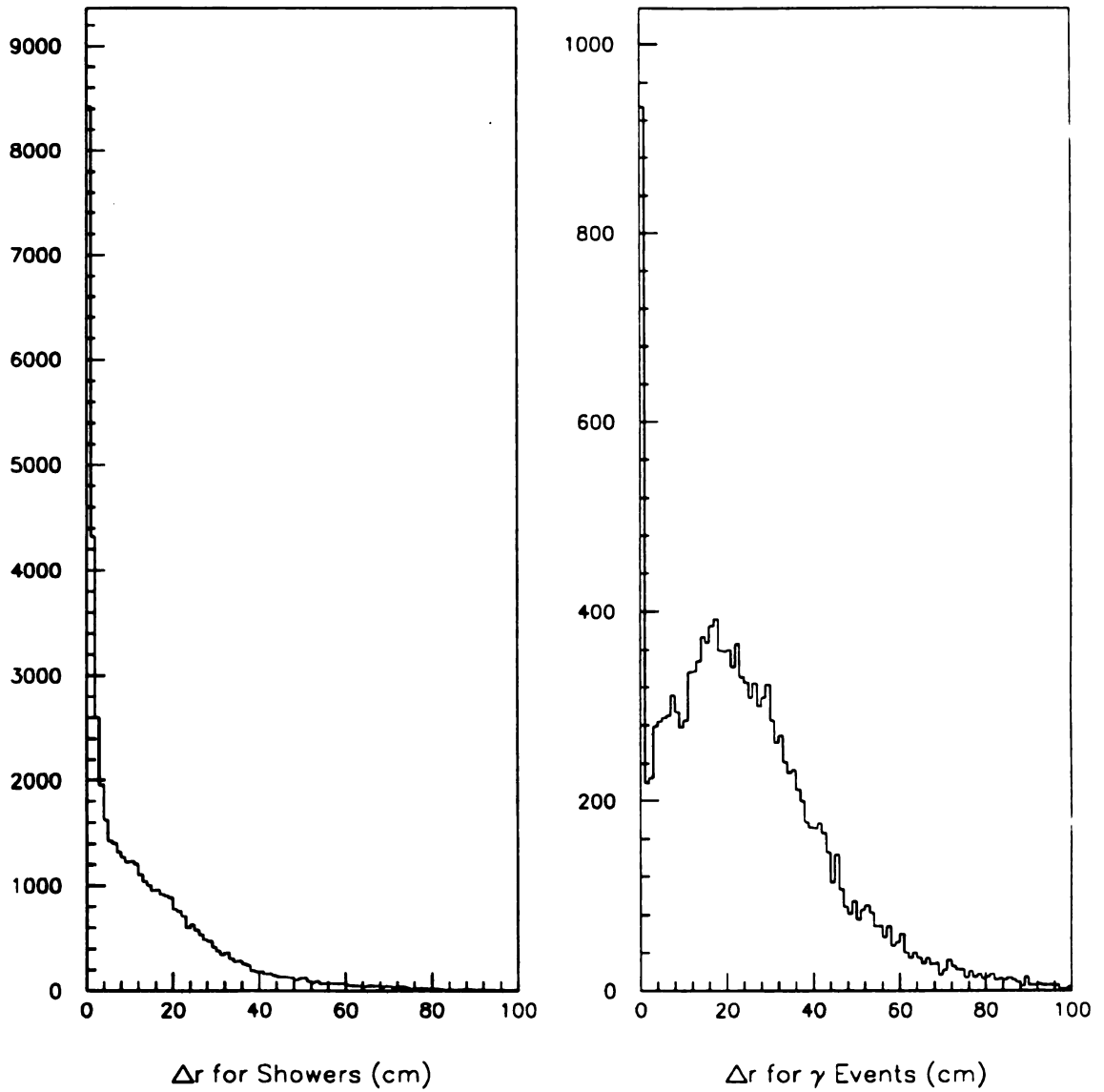


Figure 4.5: Δr between showers and nearest tracks (left);
 Δr between high p_{\perp} photons and nearest tracks
(right)

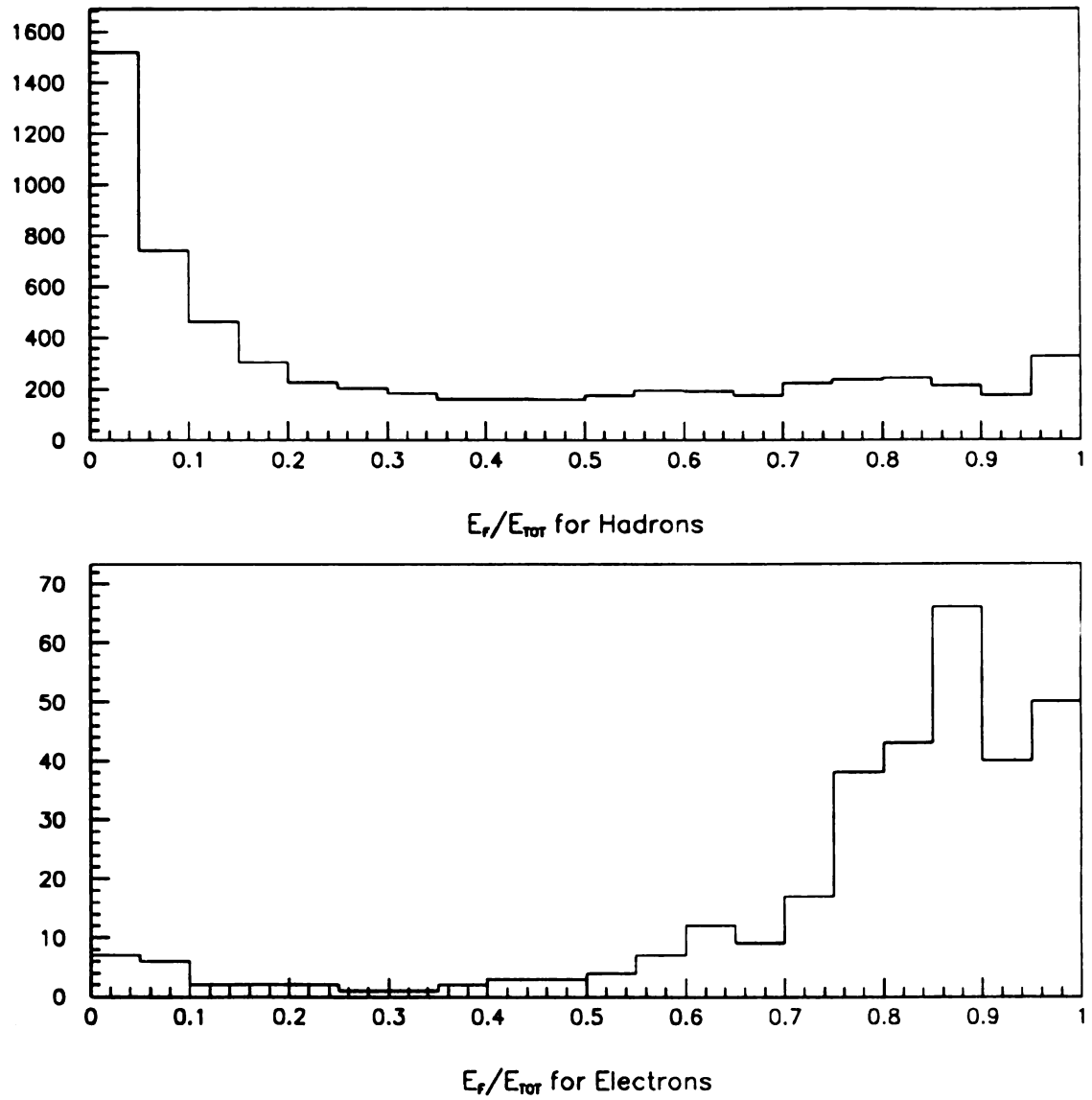


Figure 4.6: E_{front}/E_{total} for Hadron Showers (top) and Electron Showers (bottom).

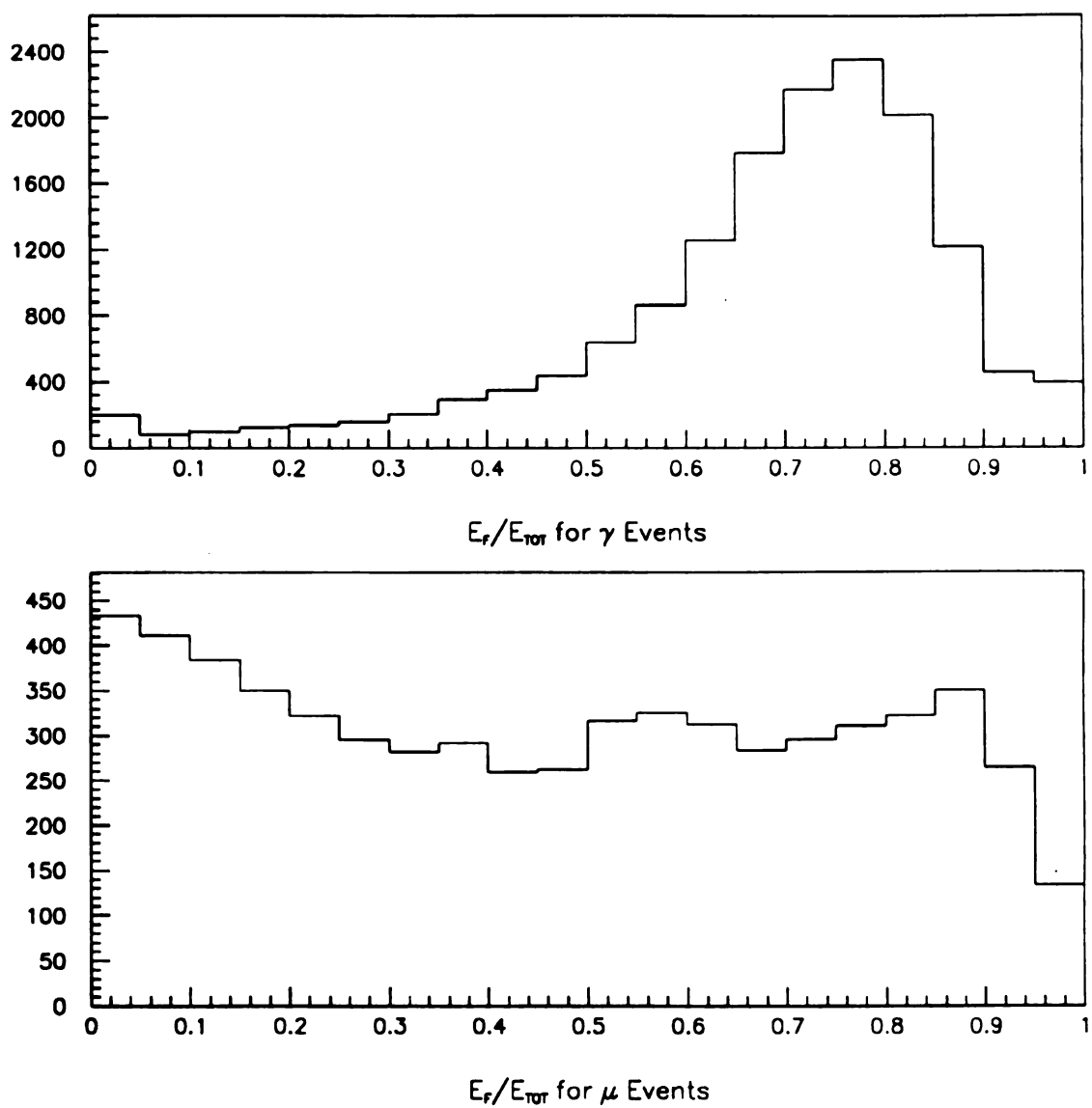


Figure 4.7: $E_{\text{front}}/E_{\text{total}}$ for High p_{\perp} Photon Showers (top) and μ Showers (bottom).

flatness is expected, however, because muons can penetrate considerably into the EMLAC before emitting a hard bremsstrahlung photon. In order to eliminate neutral hadrons and compensate for inefficiencies in the tracking reconstruction, a cut on the $E_{\text{front}}/E_{\text{total}}$ ratio will be imposed on all direct photon candidate events.

4.3 π^0 RECONSTRUCTION

For the highest p_{\perp} trigger octant all 2-photon mass combinations were used to obtain a mass distribution. This distribution is shown in Figure 4.8 for all asymmetries and for asymmetries less than 0.75. Asymmetry is defined as

$$A = \frac{|E_1 - E_2|}{E_1 + E_2} \quad (4.3)$$

where E_1 and E_2 are the energies of each photon. The π^0 and η peaks at ~ 135 MeV and ~ 550 MeV respectively are clearly visible above the combinatorial background. The uncut distribution has a considerably larger low mass region below 110 MeV than the plot with the 0.75 asymmetry cut. In fact, the cut plot has a pretty symmetric background around the π^0 peak. The low mass pairs have been studied extensively [38]. The majority of them are produced from single high energy showers that happen to fluctuate into two showers. The systematic loss of π^0 s due to shower energy fluctuations is very small.

The mass region from 110 – 160 MeV has been designated as the π^0 mass band. An event is labelled a π^0 event if it satisfies the following criteria:

- All whole-event cuts are satisfied
- An octant has a diphoton pair with $110 \text{ MeV} < M_{\text{pair}} < 160 \text{ MeV}$
- The diphoton pair has $A < 0.75$

Similarly, if the diphoton pair has a mass between 500–620 MeV, the event is labelled an η event. Otherwise, the event is considered a direct photon candidate.

The π^0 sideband regions have been designated as 75–100 MeV and 170–195 MeV. These regions are used to estimate the combinatorial background underneath the π^0 peak. Any π^0 distribution i.e. A, Mass, E, is made for the peak and sidebands separately. The sideband distribution is then subtracted from the peak distributions. The π^0 mass has been studied as a function of radius and azimuth in the octants. The sundry distributions show a number of dips in the mass, indicative of energy losses. These losses occur near the various boundaries. Such losses can result from only part of the shower being contained in an active region. They can also arise from the reconstruction program incorrectly splitting showers in multiple peak groups, and/or failing to properly correlate showers between views. For this reason, a set of fiducial cuts have been imposed on all photons used to reconstruct a high p_{\perp} γ , π^0 , or η :

- A photon must have its r coordinate in the interval $24 \text{ cm} \leq R_{\gamma} \leq 138 \text{ cm}$.
- A photon must lie more than 2.0 cm away from any radial boundary of an octant.

The asymmetry distributions for π^0 s with and without sideband subtraction are displayed in Figure 4.9. There is no asymmetry cut so that the roll-off at high asymmetry can be observed. Ideally, one expects a flat asymmetry distribution because the π^0 is a spin 0 particle undergoing a two-body decay to photons. In the rest frame of the π^0 the photons emerge back-to-back isotropically. Consequently, the A distribution should be flat in any frame for which the motion of the π^0 is very relativistic. However, the plots of Figure 4.9 are fairly flat out to .75 after which significant losses of π^0 s occur with increasing A. Such behaviour is due to the increasing inefficiency of the LAC for photon energies below 10 GeV. This is the reason for the .75 A cut on reconstructed π^0 s. All 2γ masses above .75 A are classified as direct photon candi-

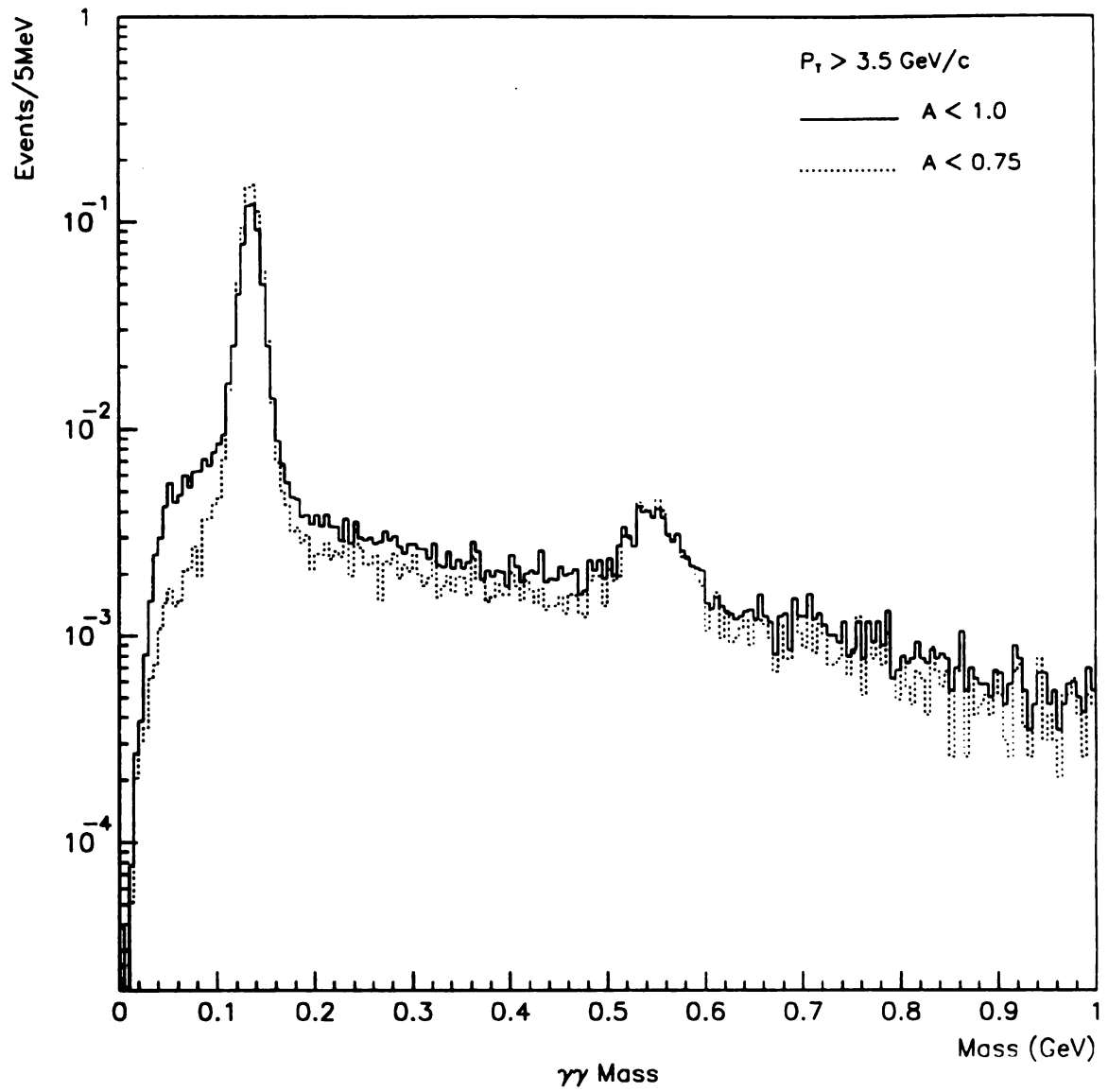


Figure 4.8: $\gamma\gamma$ Mass Spectrum

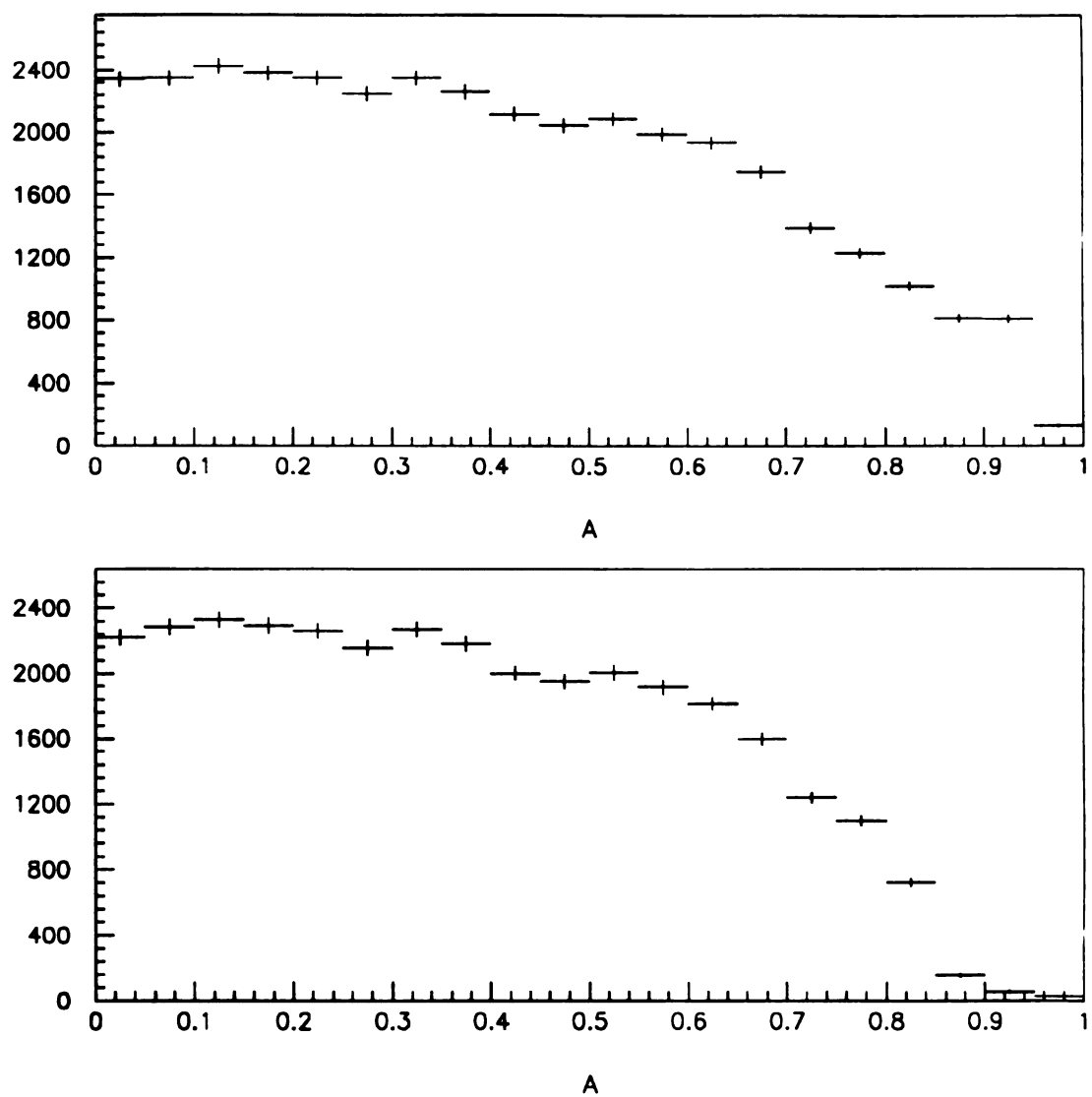


Figure 4.9: Asymmetry distributions for π^0 s without sidebands subtracted (top) and with sidebands subtracted (bottom).

dates if the highest p_{\perp} photon passes all other direct photon criterion. It is these π^0 s with $A > 0.75$ that are the source of direct photon background after cuts.

4.4 SINGLE PHOTON RECONSTRUCTION

An event is classified as a direct photon event if it meets the following conditions:

- All whole event cuts were satisfied.
- No diphoton pair formed a mass in the π^0 or η mass bands
- The highest p_{\perp} photon had $\delta_r < 0.4\text{cm}$
- If timing information was available, then $-15\text{ns} < \text{TVC}_{\text{time}} < 40\text{ns}$
- There was no charged track within 1.0 cm of the highest p_{\perp} shower
- $E_{\text{front}}/E_{\text{total}} > 0.2$

The octant multiplicity distribution for the single photon sample shows that about 30% of the events have more than one photon in the octant, containing the reconstructed single photon. This indicates that π^0 s, which decayed asymmetrically, are present. However, even the events with only one photon contain π^0 background from decays in which a photon was lost due to acceptance or inefficiency.

4.5 SYSTEMATICS

Both the whole event cuts and the single photon cuts resulted in losses of reconstructed γ , π^0 , or η that must be accounted for. The π^0 s are affected only by the whole event cuts. The direct photon candidates also have to be corrected for timing, directionality, track isolation, and $E_{\text{front}}/E_{\text{total}}$ losses. Furthermore, the direct photon

events must in principle be corrected for residual muon background. However, studies indicate that this background is consistent with zero, given the available statistics [39]. Table 4.2 summarizes the corrections for the whole event and muon cuts.

Besides correcting for cuts, corrections must also be applied to compensate for trigger inefficiency, reconstruction losses, and conversions of high p_{\perp} photons in the target material. The correction for reconstruction inefficiency is different for π^0 s and single photons because π^0 s are also affected by geometric acceptance losses as well. Studies have been done to determine these corrections, and routines exist in the library of data summary programs to compute them on an event-by-event basis. The analysis presented in the following chapters utilizes these standard routines in making the various corrections as they are currently available.

There is still one very important correction, which is critical in obtaining absolute cross sections. This is the correction to individual photon energies that takes into account the electromagnetic calorimeter's response (energy scale), and the energy loss due to the three radiation lengths of material in front of the detector. This energy correction is critical because the cross sections fall steeply with p_{\perp} . This systematic uncertainty must be known to better than 1% if the cross sections are to be known to better than 10%. The localization of shower energies in liquid argon sampling calorimeters, and the ionization mechanism's stability makes these device capable of such precision. It is thus imperative to understand the energy loss in the material between the vertex and the calorimeter. Studies have been done using the ZMP's reconstructed from the tracking system to determine the photon energy correction. The correction is also available in the data summary library, and has been used in the following analysis. If the reader is interested in the details of how all the corrections were obtained, he will find a summary of them in an appendix.

Table 4.2: Corrections for whole event cuts, and cuts for single photons.

Cut	Correction	
	Negative Beam	Positive Beam
Veto Wall	$1.111 \pm .033$	$1.099 \pm .006$
Vertex	$\epsilon_{\text{vertex}} = 1.0019 - 0.0079 \times V_z$	
Track Isol.	$1.043 \pm .002$	
Timing	$1.034 \pm .004$	
Directionality	$1.005 \pm .001$	
$E_{\text{front}}/E_{\text{total}}$	$1.015 \pm .001$	
C_{cuts}^γ (total correction)	$1.230 \pm .007$	$1.216 \pm .009$

4.6 π^0 BACKGROUND CALCULATION

After muons the major source of direct photon background is the decay products of highly asymmetric π^0 s. Because of the asymmetry cut of 0.75 on reconstructed π^0 s, 25% of all triggering π^0 s could contribute. The p_\perp distribution of fake direct photons has to be calculated, and for this task a monte carlo program was developed.

The monte carlo used events from the DST stream as input. The input set consisted of all events with a high p_\perp diphoton pair in the mass range 0 – 175 MeV. The diphoton pair must have sufficient p_\perp so that a reliable trigger correction exists, and each member of the pair must reside in the same octant. However, no asymmetry cut is applied to the pair of photons. All of the extra photons in the octant containing the high p_\perp pair are also included. Relaxing the mass and asymmetry cuts on the π^0 candidates allows the simulated energy fluctuations to reproduce the actual 2γ mass spectrum obtained from the data. This provides yet another check on the monte carlo.

Each event is processed through a GEANT simulation of the detector a total of 5 times. On each successive generation the entire event is rotated by $\pi/4$ into a neighboring octant. Since the π^0 decay is uncorrelated with the underlying event topology, the π^0 is redecayed with a new asymmetry and rotation of the decay photons about the direction of motion on each generation. The simulated raw data is then processed by EMREC and a binary DST output file is written. The monte carlo DST is then processed by the high level reconstructor and the p_\perp distributions of π^0 s and fake direct photons are generated. Each entry in these distributions is corrected by the event weight of the corresponding input event and the acceptance, reconstruction, and conversion weights corresponding to the generated event. The quotient distribution yields a set of numbers in p_\perp which are used to correct the direct photon p_\perp distribution. The bin contents of the quotient distribution are the so called f_γ numbers in p_\perp . These numbers have been computed separately for the proton and π^- data sets. Although the f_γ numbers from both sets are statistically consistent, the ensuing analysis will use the set of f_γ numbers that corresponds to the beam type used to generate a specific data set. Table 4.3 gives the fake gamma, f_γ , numbers for both types of beam together with their uncertainties.

While the background from asymmetric π^0 decays is dominant, there are measurable contributions from η , η' , and ω decays into two photons. The calculation of these contributions to the direct photon background was performed in the same manner as for π^0 s. The same input data was used in each case, but the η , η' , or ω mass was assigned to the diphoton pair instead before redecaying it. In addition, these events had an additional weight factor assigned to them, which accounts for their respective production rate and branching ratio relative to π^0 s. The relative production rate for η s was obtained from the world data. The world data is consistent with an η/π^0 ratio of 0.45. Based on results for the relative rate of high p_\perp K to π production [40], the other relative production rates were assumed to be the same as for the η .

Table 4.3: False γ fractions in p_{\perp} for proton and π^{-} beams.

p_{\perp} (GeV/c)	f_{gam} Numbers	
	Proton Beam	π^{-} Beam
4.375	$.169 \pm .006$	$.192 \pm .006$
4.625	$.162 \pm .006$	$.185 \pm .006$
4.875	$.156 \pm .006$	$.178 \pm .006$
5.250	$.146 \pm .006$	$.166 \pm .007$
5.750	$.133 \pm .008$	$.152 \pm .008$
6.500	$.113 \pm .011$	$.129 \pm .010$
7.500	$.087 \pm .016$	$.099 \pm .013$
9.000	$.048 \pm .023$	$.055 \pm .018$

Chapter 5

Event Features

Attention is now turned to the charged particle structure of high p_{\perp} π^0 and single γ events. The distributions of charged particles in both the recoil and same-side hemispheres will be examined. One purpose of this study is to determine if there are any differences between high p_{\perp} single γ candidates and π^0 events. Another purpose is to demonstrate the existence of jet structure in the recoil hemisphere. The results presented in this chapter are qualitative in nature. Nevertheless, it will be shown that a direct photon signal exists in the data without the application of a π^0 background subtraction, but employing all of the selection criteria described in the previous chapter. The existence of dynamical correlations among the recoil charged particles will also be investigated.

5.1 DIFFERENCES BETWEEN γ S AND π^0 S

The azimuthal distributions of charged particles with respect to the trigger axis have been used to find differences in the overall features of π^0 and single γ events. Sets of distributions have been made for different trigger p_{\perp} intervals. These intervals are $5.0 \leq p_{\perp} < 5.5 \text{ GeV}/c$, and $p_{\perp} \geq 5.5 \text{ GeV}/c$. The only cuts made on the charged particles, besides the general track quality cuts discussed in chapter 3, were p_{\perp} cuts and a rapidity cut of $|y| < 0.7$. The rapidity cut was intended to cut down on the background from spectator jet fragments. The spectator fragments emerge in narrow cones about the beam axis, the particle density having an $\exp^{-6p_{\perp}}$ dependence. This cut should not compromise the comparison of γ and π^0 events.

Sets of plots were made for each of the following p_{\perp} intervals: $p_{\perp}(\text{tracks}) > 0.05 \text{ GeV}/c$, $p_{\perp}(\text{tracks}) > 0.3 \text{ GeV}/c$, $p_{\perp}(\text{tracks}) > 0.5 \text{ GeV}/c$, and $p_{\perp}(\text{tracks}) >$

0.75 GeV/c. This was done in order to minimize the spectator jet background. The particles emanating from the hard scatter should be enhanced in p_{\perp} while those produced by the other “soft” part of the interaction should be strongly suppressed with respect to this variable. More importantly, however, was to check the stability of any observed trend in the ϕ distributions as a function of p_{\perp} . The plots presented here correspond to the 0.3 GeV/c p_{\perp} cut. The features appearing in this data set are present in all of the others as well.

The azimuthal plots have been constructed over the interval $0 \leq \phi \leq \pi$. If the $\Delta\phi$ value computed for a track fell outside this interval, it was transformed into the corresponding value lying within the interval. All plots have been normalized to the corresponding number of π^0 or single γ triggers. The corresponding plots for proton and π^- beam appear in the same figure. The γ and π^0 distributions for the same data set and cuts appear superimposed in the same plot to facilitate the comparison.

Three different types of azimuthal distributions have been constructed. First, there are the simple number density distribution of charged particles about the trigger axis. These are shown in Figures 5.1 and 5.2. The π^- beam data gives reveals an unambiguous difference between single photons and π^0 s for $p_{\perp} \geq 5.5$ GeV/c. Here the photons appear more isolated within the trigger hemisphere than do the π^0 s. Such an effect is expected since direct photons are produced in lowest order with no accompanying hadrons whereas high p_{\perp} π^0 s are just one of several hadrons resulting from the hadronization of the hard-scattered parton in the trigger hemisphere. The proton data shows a similar trend in both p_{\perp} intervals, but it isn't as significant.

Another type of ϕ distribution is one in which each entry is weighted by the p_{\perp} of the corresponding track. Such a weighting has a sensitivity to jet structure in so far as jet particles tend to have more p_{\perp} than non-jet particles. The p_{\perp} weighted plots appear in Figures 5.3 and 5.4. Again the π^- data shows the γ s as being definitely more isolated than the π^0 s for $p_{\perp} \geq 5.5$ GeV/c. In addition, the same trend appears

for the lower p_{\perp} interval although it is confined to the bin closest to the trigger particle. The proton data follows a trend consistent with the direct photons being isolated but again it is not very significant statistically.

A third type of distribution arises by weighting the entries by the quantity q_{\perp} defined as follows,

$$\begin{aligned} q_{\perp} &= \frac{p_{\perp}(\text{track}) \cdot p_{\perp}(\text{trigger})}{p_{\perp}^2(\text{trigger})} \\ &= \frac{p_{\perp}(\text{track})}{p_{\perp}(\text{trigger})} \cos \Delta\phi \end{aligned} \quad (5.1)$$

This quantity is similar to a p_{\perp} weighting, but it also takes into account the expected spatial orientation of the jet in azimuth. Such a weighting is useful in conjunction with a p_{\perp} weighting since systematic effects due to misreconstruction of track momenta enter differently. Consistency with the p_{\perp} weighted plots indicates that this systematic effect is not determining the observed features. The q_{\perp} weighted plots are shown in Figures 5.5 and 5.6. They display the same trends observed in the p_{\perp} weighted distributions.

In summary all of the π^{-} distributions show a clear and consistent difference between γ s and π^0 s above 5.5 GeV/c in p_{\perp} . The p_{\perp} and q_{\perp} weighted plots show the isolation of direct photons at lower p_{\perp} but the ϕ density distributions do not. The trends in the proton data are consistent with this observed difference, but have little statistical significance. This could be due to a greater relative amount of background from π^0 and η decays in the reconstructed photon sample than is present in the negative data. Such an effect is expected from naive QCD considerations. There are two direct photon production mechanisms in π^{-} data, but only one in proton. While the annihilation process can contribute to high p_{\perp} π^0 production in the negative data as well, it makes a much smaller relative contribution because the overall number of contributing subprocesses is much larger than for direct photons. Finally, a set of ϕ

distributions was made for $4.5 \leq p_{\perp} < 5.0 \text{ GeV}/c$. No differences between γ s and π^0 s were observed.

Besides finding a difference between reconstructed photon and π^0 events in at least some portion of the data, all of the azimuthal distributions show a dominant peak opposite the trigger. This peak begins near $2\pi/3$ away from the trigger particle and has its maximum at π . Furthermore, these ϕ plots possess only two peaks; a dominant peak at π and a small bump about the trigger particle's direction. Such behavior is consistent with a 2-body hard scattering among pointlike constituents, *i.e.* partons. This recoil feature will be utilized in the following chapters to ascertain the direction of the jet recoiling from either a high p_{\perp} π^0 or single photon. Similar analyses of charged particles associated with single high p_{\perp} particle production have been done at the ISR [41].

5.2 RAPIDITY CORRELATIONS

The azimuthal distributions showed a very strong clustering of particles opposite the trigger in the plane transverse to the beam. If jets indeed exist, then correlations should also exist in the plane defined by the beam axis and the transverse axis of the hard scatter. Orientation in this plane can be measured as a function of $\cos \theta$ where θ is the polar angle. However, a more desirable quantity is the rapidity, y . A particle's rapidity has very simple Lorentz transformation properties along the z -axis. In addition, differences in the rapidities of a pair of particles are invariant under Lorentz boosts parallel to the beam direction. Δy distributions are the same whether they are constructed in the lab frame, the beam-target cm frame, or the rest frame of the colliding partons.

The difference in rapidity between recoiling charged particles will be used to see whether or not they are dynamically correlated. If this experiment is sensitive to jet structure, then one would expect the highest p_{\perp} charged particles to cluster together

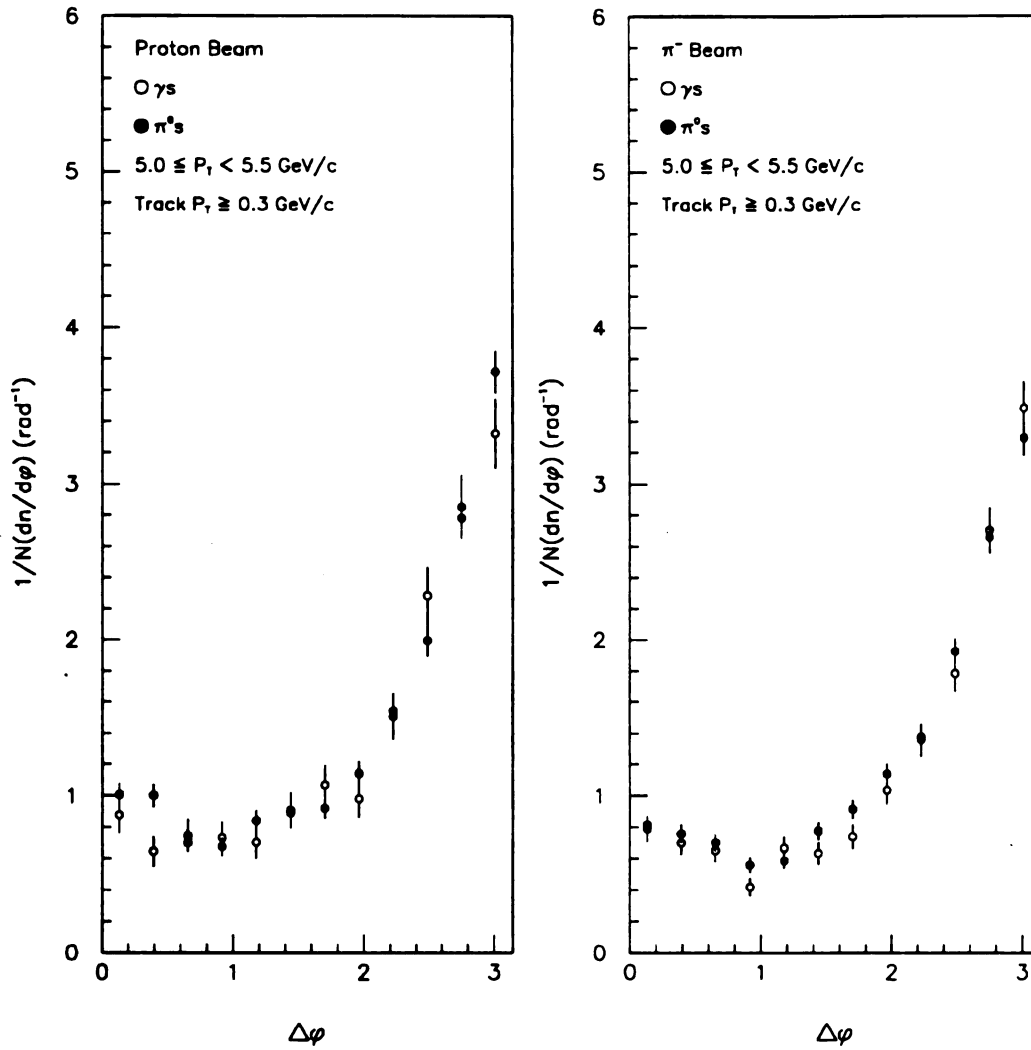


Figure 5.1: ϕ density distributions for charged particles in high p_{\perp} π^0 and single photon events with $5.0 \leq p_{\perp} < 5.5$ GeV/c.

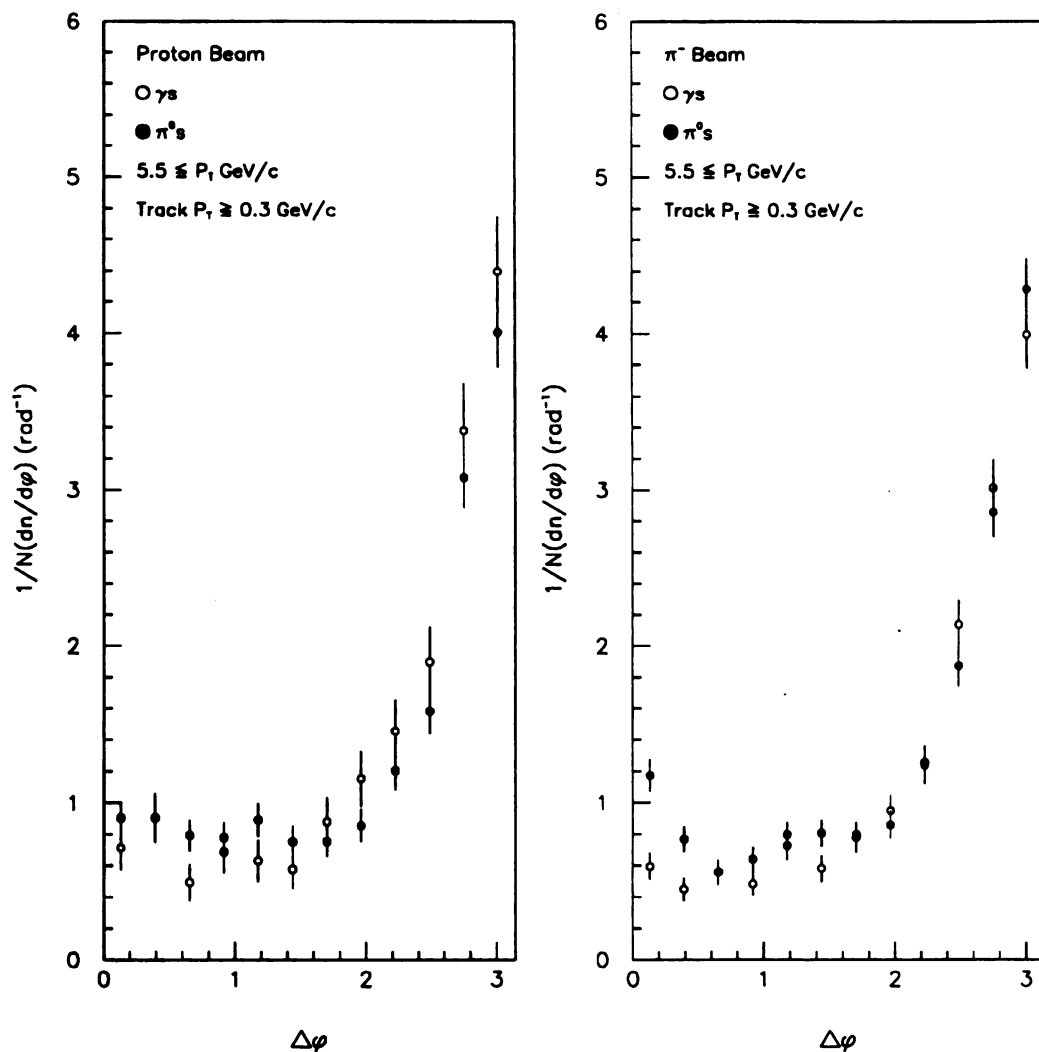


Figure 5.2: ϕ density distributions for charged particles in high p_{\perp} π^0 and single photon events with $p_{\perp} \geq 5.5$ GeV/c.

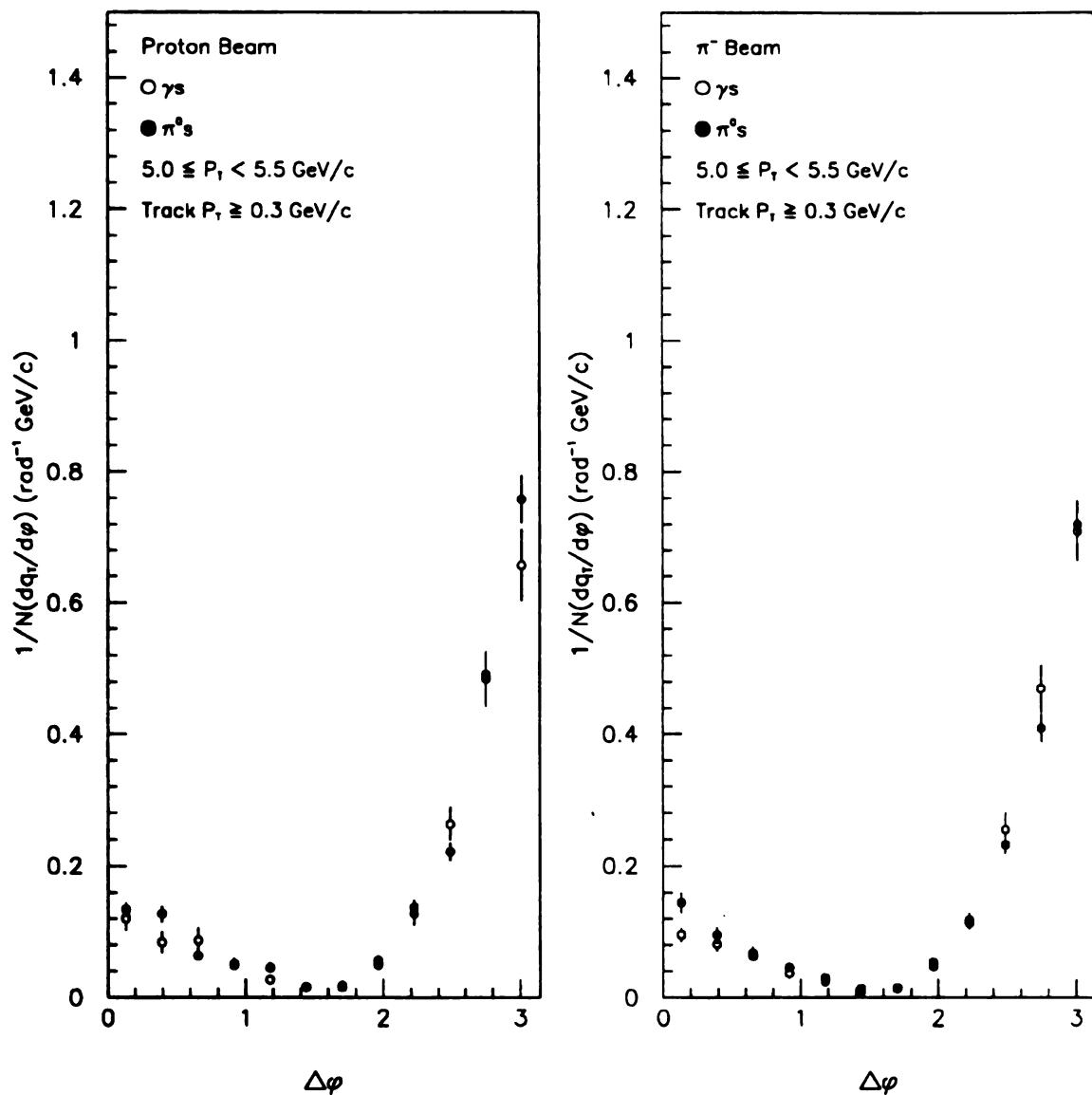


Figure 5.3: q_\perp weighted ϕ distributions for charged particles in high p_\perp π^0 and single photon events with $5.0 \leq p_\perp < 5.5 \text{ GeV/c}$

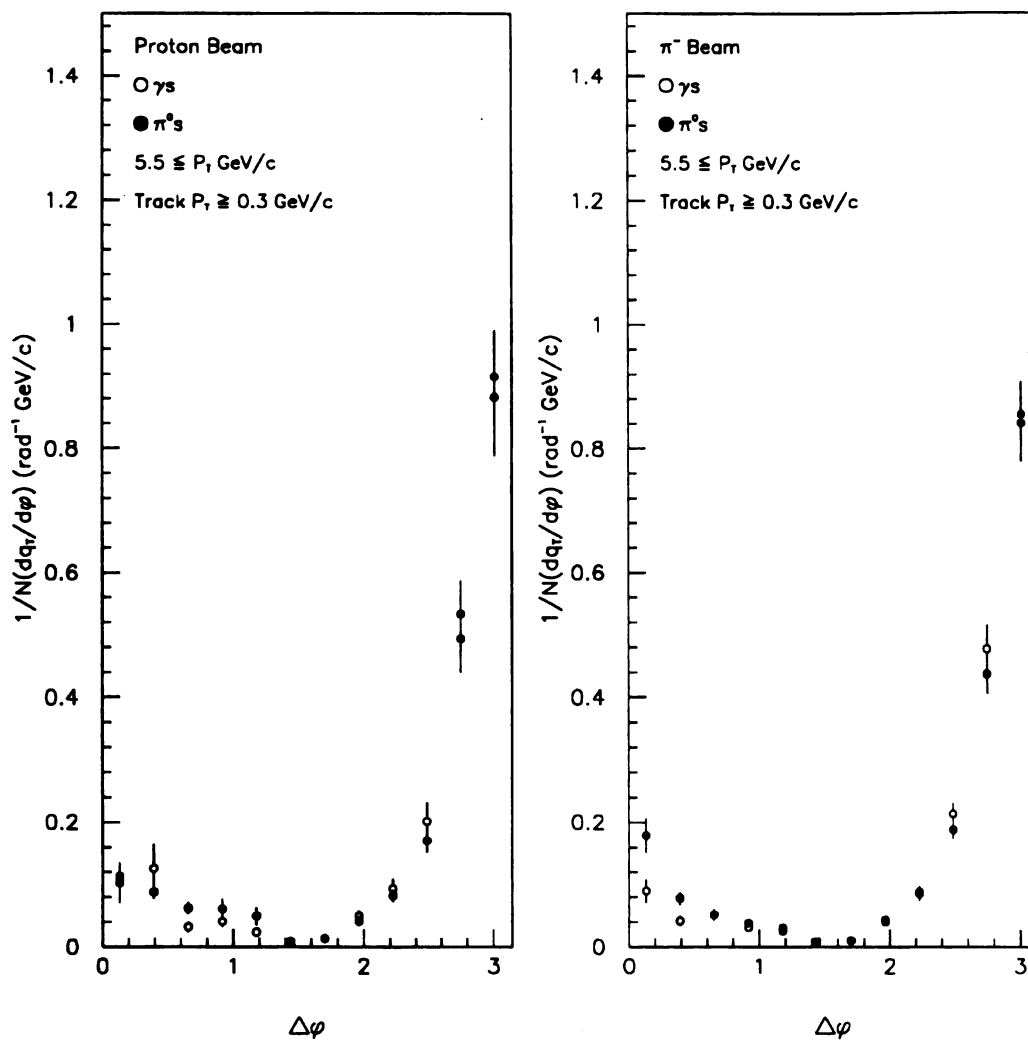


Figure 5.4: q_\perp weighted ϕ distributions for charged particles in high $p_\perp \pi^0$ and single photon events with $p_\perp \geq 5.5 \text{ GeV/c}$.

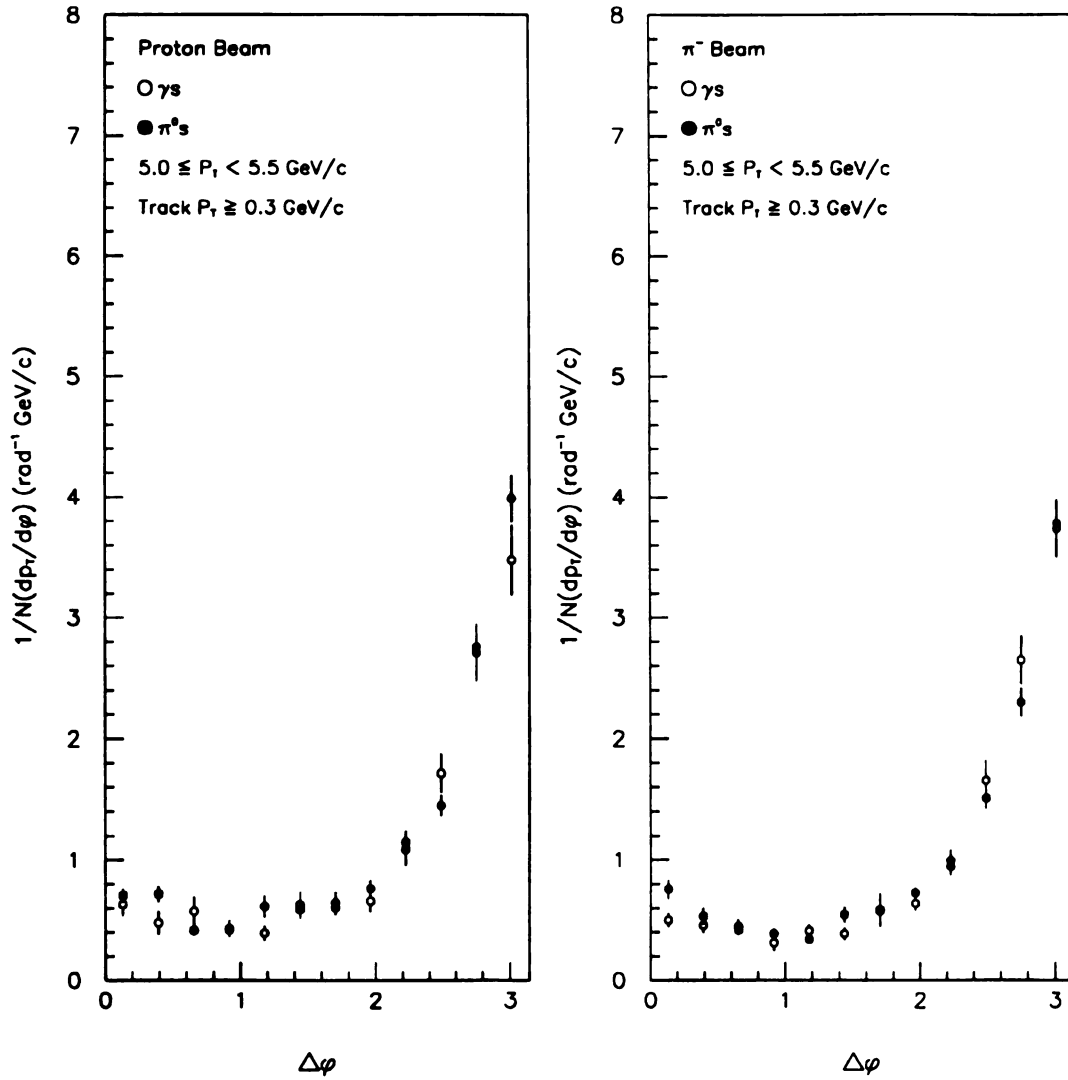


Figure 5.5: p_\perp weighted ϕ distributions for charged particles in high p_\perp π^0 and single photon events with $5.0 \leq p_\perp < 5.5 \text{ GeV/c}$.

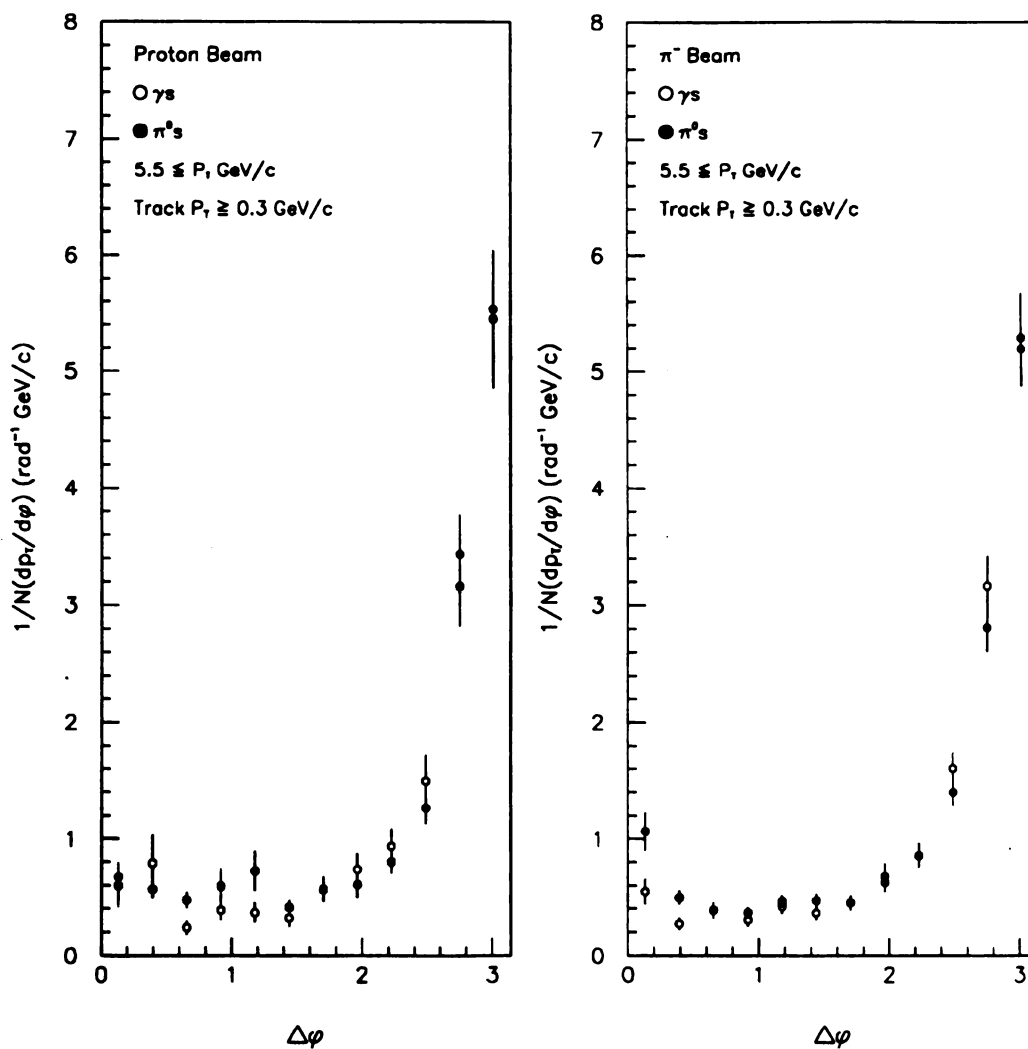


Figure 5.6: p_{\perp} weighted ϕ distributions for charged particles in high p_{\perp} π^0 and single photon events with $p_{\perp} \geq 5.5$ GeV/c.

in rapidity producing a peak in the Δy distribution about 0. Of course, some of the clustering around zero can be due to accidental coincidence. Even perfectly flat rapidity distributions will produce a Δy distribution peaked at 0. It is important therefore, to compare any observed correlation in rapidity against that which is attributable to random coincidence. The degree of random coincidence is governed by the shape of the particles' rapidity distributions; these are in turn governed by the physics of the hadron-hadron collisions as well as the acceptance and overall efficiency for finding tracks.

The Δy plots appearing in the following figures have the uncorrelated background superimposed as a smooth curve. The uncorrelated Δy distributions are constructed by choosing values from the rapidity distributions of those particles used in making the corresponding data plots. The values are chosen such that if plotted the shape of the parent distribution is preserved. As with the azimuthal distributions, a set of selection criteria have been applied to the tracks used in this study. These criteria are essentially the same as for the ϕ distributions except that the rapidity cut was extended to ± 1.5 in the beam-target center of mass, and only p_{\perp} cuts of 0.3 and 0.5 GeV/c were applied. The results from the two sets in track p_{\perp} are the same, and so only the study employing the low p_{\perp} cut will be discussed. Finally, the plots have been folded into the interval from 0 to 3.0 units of rapidity, the data for different trigger particle's and beam types have been combined, and all plots are area normalized.

Figure 5.7 shows the rapidity differences between the two highest p_{\perp} tracks in the recoil hemisphere, and between the highest p_{\perp} track and all other tracks besides the second highest which pass the selection criteria. Both plots show a definite correlation above the level of accidentals. The correlation is strongest between the highest p_{\perp} tracks. This is probably due to a larger fraction of non-jet tracks in the other distribution. Such a correlation has also been reported by the AFS collaboration [42].

Before the observed correlations can be interpreted as dynamical in origin it has to be demonstrated that they are not an artifact of phase space. In particular, it could be argued that the enhancement around $\Delta y = 0$ is due to longitudinal momentum, p_z , conservation and/or energy conservation.

If p_z conservation is responsible for the correlation, then the highest p_\perp recoil particle should be correlated in rapidity with the trigger particle. Figure 5.8 clearly shows this not to be the case; all correlation is merely accidental. Such a result is consistent with a hard-scattering of nucleon constituents in relative motion. The colliding partons' rest frame does not generally coincide with the rest frame of the colliding hadrons.

To understand the effect of energy conservation on the correlation one must resort to a phase space monte carlo. Such a monte carlo produces a spectrum of particles, governed only by the constraint of energy-momentum conservation. The phase space monte carlo GENBOD was chosen for this study. It exists in the CERN library of FORTRAN callable routines. Events were generated in which all particles were assumed to be pions with equal numbers of π^+ , π^- , and π^0 s present; the conservation of electric charge and isospin was thus automatically insured. The data presented here was generated with 30 particles per event. Parallel studies in which the multiplicity varies from 20 to 50 tracks have yielded the same result. A generated event was selected for output, provided it contained a high p_\perp π^0 with $p_\perp \geq 4.0 \text{ GeV}/c$ and $|y| < 0.7$. The Δy histograms were filled in accordance with the same selection criteria as used on the charged tracks in the data. The effect of the analyzing magnet's field together with the MWPC's geometric acceptance, and the effect of the planes' efficiencies have also been accounted for.

Figure 5.9 shows the phase space result for the two highest p_\perp tracks recoiling from a π^0 . No correlation above the accidental background is observed! Also shown is

a plot from the ISAJET monte carlo where each event contains a high $p_{\perp} \pi^0$. The ISAJET result is very similar to the real data. In fact, Figure 5.10 shows the data Δy distribution with the ISAJET prediction superimposed. Although this physics monte carlo differs from the data in the tails, there is good agreement near $\Delta y = 0$. The ISAJET data has been subjected to the same cuts, track selection criteria, and detector effects as the GENBOD generated set.

It appears that the observed correlations in the data are artifacts of the underlying collision dynamics. They are consistent with those observed in the ISAJET generated distributions. If one interprets the Δy and ϕ correlations in the recoil hemisphere as arising from the presence of jets in the high p_{\perp} data, then these correlations can be utilized on an event by event basis to ascertain the direction of a recoiling jet in the apparatus. This is the subject of the following chapter.

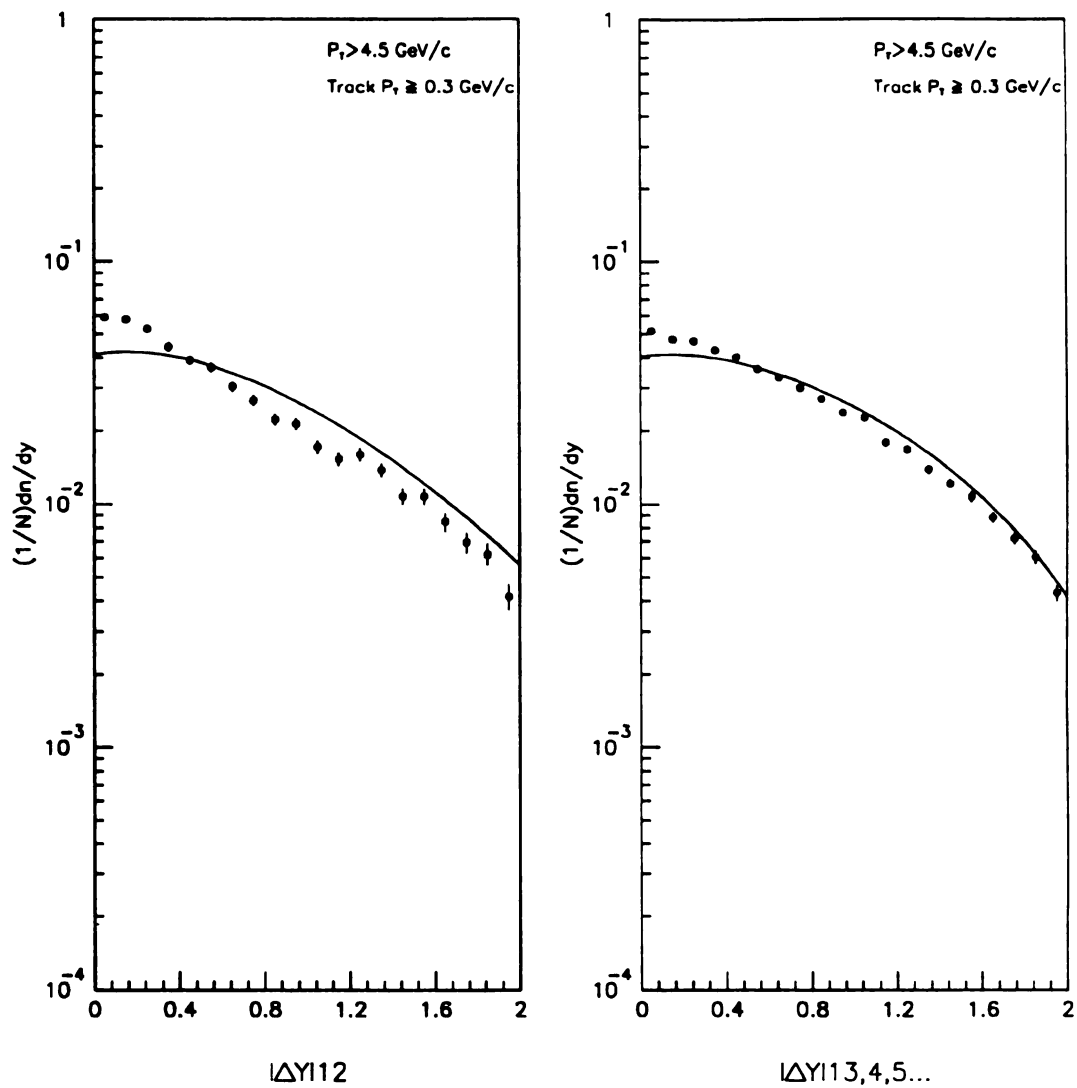


Figure 5.7: Δy distributions for 1st and 2nd highest p_\perp recoil tracks (left), and 1st, 3rd, 4th, ... highest p_\perp tracks (right).

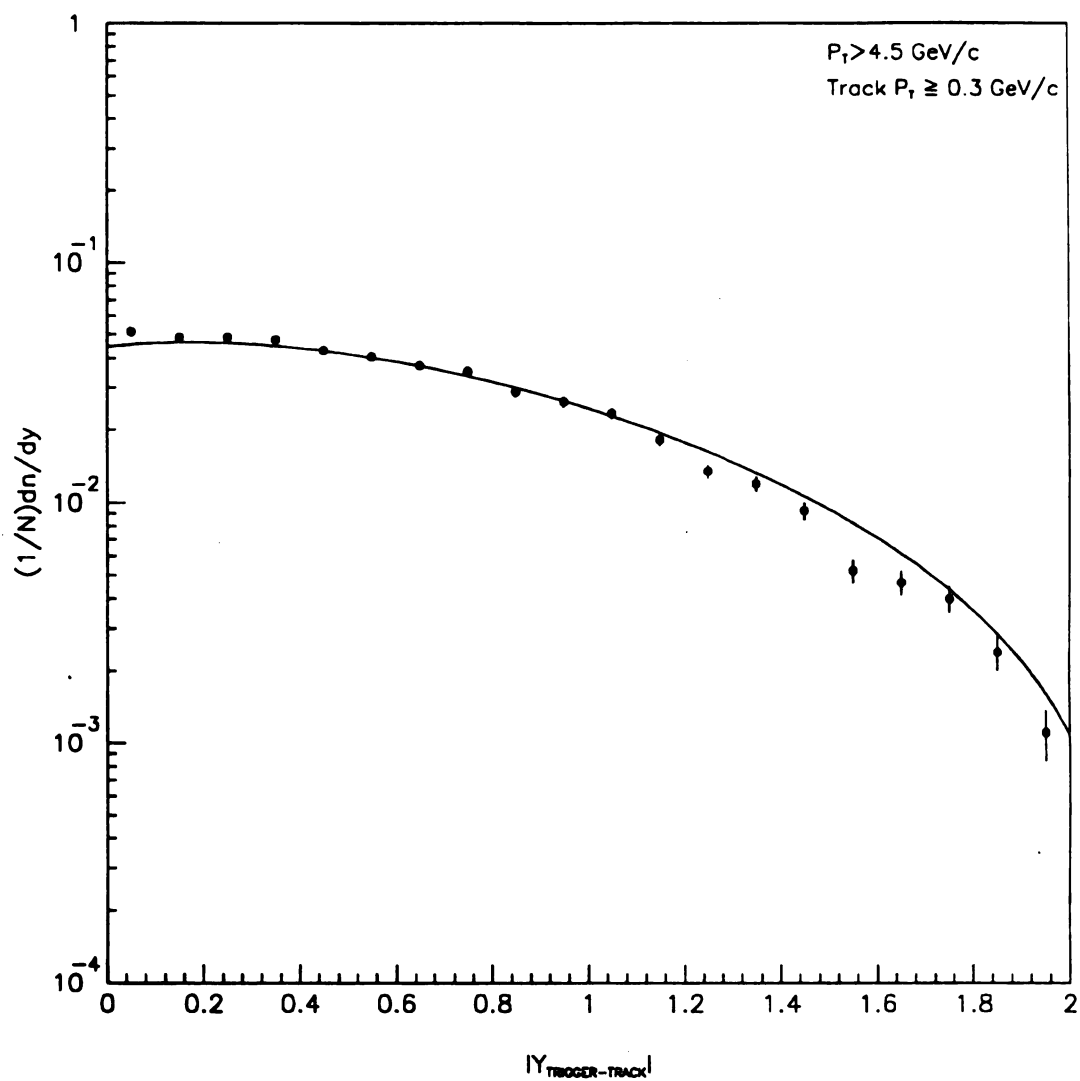


Figure 5.8: Δy between highest p_{\perp} recoil track and the trigger particle.

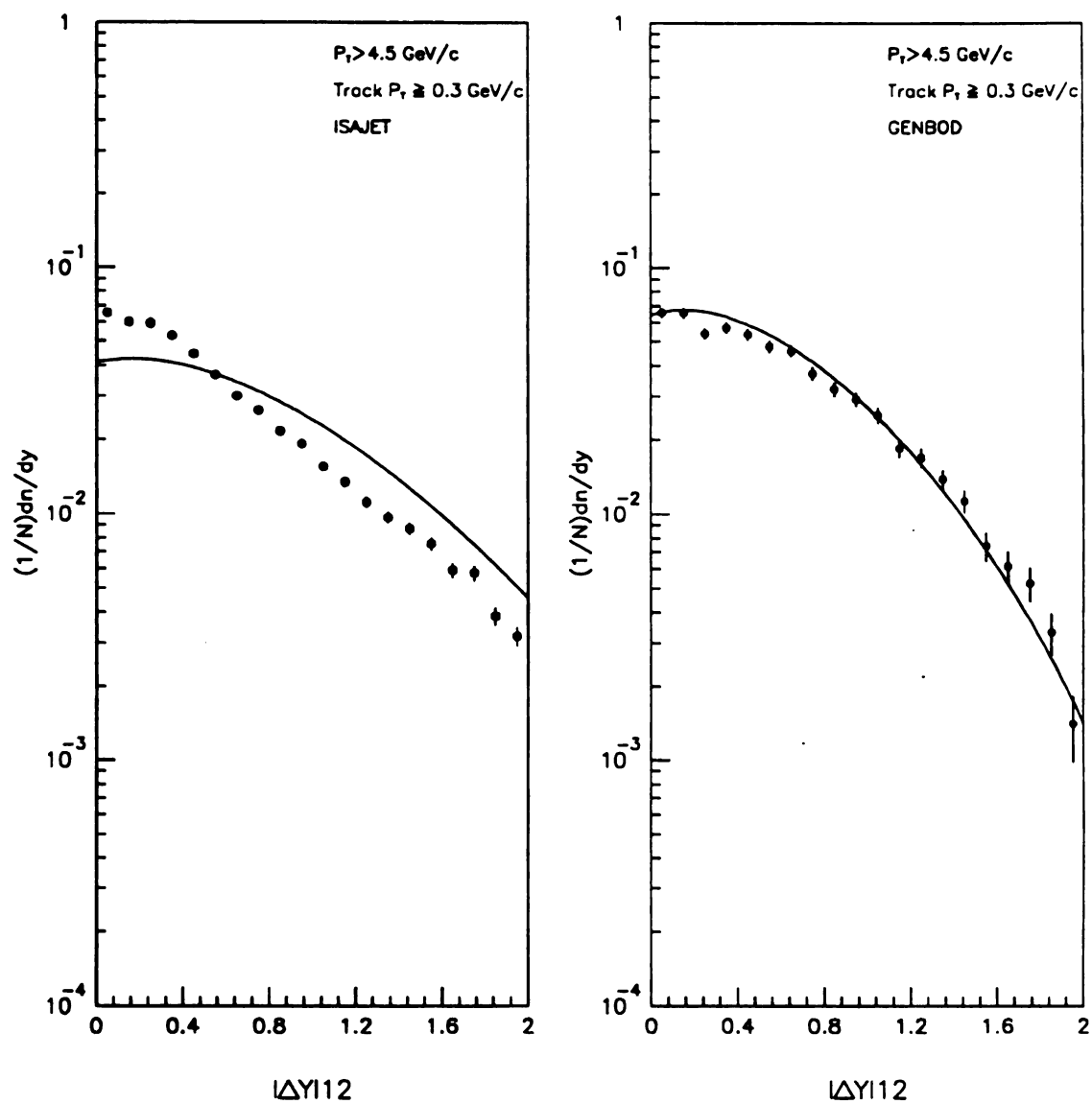


Figure 5.9: Δy distribution of highest p_{\perp} recoil charged pair for ISAJET generated data (left), and phase-space monte carlo data (right). The uncorrelated Δy distributions appear as smooth curves.

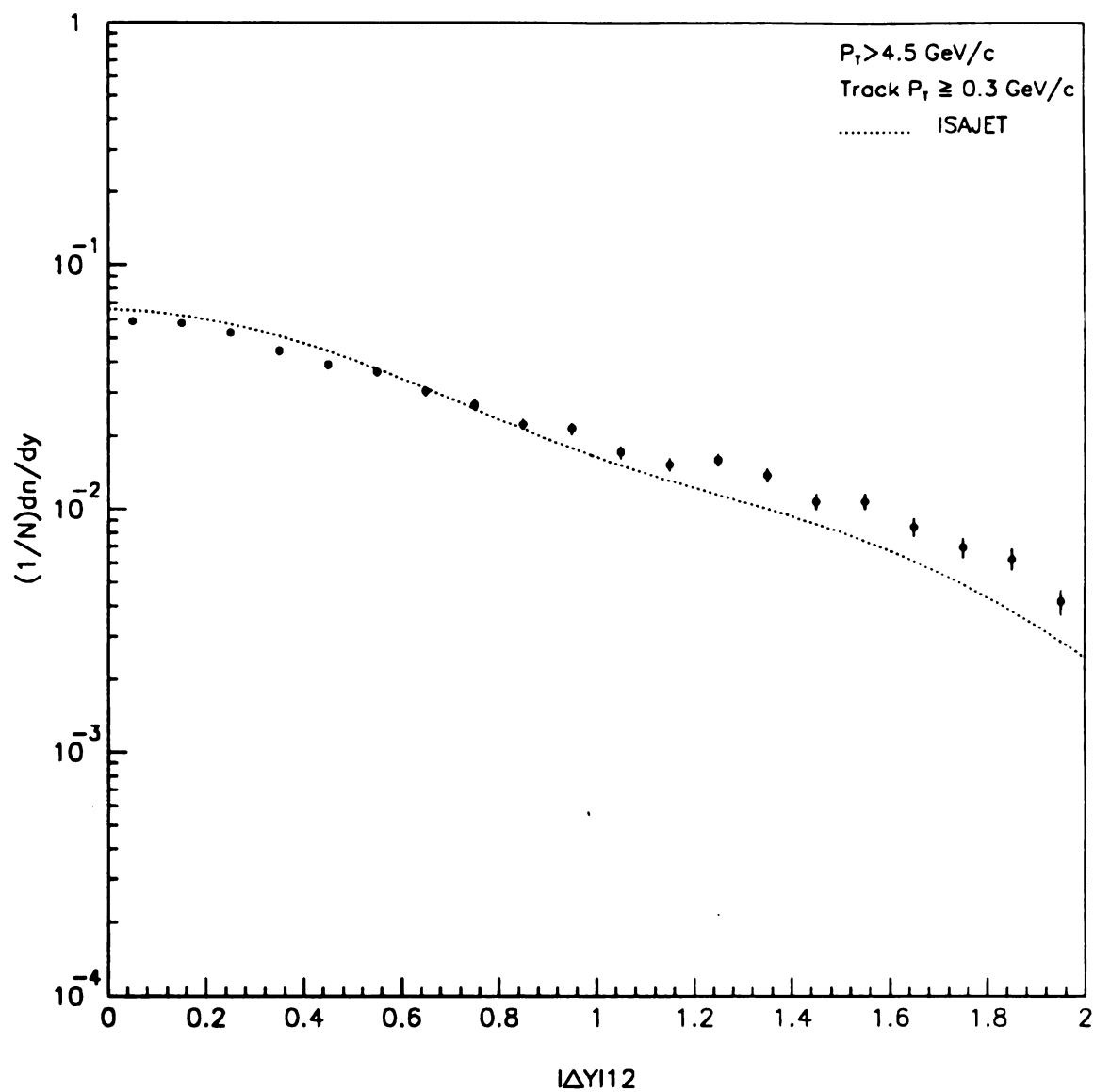


Figure 5.10: Δy between the highest p_\perp recoil charged pair in data with the corresponding ISAJET result superimposed as a smooth curve.

Chapter 6

Jet Reconstruction

The previous chapter contained a study of the correlations associated with jet structure. The study revealed that the recoil jet is contained within the tracking system's acceptance a fair fraction of the time. This chapter focuses on the reconstruction of the recoil jet's 4-vector. The goal is to show that $\cos \theta^*$ and $M \tau \sqrt{s}$ are measurable quantities within the realm of a physics monte carlo. If the corresponding distributions in the data are similar, then one might be inclined to believe the data distributions are meaningful as well.

Achieving this goal requires several intermediate steps. First, the jet axis must be reconstructed with some reasonable efficiency, and the resolution estimated. This task is accomplished by implementing a jet reconstruction algorithm. Second, the recoil jet's momentum must be computed, and values of x_1 and x_2 obtained. The sources of systematic uncertainty in these variables have to be understood, and their magnitudes estimated. Understanding the origin of these effects allows one to decide if meaningful $\cos \theta^*$ and M distributions can be constructed.

6.1 JET ALGORITHMS

Two jet algorithms will be studied and compared against one another. A cone type algorithm, familiar to collider experiments, has been chosen since it is directly sensitive to the jet correlations described in the previous chapter. The other algorithm has been used by the WA70 [43] collaboration in their study of jets recoiling from high p_\perp single photons and π^0 s. Use of the WA70 procedure allows the results from this analysis to be compared directly with those of another experiment in a similar kinematic regime.

Both algorithms only make use of the charged tracking data. They utilize the same initial set of jet candidate tracks, and employ the leading charged particle as the initial or “seed” jet direction. The input set of tracks is defined by the following criteria:

- All tracks must be more than $\pi/2$ radians away from the trigger particle (Hemisphere Cut).
- All tracks must have $p_{\perp} \geq 0.3 \text{ GeV}/c$.
- All tracks must have $\eta \leq 1.5$.

The last cut is intended to provide a symmetric acceptance, but it also removes tracks belonging to the forward spectator jet. Such tracks can have considerable momentum and as a result, bias the jet reconstruction. In addition to these criteria, two additional constraints are imposed on the leading charged particle. One, the leading charged track must have $p_{\perp} \geq 0.5 \text{ GeV}/c$, and two, this track must be more than $2\pi/3$ radians from the trigger particle in azimuth.

6.1.1 Cone Algorithm

The cone algorithm selects tracks from the input set based on the value of ΔR associated with them. This quantity is defined as follows:

$$\Delta R = \sqrt{\Delta^2 \eta + \Delta^2 \phi} \quad (6.1)$$

where $\Delta\eta$ and $\Delta\phi$ are the differences in pseudorapidity and azimuth, respectively, between the candidate jet track’s orientation and the jet axis’s direction. Of course, on the first iteration the jet axis is just the direction of the leading charged track. The $\Delta\phi$ and Δy plots, presented in the last chapter, indicate that strong correlations exist between particles in the recoil hemisphere for $\Delta\phi \lesssim \pi/3$ and $\Delta y \lesssim 1.0$. For this reason a cut value of 1.0 has been chosen for ΔR . While not all jet tracks will

be included by this procedure, it is expected that the fastest jet tracks will be and that most spectator tracks will be excluded.

After making a selection based on ΔR the momentum vectors of the tracks assigned to the jet are summed, and the jet axis's direction computed. The new estimate for the jet direction is used to make another ΔR selection on the initial input set of tracks. Another jet axis is calculated from the second set of jet candidate tracks. This process is repeated until a maximum number of tracks are assigned to the recoil jet, or the algorithm oscillates between a solution containing N tracks and one possessing $N + 1$ tracks. In the latter case the solution with $N + 1$ tracks is chosen.

A final check is made on the jet axis calculation. First, a reconstructed jet must have two or more tracks assigned to it. Second, the reconstructed jet axis must be more than $2\pi/3$ radians from the trigger in ϕ . These cuts on the reconstructed jet reduce the number of jets biased by spectator fragments and insure that the events represent true 2-2 hard scatters rather than multi-jet events, which are difficult to interpret.

6.1.2 WA70 Algorithm

The algorithm developed by the WA70 group is based on an e^+e^- sphericity algorithm. The routine has been modified for use in a hadro-production environment by including a means of discriminating between particles belonging to the recoil jet and those belonging to the spectator jets. Furthermore, the sphericity tensor is not actually used in calculating the jet axis because the trigger and recoil jet axes are not generally back-to-back in the rest frame of the colliding hadrons.

The WA70 routine is the same as the cone algorithm except that instead of making a jet track selection based on ΔR , a selection based on the probability, P , that a track belongs to the recoil jet as opposed to the spectator jet is performed. P is calculated

from weights w_1 and w_2 . These weights are formulated mathematically as

$$\begin{aligned} w_1 &= \frac{P_{||\text{JET}}}{P} \exp(-3.0 p_{\perp \text{JET}}) \\ w_2 &= \frac{P_{||\text{BEAM}}}{P} \exp(-3.0 p_{\perp \text{BEAM}}) \\ P &= \frac{w_1}{(w_1 + w_2)}, \quad P > 0.5 \text{ (cut criterion)} \end{aligned} \quad (6.2)$$

The subscript, JET, refers to the momentum component parallel or transverse to the current estimate of the jet direction. The subscript, BEAM, has an analogous meaning for a track's momentum components with respect to the beam direction, taken as the z-axis in the experiment's coordinate system. In addition, the same pair of cuts are applied to the final estimate of the jet axis.

6.2 THE JET MONTE CARLO

The monte carlo used to study jet reconstruction and resolution has two distinct parts: an event generator that produces simulated events according to the current understanding of hadronic interaction, and another program which simulates the detector's response to the passage of high energy particles. The ISAJET monte carlo was chosen as the event generator. Version 6.36 has been used since it allows for efficient generation of high $p_{\perp} \pi^0$ events. All events were generated on the VAX family of computers, possessing 32 bits of precision.

6.2.1 Implementation of ISAJET

The physics monte carlo employs the independent fragmentation model, and the factorization scheme outlined in the introduction. The results from perturbative QCD are used to simulate the high Q^2 parton-parton scatter. It should be noted that the event generator for direct photons contains only the Compton and annihilation subprocesses; there is no bremsstrahlung component in the direct photon monte carlo

data. Unless otherwise stated, the events were generated with the default set of parameters. This implies a 6 GeV/c radiative cutoff and a $\langle k_{\perp} \rangle$ of 0.95 GeV/c.

As described in the chapters on the experimental apparatus and event selection, the type of trigger utilized in detecting high p_{\perp} π^0 s and single photons relied on only one large deposition of p_{\perp} in the electromagnetic calorimeter. There is then the possibility of a net p_{\perp} for the trigger+recoil-jet system in the direction of the trigger particle due to fluctuations in the transverse momenta of the colliding partons. Recent results from the WA70 group indicate a rather substantial $\langle k_{\perp} \rangle$ of 0.95 GeV/c [44]. This explains the value currently implemented in ISAJET.

In order to take into account the effects of the single-local trigger, the p_{\perp} thresholds for jets 1 and 2, produced by the monte carlo, were set at different levels. Jet 1 was required to have $p_{\perp} \geq 4.0$ GeV/c while jet 2 was only required to have $p_{\perp} \geq 3.0$ GeV/c. The plot in Figure 6.1 reveals a significant spread in Δp_{\perp} with a mean of ~ 1.0 GeV/c. As a matter of fact, there is evidence in the E706 data sample for such a p_{\perp} imbalance in the direction of the trigger particle. This imbalance represents the minimum imbalance in the acceptance for tracks and showers outside the beam halo region of the LAC [45].

6.2.2 Detector Simulation

Ideally the ISAJET generated data would be input to a full detector simulation program. The simulation used by the E706 collaboration is an implementation of the GEANT monte carlo package. The output from GEANT would be run through the same chain of reconstructor code used on the real data. Finally, a compressed DST is made from the reconstructor output, and the monte carlo DST's are subsequently processed by the high level DST reconstruction code. The advantage of this method is that the systematics associated with data reconstruction, *e.g.* "bugs" in the code, are duplicated in the monte carlo.

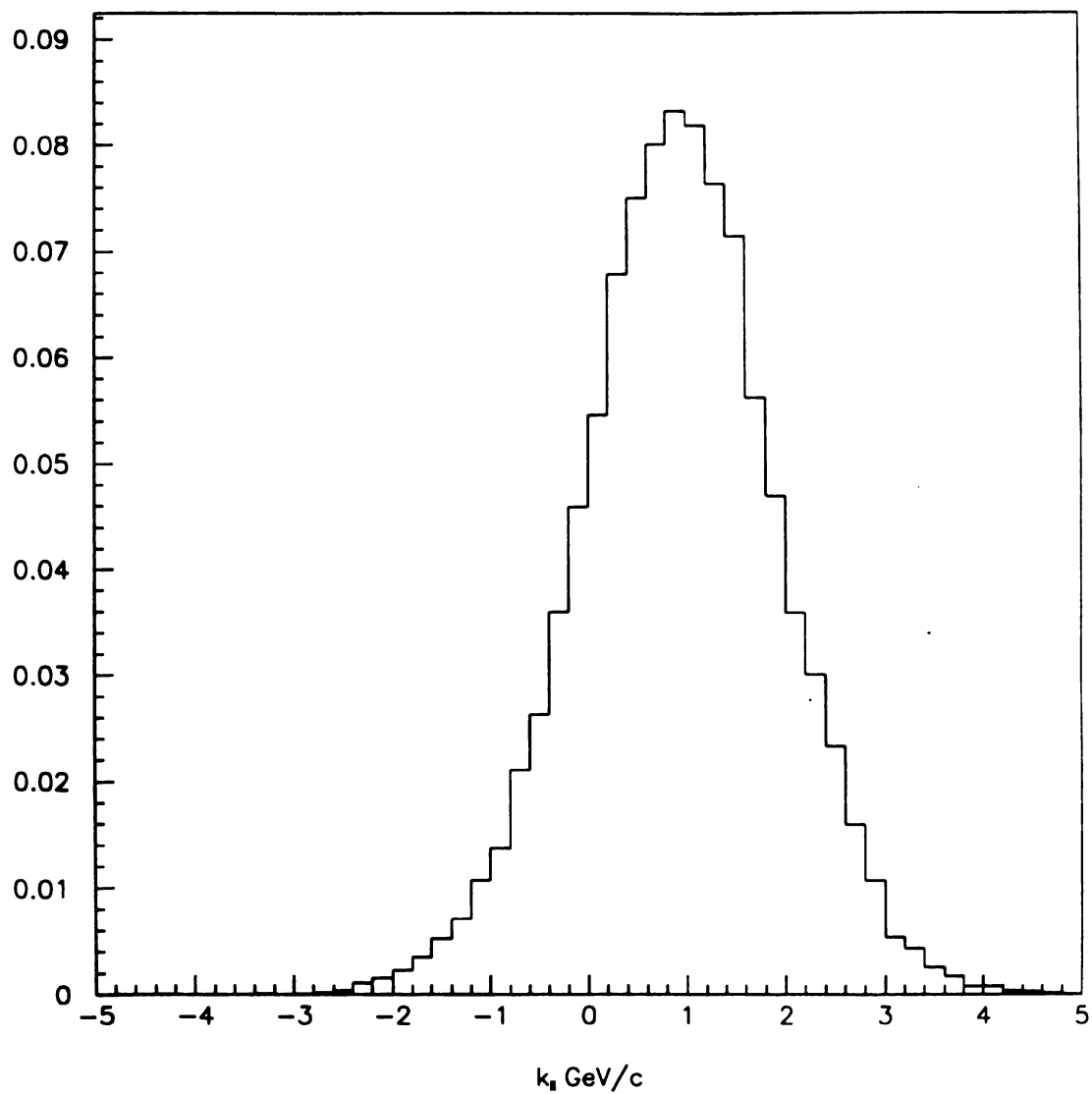


Figure 6.1: The p_{\perp} imbalance between the two hard scatter jets in ISAJET with $\langle k_{\perp} \rangle = 0.95 \text{ GeV}/c$.

Unfortunately, such a thorough procedure represents a huge investment of computer time. A more expedient solution was used in this analysis. A simplified detector simulator was written which takes into account the acceptance of the magnet and MWPC system, the efficiencies of the individual chamber planes, and the effects of the analyzing magnet's field on charged tracks that traverse it. The field is modeled as a simple dipole with an effective length as measured from the data. This same magnetic field model, incidentally, is used by the GEANT monte carlo as well. All charged ISAJET particles within the fiducial volume of the detector are projected through the magnet into the MWPC system. A detailed description of this simple monte carlo for the tracking system is found in chapter 3. In addition, the interested reader will find a comparison of this monte carlo with data.

Except for the trigger particle, no neutral particles from the monte carlo were analyzed by the DST level reconstruction routines. No simulation of the calorimeter's response to the high p_{\perp} trigger particle was implemented here. Such a response was modeled, however, for the π^0 background calculation to the direct photon signal; the details of this monte carlo procedure are given in the next chapter. The acceptance cuts in rapidity that were applied to the real data have also been imposed on the high p_{\perp} single photons and π^0 s generated by ISAJET.

6.3 JET ALGORITHM PERFORMANCE

The performance of the Cone and WA70 algorithms is summarized in this section. There are three basic performance characteristics relevant for later studies. First, there is the question of how well each algorithm can determine the recoil jet's direction. Second, does the jet reconstruction algorithm find the recoil jet a substantial fraction of the time. While the results for $\cos \theta^*$ and M do not depend critically on the reconstruction efficiency, a low efficiency means a loss of statistics. The third issue concerns the precision and accuracy with which x_1 and x_2 are calculated. Of

immediate concern is the issue of jet axis resolution since this determines if $\cos \theta^*$ and M are measurable. In addition, it can provide a measure of how often the jet is misreconstructed. All subsequent studies of reconstructed jets will involve a pseudorapidity cut of $|\eta| \leq 1.0$. Such a cut is necessary because of the pseudorapidity cut on individual tracks ($|\eta| \leq 1.5$).

6.3.1 Jet Axis Resolution

The previous work with the ϕ distributions indicates that things are alright transverse to the collision axis. The particles clearly recoil from the trigger. The events are not expected to always be planar, but the ϕ variable plays no role in determining x_1 or x_2 . What is of great interest is how well a jet's longitudinal direction is ascertained. A number of variables can be used to express the longitudinal direction. $\cos \theta$ and η in the rest frame of the colliding hadrons are the most relevant for this study; all results will be expressed in terms of them. Figure 6.2 plots the difference, $\delta \cos \theta$, between the reconstructed and generated directions in $\cos \theta$ as a function of the sum $\cos \theta_{\text{ALG}} + \cos \theta_{\text{GEN}}$ for each algorithm. This particular choice of variables allows for a symmetric distribution of points centered about $\delta \cos \theta = 0$ over the entire acceptance. Such a plot has absolute boundaries formed by the intersection of lines through the points $(-2, 0)$, $(0, 2)$, $(2, 0)$, and $(0, -2)$. The allowed region of scatter is therefore a square. However, the plots in Figure 6.2 appear bounded by a parallelogram with the extrema in $\delta \cos \theta$ shifted away from $\cos \theta_{\text{ALG}} + \cos \theta_{\text{MC}} = 0$. This effect is due solely to the pseudorapidity cut on the reconstructed jet axis.

By inspection one can see that both algorithms yield very similar results. There is a dense band of points, centered about $\delta \cos \theta = 0$, extending across each plot with an absolute width of about 0.3. In addition, there is a sparse uniform scatter of points away from the band in each plot. The dark band represents the resolution of each jet algorithm, while the diffuse scatter indicates the frequency at which the jet is

misreconstructed. Fortunately, the fraction of misreconstructed jets is rather small. A projection of each plot into $\delta \cos \theta$ appears in Figure 6.3. The HWHM indicates a uniform resolution in $\cos \theta$ of 0.1 for both algorithms.

An estimate of the misreconstruction frequency can be obtained by measuring the fraction of each distribution in Figure 6.3 comprised by the tails. Out to $|\delta \cos \theta| = 0.3$ the jets should be deemed properly reconstructed. Outside this interval there is a mixture of correctly and incorrectly reconstructed jet axes with the relative fraction of misreconstructed axes increasing with increasing $|\delta \cos \theta|$. By deeming all jets for which $|\delta \cos \theta| > 0.5$ as improperly formed, and using this fraction to determine the “wrong” jet contribution between 0.3 and 0.5 in $\delta \cos \theta$, the misreconstruction frequency has been found to be about 7% for the Cone and WA70 algorithms.

It is also interesting to know how well the jet reconstructors track each other event-by-event. An advantage in studying the difference in $\cos \theta$ between the two algorithms versus $\cos \theta_{\text{CONE}} + \cos \theta_{\text{WA70}}$ is that the monte carlo can be compared with the data! Such a study appears in Figure 6.4. It is easy to see that the data and monte carlo are similar and that the algorithms track each other very well. The dense band about $\delta \cos \theta = 0$ is much narrower than in Figure 6.2, implying the reconstructors do not differ significantly in their estimates of the jet’s longitudinal orientation. Such a systematic correlation between the two algorithms is expected because they both rely on the same input track set.

The diffuse spread of points in the Figure 6.4 represents the frequency for either one or both algorithms to misreconstruct the recoil jet direction. However, the central band contains those events for which both routines either correctly or incorrectly determined the recoil jet axis. The fraction of those events for which the “wrong” jet was reconstructed represents the frequency for which the input track set contains insufficient information. A study has been done in which the difference between both jet algorithms is plotted against the difference between each algorithm and the monte carlo

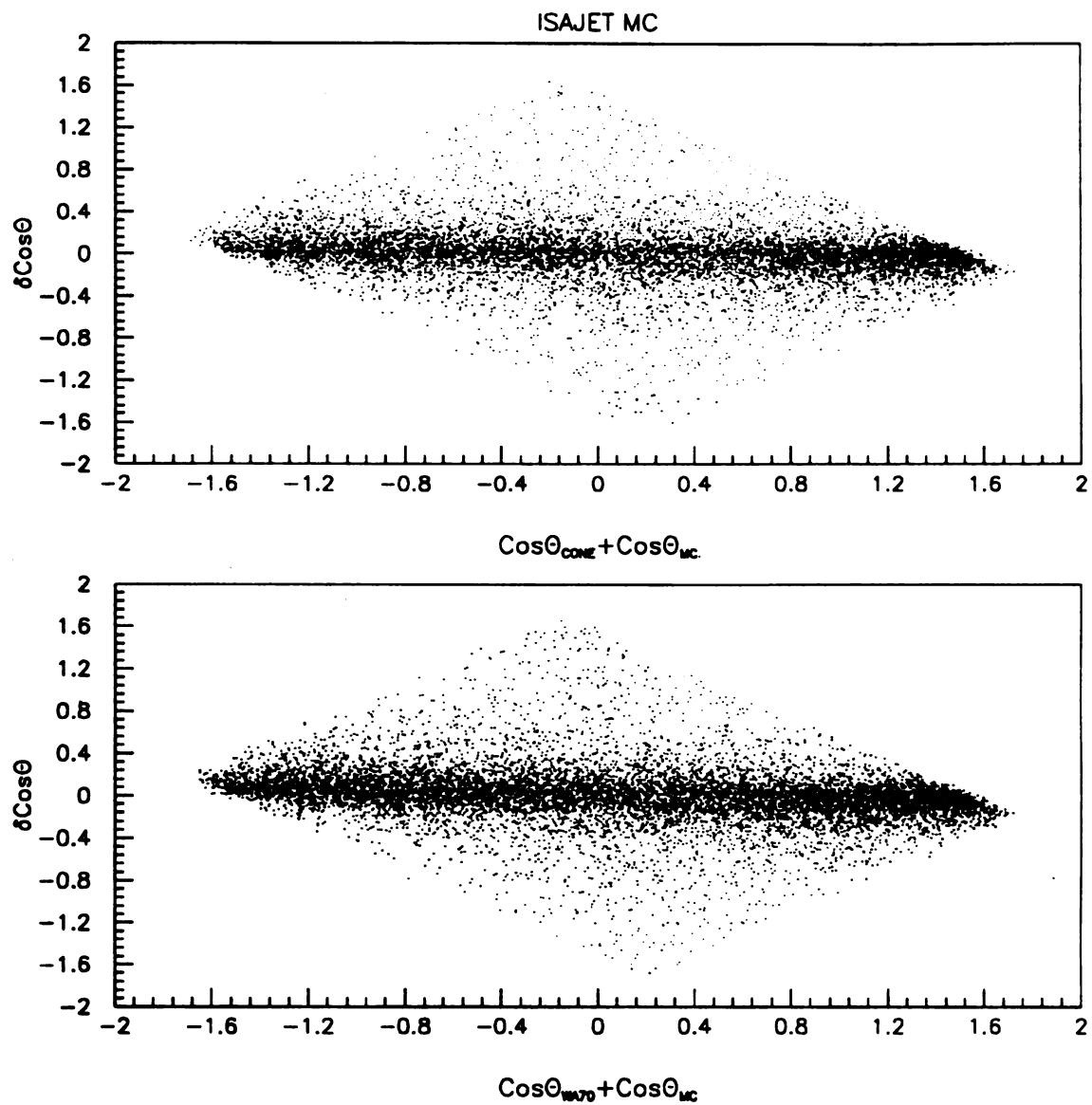


Figure 6.2: Scatter plots of jet resolution over the acceptance for Cone (Top) and WA70 (Bottom) algorithms.

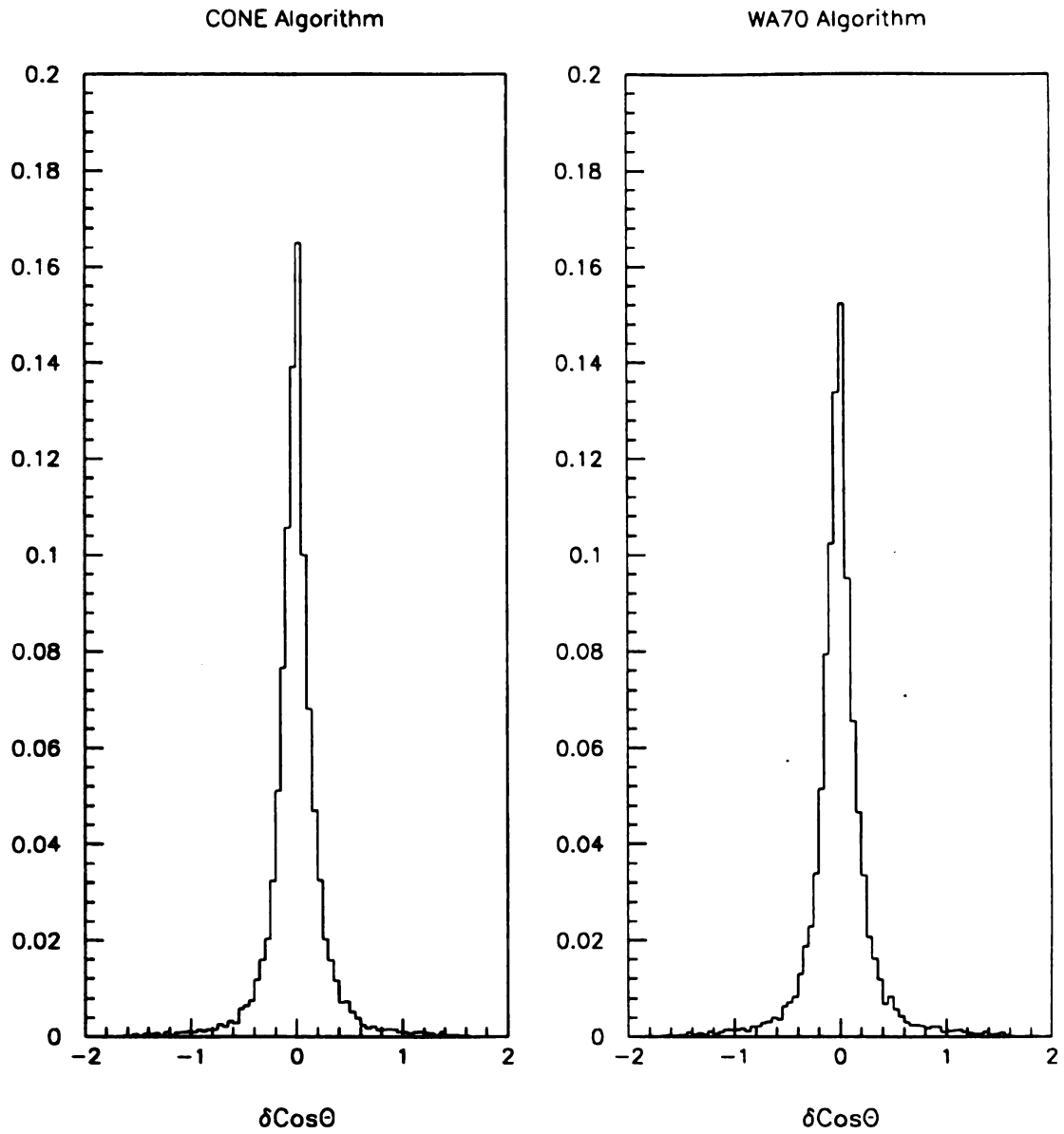


Figure 6.3: $\delta \cos \theta$ distributions for Cone (Left) and WA70 (Right) algorithms integrated over the acceptance.

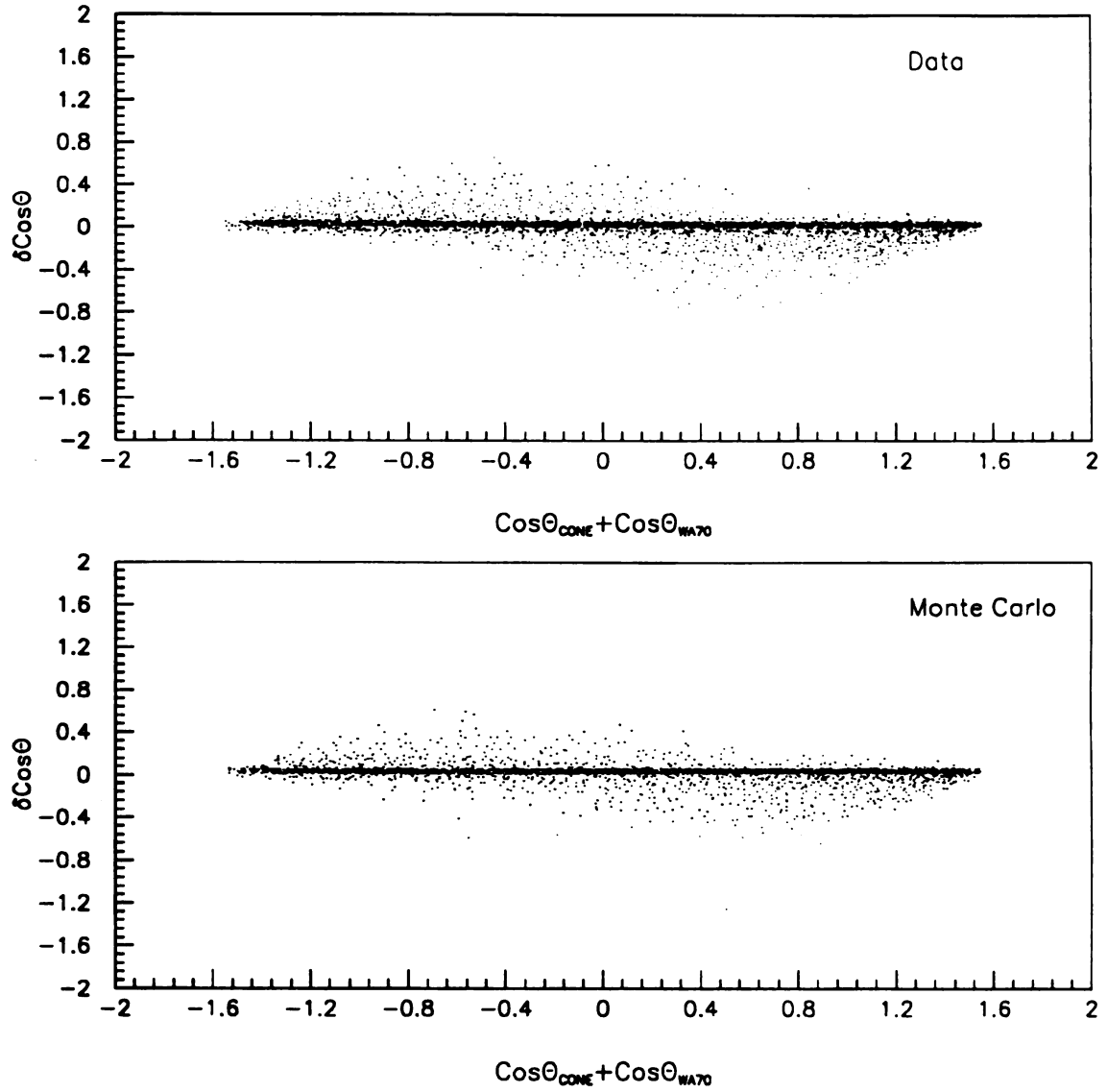


Figure 6.4: Scatter plots of $\delta \cos \theta$ between WA70 and Cone algorithms over the acceptance for data (Top) and monte carlo (Bottom).

The abscissa in each plot is projected out for $|\delta \cos \theta| < 0.2$. Again, the technique of measuring misreconstruction by examining the tails of these distributions is used to determine the fraction of “wrong” jets beyond $|\cos \theta_{\text{ALG}} - \cos \theta_{\text{MC}}| = 0.3$. This fraction is 5%. Clearly, it is the input track set which is responsible for most of the jet misreconstruction.

Comparing one reconstruction technique against another also allows one to study the variation in resolution as an algorithm’s parameters are varied. Such a study has been done where ΔR was allowed to vary between 1.0 and 2.0, while the factor in the exponential terms for w_1 and w_2 was varied between 2.0 and 5.0. No significant changes in resolution were observed for either jet reconstructor. This indicates that the systematics associated with jet axis reconstruction are not critically dependent on the reconstruction technique.

6.3.2 Jet Finding Efficiency

There are a number of viewpoints concerning the jet finding efficiency. In the previous discussion, inefficiency was viewed in terms of how often the recoil jet axis is formed incorrectly. There is also the question of how frequently a jet is found given that an event contains a high $p_{\perp} \pi^0$ or single photon. One expects that within the hard-scatter picture any event possessing such a high p_{\perp} object will have a recoil jet. However, the limited acceptance of the experiment’s spectrometer, the p_{\perp} cuts on the jet candidate tracks, the leading charged particle cuts, and the selection criteria of the jet algorithms all conspire to produce a jet finding efficiency substantially less than one.

The jet finding efficiency can be estimated by taking the trigger’s p_{\perp} spectrum for those events with a reconstructed jet, and dividing it by the inclusive p_{\perp} spectrum. This method has the advantage of being able to compare the monte carlo with data.

The jet finding efficiencies for both jet algorithms are plotted in Figure 6.5; the data is plotted with error bars and the monte carlo is superimposed as a dashed line.

All plots show an increase in efficiency with p_{\perp} . This is due to kinematics, which favors the trigger and recoil jet to be at 90 degrees in the nucleon-nucleon rest frame at high p_{\perp} , and the scaling of the fragmentation functions. The WA70 algorithm appears to be more efficient than the Cone algorithm, implying the ΔR cut is a bit more selective. The greatest source of inefficiency are the leading particle cuts, which represent a 20% loss. Overall the monte carlo data is 10% more efficient at low p_{\perp} with the data and monte carlo coming into agreement above 5 GeV/c p_{\perp} . This effect is not due to hardware or PLREC systematics since they should possess no p_{\perp} dependence. Rather, this difference stems from the fragmentation functions being steeper, and/or the structure functions peaking at lower x values in the data than the monte carlo.

6.3.3 Parton Variables

Before x_1 and x_2 can be calculated the recoil jet's momentum must be determined. This analysis makes an estimate based on the assumption that p_{\perp} is balanced between the trigger particle and the recoil jet. It is important to see how well this premise works when intrinsic k_{\perp} and fragmentation effects are present. Figure 6.6 illustrates the difference between generated and reconstructed jet momenta as a fraction of the reconstructed momentum. Both algorithms give consistent results. The peaks are centered about zero with HWHM's of 25%. From the expression for the momentum of the recoil jet,

$$P_{JET} = p_{\perp} / \sin \theta_{JET} \quad (6.3)$$

and the estimated resolution for the reconstructed jet axis one can easily calculate the contribution to the smearing of P_{JET} over the acceptance. This contribution alone

represents $\simeq 80\%$ of the total observed smearing in the peak of $\delta P/P$! In Figure 6.7 the corresponding plots for single photon events are shown. By inspection the reader can see they yield slightly better estimates of the jet momentum resolution.

All of these plots have an asymmetric tail extending towards increasing $\delta P/P$. This tail is a combination of events with misreconstructed jets, and those containing a large k_{\perp} enhancement in the direction of the trigger. No correlation between the frequency of jet misreconstruction and large $\delta P/P$ values has been found. So, the right hand tails of the $\delta P/P$ plots indicate the magnitude of the effect intrinsic k_{\perp} has on the misreconstruction of jet momenta. By subtracting the left portion of each histogram from the right half one determines the fraction of incorrect momenta to be 15%. Although the contribution of jet axis misreconstruction to the tails of the $\delta P/P$ distributions is quite small, it does bring into consideration the application of general kinematical cuts, i.e. $P_{\text{JET}} < \sqrt{s}/2$, and $x_1, x_2 < 1$.

The resolution for x_1 and x_2 is estimated from the monte carlo by computing $\delta x/x$. Recall that in addition to the p_{\perp} balancing assumption, the trigger and recoil jets are assumed to be massless in calculating x_1 and x_2 . Figure 6.8 and Figure 6.9 display the parton x resolution functions for π^0 and single photon events, respectively. Once, again both jet reconstruction algorithms yield consistent results. The asymmetric tails in the momentum resolution plots do not, however, carry over into these distributions.

The $\delta x/x$ distributions for γ events are centered near 0 with a HWHM of 10%. Unfortunately the π^0 plots are smeared about twice as much and are systematically shifted below 0 $\gtrsim 10\%$. This systematic shift arises because π^0 s are usually only one of the trigger jet's fragments. This difference between single photons and π^0 s implies that the kinematic regions for both classes of events, used to construct the $\cos \theta^*$ and M distributions do not coincide exactly.

In summary, both jet algorithms have yielded consistent results as far as the resolution of various quantities is concerned. It is expected that the same behaviour

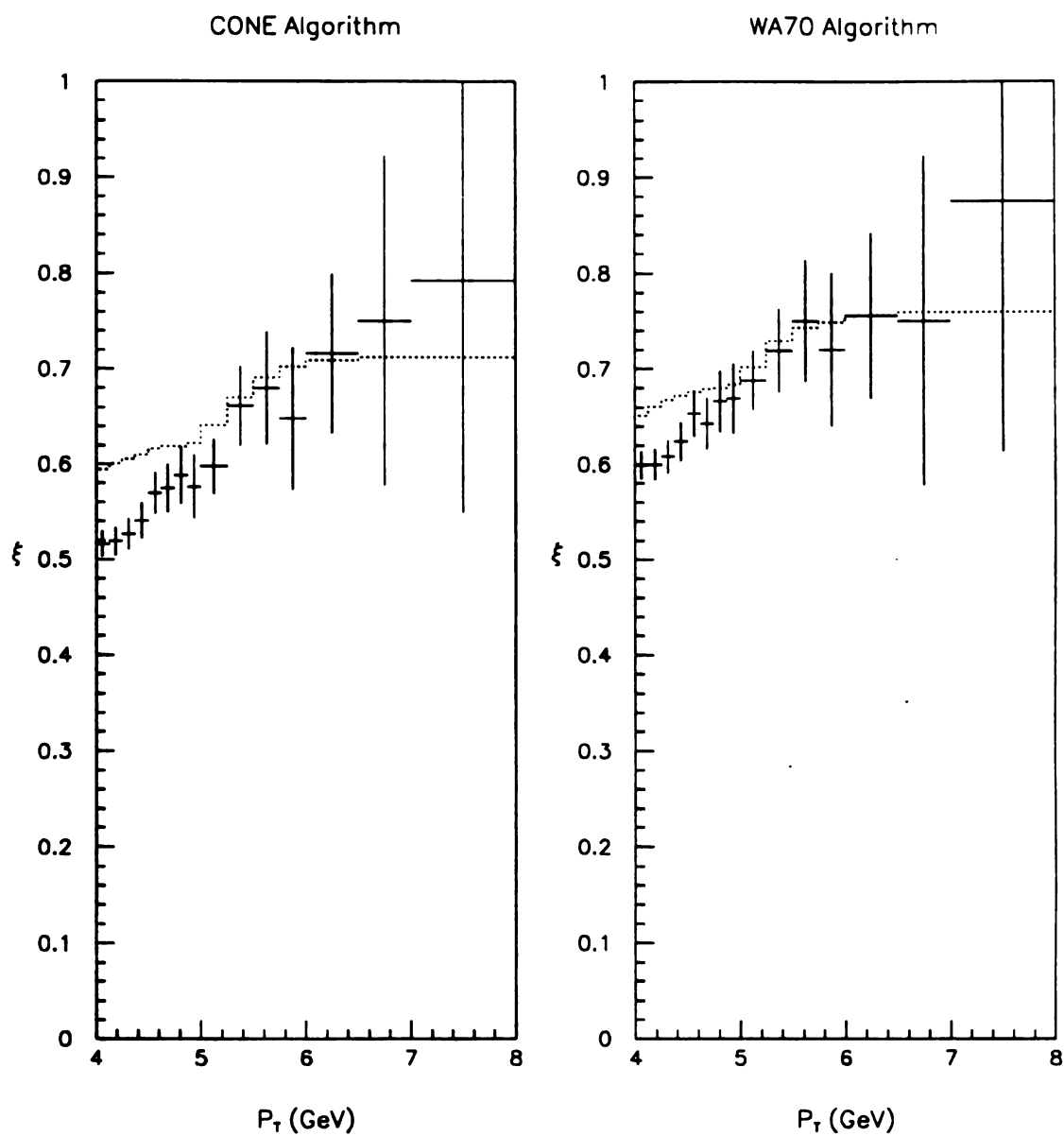


Figure 6.5: The jet finding efficiency for Cone and WA70 algorithms as a function of the trigger's p_{\perp} . Monte carlo is superimposed on the data.

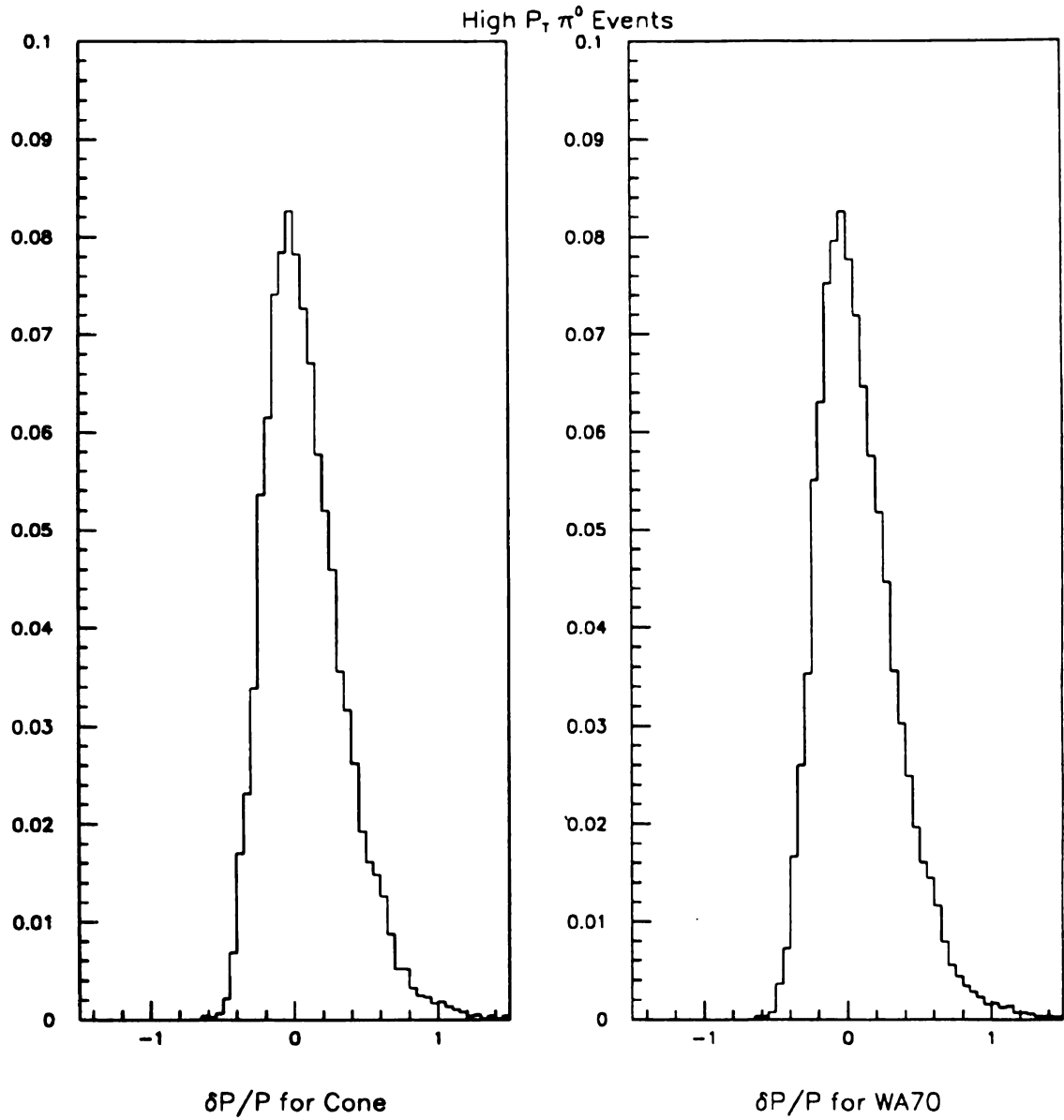


Figure 6.6: Resolution plots of the reconstructed jet momentum for π^0 triggers integrated over the acceptance.

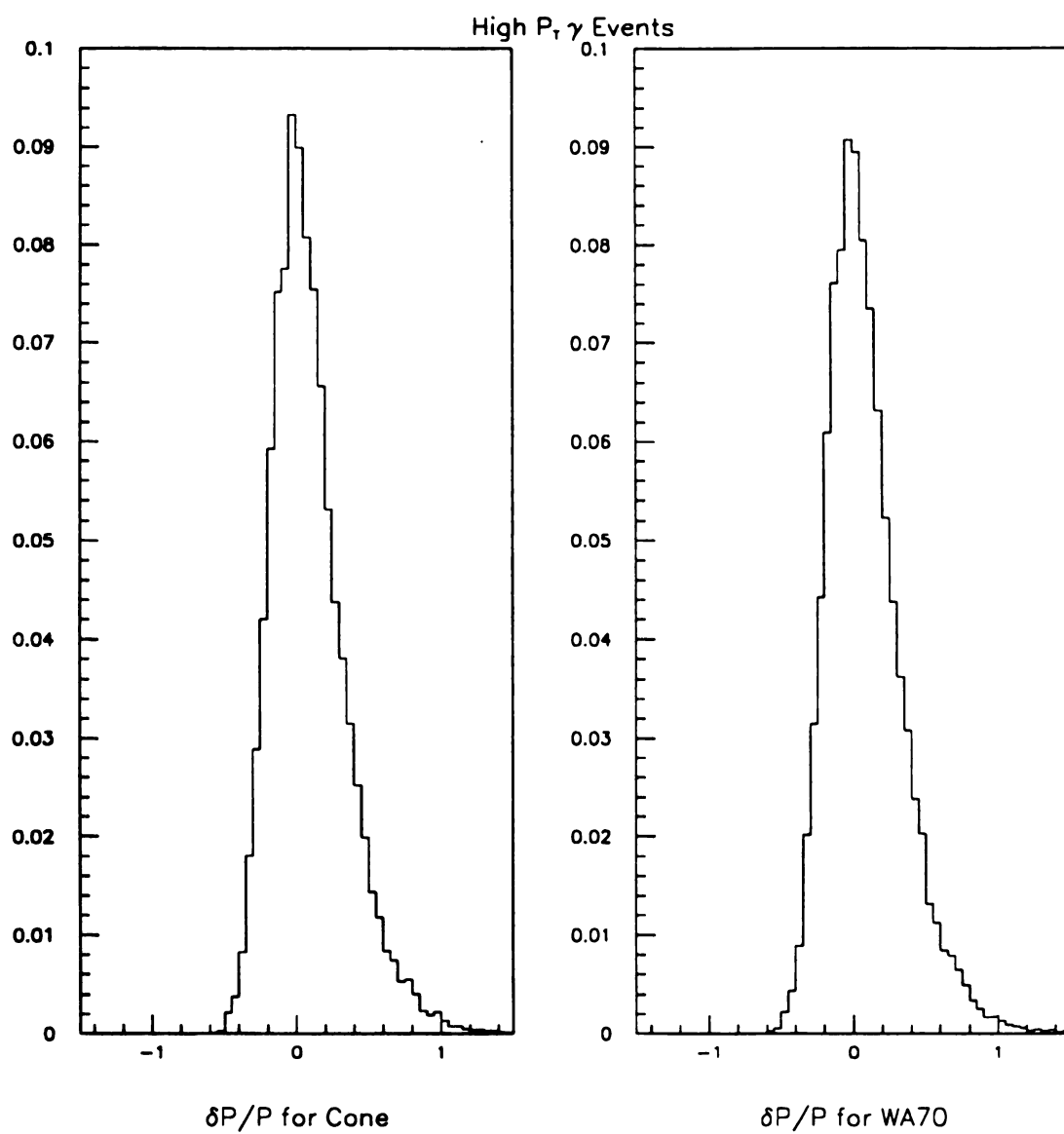


Figure 6.7: Resolution plots of the reconstructed jet momentum for γ triggers integrated over the acceptance.

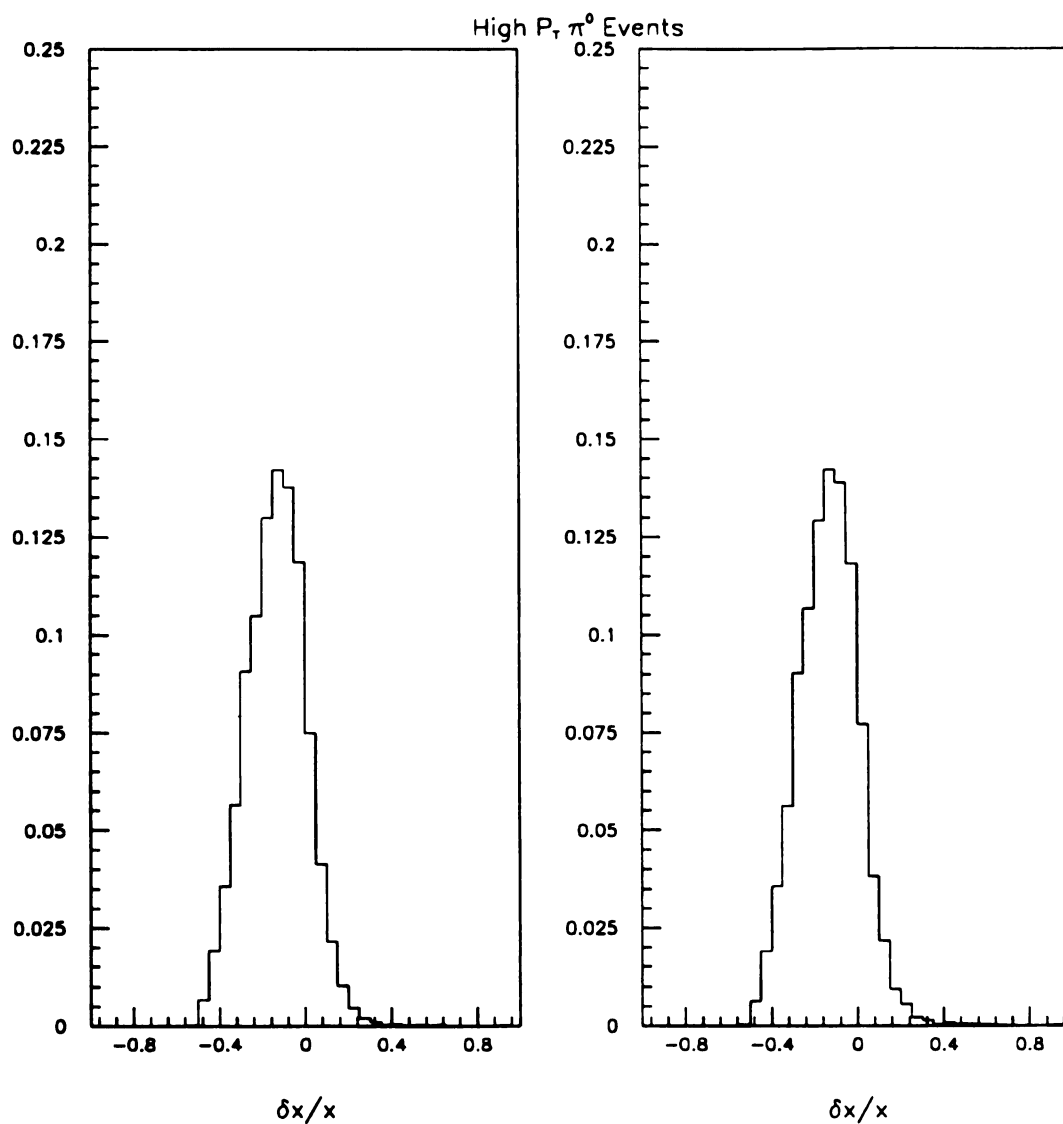


Figure 6.8: $\delta x/x$ resolution plots for parton momenta in high $p_\perp \pi^0$ events, integrated over the acceptance.

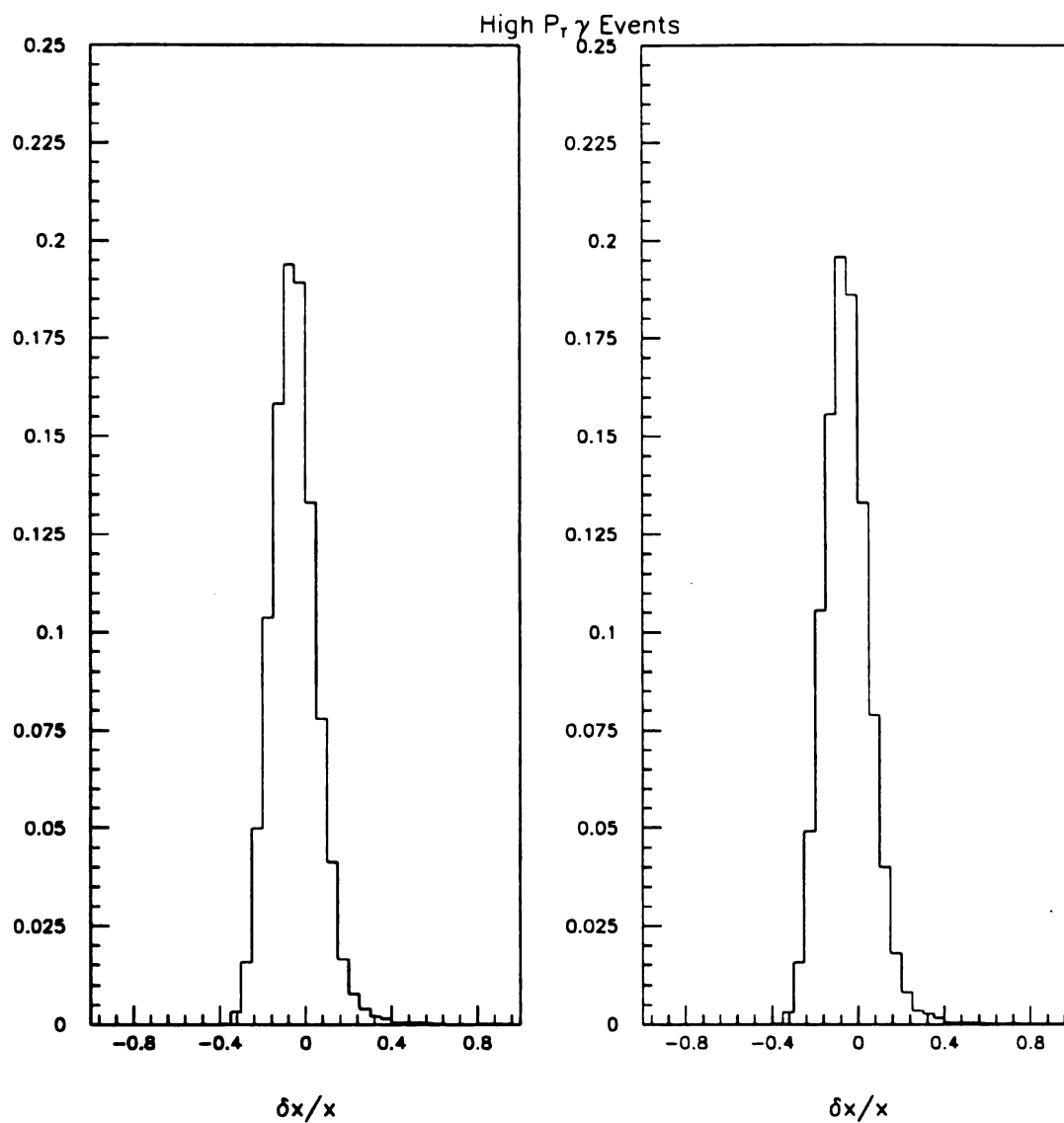


Figure 6.9: $\delta x/x$ resolution plots for parton momenta in high p_{\perp} single photon events, integrated over the acceptance.

will be observed in $\cos \theta^*$ and M as well. From the lack of sensitivity to a particular jet algorithm, even under a reasonable variation of its parameters, it can be concluded that the information required for this analysis is contained in the leading jet particles. This property is an artifact of the independent fragmentation scheme, but it appears to adequately represent the data for the task at hand.

6.4 MEASUREMENT OF $\cos \theta^*$ AND M

For the studies of $\cos \theta^*$ and M only the Cone algorithm will be utilized. There is still the issue of what it means to measure these quantities. By measuring the $\cos \theta^*$ and M distributions for the $\gamma + \text{jet}$ and $\pi^0 + \text{jet}$ systems it is hoped that one is essentially reconstructing the same distributions for the final state partons. To check whether or not this is indeed the case the angular and invariant mass distributions at the parton level will be compared to those reconstructed from the complete event generation. The parton level distributions will be constructed from ISAJET data generated without any evolution (k_\perp smearing, underlying event) or hadronization processes activated.

There are several general kinematical cuts that will be applied to the monte carlo data in performing this study, and in subsequent studies with the real data. Because the possibility exists for misreconstructing the recoil jet's direction, unphysical values for the jet's momentum and/or the parton momentum fractions may occur. By definition x_1 and x_2 can never be negative, but they can exceed 1. Such misreconstructed events will be eliminated from consideration by imposing the following kinematical constraints

$$\begin{aligned}
 P_{\text{JET}} &\leq \frac{\sqrt{s}}{2} \\
 x_1 &\leq 1 \\
 x_2 &\leq 1
 \end{aligned}
 \tag{6.4}$$

6.4.1 $\cos \theta^*$

Figure 6.10 illustrates the effects of applying those cuts in succession that provide uniform acceptance in $\cos \theta^*$. Clearly the edges of the reconstructed distribution rise relative to the central region in accordance with the discussion presented in the first chapter. The smearing observed in the reconstructed parton momentum fractions is also present in M . In addition, this smearing is different for γ s and π^0 s. This doesn't compromise the M cut's effectiveness, however. M is proportional to the p_\perp of the trigger particle, and it is the p_\perp cut on the data which introduces the bias in $\cos \theta^*$. So, if M is cut on accordingly, the bias is removed. Figure 6.11 shows the η_B distribution generated by ISAJET, and the interval of η_B for which there is uniform acceptance in $\cos \theta^*$. Any smearing in this variable will tend to "feed" down from bins of smaller η_B to bins of larger η_B . Hence, the smearing may produce a net loss of events, but it will not affect the reconstructed distribution's shape provided the smearing is uniform over the acceptance used in constructing $\cos \theta^*$.

The absolute $\cos \theta^*$ distributions for π^0 s and direct photons are shown in Figures 6.12 and 6.13 respectively. The $\cos \theta^*$ distribution for π^0 s agrees very well with the one corresponding to just 2-2 parton scatters. The parton distribution is plotted in Figure 6.14 as a smooth curve. All of the parton level distributions are referred to as the generated distributions. The parton level distribution for direct photon events, however, appears to rise faster than the reconstructed distribution. The effect is not very large, and the ability to discriminate between the two types of events in $\cos \theta^*$ is not compromised. The reconstructed monte carlo $\cos \theta^*$ distributions will be used in comparing these results with the actual data.

6.4.2 Cross Sections in M

Reconstructed invariant mass cross sections for high p_\perp π^0 and direct photon events are displayed in Figures 6.14 and 6.15 respectively. Again the corresponding

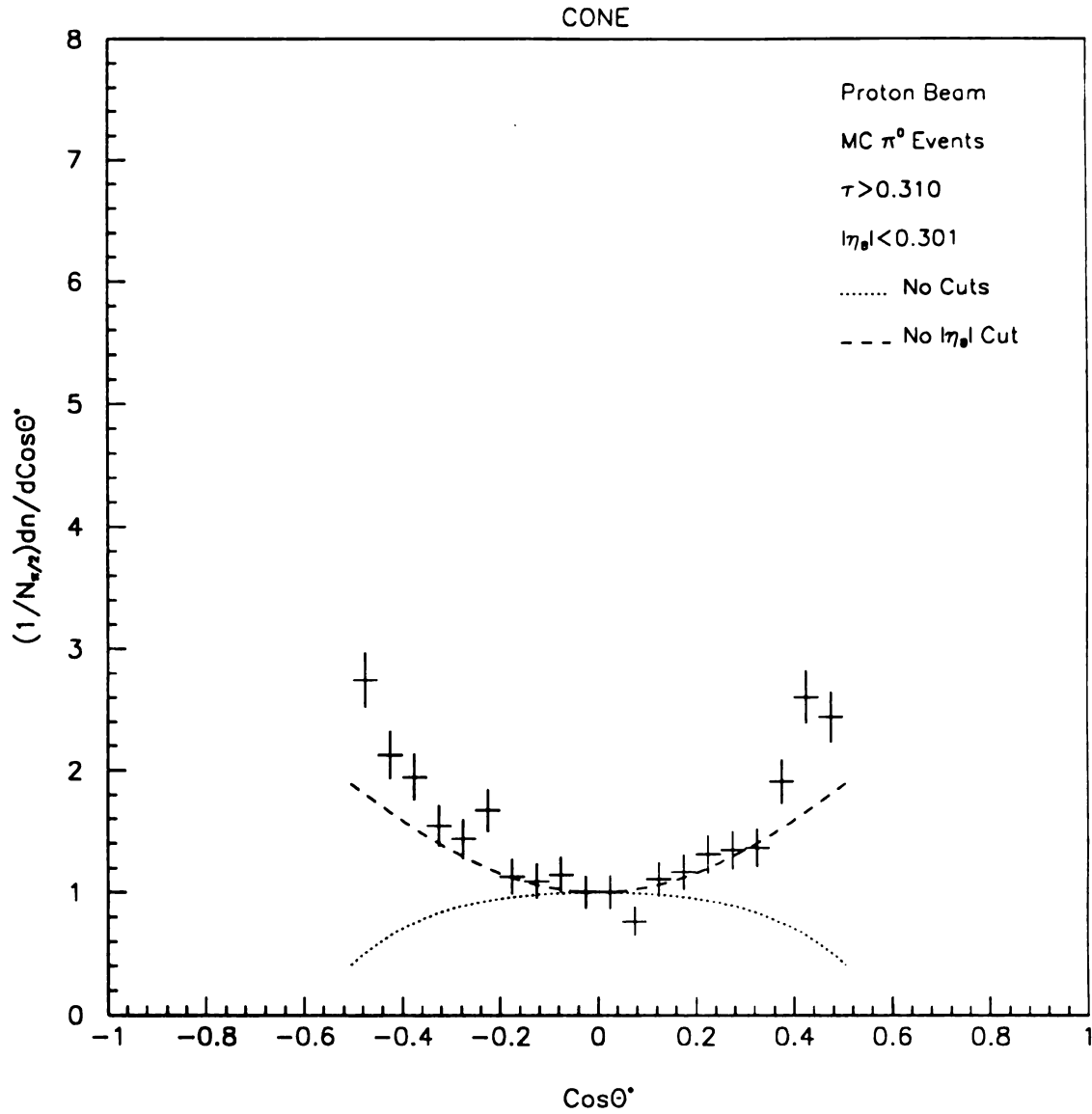


Figure 6.10: Effects of M and η_B cuts which unbias the reconstructed $\cos \theta^*$ distribution.

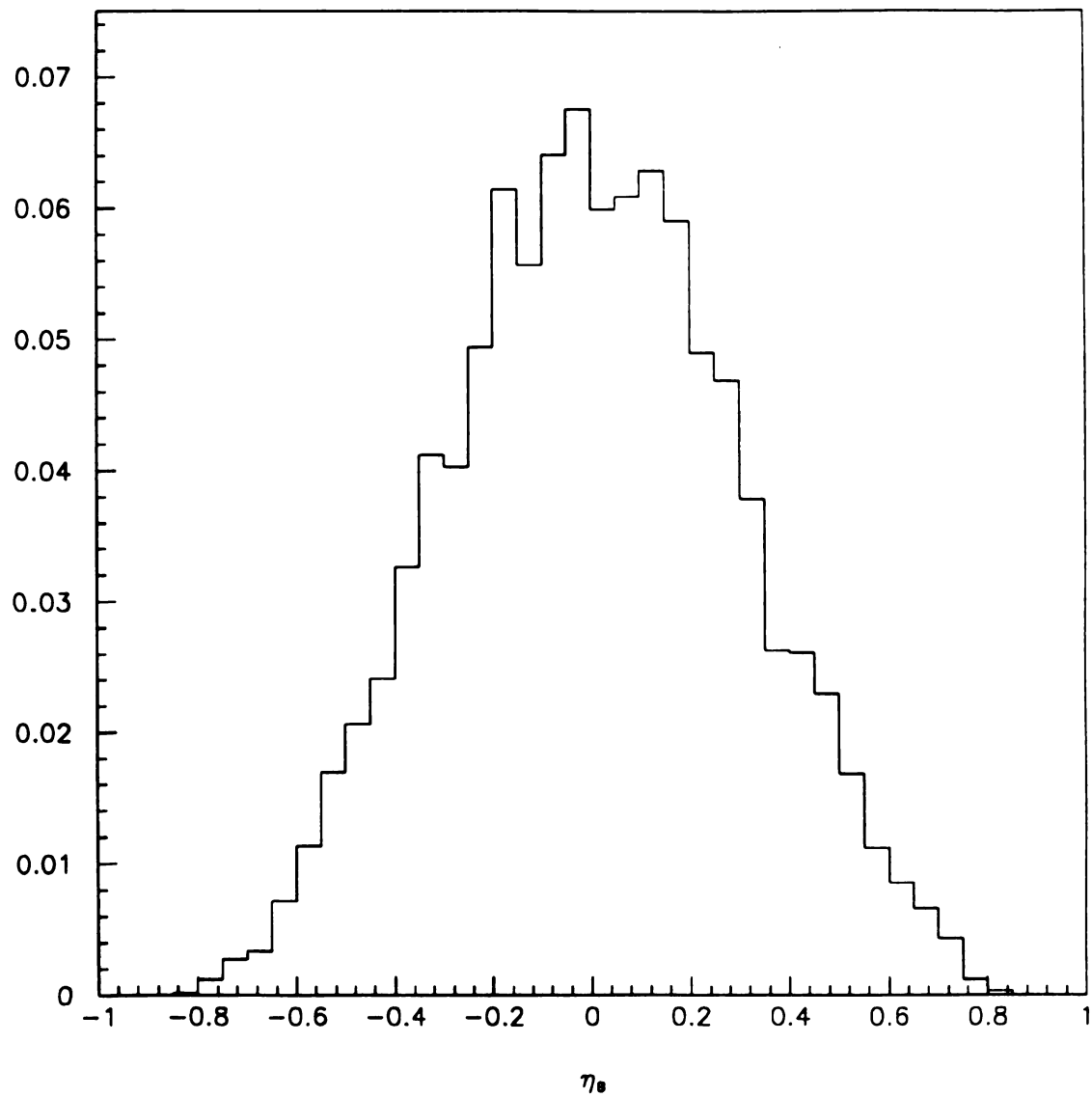


Figure 6.11: η_B for high p_\perp π^0 s produced via proton-nucleus collisions.

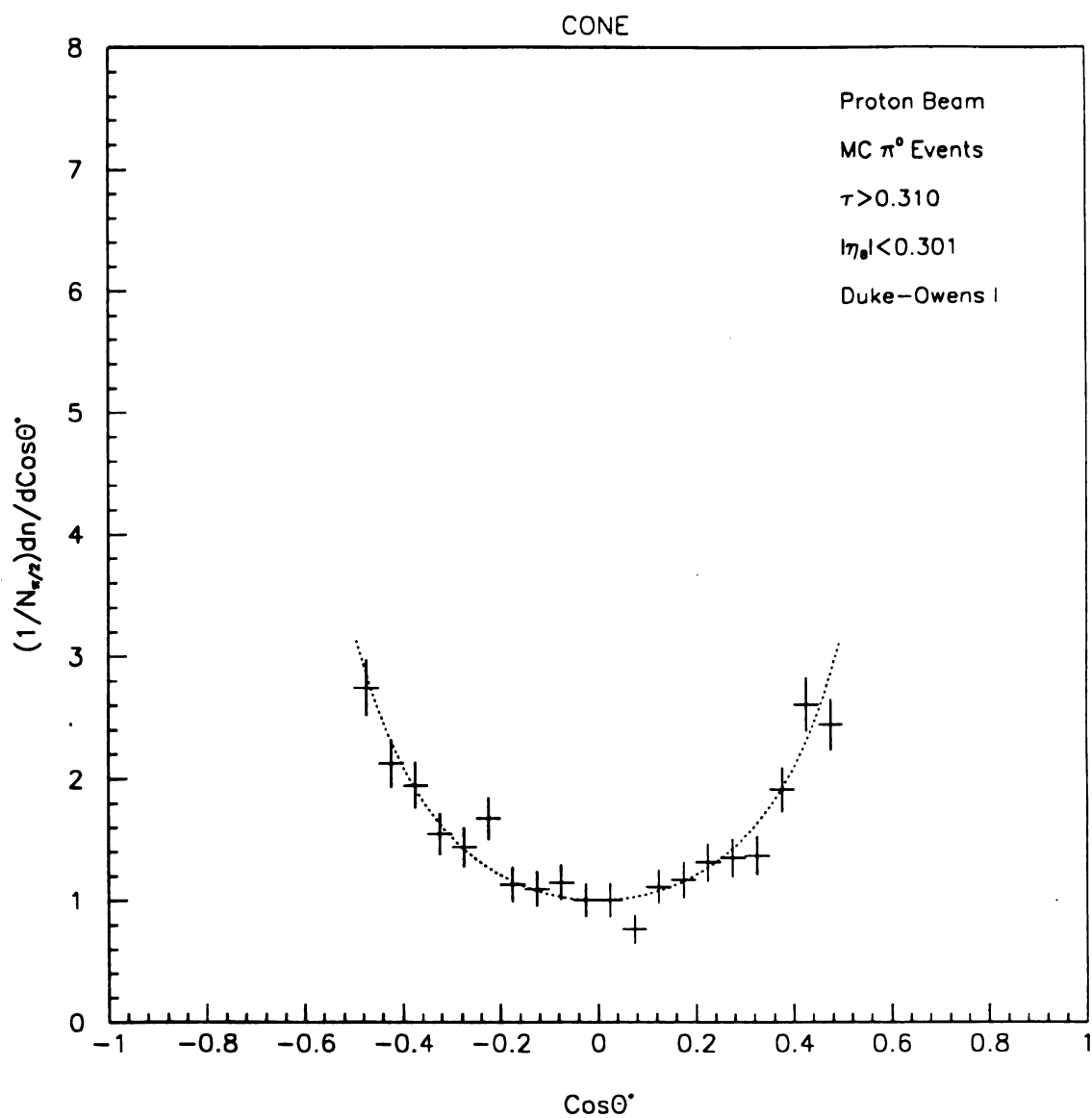


Figure 6.12: Reconstructed and parton level $\cos\theta^*$ distributions for high p_{\perp} π^0 events. The parton level distribution is shown as a smooth curve.

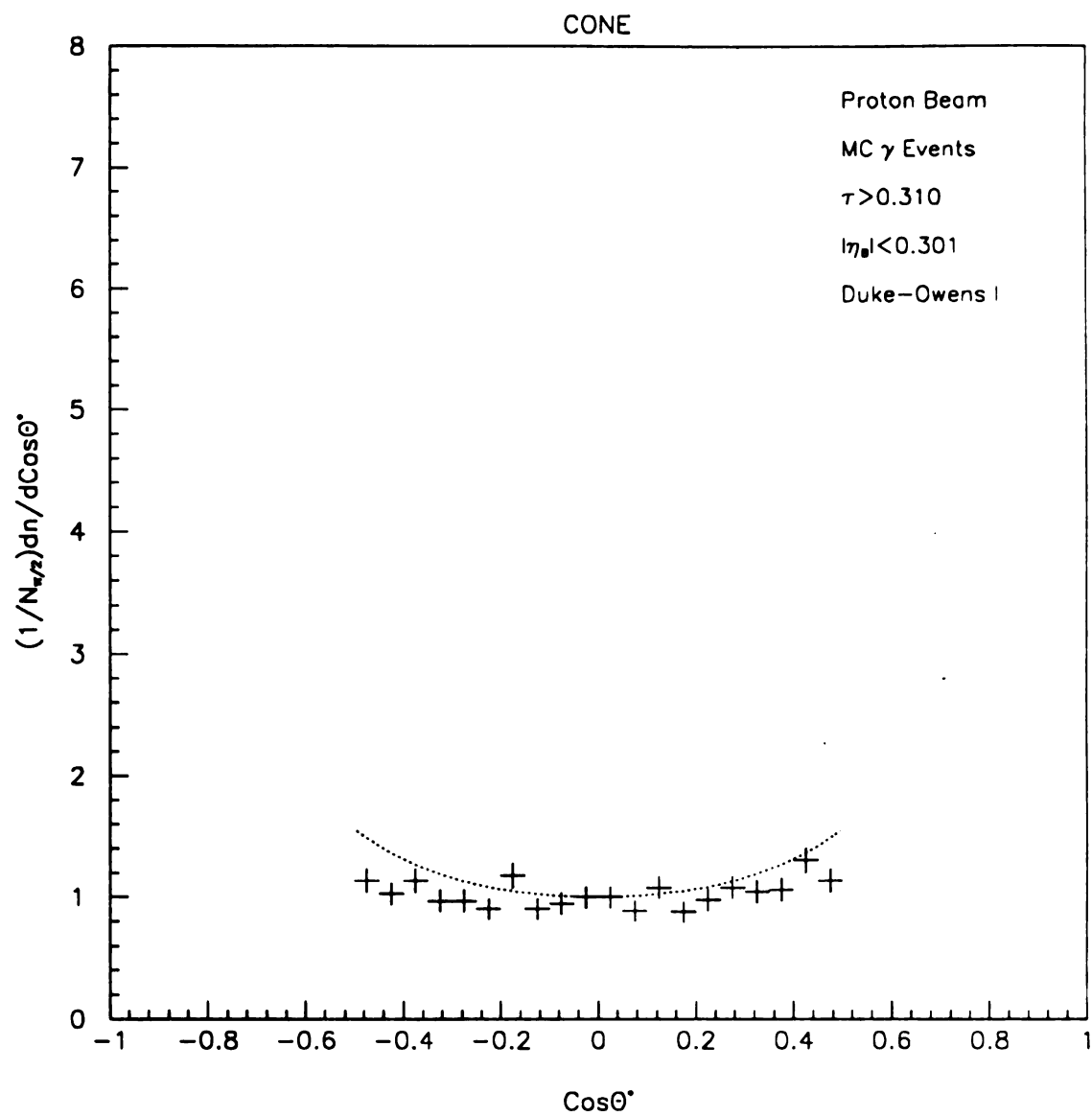


Figure 6.13: Reconstructed and parton level $\cos\theta^*$ distributions for high p_{\perp} single photon events. The parton level distribution is shown as a smooth curve.

parton level (generated) distributions are superimposed as smooth curves. These cross sections have been normalized according to the convention of ISAJET version 6.36. They are unbiased with respect to the trigger threshold, having a cut in $\cos \theta^*$ of ± 0.4 applied to them along with a corresponding cut in $M(\tau)$. The η_B cut is unnecessary in obtaining uniform acceptance in M because the geometric losses are the same for all bins in M allowed by the $\cos \theta^*$ and M cuts.

The reconstructed M distribution for direct photon events, shown in Figure 6.15, is shifted above the corresponding distribution for pure parton scatters. The p_\perp balancing and massless jet assumptions used in the reconstruction procedure tend to cancel one another in the calculation of M . However, it appears that the effect of p_\perp balancing is dominant. What is happening is that hard scatters are generated below the p_\perp of the γ , but are evolved upwards in p_\perp by the k_\perp mechanism. Some of these events get reconstructed and pass all of the analysis cuts. Because the cross section falls steeply with M , these events produce a net enhancement of the reconstructed cross section across the measured spectrum.

Besides the effect of k_\perp smearing, the π^0 cross section shown in Figure 6.14 has an additional smearing from ignoring the π^0 's fragmentation function, *i.e.* z is assumed to be 1. This effect results in a change of slope for the reconstructed distribution compared to the parton level distribution because a fraction of higher mass events are reconstructed as lower mass events.

While one can always compare reconstructed monte carlo distributions with data, there is still the question of whether the smearing is the same in both cases. However, these effects should not change in the π^- data so a good method of comparison is to plot the ratios of cross sections for π^- to proton beams. The ratios must be taken between spectra of the same trigger particle type. Otherwise, the systematics will not divide out, and the monte carlo comparisons will be more ambiguous. As was pointed out in Chapter 1, it is the ratio for direct photon events which is of primary

interest. The corresponding ratio for π^0 s can serve as a benchmark in judging the agreement between data and monte carlo.

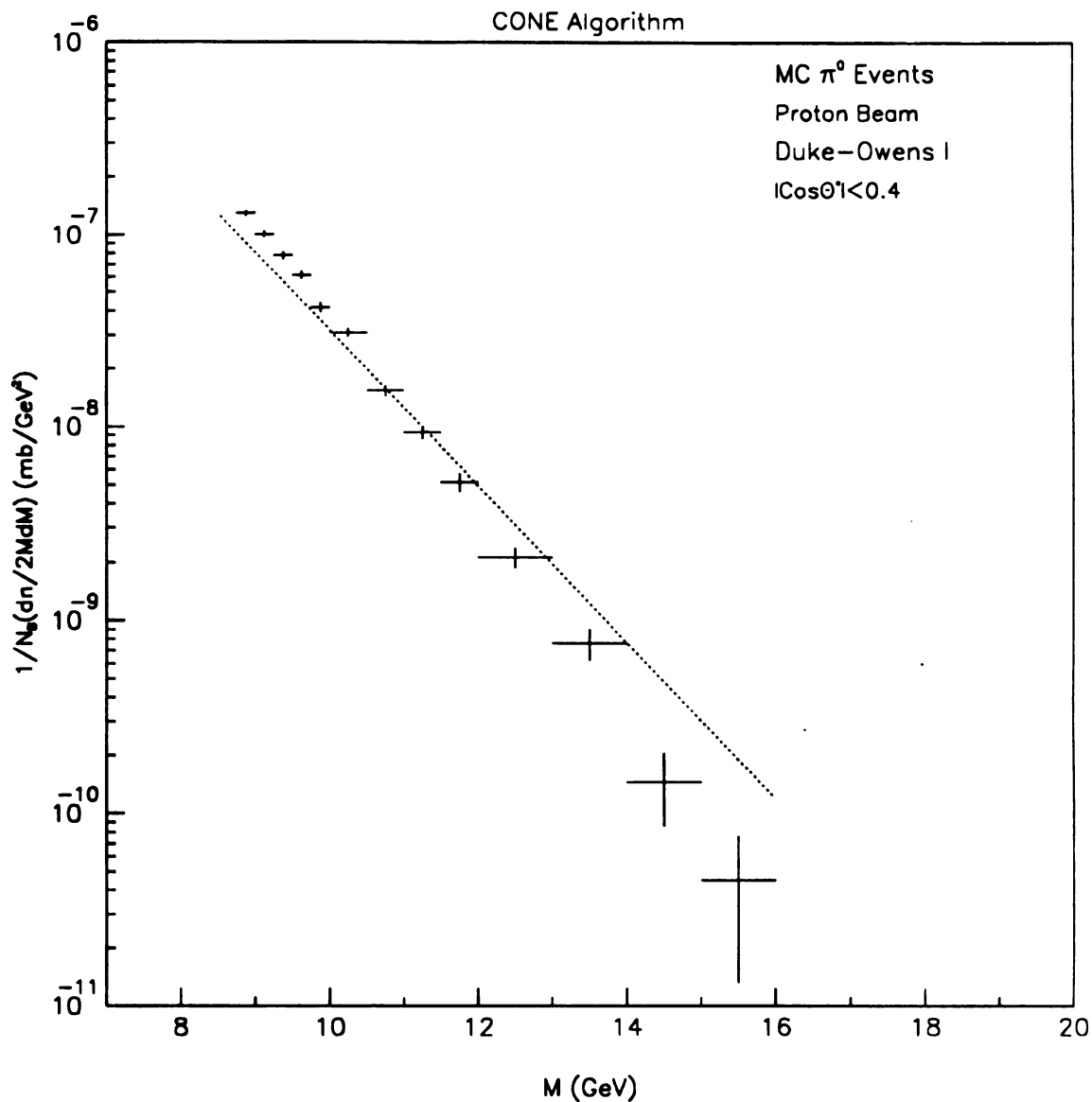


Figure 6.14: Reconstructed and parton level M distributions for high p_{\perp} π^0 events. The parton level distribution is shown as a smooth curve.

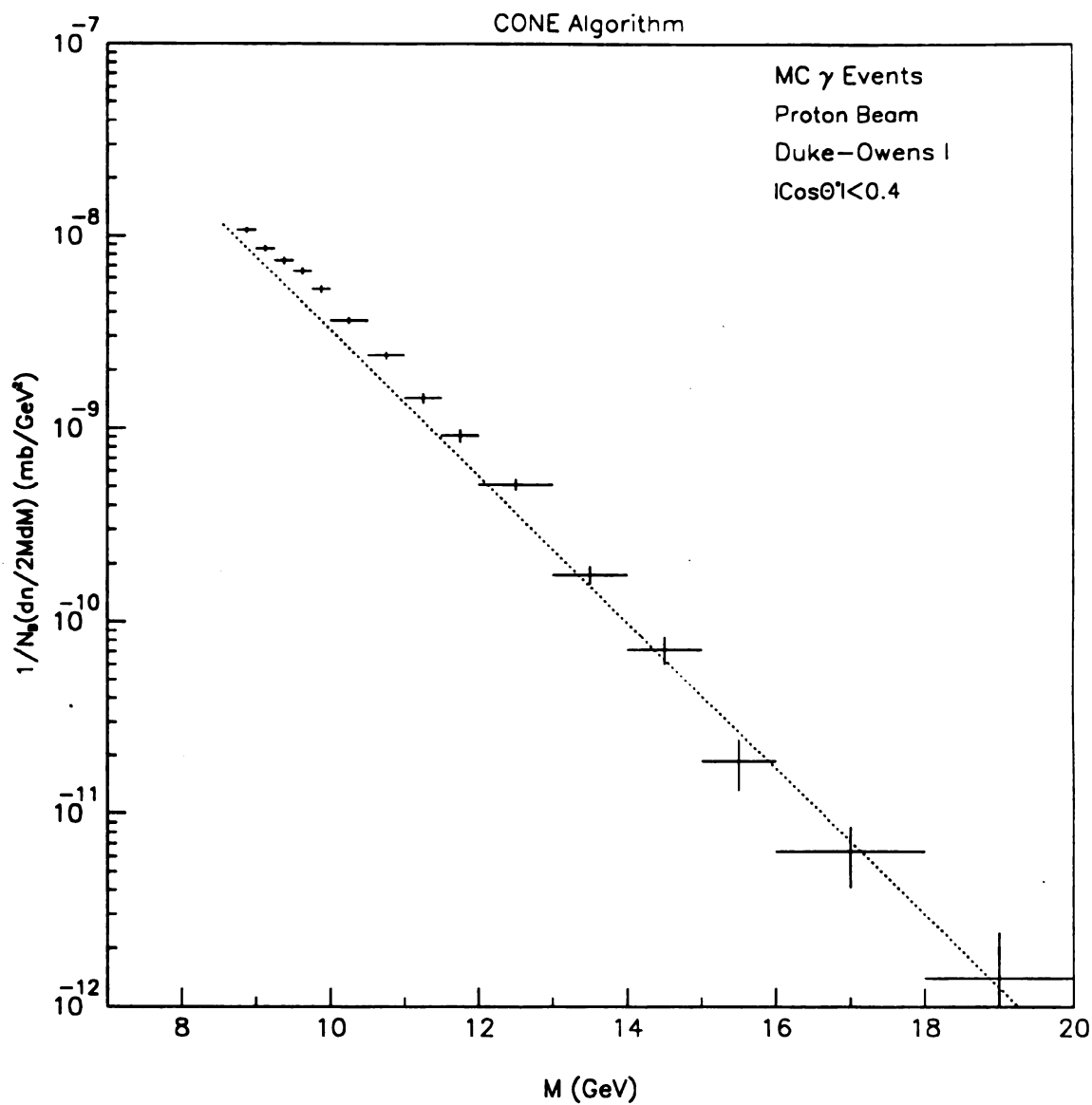


Figure 6.15: Reconstructed and parton level M distributions for high p_{\perp} direct photon events. The parton level distribution is shown as a smooth curve.

Chapter 7

Final Results

The last chapter demonstrated the feasibility of studying $\gamma + \text{jet}$ and $\pi^0 + \text{jet}$ systems within the kinematic regime accessible by the experiment. The jet reconstruction techniques that have been developed will be used in reconstructing the M and $\cos \theta^*$ distributions from the real data. Here, the emphasis is on comparing γ and π^0 distributions. Attempts will be made to show just how different corresponding distributions are. However, comparisons with ISAJET will also be performed. In particular, the data will be examined to see whether or not the Duke-Owens I or Duke-Owens II [46] structure functions are preferred.

Because of its simplicity and explicit use of correlations among recoil charged particles, indicative of jet structure, the cone algorithm is used exclusively in the following analysis. A complete description of this algorithm is found in the previous chapter. Only jets reconstructed between $\pm .85$ in pseudorapidity are used in obtaining the mass and angular distributions of $\gamma + \text{jet}$ and $\pi^0 + \text{jet}$ systems.

There are a number of corrections applied to high p_{\perp} π^0 and γ events. They include corrections for trigger inefficiency, reconstruction efficiency, acceptance (relevant for π^0 s which decay into two photons), for photons converting into e^+e^- pairs in the target, a correction to individual reconstructed photon energies, and corrections for whole event cuts. These corrections are applied on an event-by-event basis to all data distributions presented in the following figures. They are important in obtaining the correct shape of the $\cos \theta^*$ distributions, especially for π^0 s, and the absolute normalization of cross sections. The reader interested in the details of these corrections should consult Chapter 4, which discusses the selection of high p_{\perp} π^0 and γ events.

The ISAJET comparison involves generating monte carlo events with V6.36, and passing charged particles through a simple simulation of the tracking system. This

simulation takes into account the MWPC acceptance, the efficiencies of individual planes, and the effect of the analyzing magnet's field. A description of this simulator program is found in Chapter 3. The simulator's output is subsequently used in jet reconstruction. The mass and angular distributions are then constructed from the monte carlo data, using the same cuts in M , $\cos \theta^*$, η , and η_B as applied on the real data. The monte carlo distributions have been generated in the same kinematic range as the real data. Sets corresponding to different trigger thresholds were not generated, however. Both γ and π^0 monte carlo data sets have a trigger particle p_\perp cut of 4.0 GeV/c. All monte carlo distributions have been fitted with sundry functional forms; these fits are superimposed on the data as smooth curves.

Separate sets of monte carlo data have been produced with proton and π^- beam particles. Within each set are equal numbers of proton and neutron target hadrons. This is done in order to simulate the approximate isoscalar character of the target material. All coherent nuclear effects are ignored by this procedure as well as nuclear rescattering effects.

The standard ISAJET package is not equipped to simulate hadron collisions involving mesons. A member of the E706 collaboration, S. Mani, has provided an implementation for π^- and π^+ beams into the standard ISAJET program, as well as making the Duke-Owens set I (DOI) and Duke-Owens set II (DOII) structure functions available [47]. The point in studying these two sets is that they represent the limits of gluon "hardness" and "softness" via the value of η_G each one incorporates. The η_G parameter appears as an exponent in the following form both sets use for the gluon momentum distribution,

$$xG(x, Q_0^2) = A_G(1 + \gamma_G x)(1 - x)^{\eta_G} \quad (7.1)$$

Direct photon production is directly sensitive to the gluon distribution within hadrons, and should therefore be able to discriminate among the various choices for η_G partic-

ularly at high x values.

The hard scattering in ISAJET is a next to leading log calculation for π^0 production, but direct photons are generated at the Born level only. Furthermore, there is no Bremsstrahlung mechanism present for direct photon generation. It should be noted that a consistent generation of events with the DOI and DOII sets involves using different values of Λ_{QCD} . For DOI Λ_{QCD} must be set to 0.2 GeV/c, while for DOII a value of 0.4 GeV/c is required. All the monte carlo data has been generated with the following Q^2 definition,

$$Q^2 = \frac{\hat{s}\hat{t}\hat{u}}{(\hat{s}^2 + \hat{t}^2 + \hat{u}^2)} \quad (7.2)$$

The QCD radiative cutoff has been set at 6 GeV for final state radiation, and, as mentioned earlier, an intrinsic k_{\perp} value of 0.95 GeV/c has been employed. The scattered quarks and gluons are fragmented into hadrons using the independent fragmentation ansatz of Field and Feynman. This physics monte carlo provides for absolute normalization via a weighting function whose value is obtained event-by-event, and can be loaded as a weight for a particular histogram. Table 7.1 shows the number of events generated for each type of collision, trigger particle, and structure function set.

7.1 π^0 BACKGROUND SUBTRACTION

A general technique of constructing the π^0 background component of a given reconstructed photon distribution will now be discussed. This method is an extension of the one used for the inclusive photon p_{\perp} spectra. A description of the monte carlo used in obtaining the false direct photon p_{\perp} spectrum appears in Chapter 4.

The ratio of the false photon and monte carlo π^0 p_{\perp} spectra is taken bin-by-bin in order to produce a set of so called f_{gam} numbers. Each p_{\perp} bin of the π^0 spectrum, reconstructed from the actual data, is then weighted by the appropriate f_{gam} number; the resulting distribution represents the π^0 background present in the reconstructed

Table 7.1: Monte carlo data sets by collision and trigger particle type.

Trigger	Collision	Events for DOI	Events for DOI
π^0	PP	10143	10162
π^0	PN	10284	10018
π^0	π^- P	11424	10993
π^0	π^- N	11259	11013
γ	PP	10021	10290
γ	PN	9987	10108
γ	π^- P	11334	11152
γ	π^- N	11149	11352

photon p_\perp spectrum. Subtraction of this background from the reconstructed photon spectrum yields the actual direct photon p_\perp distribution in the data. A major advantage of this technique is the final result's stability against small differences in energy scale between the real data and the monte carlo.

The γ/π^0 ratios in p_\perp for π^- and proton data are displayed in Figure 7.1 and Figure 7.2, respectively. Each figure has a plot of the unsubtracted ratio together with the estimated background as well as a plot of the subtracted γ/π^0 ratio. All distributions have been integrated over the rapidity interval $-.85$ to $.85$; the f_{gam} numbers used in the ensuing analysis are also integrated over this interval. Notice the much stronger rise with increasing p_\perp for the π^- data than for the proton data. Such behavior is consistent with two production mechanisms for direct photons in π^- beam as opposed to just one in proton beam.

These ratios are consistent within errors with those of the inclusive analysis group's. The γ/π^0 ratios for $|y_{trig}| \leq 0.7$ have been constructed also, and found not to differ significantly from the ones shown. There are three small systematic corrections

applied to the inclusive analysis group's data that are currently unavailable in the DST library. It is assumed they are responsible for the observed differences. All of the following analysis ignores a rapidity dependence for the f_{gam} numbers. Such a consideration is beyond the available statistics.

The set of f_{gam} numbers used on the inclusive spectra can also be used to construct the background distributions in $\cos \theta^*$ and M . First, scatter plots of $\cos \theta^*$, M , or any other two-body variable for that matter versus p_\perp are constructed using events containing a high $p_\perp \pi^0$. Second, a given scatter plot is unpacked and each slice in p_\perp is weighted by the appropriate f_{gam} number. Finally, the two dimensional distribution is integrated in p_\perp , resulting in the π^0 background distribution for a particular two-body variable. This background distribution is then subtracted from the corresponding reconstructed photon distribution to obtain the estimated true direct photon spectrum in that variable.

This background subtraction procedure ignores a possible rapidity dependence for the f_{gam} numbers. However, because of the η_B distribution's width a particular value of $\cos \theta^*$ or M is integrated over a large part of the acceptance in rapidity. Thus, one does not expect a significant dependence of the background in $\cos \theta^*$ or M on rapidity. This hypothesis has been checked by employing the tracking information in the data-driven monte carlo, which was used to calculate the f_{gam} numbers. The fake γ angular and invariant mass distributions were constructed, and the ratios of these distributions to those for the reconstructed monte carlo π^0 events were then taken. The ratios are just the spectra of f_{gam} numbers in $\cos \theta^*$ and M . These f_{gam} numbers were then used to construct the π^0 background distributions in $\cos \theta^*$ and M for the real data in the same manner as is done in p_\perp . The two methods of background subtraction yield the same π^0 background spectra well within the uncertainties. The first method has been chosen because of its superior precision since the calculation of

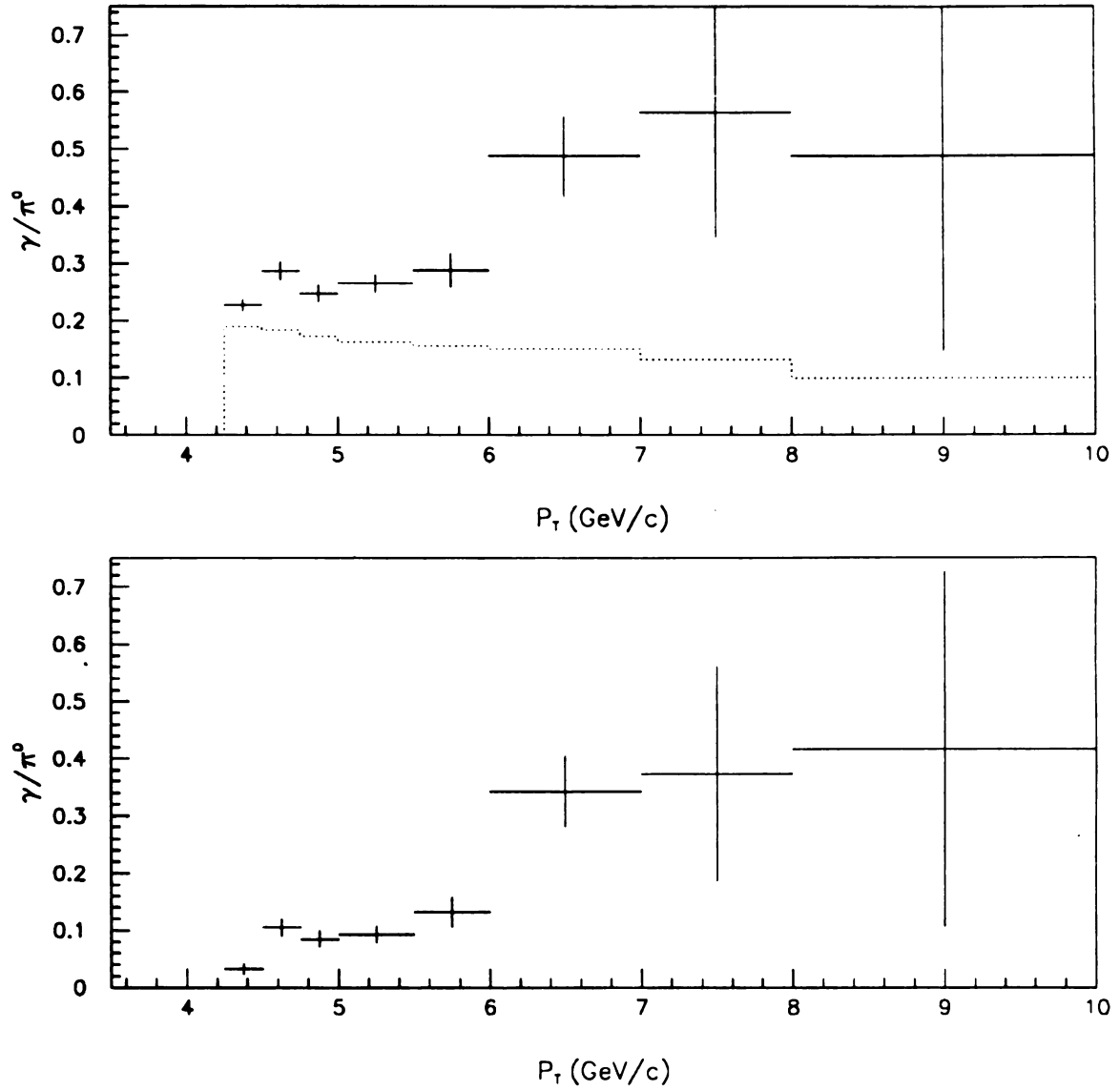


Figure 7.1: Inclusive γ/π^0 ratio for π^- -nucleus collisions

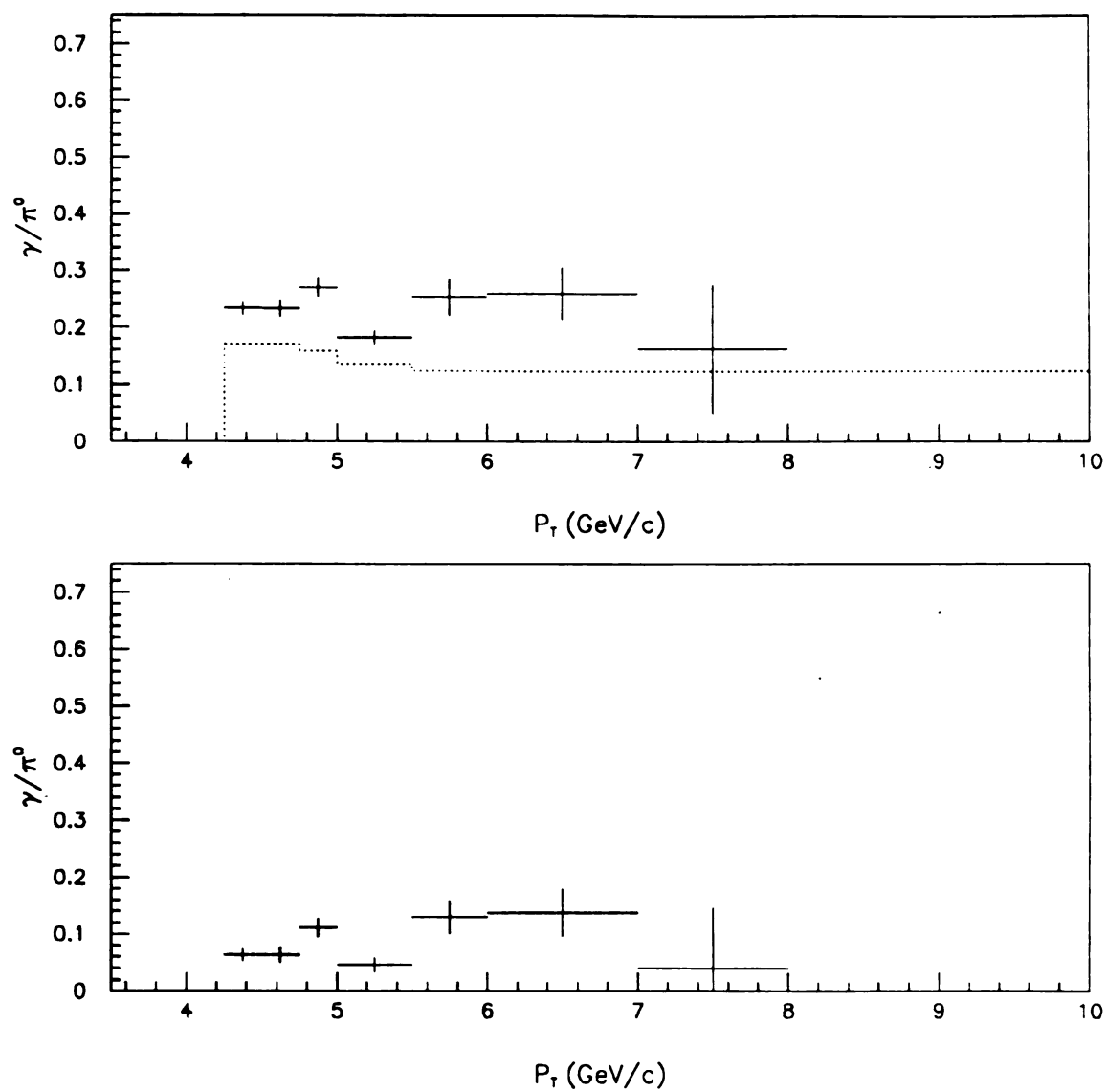


Figure 7.2: Inclusive γ/π^0 ratio for proton-nucleus collisions

the f_{gam} numbers does not depend on the jet reconstruction efficiency.

To facilitate the analysis the normalization of $\cos \theta^*$ and M distributions always occurs after subtraction. Also, the background histograms are fitted to sundry functional forms, discussed below, and it is the fitted results which are subtracted off of the reconstructed photon distributions. Such a procedure reduces the uncertainty in the subtraction, reducing the error bars of the true direct photon distribution. Figure 7.3 shows actual scatter plots of $\cos \theta^*$ and M versus p_\perp for high p_\perp π^0 events.

7.2 RESULTS FOR $\cos \theta^*$

The $\cos \theta^*$ distributions obtained from the data will now be presented along with the ISAJET results for comparison. Plots for π^0 and γ triggers in proton and π^- beams are shown in the following figures. In addition, separate histogram sets have been generated for the standard p_\perp cut of 4.25 GeV/c (large background), and for a cut of 5.0 GeV/c (small background). Since no significant forward-backward asymmetries have been observed, all results are folded into the interval $0 \leq \cos \theta^* \leq 1$.

The emphasis here is on the difference in shape between $\gamma + \text{jet}$ and $\pi^0 + \text{jet}$ angular distributions. As pointed out at some length in the Introduction, QCD predicts a difference between γ s and π^0 s in this variable. Direct photon subprocesses contain only quark (fermionic) propagators at the Born level while π^0 events possess a number of subprocesses with gluon (bosonic) propagators in lowest order. Fermionic propagators result in at most a $1/(1 \pm \cos \theta^*)$ dependence. Bosonic propagators, on the other hand, yield $1/(1 \pm \cos \theta^*)^2$ terms in their respective angular distributions.

A further refinement to the general background technique has been added for the $\cos \theta^*$ analysis. All fake γ distributions have been fitted with the following 1-parameter function,

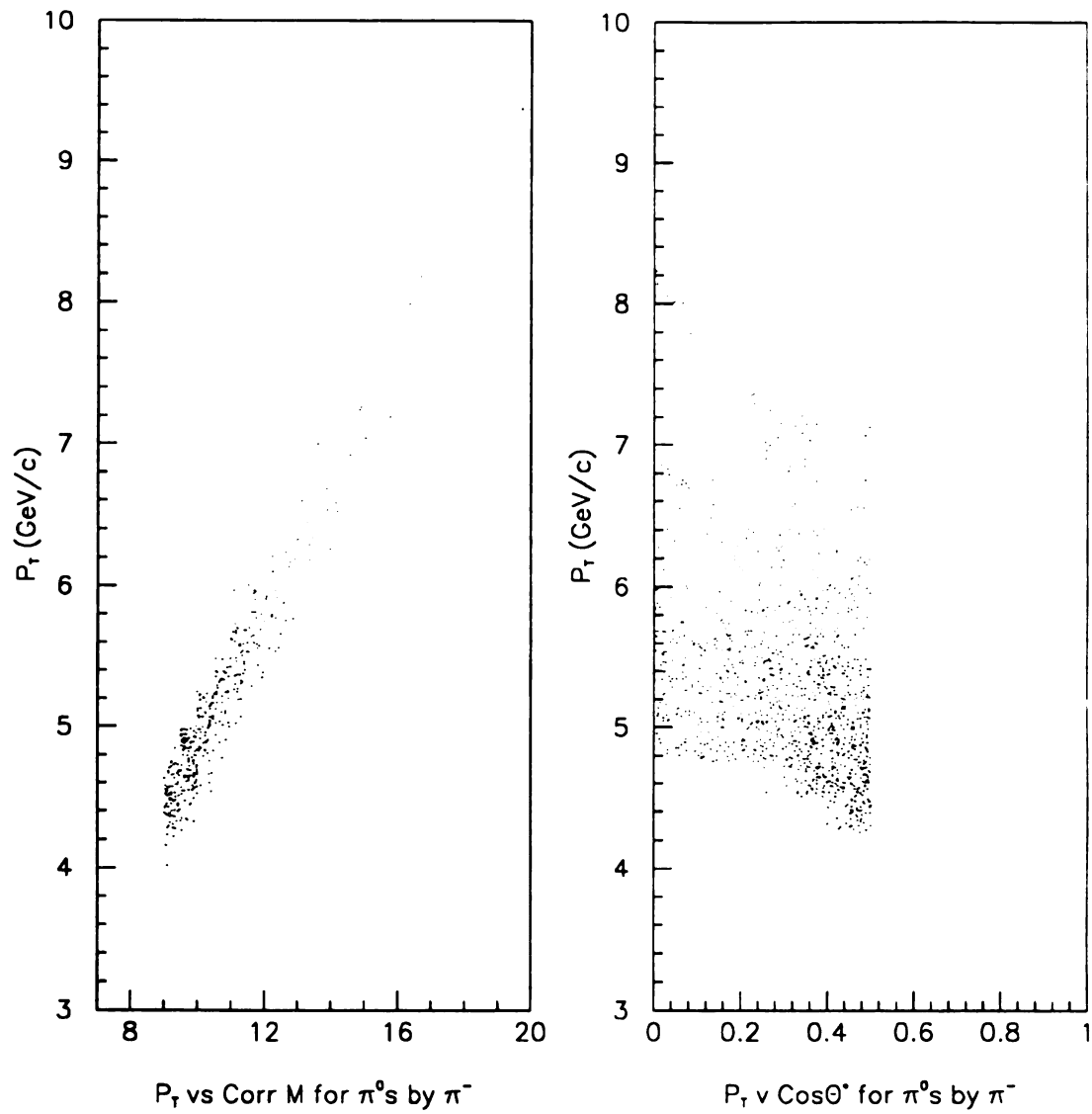


Figure 7.3: Scatter plots of $\cos\theta^*$ and M versus p_\perp for π^0 events

$$\left. \frac{dn}{d \cos \theta^*} \right|_{fgam} = \frac{\langle N_{\frac{\pi}{2}} \rangle}{2} \left[\frac{1}{(1 + \cos \theta^*)^\alpha} + \frac{1}{(1 - \cos \theta^*)^\alpha} \right], \quad \alpha \in \mathcal{R} \quad (7.3)$$

α is taken as real since there is no a priori reason for it to be integer. The smearing in the reconstructed recoil jet's direction together with variations in the π^0 background across the LAC's acceptance mitigate against such an assumption. This functional form has yielded an excellent $\chi^2 (\lesssim 1)$ on all calculated backgrounds. The uncertainty in α , $\delta\alpha$, obtained from the fitting procedure was used to compute $\delta dn/d \cos \theta^* |_{fgam}$ point-by-point. A histogram was filled for each fit; the contents and errors for each bin were computed from the mean values of the integrals of $dn/d \cos \theta^* |_{fgam}$ and $\delta^2 dn/d \cos \theta^* |_{fgam}$ over each bin. What this procedure does is make the backgrounds' contributions to the uncertainty in the corresponding subtracted photon distributions negligible.

Finally, a word needs to be said about normalization. Because only the shapes of the angular distributions are of interest, and in keeping with standard practice, all $\cos \theta^*$ distributions are normalized to 1 at $\cos \theta^* = 0$, ($\theta^* = 90^\circ$). The angular distributions are flat near $\cos \theta^* = 0$ so the two central bins are averaged; this average is used to scale all other bins. The bin closest to $\theta^* = 90^\circ$ is set to 1.

The absolute angular distributions (M and η_B cuts) for the standard p_\perp cut are displayed in Figure 7.4 and Figure 7.5. In Figure 7.6 one finds the corresponding γ/π^0 ratios. The ratios are formed from distributions without η_B cuts. As far as geometry is concerned, the systematic losses are the same for γ s and π^0 s so they should divide out in the ratio anyway. Furthermore, these losses do not drastically affect the data; they represent $\lesssim 50\%$ effects. This allows the γ/π^0 ratios to have greater statistical significance without being compromised by systematic effects.

One obvious feature in the absolute $\cos \theta^*$ plots is the size of the direct photon distributions' error bars. The backgrounds are large at low p_\perp as manifested in the inclusive γ/π^0 ratios shown earlier. This together with a steeply falling cross section in

p_{\perp} causes a sharp increase in the relative uncertainties on the subtracted distributions over those in the unsubtracted ones. For this reason, the single photon histograms have been rebinned to half as many bins as those for the π^0 events.

The plots in the foregoing figures show the expected trends and differences for the π^- data only. The γ/π^0 ratio is clearly different from 1, which is the result if no shape difference is present. There appears to be no statistically significant difference between γ s and π^0 s in the proton data. The size of the direct photon distribution's error bars indicate a very large background given the available statistics. Even if one were to conjecture that the background had been underestimated in this case, and that this was the cause for the shapes being so similar, the errors would increase still further destroying any significance of the result with an improved background estimate.

As far as the ISAJET comparison is concerned, the $\pi^0 + \text{jet}$ distributions show a dramatic agreement with the QCD prediction! The monte carlo data have also been fitted with the form given by equation 7.1. Such a procedure has been recommended by Owens [6]. However, α is allowed to take on real values in order to accommodate the smearing in the reconstructed jet's direction. The results from the fitting procedure have been superimposed on the real data. Each plot has two curves associated with it. One curve corresponds to the DOI set of structure functions, and the other to the DOII set. Both sets agree with the data there being no significant preference of one over the other. This is consistent with naive expectations. While the parton momentum distributions are different for the two sets, especially for the gluons, they do not result in monte carlo data being generated in dramatically different regions of phase space. Of course, the large uncertainties on the direct photon plots don't allow for much discrimination anyway.

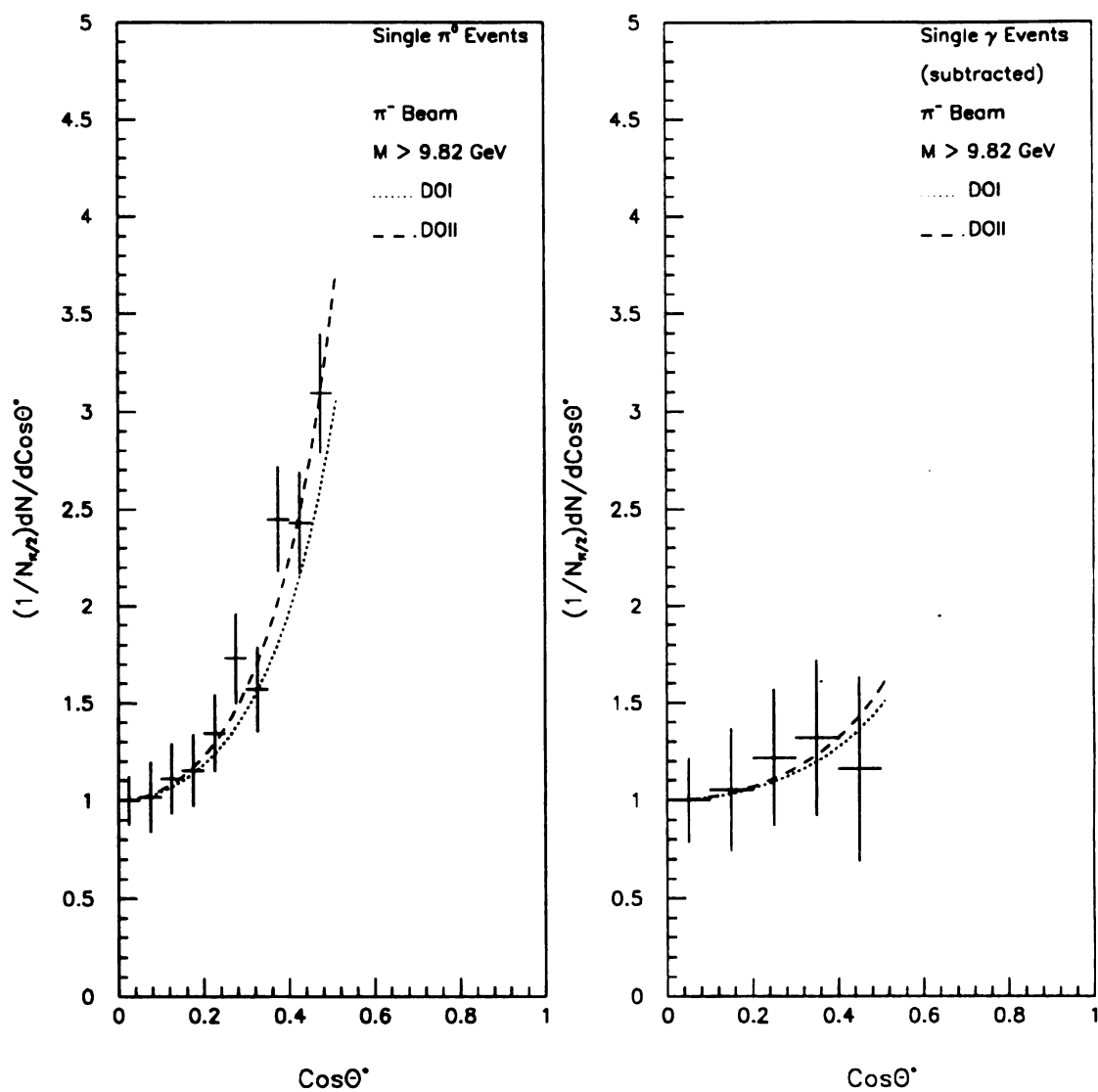


Figure 7.4: Absolute $\cos \theta^*$ plots for γ s and π^0 s in π^- data

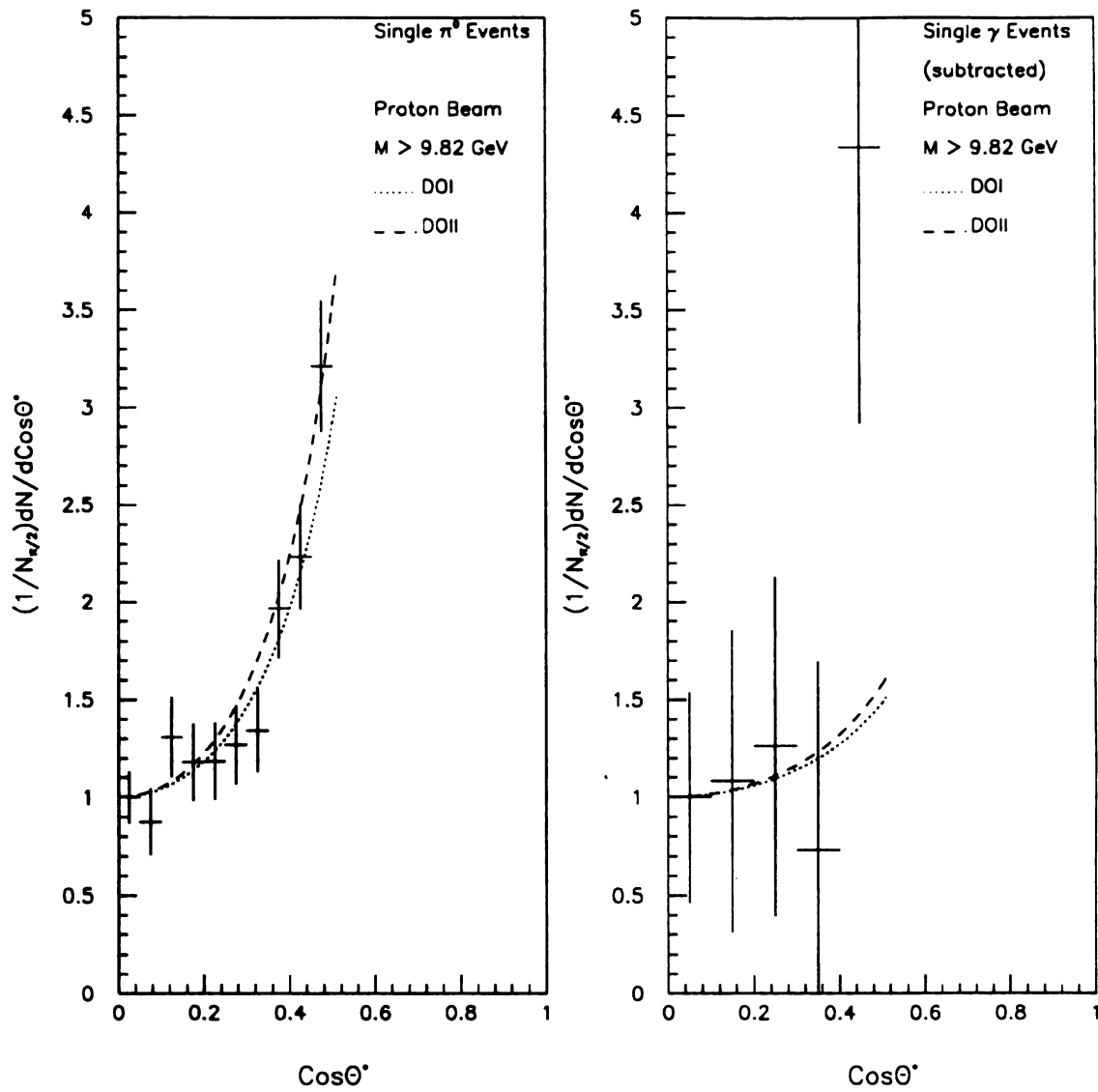


Figure 7.5: Absolute $\cos \theta^*$ plots for γ s and π^0 s in proton data

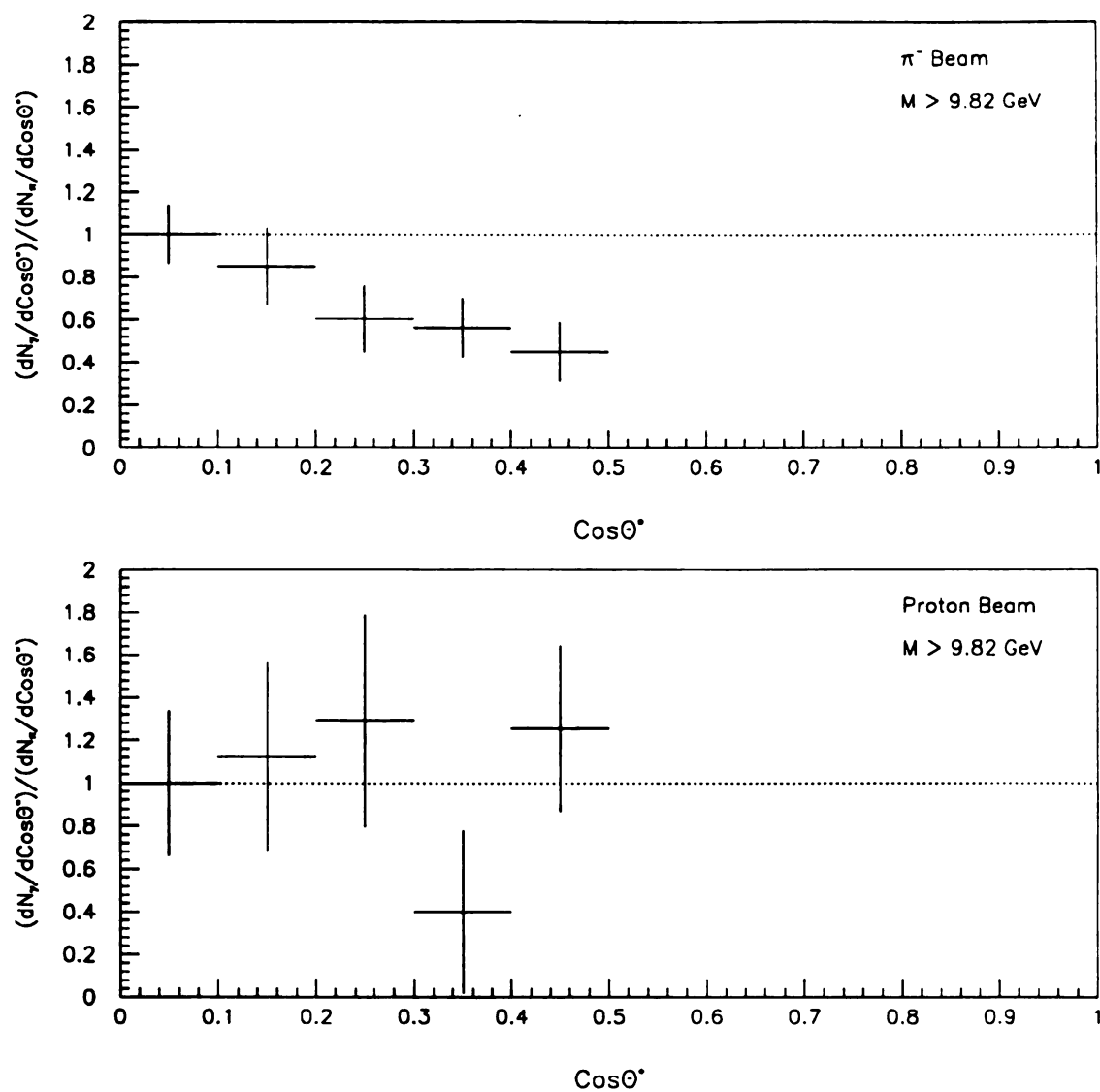


Figure 7.6: γ to π^0 ratio in $\cos\theta^*$ for π^- data (top) and proton data (bottom)

Figures 7.7 through 7.9 display another set of $\cos \theta^*$ plots for $p_{\perp} \geq 5.0 \text{ GeV}/c$. The π^- data shows the same trends as the low p_{\perp} sample albeit with greater significance. The proton data is quite different though. At high p_{\perp} it has the same behaviour as the negative data! These trends are expected from QCD as well. Of course, the observed change is due entirely to a change in the shape of the direct photons' angular distribution. An explanation for this change is that there is less π^0 background at high p_{\perp} . The difference between γ s and π^0 s in the high p_{\perp} proton data is not as significant as it is for the π^- sample, but the γ/π^0 ratio doesn't rise as fast for protons either.

The high p_{\perp} sample exhibits a direct photon signal without background subtraction as Figure 7.10 and Figure 7.11 reveal. Only the π^- data shows such an effect. This behavior is consistent with that observed in the $\Delta\phi$ distributions, presented in Chapter 5.

What appear to be definite differences between the $\gamma + \text{jet}$ and $\pi^0 + \text{jet}$ systems by visual inspection are quantified below. A simple way to do this is to compute the χ^2 difference between corresponding angular distributions as follows,

$$\chi_{\text{PDF}}^2 = \frac{1}{4} \sum_{i=1}^4 \left(\frac{(\cos \theta_{\gamma i}^* - \cos \theta_{\pi^0 i}^*)^2}{\delta^2 \cos \theta_{\gamma i}^* + \delta^2 \cos \theta_{\pi^0 i}^*} \right) \quad (7.4)$$

The χ^2 is for four degrees of freedom because the central bins have no information content. Note that the π^0 distributions have been rebinned for this operation. The observed differences in the angular distributions are summarized in Table 7.2. The meaning of % confidence in the table's last column is the percent chance that the computed difference (χ^2) is *not* due to a statistical fluctuation.

A simple linear fit has been applied to the various γ/π^0 ratios. Except for the low p_{\perp} proton data, the results are consistent with a $1 - \cos \theta^*$ dependence at $> 3\sigma$ significance. The ratio plots are inconsistent with a constant value of 1, which is expected in the case of no difference between γ s and π^0 s. Indeed, the γ/π^0 ratio for the proton data with a p_{\perp} cut of $4.25 \text{ GeV}/c$ is consistent with 1 across the whole

Table 7.2: Summary of differences between γ s and π^0 s in $\cos \theta^*$

Beam	p_{\perp} Cut (GeV/c)	χ^2_{PDF}	% Confidence
Proton	4.25	0.583	> 32.4
Proton	5.0	2.93	> 98.0
Proton	5.0 (Unsubtracted)	1.31	> 73.2
π^-	4.25	2.45	> 95.4
π^-	5.0	5.15	> 99.9
π^-	5.0 (Unsubtracted)	2.83	> 97.5

accessible range of $\cos \theta^*$ (see Figure 7.6).

7.3 $\pi^0 + \text{jet}$ AND $\gamma + \text{jet}$ M DISTRIBUTIONS

The invariant mass distributions are presented as absolute cross sections, and as ratios of absolute cross sections. The $\pi^0 + \text{jet}$ and $\gamma + \text{jet}$ cross sections are given by,

$$\frac{1}{2M} \frac{d\sigma}{dM d\cos \theta^* d\phi} = \frac{N_{\text{Events}}}{N_{\text{Beam}}} \cdot \frac{C}{2\pi \Delta M 2M \Delta \cos \theta^*} \quad (7.5)$$

N_{Events} = the number of reconstructed events

N_{Beam} = the number of incident beam particles

ΔM = the bin size in M

$\Delta \cos \theta^*$ = interval of $\cos \theta^*$ integrated over

C = the trigger particle corrections

$1/(2\pi \Delta M 2M \Delta \cos \theta^*)$ = normalization to an element of phase space

The calculation of N_{Beam} is essentially just the total beam particle count, corrected for the time the apparatus could not take data. There are additional corrections for inefficiencies in the discrete logic as well as beam absorption in the target. The details involved in calculating the live-triggerable-beam (LTB) are found in Chris

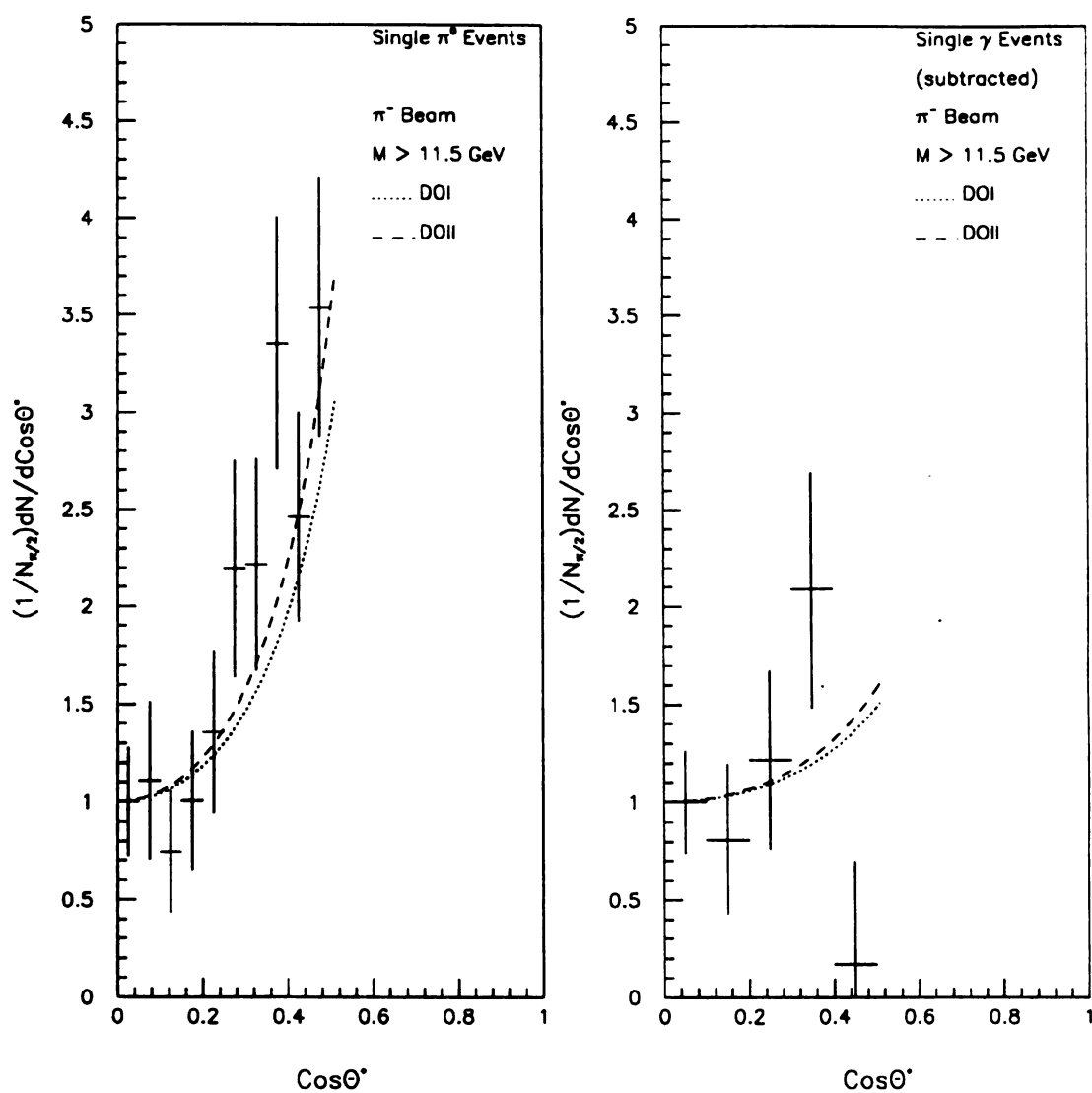


Figure 7.7: Absolute $\cos\theta^*$ plots for γ s and π^0 s in π^- data

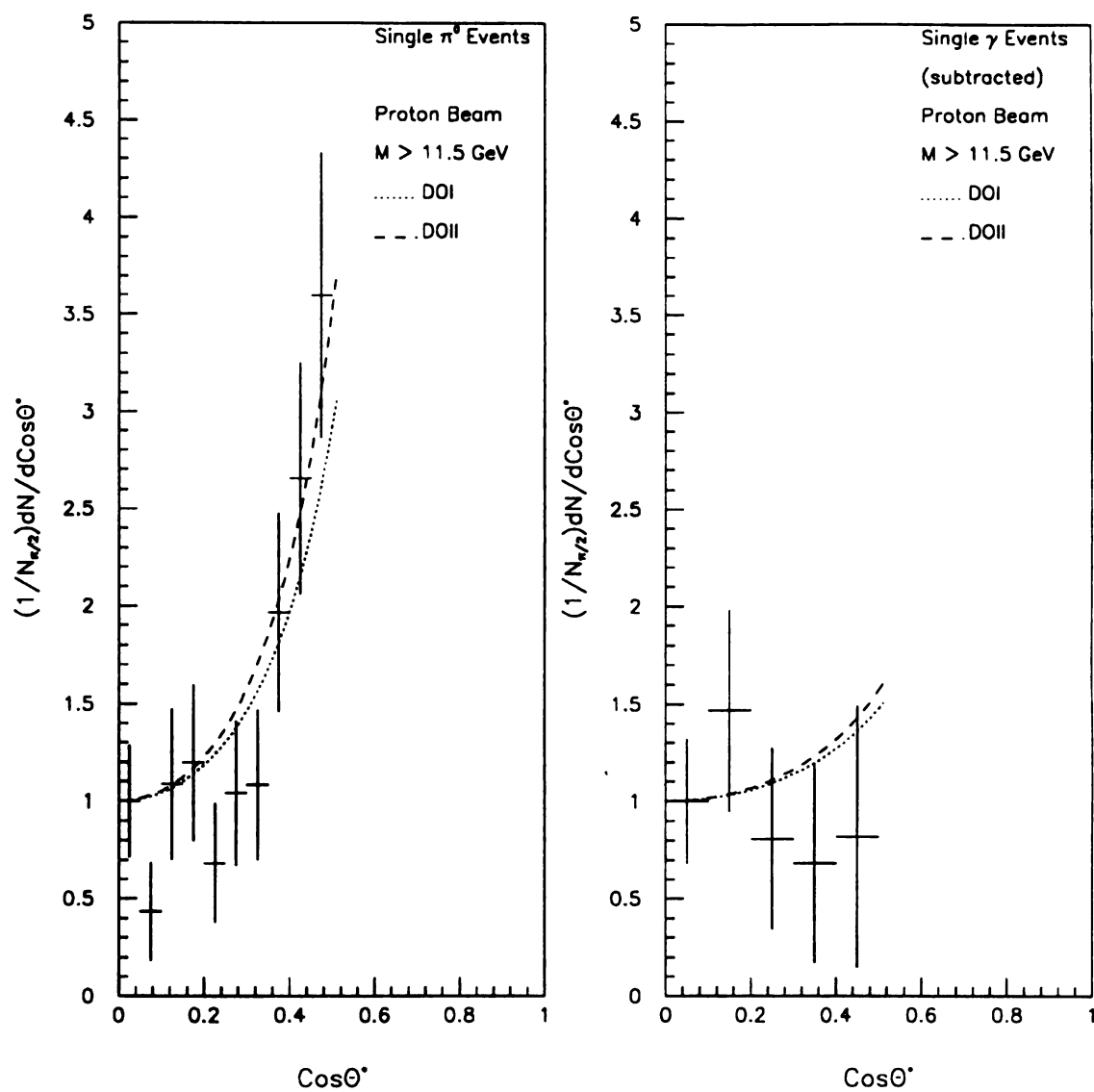


Figure 7.8: Absolute $\cos \theta^*$ plots for γ s and π^0 s in proton data

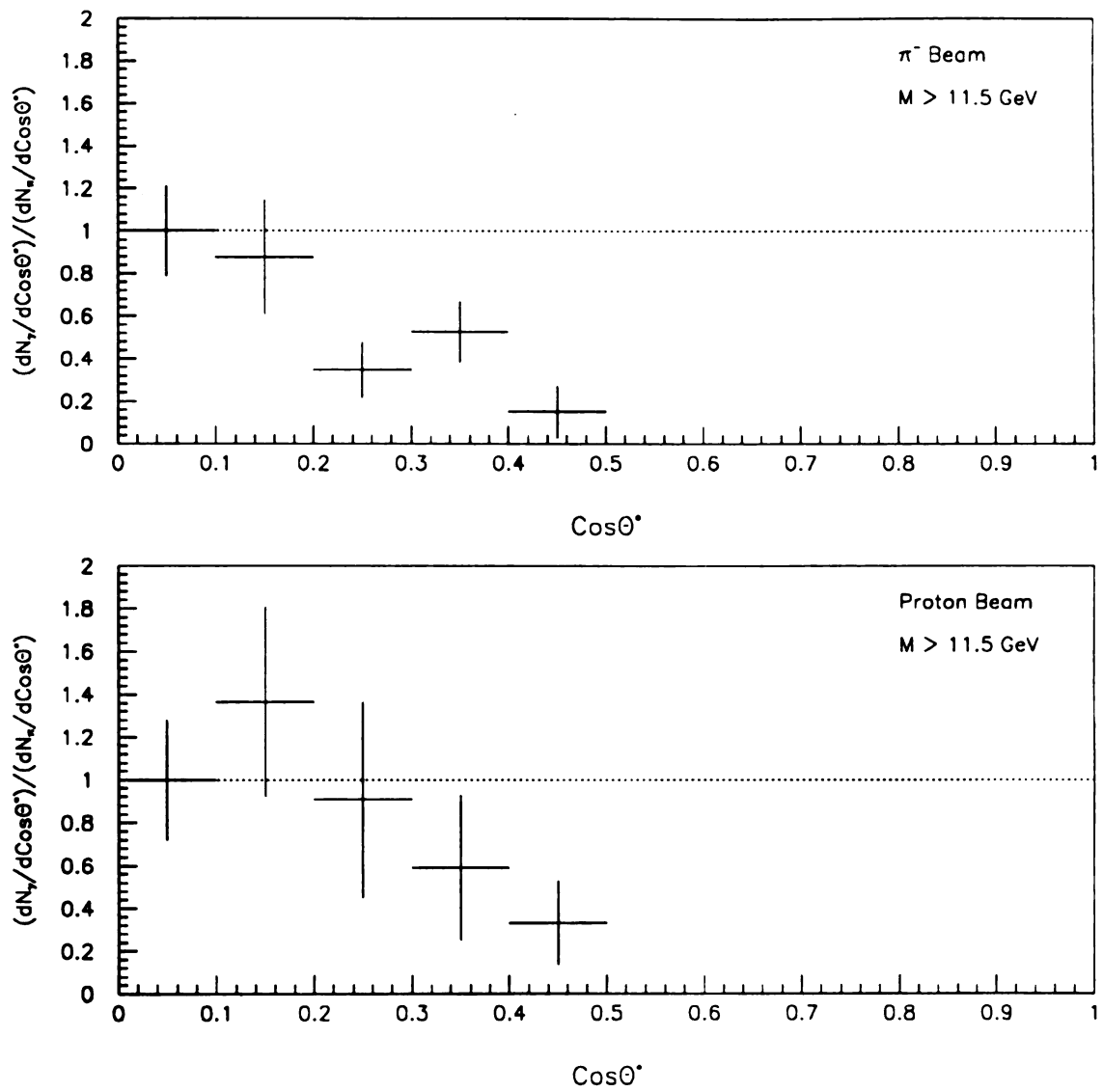


Figure 7.9: γ to π^0 ratios in $\cos\theta^*$ for π^- data (top) and proton data (bottom)

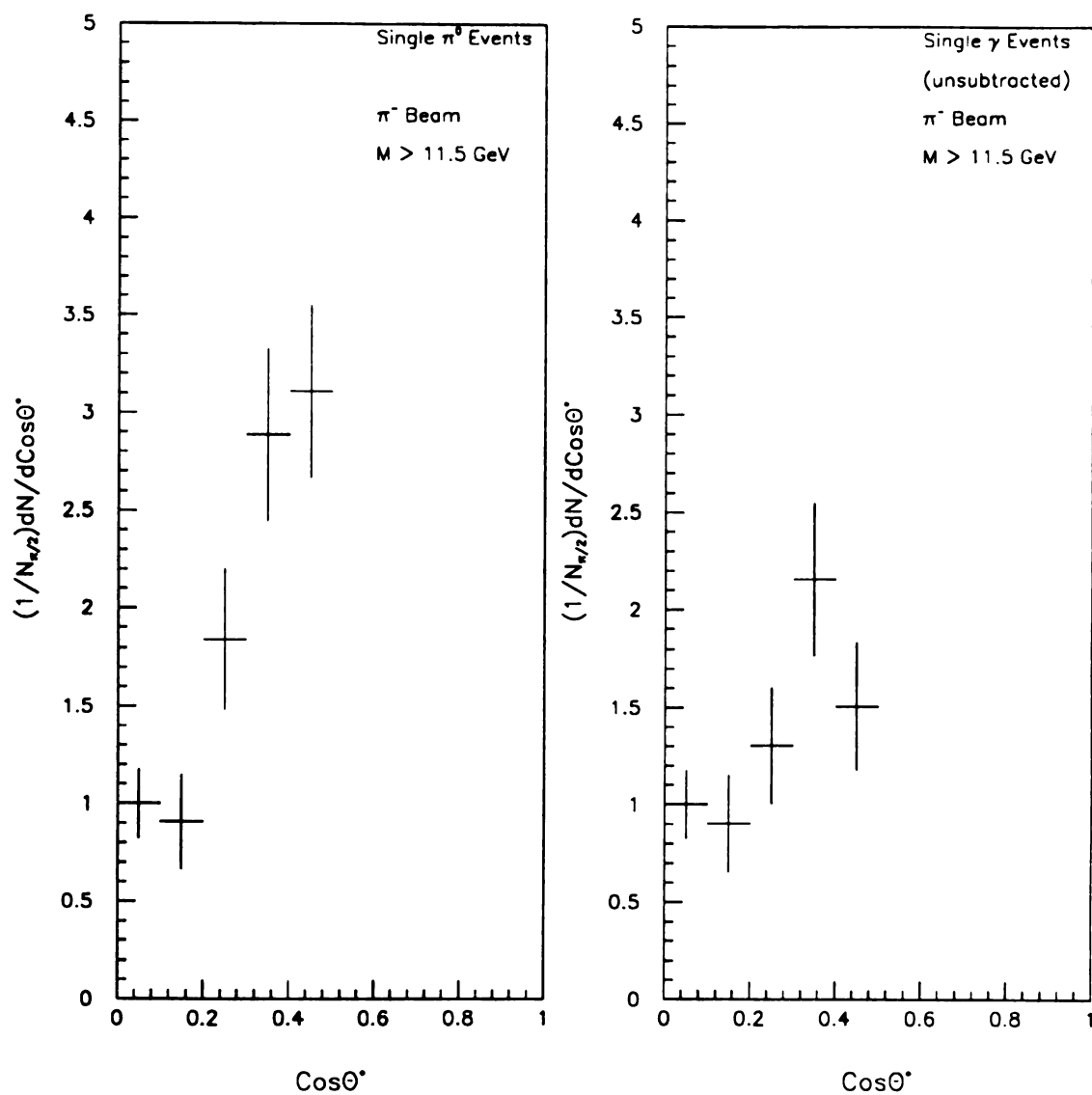


Figure 7.10: Absolute $\cos\theta^*$ plots for γ s and π^0 s in π^- data with no π^0 background subtraction for the γ s

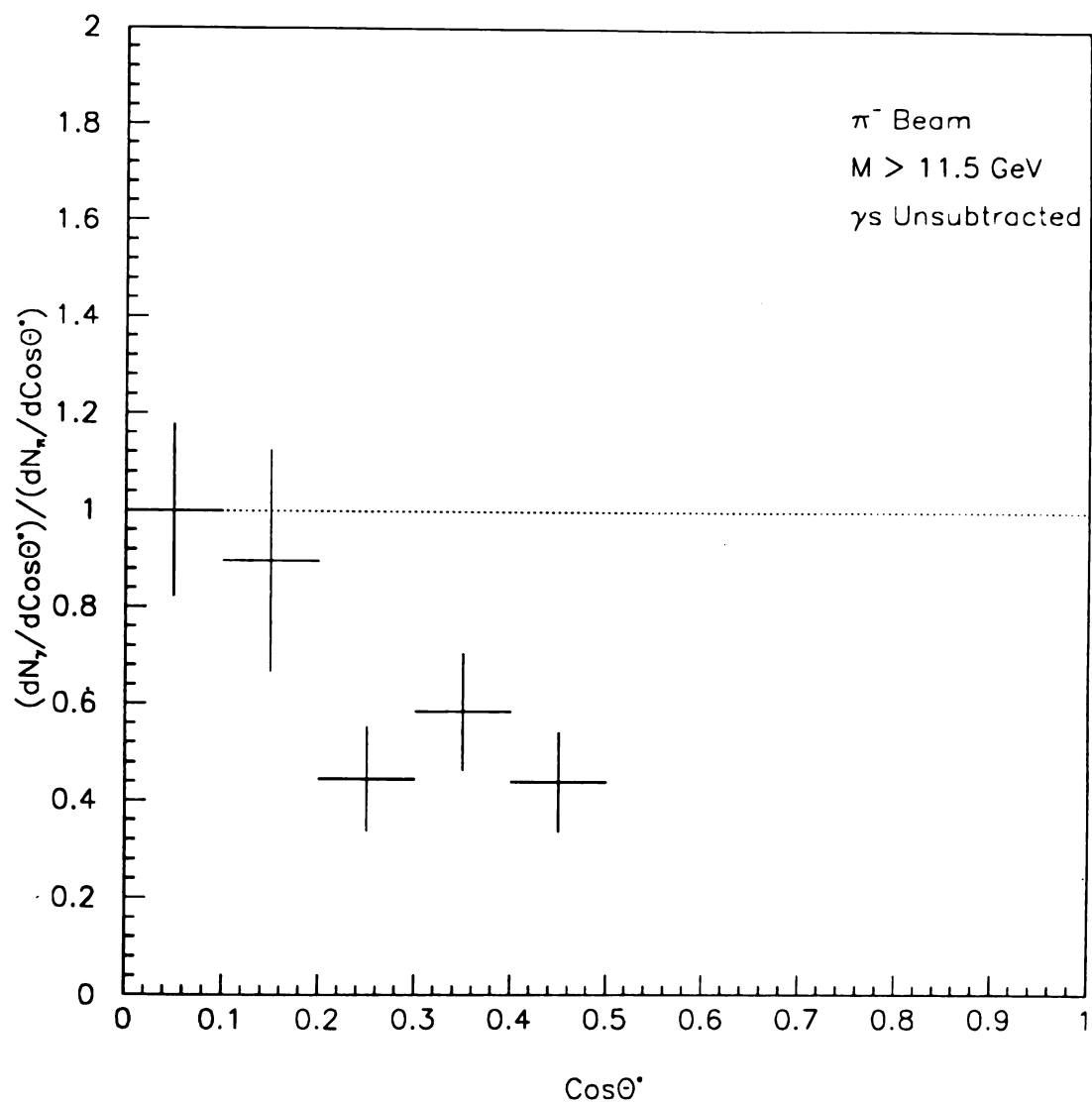


Figure 7.11: γ to π^0 ratio in $\cos\theta^*$ for π^- data without π^0 background subtraction

Lirakis' thesis [48]. Absorbed into N_{Events} , is the number of target nucleons per unit area. The conversion factor from events to nucleons per unit area is given by,

$$\frac{N_0 A L \rho}{MW} C \quad (7.6)$$

N_0 = Avogadro's number

A = the atomic mass number

L = the target length

ρ = the target's density

MW = the atomic weight in g/mol

C = conversion from cm^{-2} to mb

All cross sections in M are given in units of mb/GeV^2 . The target was composed of copper and beryllium elements; the configuration did change to just beryllium for certain data sets. N_{Events} has been computed for the whole target in accordance with the actual copper-beryllium configuration on a run-by-run basis.

A cut in $\cos \theta^*$ is necessary for the absolute M distributions because different trigger threshold sets are to be combined. A cut in η_B is not required as long as the monte carlo data is processed in like fashion. The reason is that the geometric acceptance in η_B is the same for all M .

The results of the ISAJET analysis are superimposed on the data as parametrized fits. The absolute M cross sections for π^0 events have been parametrized as exponentiated linear fits. Those for direct photon events have been parametrized as exponentiated quadratic fits. The results from both the DOI and DOII structure function sets will be presented.

Figures 7.12 through 7.15 show the absolute M cross sections for $\pi^0 + \text{jet}$ and $\gamma + \text{jet}$ events. It is clear from inspecting all four plots that the data is tracked by the DOI and DOII monte carlo sets. There does not seem to be a great deal of preference for one set of structure functions over the other, particularly in the direct photon data.

More statistics are required. However, the $\gamma + \text{jet}$ cross section for π^- data definitely has a shallower slope than the corresponding $\pi^0 + \text{jet}$ distribution. It appears that the two mass distributions cross over, *i.e.* $\gamma/\pi^0 \simeq 1$ at 18 GeV. This corresponds to a p_\perp of 9 GeV at 90° . The shape difference is also present in the unsubtracted $\gamma + \text{jet}$ cross section as Figure 7.16 clearly shows. Note how the unsubtracted distribution turns up at low M indicative of a substantial π^0 background there (low p_\perp).

Unfortunately, the $\gamma - \pi^0$ difference is not very significant in the proton data. This is mainly due to a lack of statistics as is evident from the size of the error bars. Part of the problem may also be that the low M region rises too steeply because of residual π^0 background. Such behavior is consistent with earlier results in $\Delta\phi$ and $\cos\theta^*$ at low p_\perp .

The absolute M cross sections are plagued by a number of large systematic effects. Most notable is the smearing that results from the assumptions of massless jets, and p_\perp balancing between the trigger particle and recoil jet. There is the uncertainty in the electromagnetic calorimeter's energy scale too ($\sim 1\%$); this affects the trigger particle's reconstructed four-vector. These effects are very substantial because the cross sections are so steeply falling. In fact, there is already a 25% systematic uncertainty on the inclusive cross sections alone! Besides these experimental uncertainties there are theoretical ones as well. They are the value of Λ_{QCD} , the definition of Q^2 and the amount of primordial k_\perp . High p_\perp π^0 's suffer an additional uncertainty due to an incomplete knowledge of the z -distribution or fragmentation function. All of these problems can be minimized, even cancelled, by studying the ratio of corresponding cross sections for π^- and proton data. The variation of these ratios in M is dependent on the hadrons' internal structure, if any, and the behavior of γ s and π^0 s should be different.

For direct photon events, the ratio is particularly sensitive to the value of η_G . In principle it should be able to discriminate between the DOI and DOII sets. The physics

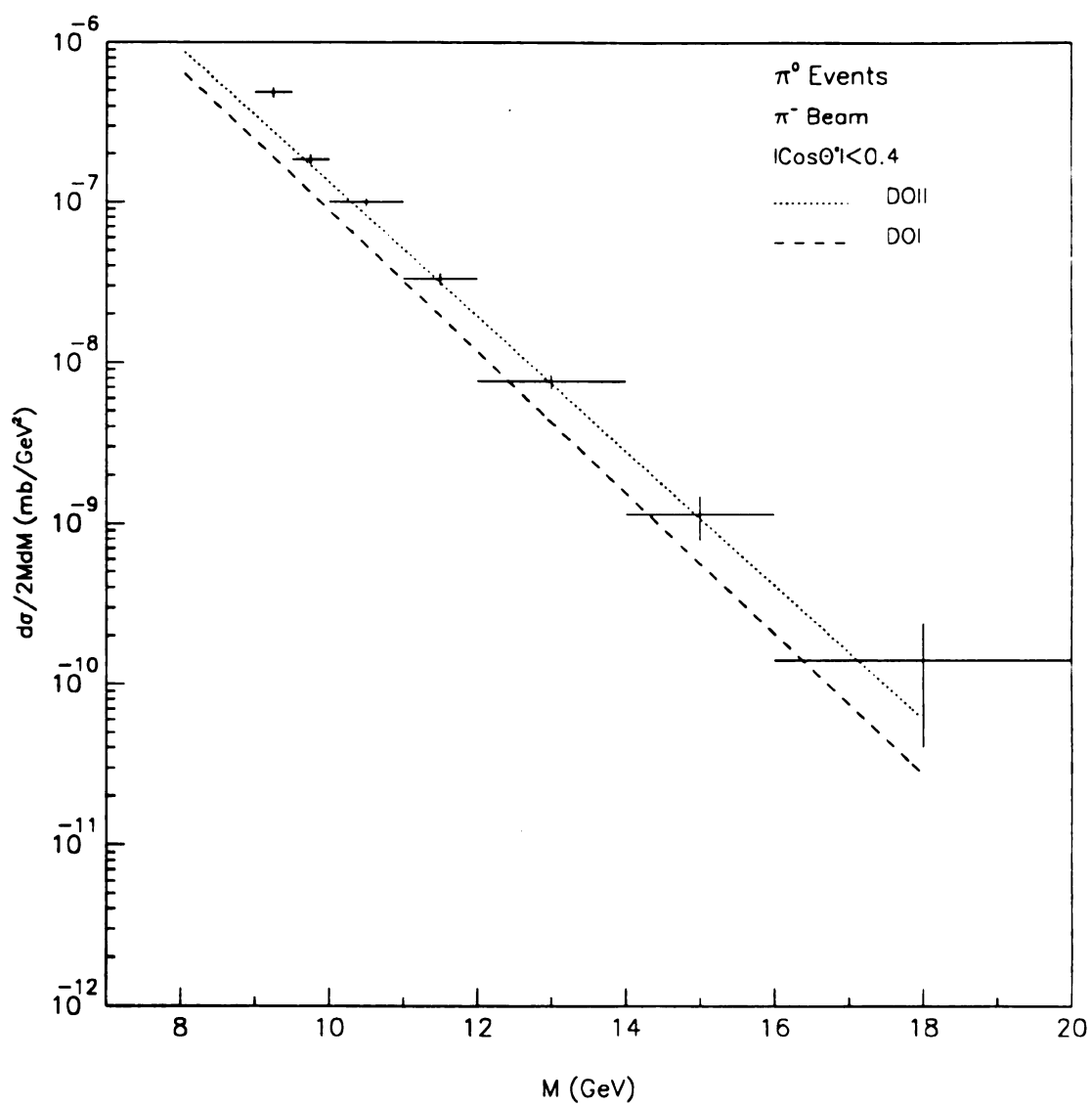


Figure 7.12: π^0 + jet cross section in M for π^- beam

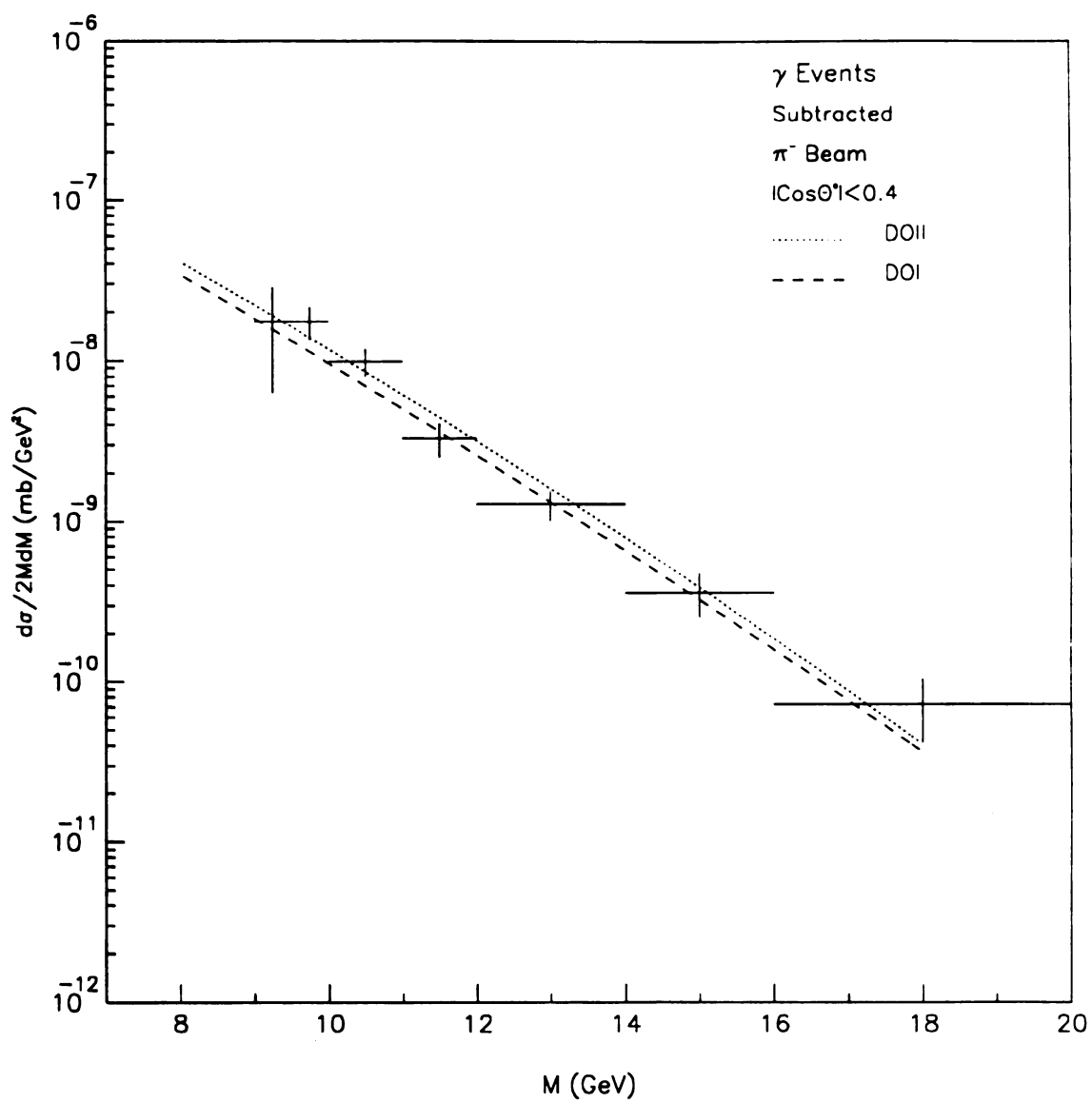


Figure 7.13: γ + jet cross section in M for π^- beam

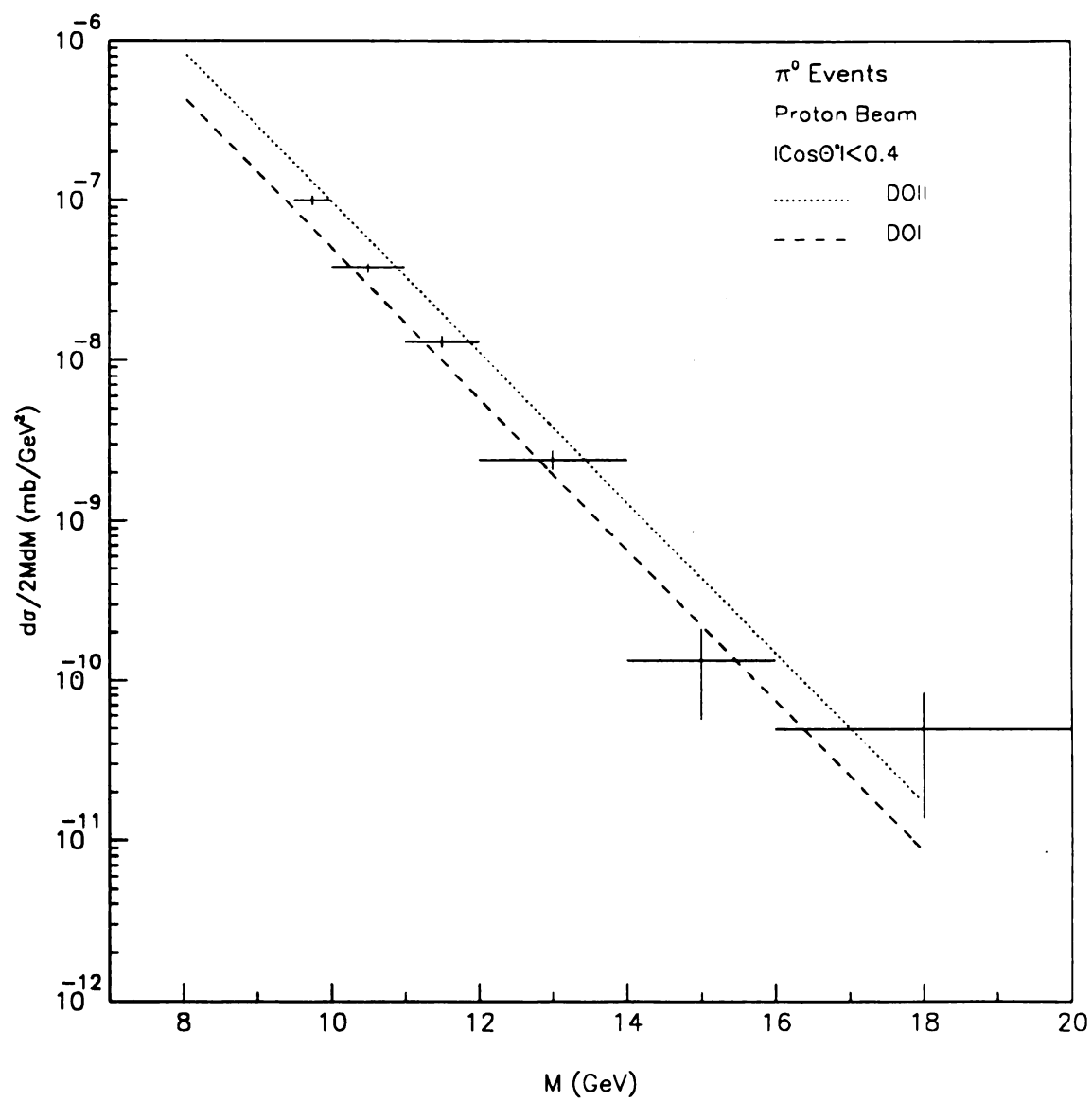


Figure 7.14: π^0 + jet cross section in M for proton beam

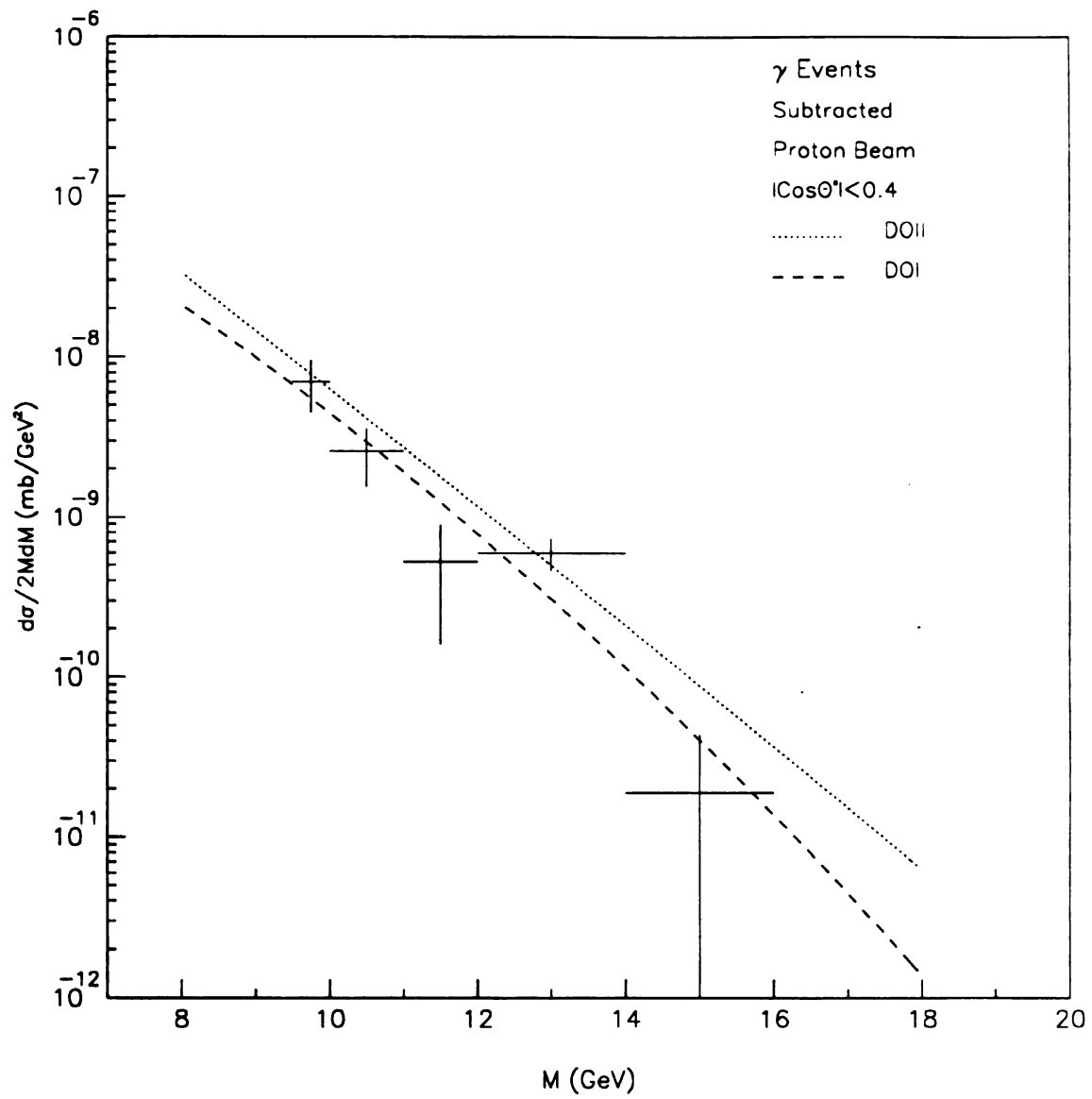


Figure 7.15: γ + jet cross section in M for proton beam

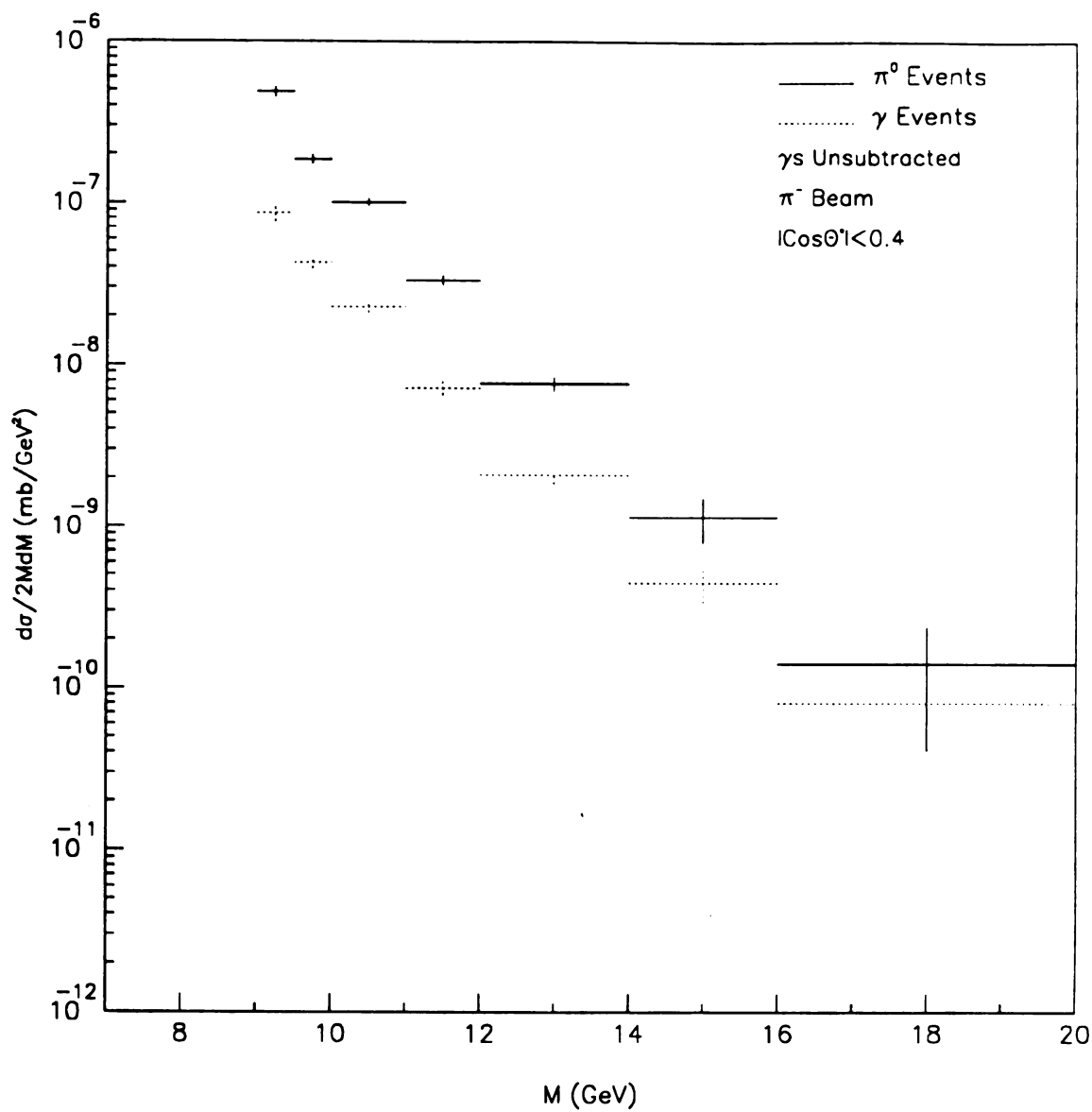


Figure 7.16: π^0 + jet and γ + jet cross sections in M for π^- beam. The γ distribution is unsubtracted.

behind this is very simple, and is described in chapter 1. Since the DOI and DOII sets of structure functions are distinguished by their values for η_G , it is expected that they will yield rather different predictions for this ratio.

Studying the ratios of cross sections has yet another advantage. No cut in $\cos \theta^*$ is required, allowing the full sample of data to be used, and thereby reducing the error bars. The systematic effect due to the trigger threshold can be divided out as follows. The absolute cross sections are calculated separately for each threshold set. They are then averaged together and the ratio is taken. The averaging procedure insures that the trigger-turn-on effect appears equally in the π^- and proton data. This method works because the p_\perp cuts for π^- and proton data have the same values.

The π^- /proton ratio of $\pi^0 + \text{jet}$ cross sections appears in Figure 7.17. The ISAJET predictions are again superimposed as smooth curves. The actual monte carlo histograms were fit with the following form,

$$\frac{d\sigma(\pi^- N \rightarrow \pi^0 + \text{jet} + X)}{d\sigma(p N \rightarrow \pi^0 + \text{jet} + X)} = a + \exp(b + c \cdot M) \quad (7.7)$$

The bin-by-bin uncertainties in the fit are insignificant compared to those in the data. One can see by inspection that the ratio is greater than 1, being centered around 1.5. Such a trend is expected since the pion contains half as many partons on average as the proton, and the beam energies were the same. Thus, the value of x is typically larger for a pion than for a proton, and M is proportional to the geometric mean of x_1 and x_2 . It is fair to say that the DOI and DOII sets merely bracket this sample.

The ratio for $\gamma + \text{jet}$ events appears in Figure 7.18. The general trend here is for a larger ratio at high M than for π^0 s. Although the error bars are quite large, such an effect is consistent with an additional enhancement over parton counting due to a larger relative contribution of the annihilation mechanism in π^- data for direct photons as opposed to π^0 s. Most dramatic of all is the difference between the DOI and DOII predictions with the data clearly favoring DOII. If the low point at small

M is ignored, a χ^2 difference between the monte carlo curves and the data shows the DOI prediction to be inconsistent.

Some qualifications are in order. The major contribution to the χ^2 occurs in the last bin and the statistics are pretty low. While tantalizing to say the least, this result can only be of a preliminary nature. Five events from the π^- data and two events from the proton data contribute to the last point. The error bars have been calculated using the assumption of Gaussian statistics. The proton data events are all above 7 GeV/c in p_\perp , while those from the π^- data are all above 6 GeV/c. The trigger particle rapidities are all within $y = \pm 0.7$, which is the range used in the inclusive analysis. The acceptance and reconstruction efficiency corrections are well understood within this region. Finally, the ISAJET rapidity distributions for high p_\perp single photons are in agreement with the subtracted data distributions, especially for $p_\perp \geq 5.0$ GeV/c. There is therefore no apparent systematic bias in the last data point. However, the issue of just what the value of η_G is needs to be resolved with a higher statistics sample, whose systematics are better understood than at present.

7.4 ERRORS

A few comments about errors are in order. The error bars on the data distributions are the statistical errors multiplied by the systematic corrections to the trigger particle. All corrections currently available in the data summary library of E706 analysis code have been applied. The shape of the $\cos \theta^*$ distributions could in principle be driven by the corrections. However, studies of $\cos \theta^*$ versus the various corrections have been done and it has been determined that they are not responsible for the observed shape differences between the two types of events.

As mentioned earlier, the absolute cross sections possess large systematic uncertainties. The uncertainty from the inclusive analysis is 25 %. This number was arrived at from a careful study of the data and varying the input parameters to the data driven

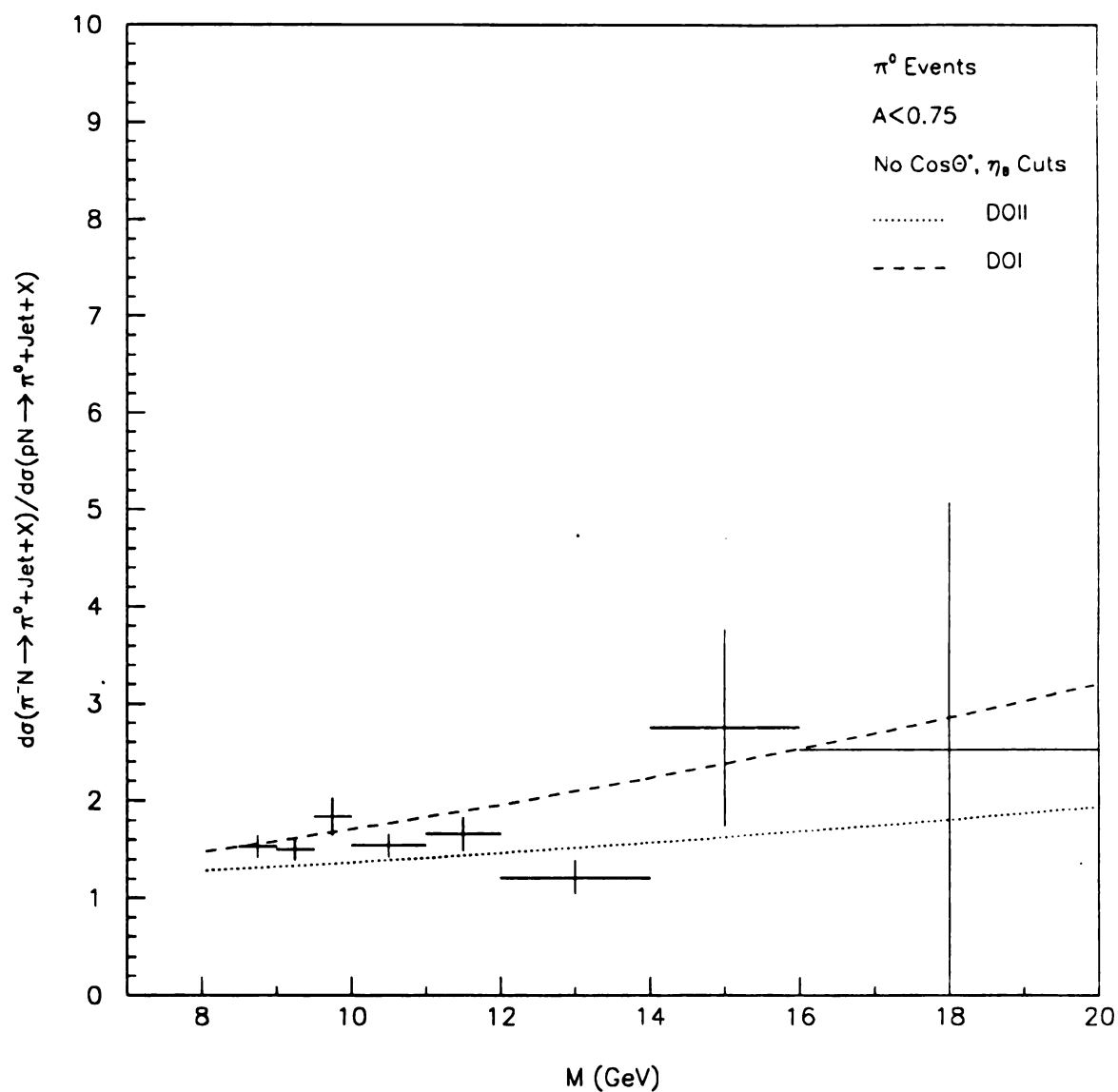


Figure 7.17: Ratio of absolute π^0 + jet cross sections between π^- and proton beams. There is no $\cos\theta^*$ cut.

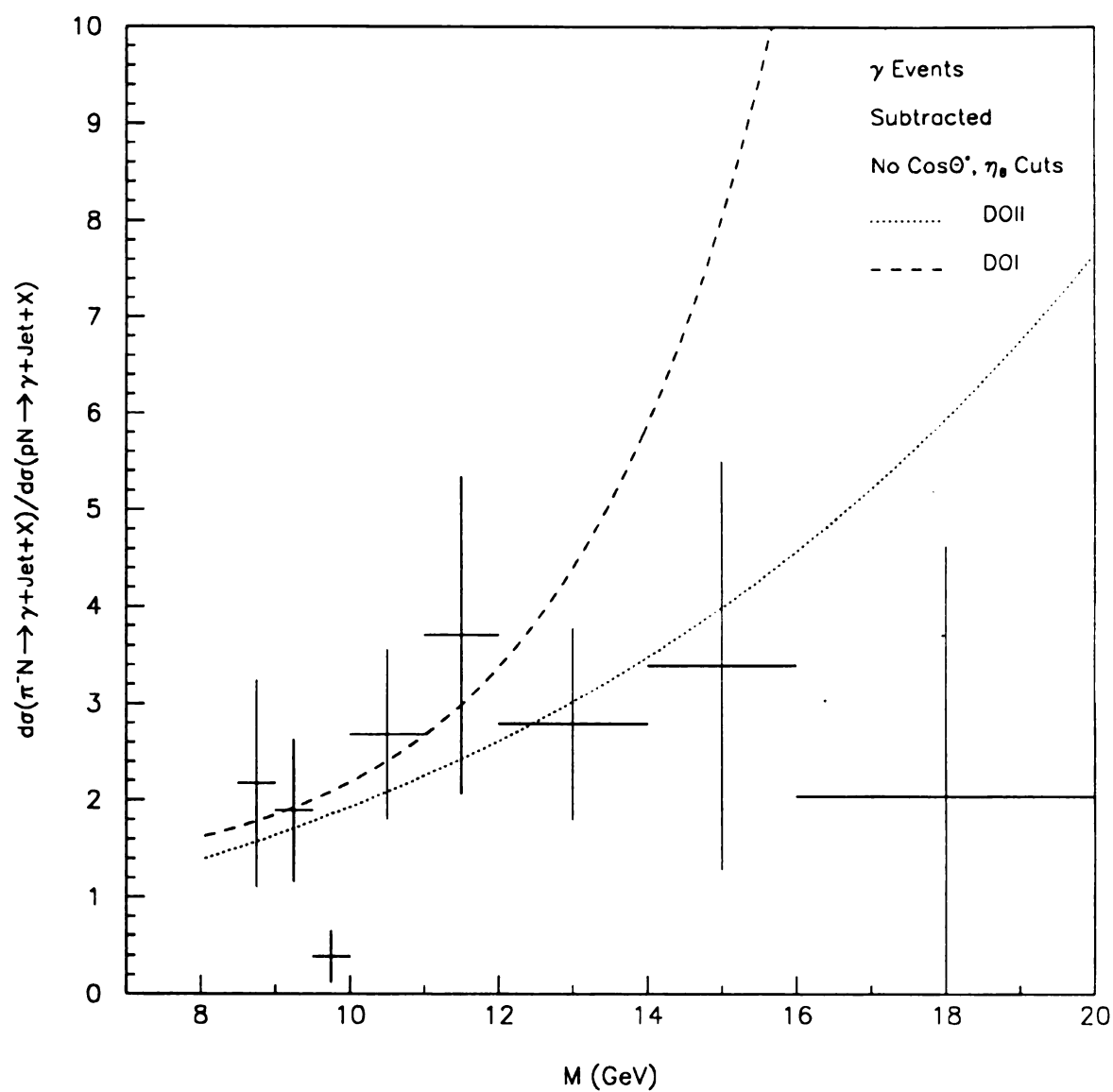


Figure 7.18: Ratio of absolute $\gamma + \text{jet}$ cross sections between π^- and proton beams. There is no $\cos\theta^*$ cut.

background monte carlo over known limits [49]. Unfortunately, the systematic error arising from the jet reconstruction technique cannot be determined in any absolute sense, but is inherently model dependent. No physics monte carlo corrections have been applied to any of the results presented in this chapter. Rather, cuts have been applied to unbiased the data as much as possible, and the monte carlo data has been subjected to the same jet reconstruction procedure and cuts. Finally, the γ/π^0 ratio in $\cos \theta^*$ and the ratios of cross sections in M minimize the effects of smearing on the result since numerator and denominator are similarly effected.

Chapter 8

Summary and Conclusion

This analysis represents a logical extension of the inclusive π^0 and direct photon analysis. After selecting a high p_{\perp} sample of π^0 and single γ candidate events attention turned towards the associated event structure. In particular, the charged particle structure has been used to establish the existence of jets in these events. The presence of jets is manifested in the correlations found in the $\Delta\phi$ and Δy distributions presented in chapter 5. These correlations are consistent with a 2-2 hard scattering mechanism, acting among hadron constituents. Furthermore, these correlations have been utilized by a jet-finding algorithm to reconstruct the recoil jet's spatial orientation event-by-event. The recoil jet's direction together with the trigger particle's four-vector have subsequently been used to reconstruct the $\cos\theta^*$ and M distributions of the $\pi^0 + \text{jet}$ and $\gamma + \text{jet}$ systems in their rest frames.

The principle thrust of these studies has been to determine if γ and π^0 events are different from one another as QCD predicts they are. The π^- data has proven very fruitful in this regard. The shapes of the $\Delta\phi$, $\cos\theta^*$ and M distributions for single photons are all significantly different from those for high p_{\perp} π^0 s. In addition, the π^- data above 5.0 GeV/c in p_{\perp} reveals these differences without any π^0 background subtraction, and at a high degree of significance. Unfortunately the proton beam data's results are not very convincing. No direct photon signal was found below 5.0 GeV/c in p_{\perp} even with a background subtraction. Above 5.0 GeV/c however, the angular distributions do show the expected difference. The differences observed in $\cos\theta^*$ have also been seen by the high energy collider experiments CDF and UA2 [50, 51]. The M distributions reveal only a slight difference in slope. Finally, the ratios of $\gamma + \text{jet}$ and $\pi^0 + \text{jet}$ cross sections in π^- and proton beams are different, but the error bars are large. Nevertheless, there is a definite trend for the $\gamma + \text{jet}$ ratio of

cross sections in π^- and proton beams to be larger than the corresponding ratio of $\pi^0 + \text{jet}$ cross sections as M increases.

The ISAJET generated data possesses similar jet correlations to the real data. The agreement between data and monte carlo is very good for the angular distributions. The DOI and DOII sets of structure functions allow ISAJET to bracket the data's M cross sections. The ratios of these cross sections in π^- and proton beam also track well, especially for the direct photons.

Indeed, the 1988 data supports a "low" value of η_G , implying a "hard" gluon distribution for hadrons. The DOII prediction is consistent with the π^- to proton beam ratio of direct photon cross sections in M while that for DOI is not. However, the statistics are rather poor, and all the errors have been assumed to be Gaussian. One can look towards the new higher statistics data sample, and an improved tracking system simulation to ascertain the value of η_G with better confidence. Hopefully, a direct photon signal before background subtraction will emerge for p_\perp values above 6.0 GeV/c in the new proton beam data.

APPENDICES

Appendix A

Corrections to the "Kick" Approximation

The following is a summary of the various corrections to the p_{\perp} "kick" approximation. These corrections are important in obtaining the correct matching of upstream and downstream tracks. Consequently, the momentum calculation becomes more reliable. The corrections described below take into account the non-negligible z-component of the analyzing magnet's field, the change in the y-view slope of a track as it traverses the magnetic field, and the momentum dependence of the intersection point in z of corresponding upstream and downstream tracks.

All of the field corrections can be expressed in terms of the angles of tracks, α and β at the entrance and exit planes of the magnet, the angle of the track with respect to the bend plane, η , and the effective length, L_0 . The reader is referred to Figure A.1 for an illustration of these quantities.

The effect for $\alpha \neq \beta$ and $\Delta p/p \sim 1$ in the x-view is given by

$$\delta x_1 = -\frac{L_0}{8}(\alpha + \beta)(\alpha - \beta)^2 \quad (\text{A.1})$$

The shift due to the $p_y B_z$ coupling is

$$\delta x_2 = -\frac{L_0}{2}(\sin \alpha - \sin \beta) \sin^2 \eta \quad (\text{A.2})$$

There are three shifts in the y-view. First, there is the effect of the $p_x B_z$ coupling

$$\delta y_1 = -\frac{\tan \eta}{2}(\sin \alpha - \sin \beta)[A_0(\tan \alpha + \tan \beta) + L_0 \tan \beta] \quad (\text{A.3})$$

where A_0 is the distance from the vertex to the entrance plane of the magnet. The correction for p_z changing in the bend plane is split into two pieces. The track inside the magnet follows a spiral path while the kick approximation assumes straight lines. Hence, the real downstream track is too high by

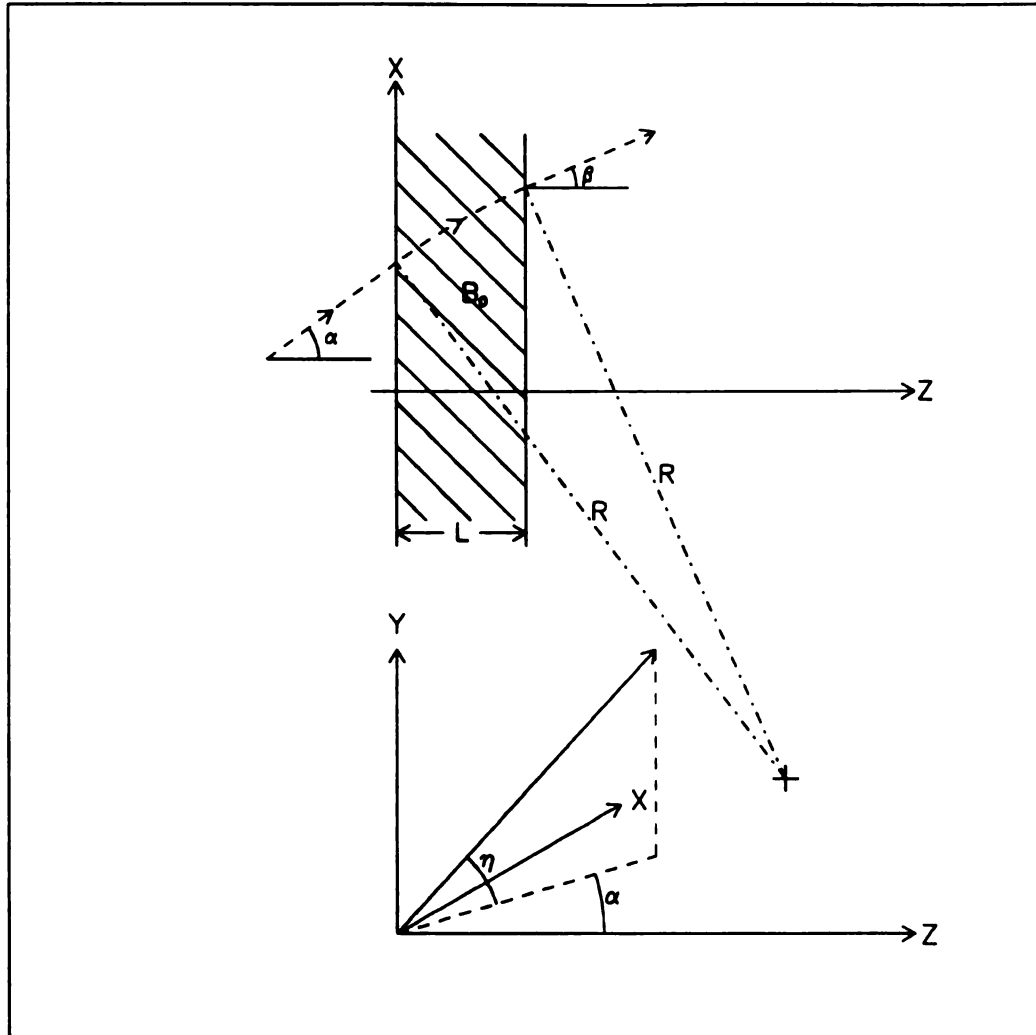


Figure A.1: Top: A track's orientation in the bend plane as it passes through the analyzing magnet's field. Bottom: The angles involved in magnetic field corrections.

$$\begin{aligned}
\delta y_2 &= \tan \eta [R(\alpha - \beta) - L_0] \\
&= L_0 \tan \eta \left[\frac{\alpha - \beta}{\sin \alpha - \sin \beta} - 1 \right] \tag{A.4}
\end{aligned}$$

$$\simeq \frac{L_0}{6} (\alpha^2 + \alpha\beta + \beta^2) \tan \eta \tag{A.5}$$

where R is the track's radius of curvature in the bend plane. The change in the x-view slope produces an offset at z_c because the apparent slopes, $\tan \eta / \cos \alpha$ and $\tan \eta / \cos \beta$, rather than the actual slope out of the bending plane. Thus,

$$\delta y_3 = \tan \left[\left(1 - \frac{1}{\cos \alpha} \right) \frac{L_0}{2} + \left(1 - \frac{1}{\cos \beta} \right) \frac{L_0}{2} \right] \tag{A.6}$$

The linking procedure is different for the X and Y projections of the space tracks. However, both methods project the upstream view tracks to the center of the magnet and attempt to match them with the proper space track projection via separate selection procedures. All of the above corrections are applied before matching is attempted.

Appendix B

Fake Tracks

The following is a description of the two methods used in estimating the fraction of fake tracks in the data. Both methods assume that the high quality 16-hit tracks are all real. Recall that a high quality track is one with $\chi^2 \leq 1$, $|b_v| \leq 1$ cm, and is linked in the x-view to an SSD track belonging to the primary vertex.

The first technique is known as the LAC method. As its name implies, it utilizes the data produced by the electromagnetic calorimeter. Scatter plots of the differences in X (ΔX) and Y (ΔY) between each track and the nearest electromagnetic shower was constructed. The tracks used in making the plots had to have momenta greater than 5 GeV/c, the LAC's "turn on" point, and $|y| \leq 0.7$, the LAC's acceptance. Two scatter plots were used. One was for all tracks satisfying the momentum and rapidity cuts, and the other was for those tracks that, in addition, had $|b_v| \leq 1$ cm. The absolute limits of each plot are 0 to 10 cm. Those tracks with $\Delta X, \Delta Y \leq 2.0$ cm were deemed to have been "seen" by the LAC. Figure B.1 displays one of these scatter plots.

In order to correct for the LAC's inefficiency the detection efficiency for all high quality 16-hit tracks as a function of their momenta was measured. The detection efficiency for all high quality tracks was measured also. Plots of these efficiencies appear in Figure B.2. Those scatter plot entries for which $\Delta X, \Delta Y \leq 2.0$ cm were then corrected by the appropriate $\xi(P)$ for high quality 16-hit tracks. A second study performed the correction using the $\xi(P)$ s coming from all high quality tracks. The ratio of weighted contents in the region $\Delta X, \Delta Y \leq 2.0$ cm to the total contents (weighted and unweighted) yields the true track fraction. The fake track percentage is just this number subtracted from 1.

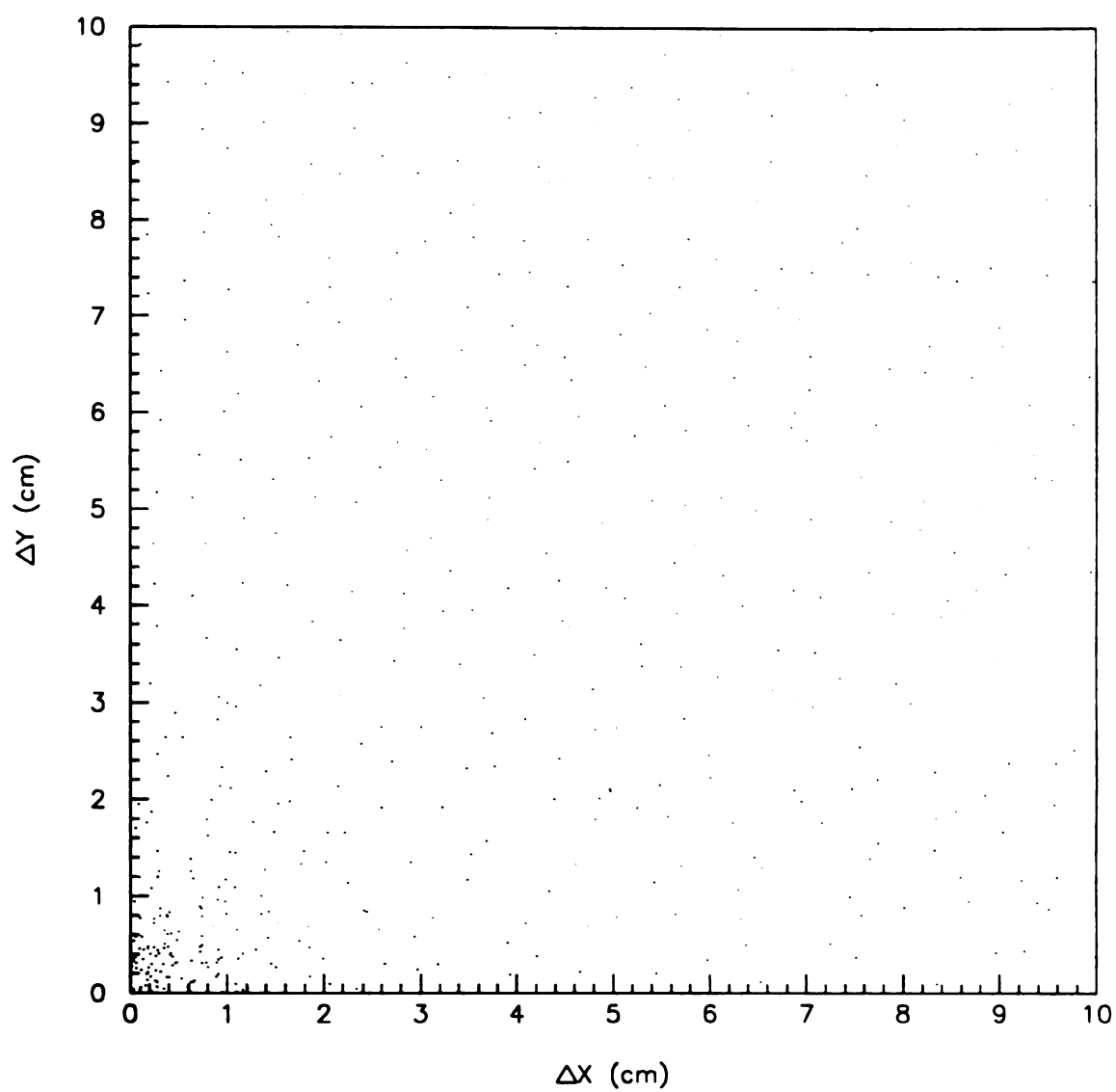


Figure B.1: Scatter plot of ΔX vs ΔY for tracks and nearest showers

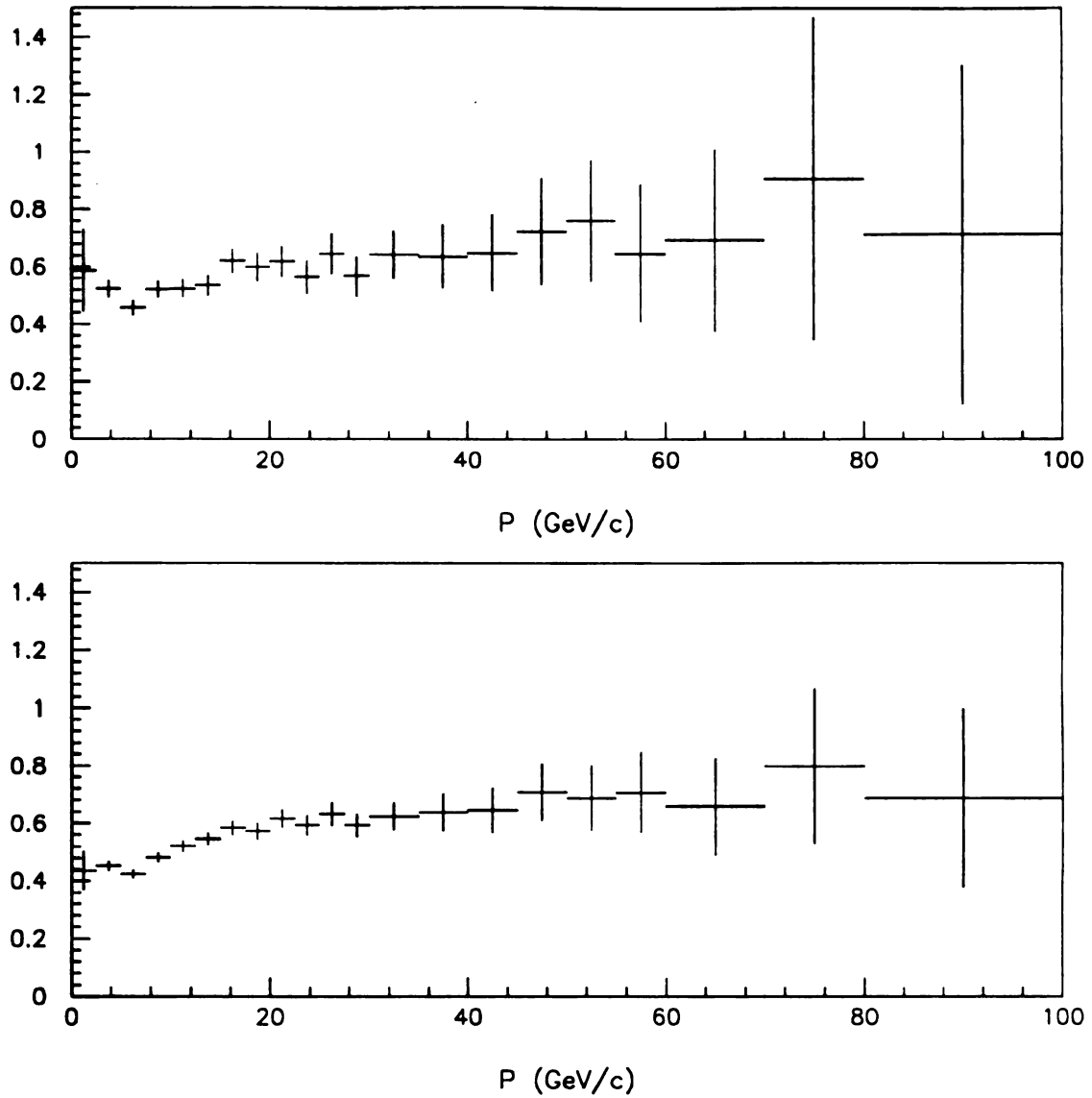


Figure B.2: EMLAC efficiency in P for high quality 16-hit tracks (top) and all high quality tracks (bottom).

The second method employs the y-view impact parameter distributions for physics tracks that are linked in the x-projection to an SSD track belonging to a primary vertex. It is known as the b_y method. Such an impact parameter distribution is shown in Figure B.3. Clearly, tracks that are linked in x to an SSD track associated with a reconstructed vertex should have small $|b_y|$; those which do not are suspicious. Those tracks for which $|b_y| \geq 2.0$ cm have been deemed fake; a flat contribution under the peak in the b_y distribution has been assumed. To account for improper linking of real tracks in the tails a similar b_y distribution was made for the high quality 16-hit tracks. The ratio of entries for $|b_y| \geq 2.0$ cm to those inside $|b_y| \leq 1.0$ cm was used to subtract off a portion of the tail in the distribution for all tracks. The fraction of fake tracks, including the contribution under the peak was then estimated from the subtracted distribution.

The results of these studies are summarized in Table B.1 for all b_y and for $|b_y| \leq 1.0$ cm. LAC1 and LAC2 refer to the separate studies using efficiency corrections for 16-hit high quality tracks and all high quality tracks respectively. Notice that the impact parameter method yields very small fractions while those measured via the LAC technique are considerable. However, the results of the LAC method, using the efficiency corrections for all high quality tracks appear consistent with the b_y method based on their variation. In addition, the error bars on the plots of Figure B.2 indicate that both sets of efficiency corrections yield consistent estimates for the percentage of fake tracks. From these studies it appears that the tracking data contains fake MWPC tracks at the $\lesssim 1\%$ level for $|b_y| \leq 1.0$ cm and $\lesssim 2\%$ overall.

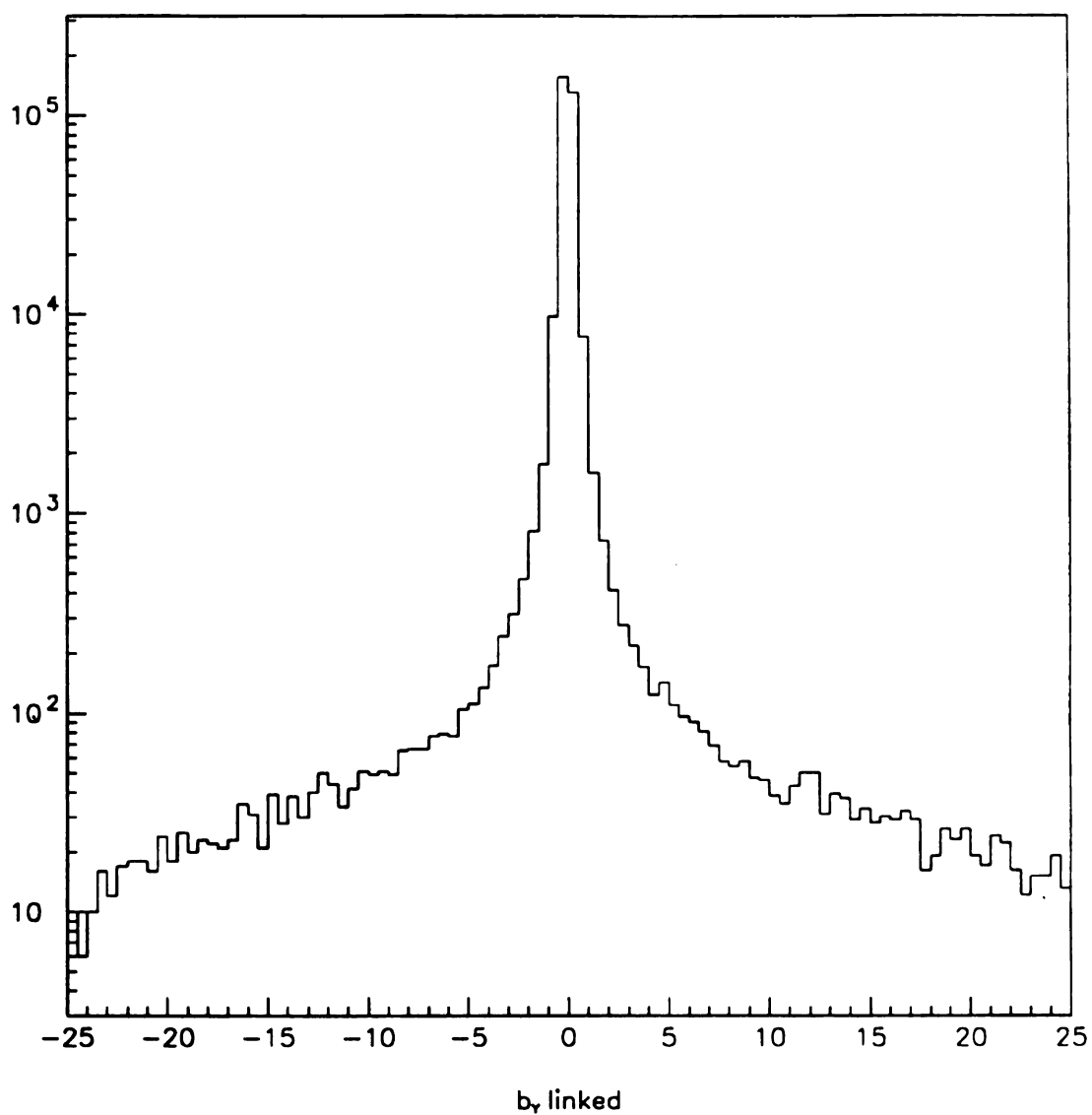


Figure B.3: b_y distribution for physics tracks that are linked in the x-view to an SSD track, assigned to the primary vertex.

Table B.1: List of fake track fractions.

Beam	Method	$ b_y \leq 1.0 \text{ cm} (\%)$	all $b_y (\%)$
+	LAC1	2.97	9.39
+	LAC2	-.946	1.82
+	b_y	.0592	1.39
-	LAC1	2.92	9.41
-	LAC2	.208	3.32
-	b_y	.0586	1.41

Appendix C

Track Reconstruction Efficiency

The issue of track reconstruction efficiency will now be addressed. This efficiency can be estimated by studying the relative multiplicities of 13, 14, 15, and 16-hit tracks. Such a distribution appears in Figure C.1 along with the MC prediction. The monte carlo prediction uses the ISAJET monte carlo's output, and projects the charged particles through a simulation of the magnet and MWPC system. Such a simulation takes into account the effects of the analyzing magnet's field, the geometric acceptance of the wire chambers, and most importantly, the planes' efficiencies on the relative multiplicity of 13, 14, 15, and 16-hit tracks. However, it completely ignores the effects of noise and the reconstruction program.

Figure C.2 shows four plots of relative hit multiplicities. Each plot is for one of the separate sets of data used in the analysis. The sets are distinguished by the time at which they were accumulated, and by the sign of the beam used to generate them. The sets are time ordered with set E being the earliest, and set A the latest. Sets A and D were generated with negative beam; sets C and E were generated with positive beam. Each of the plots has the monte carlo result superimposed on it. It is clear by inspection that the shape of the distribution has a time dependence. It also looks as though PLREC might be reconstructing 14-hit tracks in favor of 15-hit tracks because the 13-hit and 16-hit fractions are closer to the monte carlo result. This effect should not degrade the reconstruction efficiency though. Overall the monte carlo distribution does have a greater efficiency for seeing tracks than the data, except possibly for set E. Nevertheless, all the distributions are quite similar, implying that the reconstruction efficiency for the data is close to that predicted by the monte carlo.

The monte carlo reconstruction efficiency can be calculated explicitly from the plane's efficiencies. The result is 98%. One can average the efficiencies and use the

binomial probability distribution to calculate the reconstruction efficiency as well. The binomial probability distribution i.e. hit or no hit, is given by

$$P_N(k) = \frac{N!}{k!(N-k)!} <\epsilon>^k (1 - <\epsilon>)^{N-k} \quad (C.1)$$

where $N = 16$ and k is the number of hits on a track. $<\epsilon>$ is the average plane efficiency. The reconstruction efficiency is obtained by summing the probabilities corresponding to $k = 13, 14, 15$, and 16 . Again the answer is 98%.

A similar procedure can be applied to the data by finding a number ϵ such that the corresponding binomial distribution matches the data. The number ϵ takes into account PLREC inefficiencies, the effect of geometric acceptance on event topology as well as the planes' efficiencies. There is reason to believe that a major portion of the difference between data and monte carlo is due to variation in the actual planes' efficiencies over the course of the run. One reason is the observed set dependence of the relative hit multiplicity distributions. Another is that the measured efficiencies were obtained using low intensity minimum bias data over a short time period.

The effect of geometric acceptance on event topology can be removed by using only tracks that do not project outside of the acceptance at the z-position of any plane. The resulting relative hit multiplicity distributions for positive and negative beam are shown in Figure C.3. Note that the reconstruction efficiency for the monte carlo, calculated earlier, is not affected by the acceptance in this manner since the "true" efficiencies for the planes are known *a priori*. In other words a relative hit multiplicity histogram was not used to determine $<\epsilon>$. A value of $<\epsilon> = 0.92$ yields a binomial distribution which is skewed to a lower overall efficiency than the data as Figure C.3 illustrates. Here, one observes the 16-hit fraction to fall below the data while the 13, 14, and 15-hit fractions are larger. Such a value of $<\epsilon>$ corresponds to a reconstruction efficiency of better than 96%. Since the fraction of fake tracks is very small, it can be concluded that this number is representative of

the real tracks. It is clear from this discussion that the reconstruction program has a very small adverse affect indeed!

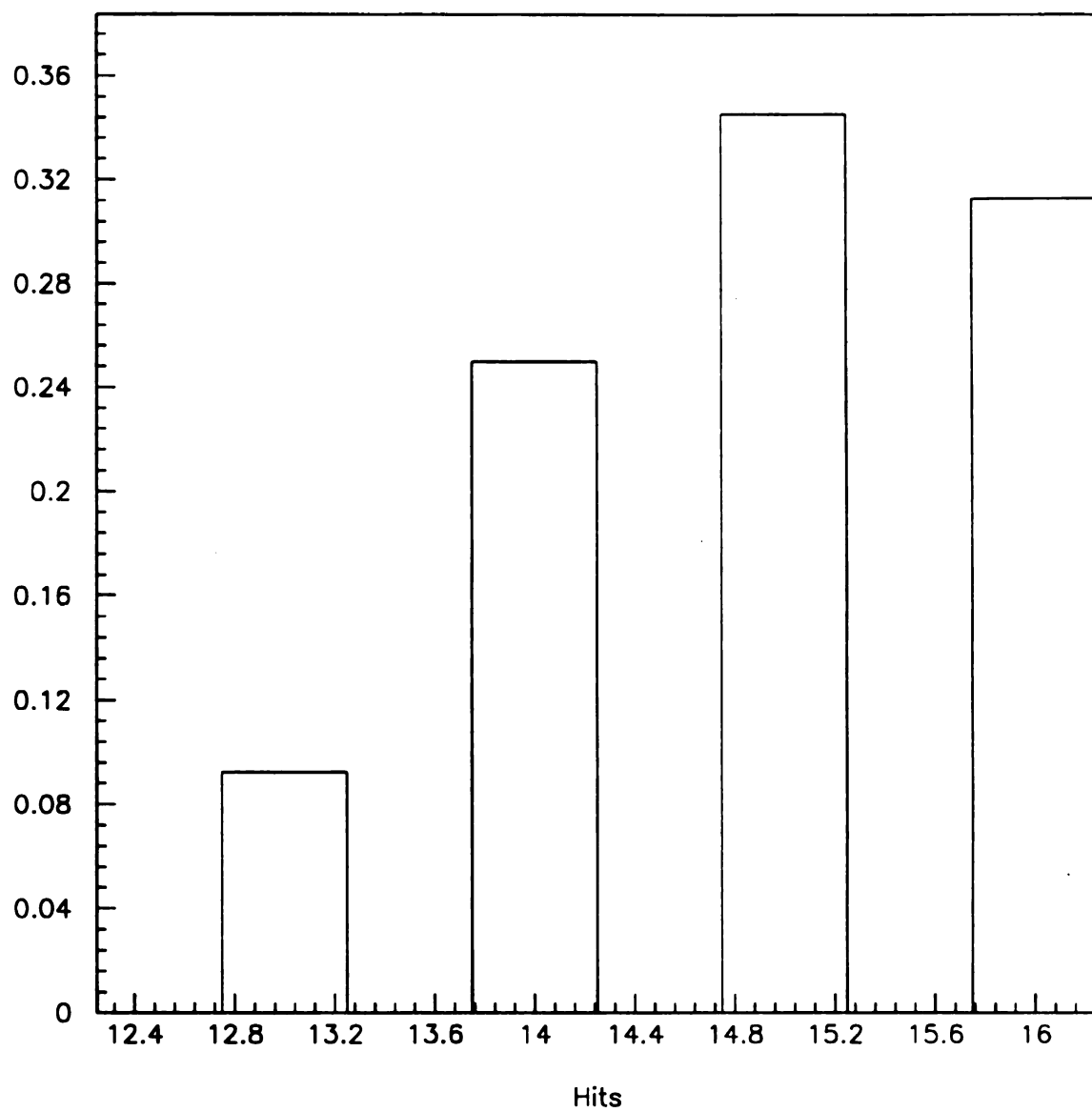


Figure C.1: A typical relative hit multiplicity distribution for the physics tracks

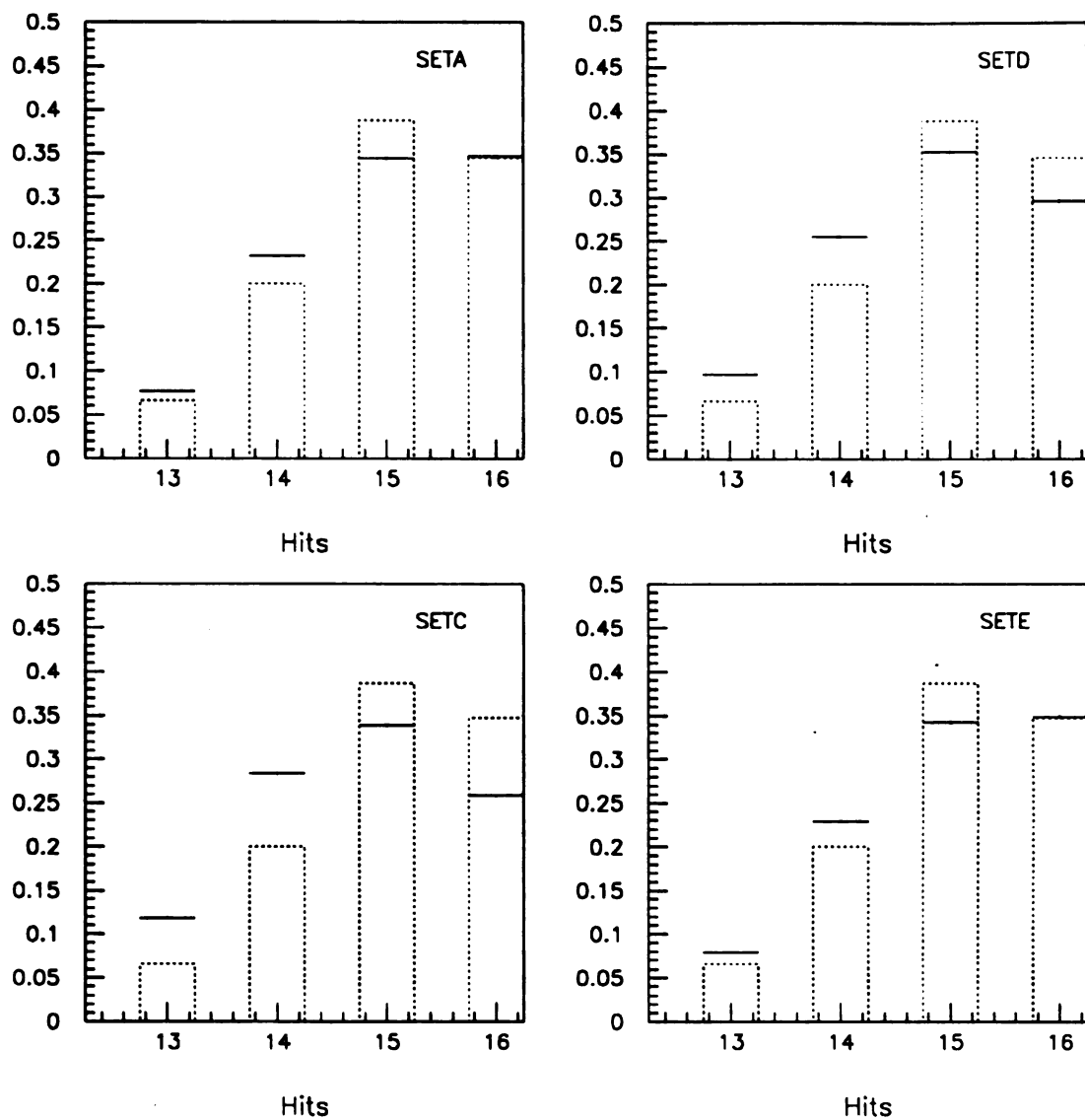


Figure C.2: Relative hit multiplicity distributions of physics tracks for the four separate data sets. The monte carlo prediction appears as the dotted bars.

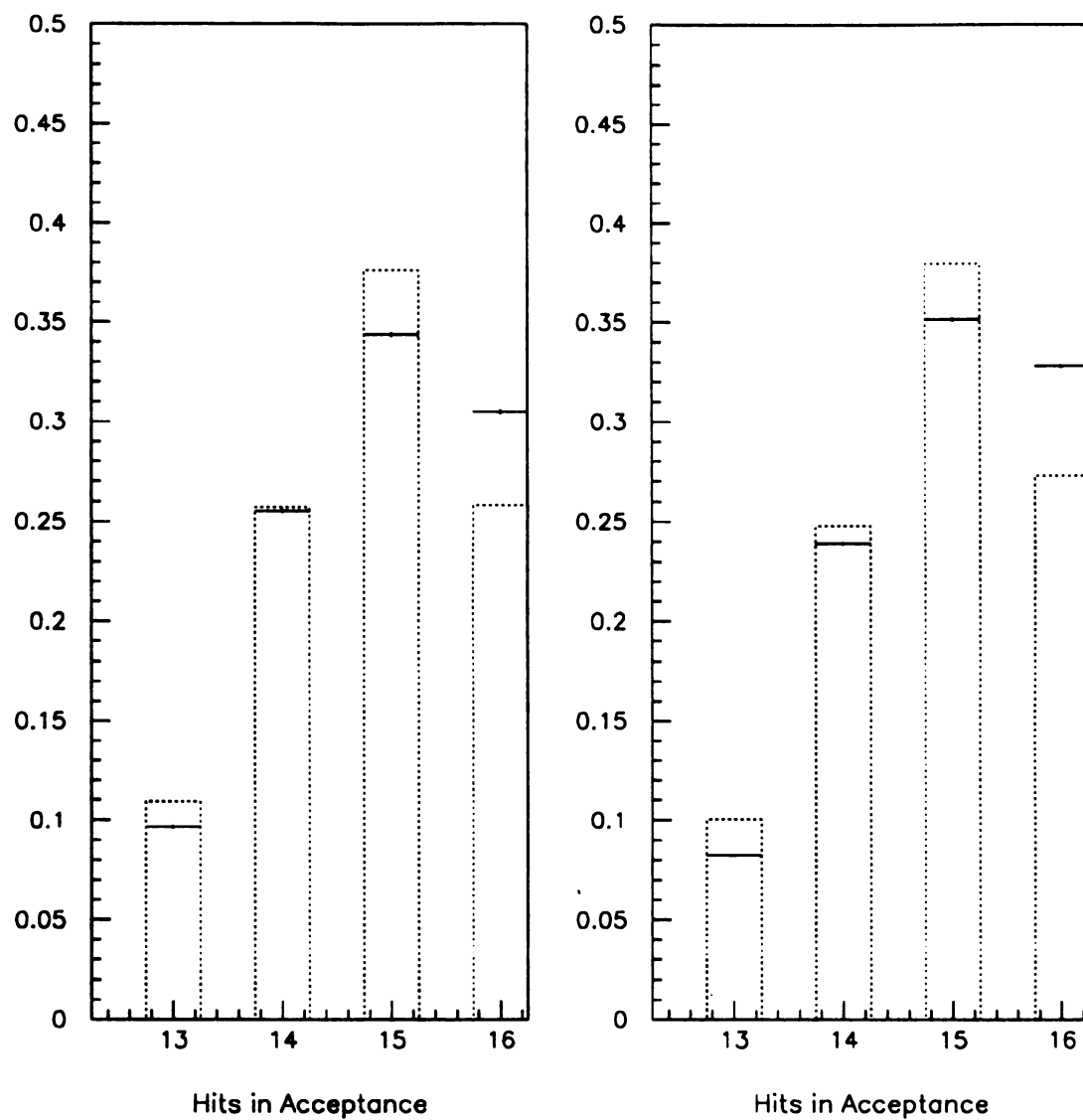


Figure C.3: Relative hit multiplicity distributions for positive data (Left) and negative data (Right). These plots are for tracks that do not project outside the MWPC acceptance. Also shown is the binomial distribution for $\langle \epsilon \rangle = 0.92$; the binomial distribution is plotted as dotted bars.

Appendix D

Trigger Particle Corrections

The following is a brief summary of the methods employed in determining the various corrections to high p_{\perp} γ , π^0 , or η events. These corrections involve those associated with the whole event and muon cuts described in Chapter 4, those for trigger and reconstruction inefficiencies, and the energy correction for individual photons. This last correction is both an energy scale correction, and an energy loss correction that takes into account all the material in front of the electromagnetic calorimeter.

D.1 CORRECTIONS FOR CUTS

The correction for vertex finding efficiency has been parametrized as a function of the z position in the target. It has the following form [52]:

$$\epsilon_{\text{vertex}} = 1.0019 - 0.0079 \times V_z \quad (\text{D.1})$$

This correction was obtained by studying the behaviour of the vertex finding algorithm on a sample of events which had been visually examined via computer graphics to see if they should have satisfied the vertex criterion. This correction is applied to each reconstructed event individually.

The δ_r correction was obtained by assuming that the true directionality distribution of photons emanating from the target was symmetric about 0. The fraction, $f_{\delta_r < -0.4}$ of photon events with $\delta_r < -0.4$ cm relative to the total number passing the directionality cut was computed. The correction is then expressed as follows.

$$\epsilon_{\delta_r} = 1 + f_{\delta_r < -0.4} \quad (\text{D.2})$$

All the other cut corrections are obtained by studying the π^0 mass distribution with sidebands subtracted. For the offline veto wall and track isolation cuts all that is

necessary to do is see how many good π^0 s remain after each cut is applied individually. The correction is just the ratio of good π^0 s without the cut to good π^0 s remaining after the cut is applied. The timing and $E_{\text{front}}/E_{\text{total}}$ corrections are obtained by examining the tails of these distributions. The timing and $E_{\text{front}}/E_{\text{total}}$ distributions for π^0 s in the mass band and the sidebands are constructed. The sideband distributions are subtracted from the mass band distribution. The ratio of the total entries in each distribution to the number satisfying the cut divided by 2 constitutes the correction. Note that the track isolation correction for π^0 s is twice that for direct photon candidates. The corrections for all cuts that are applied to the reconstructed direct photon sample are summarized in Table 4.2, along with a total correction.

D.2 CORRECTIONS FOR INEFFICIENCIES

There are additional corrections to the data. First, the trigger inefficiency has to be taken into account. Second, there are the acceptance and reconstruction efficiency corrections for π^0 s and photons. Third, the loss of photons and π^0 s through photon conversion in the target material has to be accounted for. All these corrections, along with the vertex correction, are applied to each event individually while it is being reconstructed from the DST stream.

The trigger efficiency consists of two parts. There is the efficiency of the high threshold SLOC relative to the TWOGAM trigger, and there is the pretrigger efficiency. The overall efficiency is just the product of the individual efficiencies. This breakdown of the trigger analysis is due to the fact that there are two independent hardware mechanisms responsible for producing a high p_{\perp} trigger. To simulate the hardware response to p_{\perp} deposited in the EMLAC, the actual energy of a triggering event is reconstructed by EMREC. The energy deposited in the individual r-view strips is then estimated from the reconstructed showers, and the simulation of the hardware summing schemes is performed. Thus the actual p_{\perp} as seen by the hardware

can be determined. Pedestal shifts, gain variations and discriminator thresholds can be taken into account with this method. However, no reliable model of image charge effects exists at this time.

The turn on curve for the SLOC was done using the TWOGAM trigger, which was known to be fully efficient at a p_{\perp} of 1.8 GeV/c. Recall that the TWOGAM trigger is a special coincidence of low threshold SLOC triggers. The ratio SLOC • TWOGAM/TWOGAM is plotted as a function of p_{\perp} . The calculation of p_{\perp} is done by using the reconstructed energy to estimate the energy in the r strips. The summing of overlapping groups of 16 strips is simulated and the value of p_{\perp} determined. The efficiency curve was fitted to a function of the following form:

$$P(r, p_{\perp}) = \frac{N}{\sqrt{2\pi}\sigma(r)} \int_{-\infty}^{+\infty} dx \theta(p_{\perp} + x - \tau(r)) \exp(-x^2/2\sigma^2(r)) \quad (D.3)$$

where $P(r, p_{\perp})$ is the probability a trigger was satisfied which deposited transverse momentum p_{\perp} at the position r . The integral is a convolution of a step function and a gaussian which represents an ideal discriminator affected by gaussian noise. The parameters τ and σ are the threshold and smearing respectively. Each octant is divided into five regions on the basis of statistics. The r dependence of the trigger is determined by taking the eight strips with the highest p_{\perp} and assigning that as the triggering p_{\perp} .

The pretrigger turn-on curve was made using events with SLOC triggers, and examining the octant opposite the trigger octant. The energy of the octant was reconstructed using EMREC and the strip energies estimated. The global summing scheme was simulated and a value of triggering p_{\perp} assigned. A p_{\perp} distribution for events with a pretrigger and an unbiased p_{\perp} distribution were made. The quotient distribution is the pretrigger turn-on curve. To accommodate the summing scheme each octant was divided into two regions, corresponding to inner and outer r . A fit was done to the turn-on curve for each octant, using equation D.3, although the r

dependence was simply averaged over each region. Due to a lack of statistics the outer regions' results were averaged over all octants.

There is an additional trigger correction of a purely geometrical nature. The correction is for dead octants and dead regions of octants. It is computed by dividing the number of octants by the number of active octant regions corresponding to the region that triggered the event. This correction is necessary for calculating the absolute cross sections, but can be ignored when making relative distributions *i.e.* γ -to- π^0 ratios.

To find the acceptance and reconstruction efficiency for π^0 s a monte carlo generation of events with a single π^0 was performed. The π^0 s were generated uniformly in a grid from 3.0 – 10.0 GeV/c in p_{\perp} with 0.5 GeV/c bins and $-0.85 - 0.85$ in Y with 0.2 bins. 1000 events were generated per unit mesh in the grid. The π^0 s were required to have asymmetry less than 0.75 on input to a GEANT simulation of the LAC. EMREC was run on the GEANT output and the number of π^0 s reconstructed per unit mesh was determined, yielding the correction $\epsilon_{acc}(y, p_{\perp})$. The acceptance and reconstruction efficiency for direct photons was determined in a similar fashion. The inefficiencies for photons occur at the inner-outer ϕ boundary and near the edges of fiducial regions.

A π^0 can be lost if one of its decay photons converts in the target material. The conversion probability is a function of the vertex z position in the target. A photon can be assigned a probability that it did not convert in the target material. The conversion correction for π^0 s is the square of the reciprocal of this probability, while for direct photons it is just the reciprocal

D.3 PHOTON ENERGY CORRECTIONS

Photons impinging on the front face of the EMLAC typically lose energy in the material between the event vertex and the calorimeter. In fact, there are nearly three radiation lengths of material between the outside surface of the dewar vessel and the upstream face of the electromagnetic calorimeter alone! One would therefore expect a net energy loss as a function of photon energy, which manifests itself in a systematic shift in the calorimeter's energy scale. By studying the energy scale one can determine a single function of energy which will compensate for this systematic effect on the measured photon energies.

There are other systematic effects on the energy scale, namely ambiguities in the amplifier gains, the ADC pedestals, and energy losses near the fiducial boundaries. In order to simplify the monte carlo simulation of the detector, used in this study, the pedestal shifts and gain variations were determined using the calibration procedures available during data taking. In addition, the energy losses around fiducial boundaries were compensated for by adjusting the energies of photons used in reconstructing π^0 s. This was accomplished by fixing the reconstructed π^0 mass at its nominal value. Only photon pairs with a separation greater than 5.0 cm were used for this procedure. By using separated photons one is guaranteed that no systematic correlations due to reconstructed energy sharing between the two photons occurs. The absolute energy scale was then set with the electron calibration beam data as will be described shortly. The corrections for these effects are applied to the DST data so that the energy loss corrections are independent of them.

The solution to the energy loss problem has required many months of work on the part of several individuals [53]. Only the highlights will be presented here. To start with conversion electron pairs were reconstructed from the tracking system data.

Those conversion or zero mass pair (ZMP) tracks that matched to EMLAC showers within the fiducial region of the detector were used to compute the ratio shower energy to tracking momentum. These E/P ratios were then plotted as a function of shower energy. The point at 100 GeV was determined from the calibration data, which used a 100 GeV electron beam. This was done because the track momentum resolution begins to suffer systematic uncertainties greater than 1% at momenta ~ 100 GeV/c. The E/P ratio was set to one for the calibration data point, thereby establishing the absolute energy scale for the EMLAC. This calibration factor was then applied to the E/P ratios for the ZMP data. An E/P ratio was constructed for each octant. The values of E/P thus determine an energy loss correction for electron showers as a function of their measured energy.

The corresponding correction for photons was obtained by running a monte carlo simulation of the calorimeter apparatus, including the inactive material between the target and photon detector. The mean energy loss per unit solid angle in the interval $E \rightarrow E + \Delta E$ was used to estimate the actual energy loss of photons and electrons in the inactive material. This mean energy loss is obtained from well known formulas governing the behaviour of minimum ionizing radiation [54]. The alternative to this approach is to implement a full showering scheme in the monte carlo; such a scenario was unrealistic for the computing power then available to the collaboration. The photon and electron shower energies were reconstructed by EMREC and the ratio of photon to electron energies computed as a function of the reconstructed photon energy. This ratio can then be used together with the E/P ratio obtained for showering electrons to determine the EMLAC energy scale for photons as a function of their reconstructed energy.

This method for ascertaining the reconstructed photons' energy scale was checked by calculating the γe^+e^- mass spectrum, using the reconstructed electron track momenta. By utilizing the tracking information the width and position of the mass peak

for the π^0 would be determined solely from the photon energy resolution and energy scale uncertainty. The peak revealed that the energy scale uncertainty is within the required tolerance and the width is consistent with an energy resolution of $18\%/\sqrt{E}$. Furthermore, the two photon mass spectrum for π^0 s and η s in which the two photons are separated by more than 5.0 cm were also found to be consistent with an energy scale uncertainty on the order of 1% and the above quoted energy resolution.

The photon energy corrections for the data vary according to energy, octant and run set. The corresponding set of corrections for the monte carlo, which is used to compute the π^0 background, vary only according to energy. The monte carlo energy scale corrections were determined from the two photon mass spectrum for separated π^0 s. Again, the use of separated π^0 s uncouples the energy scale correction from the effects of systematic energy sharing between two reconstructed photons that are in close spatial proximity to one another.

BIBLIOGRAPHY

- [1] R. Hagedorn. *Relativistic Kinematics*, pages 67–79. Benjamin/Cummings Publishing Co., Inc., 1978.
- [2] F. E. Close. *An Introduction to Quarks and Partons*, pages 320–322. Academic Press, 1982.
- [3] Chris Quigg. *Gauge Theories of the Strong Weak and Electromagnetic Interactions*, page 223. Benjamin/Cummings Publishing Co., Inc., 1983.
- [4] F. E. Close. *op. cit.* pp. 312–325.
- [5] G. Alteralli and G. Parisi. Asymptotic freedom in parton language. *Nuclear Physics B*, 126:298–318, 1977.
- [6] J. F. Owens. Large-momentum-transfer production of direct photons, jets, and particles. *Reviews of Modern Physics*, 59(2):494, 495, 1987.
- [7] T. Ferbel and W. R. Molzon. Direct photon production in high-energy collisions. *Reviews of Modern Physics*, 56(2):181, 1984.
- [8] Armando Lanaro. π^0 Production with Hadron Beams at 530 GeV/c. PhD thesis, University of Rochester, 1989. pp. 120–127.
- [9] V. Radeka and W.J. Willis. Liquid-argon ionization chambers as total absorption detectors. *Nuclear Instruments and Methods*, 120:221–226, 1974.

- [10] D. Dunlap. How front/back separations affect the shower shape. Internal Note 075, E-706, 1982.
- [11] T. Ferbel. Comment on front/back separation for EMLAC. Internal Note 049, E-706, 1982.
- [12] William E. Desoi. *Construction and Performance of a Liquid-Argon Calorimeter for Use in Experiment E-706 at the Fermi National Accelerator Laboratory*. PhD thesis, University of Rochester, 1990. pp. 57–61.
- [13] William E. Desoi. *op. cit.* pp. 55–68.
- [14] Dana D. Skow. *A Study of High Transverse Momentum η Meson Production*. PhD thesis, University of Rochester, 1990. pp. 63–71.
- [15] E. Engels. Silicon position sensitive detectors for the helios (NA 34) experiment. *Nuclear Instruments and Methods*, 253:523–529, 1987.
- [16] F. Sauli. Principles of operation of multiwire proportional and drift chambers. Publication, CERN, 1977.
- [17] P. Morse and H. Feshbach. *Methods of Theoretical Physics*. McGraw Hill, 1953.
- [18] T. Trippe. Minimum tension requirements for charpak chambers' wires. Internal Report 69-18, CERN, 1969.
- [19] R. Hammerström et al. Large multiwire proportional chambers for experiment NA3 at the CERN SPS. In *Wire Chamber Conference, Vienna*, 1980.
- [20] S. Ferroni et al. Development of large planar proportional chambers. *Nuclear Instruments and Methods*, 178:77–83, 1980.
- [21] G. Bergun et al. Very large multiwire proportional chambers for the NA3 experiment. Technical Report 79-13, SACLAY-DPHPE, 1979.

- [22] Keith W. Hartman. *Hadronic Production of Pizero Pairs and Associated Event Structure at 530 GeV*. PhD thesis, Pennsylvania State University, 1990. pp. 39–51.
- [23] F. Sauli. *op. cit.*
- [24] Nanometric Systems, Inc., Oak Park, IL. *Multi Wire Proportional Chamber Readout System*.
- [25] Robert Miller. *Private Communication*.
- [26] Richard S. Benson. *Characteristics of Forward Energy Production in Proton-Nucleus and Pion-Nucleus Collisions at $\sqrt{S} = 31.5$ GeV*. PhD thesis, University of Minnesota, 1989.
- [27] Richard S. Benson. *op. cit.* pp. 40–41.
- [28] Alexandros P. Sinanidis. *Particles Produced in Association with High Transverse Momentum Single Photons and π^0 s in Hadronic Collisions*. PhD thesis, Northeastern University, 1989. pp. 182–196.
- [29] R. Brun. *ZEBRA Data Management System*. CERN, Geneva, Switzerland, 1987.
- [30] John P. Mansour. *High Transverse Momentum π^0 Production from π^- and P Beams at 530 GeV/c on Be and Cu*. PhD thesis, University of Rochester, 1989. pp. 39–59.
- [31] Eric J. Prebys. *A Study of High Transverse Momentum Direct Photon Production from Beryllium and Copper Targets with 530 GeV/c Incident π^- and Proton Beams*. PhD thesis, University of Rochester, 1990. pp. 55–59.
- [32] John P. Mansour. *op. cit.* p. 49.

- [33] F. Lobkowicz. How front/back separations affect the shower shape. Internal Note 199, E-706, 1988.
- [34] Volodia Sirotenko. *Private Communication*.
- [35] Keith W. Hartman. *op. cit.* pp. 106–132.
- [36] Eric J. Prebys. *op. cit.* pp. 58–69, 78–80.
- [37] Keith W. Hartman. *op. cit.* pp. 107–115.
- [38] John P. Mansour. *Private Communication*.
- [39] Eric J. Prebys. *op. cit.* pp. 114–120.
- [40] W.M. Geist. Hadronic production of particles at large transverse momentum: Its relevance to hadron structure, parton fragmentation and scattering. *Physics Reports*, 197:306–307, 1990.
- [41] T. Ferbel and W. R. Molzon. *op. cit.* pp. 206–208.
- [42] T. Akesson et al. A comparison of particles recoiling from high p_{\perp} direct photons and π^0 s at the ISR. *Physica Scripta*, 34:106–110, 1986.
- [43] M. Bonesini et al. The structure of events triggered by direct photons in π^-p , π^+p , and pp collisions at 280gev/c. *Zeitschrift für Physik*, 44:71–78, 1989.
- [44] E. Bonvin. Intrinsic transverse momentum in the $\pi^-p \rightarrow \gamma\gamma x$ reaction at 280 GeV/c. *Physics Letters B*, 236:523–527, 1989.
- [45] Alexandros P. Sinanidis. *op. cit.* pp. 247–250.
- [46] D. W. Duke and J. F. Owens. Q^2 -dependent parametrizations of parton distribution functions. *Physical Review D*, 30(1):49–54, 1984.
- [47] Sudhindra Mani. *Private Communication*.

- [48] Christopher B. Lirakis. *A Study of High Transverse Momentum η production in 530 GeV/c Hadronic Interactions*. PhD thesis, Northeastern University, 1990. pp. 110–112.
- [49] G. Alverson et al. Production of direct photons and neutral mesons at large transverse momenta from π^- and p beams at 500 GeV/c. *Physical Review D*, 1992. Unpublished as of March 8, 1993.
- [50] Robert M. Harris. Isolated single and double direct photon production at cdf. In *The Vancouver Meeting*, pages 719–726. American Physical Society, Division of Particles and Fields, 1991.
- [51] T. Ferbel. Ten years of direct-photon physics. In *Physics in Collision*, page 8, 1988.
- [52] Dhammika Weerasundra. *Private Communication*.
- [53] Marek Zielinski. *Private Communication*.
- [54] Richard Fernow. *Introduction to Experimental Particle Physics*, pages 29–75. Cambridge University Press, 1990.

MICHIGAN STATE UNIV. LIBRARIES



31293008973186